TAL
TECH

DOCTORAL THESIS

Along-Track Satellite Altimetry to Identify Coastal Sea Level Dynamics Using a Synergized Geodetic-Oceanographic Approach

Majid Mostafavi

TALLINN UNIVERSITY OF TECHNOLOGY
DOCTORAL THESIS
11/2024

Along-Track Satellite Altimetry to Identify Coastal Sea Level Dynamics Using a Synergized Geodetic-Oceanographic Approach

MAJID MOSTAFAVI

TAL TECH PRESS

TALLINN UNIVERSITY OF TECHNOLOGY
School of Engineering
Department of Civil Engineering and Architecture
This dissertation was accepted for the defence of the degree 11/03/2024

Supervisor: Prof. Artu Ellmann
                        School of Engineering
                        Department of Civil Engineering and Architecture
                        Tallinn University of Technology, Tallinn, Estonia

Co-Supervisor: Ass. Prof. Nicole Camille Delpeche-Ellmann
                        School of Science
                        Department of Cybernetics
                        Laboratory of Wave Engineering
                        Tallinn University of Technology, Tallinn, Estonia

Opponents: Ass. Prof. Maaria Nordman
                        Department of Built Environment
                        Aalto University, Helsinki, Finland

                        Ass. Prof. Janis Kaminskis
                        Head of Geomatics Department
                        Riga Technical University, Riga, Latvia

                        Ass. Prof. Aive Liibusk
                        Chair of Geomatics
                        Institute of Forestry and Rural Engineering,
                        Estonian University of Life Sciences, Tartu, Estonia

Defence of the thesis: 11/04/2024, Tallinn

Declaration:
Hereby I declare that this doctoral thesis, my original investigation and achievement, submitted for the doctoral degree at Tallinn University of Technology has not been submitted for doctoral or equivalent academic degree.

Majid Mostafavi

_____
                                    signature

Satelliitaltimeetria pikiorbiitse andmestikuga rannikumere veetaseme dünaamika tuvastamine kasutades sünergilist geodeetilis-okeanograafilist meetodit

MAJID MOSTAFAVI

Contents

List of Publications

The list of author's publications, on the basis of which the thesis has been prepared:

I   Mostafavi, M., Delpeche-Ellmann, N. and Ellmann, A., 2021. Accurate sea surface heights from Sentinel-3A and Jason-3 retrackers by incorporating high-resolution marine geoid and hydrodynamic models. Journal of Geodetic Science, 11(1), pp. 58–74. https://doi.org/10.1515/jogs-2020-0120

II   Mostafavi, M., Delpeche-Ellmann, N., Ellmann, A. and Jahanmard, V., 2023. Determination of Accurate Dynamic Topography for the Baltic Sea Using Satellite Altimetry and a Marine Geoid Model. Remote Sensing, 15(8), p. 2189. https://doi.org/10.3390/rs15082189

III Mostafavi, M., Ellmann, A., Delpeche-Ellmann, N. 2024. Long-term and Decadal Sea Level Trend of the Baltic Sea using Along-track Satellite Altimetry. Remote Sens. 16, 760. https://doi.org/10.3390/rs1605076

Author's Contribution to the Publications

The author of this thesis contributed to all the listed publications by:

I.   conceptualizing the study in cooperation with all the co-authors; developing the methodology with all co-authors; processing the data; conducting the analysis and validation of the results and drafting the manuscript in cooperation with all the co-authors; visualizing the manuscript.

II.   conceptualizing the study in cooperation with all the co-authors; developing the methodology with all co-authors; processing the data; conducting the analysis and validation of the results and drafting the manuscript in cooperation with all the co-authors; visualizing the manuscript.

III.   conceptualizing the study in cooperation with all the co-authors; developing the methodology with all co-authors; processing the data; conducting the analysis and validation of the results and drafting the manuscript in cooperation with all the co-authors; visualizing the manuscript.

Introduction

Accurate and compatible sea level determination is vital for accessing changes in our climate and has significant implications in various applications such as marine engineering, navigation, and ocean sciences. One of the key questions often arising with utilizing sea level data are: which sea level source is the best that can be confidently used for determining offshore sea level variations? This study examines this subject from the perspective of utilizing one of the newest remote sensing techniques of satellite altimetry. In addition, we also explore the development of novel methods that can be implemented for sea level validation both in the coastal and offshore areas.

It is important to know that variations in sea level can be derived using multiple methods. This includes in-situ observation which involves tide gauge (TG) and buoy, remote sensing techniques such as satellite altimetry (SA), airborne laser scanning and global navigation satellite system (GNSS), and numerical modelling, that yield hydrodynamic models (HDM). However, a major challenge arises from the fact that these data sources differ often in terms of (i) spatio-temporal resolutions, (ii) references to vertical datum and (iii) accuracies and configurations. This disparity leads to a significant incompatibility issue, both in space and time, which can affect the accuracy and utility of these data sources.

The solution, proposed in this thesis is that utilizing a high-resolution marine geoid allows us to effectively integrate and synergize the various data sources. By utilizing this approach, it becomes possible to coherently merge different datasets, thereby creating an accurate spatio-temporal sea level model. Also, this approach indirectly identifies and quantifies problematic issues with the various data sources.

Examining the pros and cons of the various sea level sources demonstrates the motivation for the methods developed in this thesis, especially that of the validation phase. For instance, TG has traditionally been relied upon as a reliable source for measuring sea level variation (Cipollini et al., 2017). However, they suffer from limitations that prevent a broader scope analysis. For example, TGs are mostly land-bounded stations, meaning that: (i) the sea level interpretation is primarily representative within the coastal area of its location, typically within a few kilometres; (ii) since the TG are attached to land, any movement from land mass can influence the measurements and this measurement, resulting in what is known as relative sea level (RSL). For instance, regions affected by tectonic uplift or subsidence may experience vertical land motion (VLM), which is often geographically non-uniform and needs to be accounted for; (iii) the vertical datum i.e. the zero-reference point of most TGs is usually tied to some national or local vertical datum (e.g. chart datum, national reference datum), which may not be compatible on an international/global scale.

HDMs on the other hand offer the capability to produce sea level variability with extensive spatio-temporal resolution. These models utilize various inputs, including bathymetry, meteorological, atmospheric, and tidal data as well as ocean currents and circulation patterns, boundary conditions, etc. They are typically based on Navier-Stokes mathematical equations, which incorporate meteorological, hydrological, and bathymetry data as inputs (Lehmann, 1995; Ophaug et al., 2015). However, there are constraints associated with HDM that hinder its effectiveness, for instance: (i) HDM attempts to model realistic conditions of the ocean, which is inherently turbulent. The complexity of the ocean dynamics makes it challenging for models to precisely simulate reality, leading to modelling uncertainties and errors associated with input

parameters; and (ii) the vertical datum of many HDMs is often undisclosed or unknown making it difficult to compare or complement them with other data sources. Consequently, when comparing in-situ TG sea level measurements at the coast with the closest HDM data point, differences often exist between the HDM-derived sea level and the TG observation. This discrepancy can be interpreted as a bias ($Bias_{HDM}$), primarily consisting of all modelling errors, including vertical reference bias and the HDM computational errors.

Another widely utilized sea level data source that employs remote sensing techniques is Satellite Altimetry (SA). Since the 1990's SA has provided global absolute sea level (ASL) data, ranging from coastal to offshore areas, with respect to an Earth-fixed geocentric coordinate system. The operational principle of the SA measurement involves an altimeter attached to a satellite platform that emits pulses of microwave radiation toward the sea surface to estimate the distance between the satellite and the sea surface, known as the SA range (R). The satellite altitude (h_{SA}) above an ellipsoid (mathematical model of the shape of Earth), is obtained using positioning systems, e.g. satellite laser ranging (SLR), Global Positioning System (GPS), and Doppler Orthography and Redisposition Integrated by Satellite (DORIS) (Schreiner et al., 2023). A commonly used variable derived from SA data is sea surface height (SSH), where SSH = satellite altitude – range.

Multiple SA missions operate with different constellations and orbits, continuously collecting precise sea level estimates using onboard altimeters that work with radar or laser pulses. These SA missions follow predefined ground tracks, both ascending and descending, as they orbit the Earth. The SA orbits are associated with an international terrestrial reference frame (ITRF) which may differ from other sea-level data sources. Contrastingly, TGs are usually referred to as a national vertical datum. In addition, the different SA mission datasets may reference different ellipsoids and consequently, an ellipsoidal correction (ΔE) may be necessary for the inter-comparison of multi-SA missions.

One of the most significant limitations of SA is attributed to inaccurate return signals that do not always reflect the actual sea surface but instead may bounce off other substances such as land, ice, and atmosphere. As a result, the most critical or inaccurate data may often originate with the coastal areas where islands, archipelagos, and dynamic conditions may occur. Another limitation of SA data is its temporal resolution or re-visit time of the same location. Typically, the SA revisit time or so-called cycle is within the range of 10 to 35 days. This indicates that smaller temporal-scale ocean dynamics may not be adequately captured by SA. Additionally, its spatial resolution is typically around 300 m along the track, but large gaps between satellite tracks exist. As a result, capturing of some mesoscale processes may be challenging to infer, although larger-scale dynamics are still available.

In recent decades, significant progress has been made in improving the accuracy of SA data by refining the determination of necessary corrections, including atmospheric and geophysical corrections. Additionally, improvements have been made in the development of advanced waveform retracking algorithms, particularly emphasizing coastal areas. Despite these advancements, coastal areas within <10 km of the coastline still pose a challenge for SA data accuracy. These areas are often critical hubs for marine activities, hazards, recreation, and various other coastal activities. Given the multitude of missions launched (e.g. Sentinels, Jason, SWOT, etc.), each with its advancements, it becomes imperative to assess the performance of these missions, particularly in

complex coastal areas. This can be achieved through comparisons with TG and HDM data. This thesis explores these methods through **Publication I** and **Publication II** also its application of **Publication III**.

An important acknowledgment is that sea level data is characterized by different terms, each with different physical interpretations. For example, sea surface height (SSH) is commonly used with SA data. Hence the SSH refers to the ellipsoid, although the ellipsoid is a mathematical approximation of Earth's surface, and this does not represent the real sea surface. Instead, referencing the geoid (equipotential surface of the Earth) is more practical, and sea level referred to as this is associated with Dynamic Topography (DT). Therefore, DT = SSH – geoid height (N). The DT has important physical meaning and can identify sub-mesoscale features of the ocean.

The geoid therefore plays an essential role in determining DT by SA data. Geoid is a mathematical approximation of the Earth's gravitational potential, and it is determined using gravity data. The calculation of the geoid is typically done using the Stokes-Helmert approach (Vaníček et al., 1999; Ellmann and Vaníček 2007) on both regional and global scales. In this study, the focus is on the usage of a high-resolution geoid model, which provides detailed information at a few km resolutions. The separation between the ellipsoid and geoid is the geoid undulation or geoid height (N). Unlike other parameters, such as sea level, the geoid height does not typically change with time. However, changes in Earth's internal mass materials can lead to slow variations in the geoid height over time, or so-called geoid changes (ΔN).

Therefore, SA data presents an ideal solution for monitoring sea level changes as it directly measures the actual sea surface, providing both coastal and offshore data. However, for SA data to be truly efficient, two main conditions must be met: i) availability of a high-resolution geoid model; and ii) validation using other in-situ data sources such as TG.

The Baltic Sea region is favourable towards these requirements having computed a regional high-resolution geoid model i.e. NKG2015 geoid (Ågren et al., 2016) and a dense network of TG stations (over 70 stations), that all are referred to the geoid as their vertical datum. Also, since the Baltic Sea region is influenced by VLM, an accurate VLM model is available. The presence of these datasets makes this region an ideal location for validation and utilization of SA data. Thus, such research direction is explored in this thesis in **Publications I–III**.

The hypothesis of this thesis proposes that by synergizing the various sea level sources (i.e. SA, TG, and HDM), it is possible to enhance the accuracy of the corrected dynamic sea level dataset. Additionally, this integration has the potential to identify the persistent and semi-persistent problematic locations both for each data source, such as areas affected by ice presence for SA data and limitations in HDM due to the modelling issues. Thus, in **Publication II**, a method was developed to combine all the available datasets, resulting in improved sea level measurements and identification of sources of data with inherent problems, allowing for targeted improvements in data quality and reliability.
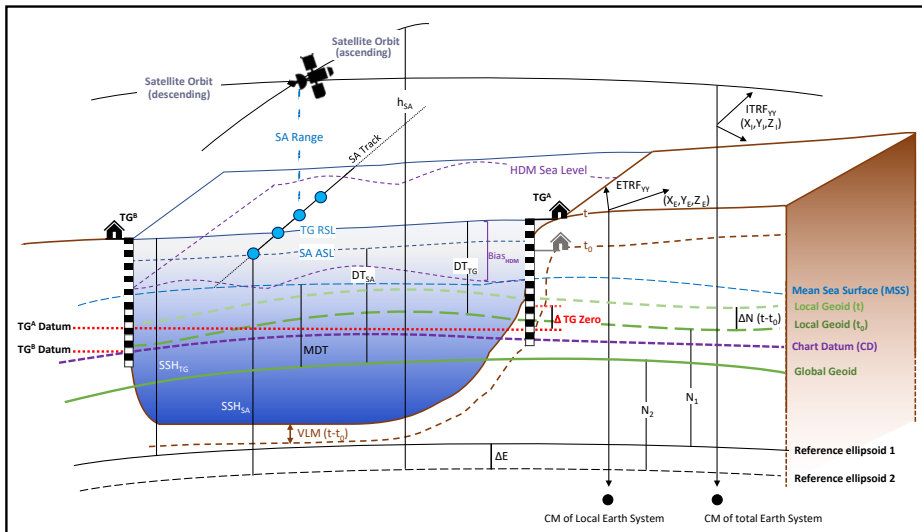
*Figure 1: Inter-relations between the participating datasets (hydrodynamic model, tide gauges, and satellite altimetry data) and geoid model, involved characteristics, and the difference between vertical references (Modified from **Publication II** and **III**).*

Rising sea levels, both globally and regionally, serve as indicators of climate change. Building upon the methodologies developed in **Publication I** and **Publication II**, the results of these methods have been applied to determine sea level trends in the Baltic Sea region. Despite extensive research on sea level trends, the precise magnitude of these changes remains uncertain. Much of the focus has been on changes in the global mean sea level (GMSL), with estimated trends varying between 2 to 4 mm/yr depending on the dataset used and the timeframe considered (e.g., Wöppelmann et al., 2009, Church et al., 2011, Jevrejeva et al., 2008, Cazenave et al., 2014; Hay et al., 2015, Chen et al., 2017, Ablain et al., 2017, Oppenheimer et al., 2019, Rateb et al., 2023).

While attributing sea level changes to global-scale climate variability, these studies fall short in providing insights into regional-scale variations. The Baltic Sea region is also affected by the post-glacial rebound thus making it necessary to calculate and understand both RSL and ASL trends. Previous studies have calculated RSL in the Baltic Sea to be between 1–3 mm/yr (Madsen et al., 2019 and Kapsi et al., 2023) and ASL rates between 3–6 mm/yr (Madsen et al., 2019, Pajak et al., 2019, Passaro et al., 2021, Kapsi et al., 2023). These were all of course examined using different data sets and different time spans. SA however has shown to be capable of determining sea level trends. So, in this study the focus is on using along-track SA data and specifics in the coastal area.

Scope and Objectives

The utilization of SA as a reliable sea level source has progressed throughout the years and has shown vast capabilities in monitoring our dynamic marine areas. This is supported by the continuous launch of missions equipped with improved sensors and complementary technology. However, as previously mentioned, SA also has drawbacks, particularly in coastal areas where land contamination can corrupt the SA signal, posing challenges in obtaining reliable and accurate data in these regions.

Publication I focuses on evaluating the performance of improved SA technology by comparing two different missions, Jason-3 and Sentinel-3A, along with their standard and improved retrackers. The study area, the Gulf of Finland, includes diverse features such as archipelagos and islands. Various datasets, including TG, HDM, and high-resolution regional geoid model, are utilized to analyse data from the coast to offshore. This publication introduces the concept of combining TG and HDM data to develop a synergized geodetic-oceanographic approach for validation purposes. Addressing the challenge of the unknown vertical reference in HDM, a simple shift is applied to achieve bias-corrected HDM data, essential for validating SA data points offshore. This study assesses SA performance in coastal areas, focusing on data accuracy and proximity to the coast for reliable SA data. Results indicate that the adaptation of localized retrackers produces more valid SA data points closer to the coast compared to standard retrackers. Additionally, the study highlights the potential of HDM to represent offshore sea level variability using a correction mechanism, which is further explored in **Publication II**.

The objective of **Publication II** was to develop a comprehensive method for accurately determining DT across the entire Baltic Sea. Building upon the findings of **Publication I**, which identified the most suitable localized retracker and examined the associated multi-mission SA data, this paper focused on computing SA-derived instantaneous DTs (DT_{SA}) in conjunction with a high-resolution regional marine geoid model. Through the synergistic analysis of these datasets, an inter-comparison was conducted, revealing interesting results. The primary outcome highlighted the capability of SA to provide a more detailed and realistic representation of DT compared to numerical models, primarily due to its higher spatial resolution. Additionally, the method employed enabled the identification of certain persistent and semi-persistent problematic areas associated with issues originating from each dataset, such as ice coverage for SA data. Moreover, inter-comparisons among multi-mission SA data facilitated the unveiling of potential deficiencies in the geoid.

In **Publication III**, an extensive exploration into sea level trend variations spanning nearly three decades has been undertaken, utilizing both SA and TG time series. The primary objectives of this study are: (i) firstly, to assess the ability of SA in estimating sea level trends in comparison to TG observations, and (ii) to quantify ASL and RSL trends by using SA and TG, deliberately excluding those located in areas identified as problematic in **Publication II**. This investigation has been done over two time frames: a long-term analysis spanning from 1995 to 2022 (28 years) and a shorter-term focus on decadal trends. The delineation between the ASL (estimated via SA) and RSL (estimated via TG) trends holds significant potential for measuring and validating VLM, particularly in regions lacking accurate VLM models. Furthermore, the study incorporates the extraction of TG observations coinciding with the SA cycle for trend estimation. The outcomes of this comparative analysis underscore the limitations of TG observations for trend estimation, especially for the stations with data gaps and specific site locations. This study emphasizes the need for understanding the limitations and advantages of each dataset in accurately estimating regional sea level trends.

So, in essence, this study at first demonstrates the method for determining instantaneous DT by utilizing along-track SA sea level data with a high-resolution geoid. The novelty of this study however lies not in the derivation of DT_{SA} but instead in the innovative validation phase, which involves the synergy of various other sea level data

sets (TG, HDM). The method developed for validation allows realistic comparison both coastal and offshore and solves the spatio-temporal and vertical reference datum limitations of the various data sources. Also, because of synergizing various sea level datasets we innovatively identify problematic geographic locations and sources of data. The utilization of SA data in this manner has not to our knowledge been performed before in other SA sea level studies. Finally, the calculation of long and short-term sea level trends is performed using the knowledge of the problematic areas and associated data sources that are not reliable.

In summary, the primary objectives of this thesis are first to ascertain a realistic sea level which enables the identification of the sea dynamics including the sea level trend. The thesis encompasses the following objectives:

- To examine and validate different SA datasets that have employed different retracking algorithms with the aim of determining the most suitable one, especially in the coastal areas for sea level variations (**Publication I**).
- To develop a method for the determination of DT as a reliable sea level dataset for sea level dynamics spanning from the coastline to offshore regions (**Publication I** and **II**).
- Identify semi-persistent and persistent problematic regions associated with each dataset (SA, HDM, or geoid) through a synergistic analysis of multi-mission along track SA data, HDM, and TG data (**Publication II**).
- Quantify ASL and RSL trends in the Baltic Sea by using multi-mission along track SA and TG observations over long- and decadal-term periods (**Publication III**).
- Comparison of sea level trend estimates using other data products including the gridded modelled data (**Publication III**).

Limitations and Challenges

There are some limitations in the presented investigations that have been addressed:
1. The limitations associated with the determination of accurate DT by each dataset:
    a. A common vertical reference datum for the multinational TG stations network. In most regions worldwide a comprehensive zero level for all associated TG stations is not available and this could differ from each data provider. Also, these data could shift at different times due to various reasons. Furthermore, the difference between the measurement systems (such as the tide system) could cause discrepancies between the station's observations.
    b. TG observations are limited to certain permanent locations (such as harbour) which are mostly located at protected locations on the coast which could affect the data quality of TG observation. Also, these observations have no insight into the offshore area and are only valid within a specific radius of the site location.
    c. The SA provides SSH variations globally and it is common to use global geoid to convert the SSH to DT. However, the global geoids do not have insufficient spatial resolution and accuracy for regional purposes.
    d. SA has unreliable data in the vicinity of the coast due to land contamination of signal echo which could lead to corrupted waveform especially when the SA overfly from land to the sea.

e. Another limitation of SA is due to the spatio-temporal resolution of SA data. The SA provides data along its pass and cannot provide any insight into sea level variations between these tracks. Also, The SA can only provide these data according to its revisit cycle which is varied from 10 to 35 days. These limitations can hinder the comparison of the SA with HDM.

f. HDM vertical reference datums are mostly undisclosed or unknown which makes its correction essential when comparing it with the SA data.

g. The spatial resolutions of HDMs are less than the SA data hence an interpolation method is needed when comparing it with the SA. However, the sea level changes in the sea cannot be easily interpreted using a simple interpolation.

2. There are certain limitations for trend estimation including:

a. The data gap in TG observation over a long period of data could have a negative impact on the accuracy of decadal sea level trend estimations. This can lead to under/overestimating of the sea level trend over specific areas.

b. Inaccurate VLM model can affect the sea level trend estimations over some regions (such as the Baltic Sea) hence a comparison of both ASL and RSL trends is necessary.

3. The other limitations in this study are associated with the study area. The Baltic Sea is a semi-enclosed sea with special characteristics that could affect the reliability of both sea level and sea level trend estimations such as:

a. The presence of numerous archipelagos and islands over the coastal area is affecting negatively the SA-derived sea level determination.

b. The presence of seasonal sea-ice especially in the sub-arctic latitudes is also affecting the SA data quality.

c. High fluctuation of annual mean sea level variations can also affect the estimation of sea level trends, especially over short-time periods including the decadal trends.

Outline of the Thesis

The dissertation is organized into four sections aimed at defining, addressing, and resolving specific problems. To maintain clarity, these sections prioritize essential details and definitions, while more detailed explanations can be found in related publications. **Section 1** explains the background theory, offering a theoretical overview and principles for determining dynamic topography, especially with respect to satellite altimetry. **Section 2** details the methodology used to analyse sea level variations using SA data and TG observations via oceanographic and geodetic methods. It encompasses necessary corrections to harmonize both datasets for comparative purposes together with the explanation of the methods to correct the HDM for comparison with SA and TG datasets. This section also provides a brief overview of sea level trends and evaluates the regional sea level trend estimations. **Section 3** introduces the study area and datasets, providing insights into the obtained results and facilitating discussions around them. Finally, **Section 4** serves as a conclusive discussion, summarizing and wrapping up the thesis by connecting the defined problems, methodologies applied, and the resulting conclusions.

Abbreviations

ASL	Absolute Sea Level
ALES	Adaptive Leading Edge Subwaveform
BSCD2000	Baltic Sea Chart Datum 2000
CD	Chart Datum
CS2	Cryosat-2
DAC	Dynamic Atmospheric Correction
DORIS	Doppler Orthography and Redisposition Integrated by Satellite
DOT	Dynamic Ocean Topography
DT	Dynamic Topography
ENV	Envisat
ERS2	European Remote-Sensing Satellite-2
ETRF	European Terrestrial Reference Frame
EUMETSAT	European Organisation for the Exploitation of Meteorological Satellites
GDR	Geophysical Data Records
GEOS	Geodynamics Experimental Ocean Satellite 3
GFO	Geosat Follow-on Satellite Mission
GGM	Global Gravitational Model
GMSL	Global Mean Sea Level
GNSS	Global Navigation Satellite System
GPS	Global Positioning System
HDM	Hydrodynamic Model
IDW	Inverse Distance Weight
ITRF	International Terrestrial Reference Frame
JA1	Jason 1 Satellite Altimetry Mission
JA2	Jason 2 Satellite Altimetry Mission
JA3	Jason 3 Satellite Altimetry Mission
LRM	Low-Resolution Mode
MA	Moving Average
MAD	Median Absolute Deviation
MDT	Mean Dynamic Topography
MLE	Maximum Likelihood Estimator
MSS	Mean Sea Surface
OCOG	Offset Centre of Gravity
OST	Ocean Surface Topography
POD	Precise Orbit Determination
PP	Peaky Peakness
RGM	Regional Geoid Model

RMSE	Root Mean Square Error
RSL	Relative Sea Level
S3A	Sentinel-3A Satellite Altimetry Mission
S3B	Sentinel-3B Satellite Altimetry Mission
S6A	Sentinel-6a Michael Freilich
SA	Satellite Altimetry
SAR	Synthetic Aperture Radar
SLA	Sea Level Anomaly
SLR	Satellite Laser Ranging
SRL	SARAL/Altika
SSH	Sea Surface Height
STD	Standard Deviation
TG	Tide Gauge
TRF	Terrestrial Reference Frame
VLM	Vertical Land Motion
WLS	Weighted Least Squares Retracker
VS	Virtual Station

Symbols

$Bias_{HDM}$ — Bias between HDM and TG

$Bias_{HDM}^{VS}$ — Bias of HDM at VS location

DT_{HDM} — DT of HDM

$DT_{HDM-corrected}$ — DT of corrected HDM

$DT_{observation}$ — DT of observed data from TG

DT_{TG} — TG derived DT

$DT_{TG@VS}$ — DT of TG approximated at VS location

$DT_{TG@SA\ cycle}$ — DT of TG at the time of SA cycle

$DT_{Relative}$ — Difference between HDM-derived DT at the location of TG and VS

DT_{SA} — SA-derived DT

$DT_{SA@TG}$ — SA-derived DT at the location of TG

ΔDT_{HDM-TG} — Difference between DT_{TG} and DT_{HDM}

ΔDT_{SA-HDM} — Difference between DT_{SA} and DT_{HDM}

$H_{mean-tide}$ — Height in mean tide system

$H_{zero-tide}$ — Height in zero tide system

$N_{mean-tide}$ — Geoid height in mean tide system

$N_{zero-tide}$ — Geoid height in zero tide system

h_{SA} — Satellite altitude with respect to a reference ellipsoid

R — Satellite range

SSH_{SA} — SA-derived SSH

SSH_{HDM} — HDM derived SSH

$MEAN_{HDM-TG}$ — Mean of difference between DT_{TG} and DT_{HDM}

STD_{HDM-TG} — Standard deviation of the difference between DT_{TG} and DT_{HDM}

N — Geoid height

ΔN — Geoid height changes

Φ, λ — Geodetic coordinates: latitude and longitude

t_i — Time Instant

t_0 — Time epoch

t_{cycle} — Time instant of SA cycle

w — Weight

ΔR — Range correction for SA

ΔE — Ellipsoidal correction

β_t^o — The observed trend at the period of t

β_t^e — Estimated trend at the period of t

1 Background on Sea Level Sources

This study explores various methods of utilizing Dynamic Topography (DT) derived from Satellite Altimetry (SA), emphasizing the synergy of different sea level data sources, especially in the validation process and the identification of data source issues. Over recent decades, significant improvements have been made in SA, ranging from technical advancements to supplementary enhancements, all aimed at achieving accurate and precise sea level determination. To comprehend the fundamental theory of sea level measurement via SA and the intricate steps involved, it is imperative to delve into the basics. The validation phase is particularly crucial in this thesis, showcasing the capabilities of SA, especially in coastal areas where tide gauges (TG) are commonly utilized. Additionally, hydrodynamic modelling is employed for offshore areas, further enhancing validation efforts. Therefore, gaining insight into the background of TG and Hydrodynamic Models (HDM), along with understanding key aspects that render them suitable as ground truth data, is essential. This comprehensive understanding lays the foundation for effective validation methodologies and contributes to advancing the accuracy of sea level determinations.

1.1 Satellite Altimetry (SA)

Since the 1990's SA-derived sea level data has become a valuable remote sensing technique globally utilized for studying climate changes and ocean dynamics. One of the most important characteristics is that it provides highly accurate spatio-temporal measurements of sea level relative to an Earth-fixed geocentric coordinate system (ASL). These features make it a more comprehensive and realistic technique compared to other sea level sources.

The basic concept of SA measurement is that it utilizes a radar altimeter, it transmits and receives radar signals to determine sea level measurements along the satellite's track. The satellite altimeter collects data in the along-track direction, aligning with the path of the SA platform. Measurements are obtained from the nadir direction, pointing vertically towards the force of gravity. The SA satellite follows a regular, repeating orbit around the Earth, known as a cycle, during which it revisits the same trajectory at specific intervals, forming an orbit pass. These passes can be ascending or descending, depending on whether the satellite is above the local horizon as viewed from the ground target.

However, a notable limitation of SA lies in its restricted applicability near the coast. Originally designed for open ocean measurements, radar echoes close to the coast exhibit distorted waveforms compared to the standard shape of the Brown model (Brown 1997) due to interference from nearby land. These distorted waveforms pose challenges for conventional retracking algorithms, leading to inaccuracies in range calculations.

SA altimeters can be operated in two distinct modes: Low-Resolution Mode (LRM) and Synthetic Aperture Radar (SAR). LRM employs traditional pulse-limited altimeter operation, constructing a waveform by tracking the reflected signal as it spreads radially across the surface. In contrast, SAR aims to achieve high along-track resolution, especially over relatively flat surfaces, by capitalizing on the Delay/Doppler effects within the return signal. Unlike LRM, SAR does not rely on the radial distance of signal spread but instead focuses on the width of the signal stripe. The Delay/Doppler technique involves coherently processing a group of pulses within each burst,

performing Doppler processing over the 64 pulses in the along-track dimension, generating 64 Doppler beams. Each received pulse contains information about the sea surface response over the circular footprint. This approach enhances the precision of measurements and is particularly valuable in addressing various challenges associated with coastal altimetry.

1.1.1 Measurements Principles and Challenges

The fundamental principle of sea level determination via SA from space involves measuring the range (R) between the satellite and the sea surface. This is achieved by the radar altimeter, which emits a radio signal with a known power towards the sea and then receives the signal that returns to the satellite (Figure 1). The received pulse is mixed on board with a pulse similar to the one initially emitted, triggered by tracker information. This mixed pulse is commonly referred to as the 'individual echo', and it offers a sampled measurement of the return power, representing a function of time, distance, or frequency. To mitigate the effects of statistical fluctuations (known as speckle) that can impact individual echoes and to facilitate real-time tracking, these echoes are averaged on board over a period that corresponds to the altimeter's duty cycle. The resulting signal is termed an 'averaged echo' or 'waveform'. By measuring the time, it takes for the signal to return to the satellite, the distance between the satellite and the sea surface can be estimated through a process called waveform retracking.

However, when the radar altimeter passes over topographic surfaces, its onboard tracking system struggles to keep the echo waveform at the nominal tracking position within the filter bank due to rapid variations in the range. This discrepancy leads to an error in the transmitted range, known as the tracker offset. The term 'retracking' is used to describe a set of non-linear ground processing techniques that aim to determine the tracker offset from the telemetered echoes, thereby allowing for the estimation of the range to the point of closest approach on the Earth's surface.

The radar signal's precision in estimating range is influenced by a variety of geophysical phenomena occurring during its journey between the satellite and the Earth's surface. These effects must be taken into consideration, due to their potential to introduce significant amplitude variations, ranging from decimetres to meters. The reflection of the radar signal at the sea surface is subject to the prevailing sea state, which can introduce a potential bias in the radar altimeter's range estimation. Additionally, as the radar echo traverses the atmosphere, its propagation experiences delays caused by various atmospheric effects. These delays can result in apparent height errors and need to be minimized through the use of correction models. The primary atmospheric delay effects encompass the presence of ionized particles in the upper atmosphere, known as the ionosphere, as well as the atmospheric composition of the lower atmosphere, particularly concerning water vapor. Accurate correction models are essential for accounting for these effects and improving the precision of range estimations obtained from radar altimetry data.

Furthermore, it's crucial to have accurate knowledge of the satellite's altitude, as this information serves as the reference point for nadir altimeter range measurements, a key component of the precise orbit determination (POD) process. Two primary measurement systems used for POD are DORIS and GPS. These systems play a vital role in monitoring the satellite's altitude with high precision, and they could be complemented by SLR, which provides exceptionally precise determinations of the

satellite's orbit. Consequently, SA faces several key challenges, including achieving accurate POD, addressing the various necessary corrections (such as instrumental, geophysical, and tidal corrections), handling problematic regions (like coastal areas, inland water bodies, and sea-ice conditions, especially in regions like the Arctic or sub-Arctic), and ensuring consistency with in-situ observations, encompassing the terrestrial reference frame (TRF), height system, tide system, and VLM measurements. These challenges collectively contribute to the robustness and reliability of SA data, particularly in complex and dynamic environments where precise SA measurements are of utmost importance.

SA data is classified into various levels, ranging from level 0 to 4, with specific levels of data processing and correlations applied at each stage. For this study, the level-2 data have been utilized which corresponds to geophysical data records (GDR) and is particularly well-suited for geodetic, oceanographic, and environmental investigations. At the level-2 data stage, essential corrections are applied by space agencies, encompassing instrumental and waveform calibrations, ensuring that the data is of high quality and accuracy. Typically, this data is formatted in NetCDF and is made available in both low-resolution (1Hz) and high-resolution (20Hz) variations. Additionally, the level-2 data includes essential correction models and validation flags, which provide valuable information to researchers and analysts, aiding in their studies related to Earth's geodetic and oceanographic characteristics as well as its environmental dynamics.

1.1.2 SA Missions

The history of satellite radar altimetry dates to the first onboard altimeter Skylab 3 (July–Sept 1973), with a precision of 0.6 meters. Subsequent missions, such as GEOS-3 (1975–1978), improved precision to 25 cm. The Seasat mission (June–Oct 1978) demonstrated the potential of satellite radar altimetry for monitoring sea levels with an impressive accuracy of 0.05 m. This success paved the way for subsequent missions like Geosat (1985–1990), ERS-1 (1991–2000), Topex/Poseidon (1992–2005), and GFO (1998–2008), marking the onset of the high-precision altimetry era. Since then, SA has been widely employed in various Earth science applications, including global and coastal oceanography, hydrology, geodesy, and cryosphere research, spanning over three decades. The sea level trend study (**Publication III**) utilizes the most reliable SA data, starting from the ERS-2 mission, to investigate sea level variations. The timeline of the utilized SA missions is illustrated in Figure 2, and the specific characteristics and constellations of each SA project, including orbit, cycle, and pass details, are summarized in Table 1. Also, more details of SA missions and different retracker algorithms have been explained in **Publications I** and **II**.
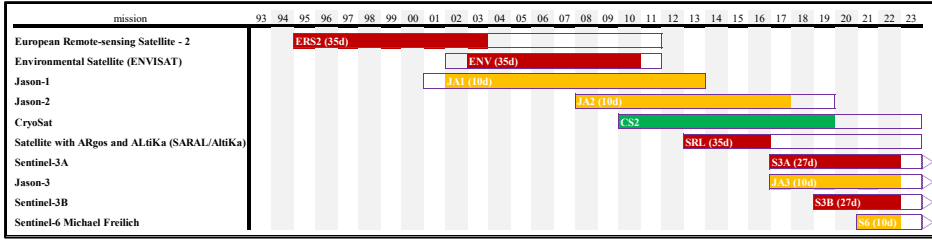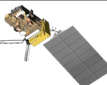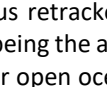
*Figure 2: Timeline of the altimeter missions used in this study. Each SA launch date and duration is shown in the box (arrow for continued missions) and the data timeline for this study is illustrated by colours based on the mission's constellation (orbit coverage; ~66°: yellow, ~98°: red, ~92°: green). The SA revisit cycles in days unit (d) are also indicated for each mission (from **Publication III**).*

Table 1: Characteristics of satellite altimetry missions used in the sea level trend study.

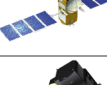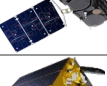| SA mission		Altimeter	Mode	Altitude [km]	Inclination [°]	Cycle [days]
ERS2		RA	SAR	785	98.5	35
ENV		RA-2	SAR	800	98.5	35
JA1		Poseidon-2	LRM	1324	66	10
JA2		Poseidon-3	LRM	1324	66	10
CS2		SIRAL	SAR-LRM	717	92	– [1]
SRL		AltiKa	SAR	800	98.5	35
S3A		SRAL	SAR	814	98.6	27
JA3		Poseidon-3B	LRM	1336	66	10
S3B		SRAL	SAR	814	98.6	27
S6A		Poseidon-4	SAR-LRM	1336	66	10

1.1.3 Waveform Retracking

Numerous retrackers have been designed to offer a global solution, with a common feature being the adoption of the Brown model (Brown 1977). This model is particularly suited for open ocean conditions. This approach allows for a standardized and globally applicable solution for SA retrackers, making it suitable for various oceanic conditions.

---

[1] CS2 has a nonsun-synchronous polar orbit it has 5344 orbits with repeat cycle of 369 days.

The retracking point is defined relative to the shape of the whole echo and found using a model fitting method. The offset of the retracking point from a reference point can be calculated which is called retracking correction. There are multiple types of retracking algorithms including (i) Analytical Retrackers which use a mathematical model to reproduce the waveform (e.g., Brown-Hayne model (Brown 1977; Hayne 1980), Ocean (Ray et al., 2015)), (ii) Empirical Retrackers which focus on the statistics of the waveform (such as Threshold, Offset Centre of Gravity, OCOG (Wingham et al., 1986), MLE (Challenor and Srokosz 1989; Tokmakian et al. 1994), WLS (Maus et al. 1998; Sandwell and Smith 2005), unweighted-LS) and (iii) Innovative Retracking Techniques such as ALES+ (Tuomi et al., 2023).

This study involved a comparative analysis of two primary standard retrackers (Ocean for the S3A mission and MLE4 for the JA3 mission) that are part of the original dataset. Additionally, a recently developed state-of-the-art retracker (ALES+) was included in the assessment. The performance of these retrackers was thoroughly examined in **Publication I**. Subsequently, the most effective retracker among them was selected for further investigations, which were carried out in **Publication II** and **Publication III**. This systematic approach allowed for the identification of the best-performing retracker, and its continued use in subsequent studies aimed at advancing our understanding of the subject matter.

1.1.4 SA Geophysical and Range Corrections

Determination of instantaneous along-track sea level variables from SA range measurements requires careful consideration of multiple perturbations and the subtraction of various corrections (details mentioned on Tuomi et al., 2023) to account for different physical phenomena including:

(i) Propagation Corrections: The altimeter radar wave experiences perturbations as it passes through the atmosphere, including the ionosphere and troposphere. To account for these perturbations, propagation corrections are essential.

(ii) Electromagnetic Bias: The radar wave is influenced by the sea state, leading to an effect known as electromagnetic bias or sea state bias. This effect needs to be corrected for accurate sea level determination.

(iii) Geophysical Corrections: These corrections account for various geophysical phenomena, including ocean, solid earth, polar tides, and loading tide effects.

(iv) Atmospheric Dynamics Correction: The ocean's response to atmospheric dynamics, particularly high-frequency variations, is addressed through dynamic atmospheric correction (DAC). By incorporating these corrections, the SA range measurements can be transformed into an accurate representation of sea level data. However, given the focus of this study on instantaneous DT, some of these corrections need to be excluded (e.g., DAC and ocean tide correction).

1.2 Sea Level Sources

The height of the sea surface can be interpreted by various parameters including Sea Surface Height (SSH), Dynamic Topography (DT), or Sea Level Anomalies (SLA). The difference between these parameters is the reference datum which they are referring to. SSH is referenced to an ellipsoid and SLA is the difference between the sea surface and its temporal average which is called the Mean Sea Surface (MSS), i.e. SLA = SSH-MSS. The MSS is the averaged SSH over a time period and it is considered semi-stationary. MSS is a relatively steady-state sea level within a finite time period

(Andersen and Knudsen 2009) which makes it time-dependent and unstable through different eras (as it contains information about sea level variation at multiple time scales, such as seasonal and interannual variations) and has large errors in sub-mesoscale features (Pujol et al., 2018) although it is widely used in many physical oceanographic applications and other disciplines (Schaeffer et al., 2012; Guo et al., 2022).

On the other hand, DT which is also known as Ocean Surface Topography (OST) and Dynamic Ocean Topography (DOT), is the difference between the instantaneous SSH and the equipotential surface of the Earth's gravity field or the geoid which is static and more reliable datum. Hence, DT represents a realistic quantification of ocean dynamics and can lead to identifying sub-mesoscale features rather than SSH.

The time-averaged DT or Mean Dynamic Topography (MDT) is the difference between MSS and the geoid where both are referenced to the same ellipsoid and a permanent tide system. MDT is a tool in oceanography to measure the long-term strength of ocean currents and the ocean's mean surface circulation (Fu and Cheney, 1995, Knudsen et al., 2011, Becker et al., 2014, etc). It can also be used for height datum purposes (e.g., Featherstone, 2000, Featherstone and Filmer, 2012, Filmer and Featherstone, 2012, Filmer et al., 2018) in geodesy. Therefore, the terminology and quantification of DT, MSS, and MDT have different interpretations as outlined by Equation (1) to Equation (3) below:

$$DT = SSH - N \qquad (1)$$

$$MSS = \sum_{t=1}^{n} SSH_t \qquad (2)$$

$$MDT = \sum_{t=1}^{n} DT_t = MSS - N \qquad (3)$$

where t is the number of time-instances and DT_t and N is the geoid height, SSH is the sea surface height.

1.2.1 Hydrodynamic Model

Hydrodynamic models (HDM) are a useful sea level data source that can provide an overview of the ocean dynamics conditions both at the coastal and offshore areas. HDM has been widely used in various research studies due to its various advantages such as spatio-temporal resolution, data availability and capable of representing the sea level of coastal areas with reasonable quality. Nevertheless, it is anticipated that there will be certain constraints in HDM sea level estimations. The primary limitation arises from the undisclosed vertical reference, which may be an arbitrary surface based on the zero level of the open boundaries condition (relative to their reference surface) and can fluctuate both spatially and temporally and is ideally referred to as an equipotential surface (Slobbe et al., 2014; Rulent et al., 2020; Jahanmard et al., 2021). In addition, errors and bias are also expected from HDMs due to modelling errors which are mainly due to parametrization, approximations, model forcings also the model's input sources errors (e.g., river discharge, bathymetry, and coastal topography data, etc.).

Consequently, the HDM can achieve greater efficiency when identifying the modelling errors and bias. This can be performed by comparison of its results with another sea level source. In this study, two HDMs (including the HBM-EST and Nemo-Nordic NS01 models) were selected for further analysis and investigations in the selected study area (see **Section 3.1.1**). They were compared with TG and SA data

source. The applied methods are fully explained in **Publication I** and **Publication II.** The corrected HDM by cooperating with the TG data can serve as a reliable source of sea level variation offshore where the SA data can be validated and vice versa. The method developed to accomplish this was an important aspect of this thesis. These data sources can now be used for investigating the sea level dynamics. This includes the identification of problematic areas associated with each data source, such an approach has not before been performed in this study area. Also, the SA-derived DT data was used for estimating the sea level trends in **Publication III**.

1.2.2 Tide Gauge

Tide gauges (TGs) are coastal monitoring stations primarily situated along the coast, providing historically accurate and highly precise sea level measurements over an extensive duration, although with some limitations. TGs are land-bounded coastal stations, and as such their measurements are referenced to the local ground level. They primarily monitor relative sea level (RSL), which is sensitive to the crustal motions including vertical land motion (VLM). In certain areas such as active tectonics and volcanic, regions susceptible to substantial ground subsidence stemming from various natural factors (e.g., sediment loading in river deltas) or human interventions (e.g., groundwater extraction and oil or gas drilling), as well as postglacial rebound locations, TG measurements are directly impacted by influenced by the corresponding ground motions. Hence, the TGs are relative to the land and VLM correction is necessary for interpretation with absolute sea level (ASL).

$$RSL = ASL - VLM \qquad (4)$$

Another constraint associated with TGs is their uneven spatial distribution along coastlines, limiting their capacity to provide RSL exclusively along the shoreline, which is not representative of offshore conditions. Also, for long-term sea-level studies, many TGs have not maintained continuous operation, resulting in anticipated significant data gaps. Another difficulty arises from data inhomogeneity when considering multiple TG networks from various providers, which may be referenced to different local vertical datums. TG data are often referred to as the theoretical MSS, Lowest Astronomical tide LAT (e.g., United Kingdom, Australia), chart datum (CD), or an arbitrary datum (specified by the data provider). The Baltic Sea Chart Datum 2000 (BSCD2000) is a new vertical datum to be utilized especially in the Baltic Sea region.

1.2.2.1 Vertical Land Motion (VLM)

Vertical Land Motions (VLM) are influenced by both internal and external geodynamic factors exhibiting spatial variations (Ostanciaux et al., 2012; Santamaría-Gómez et al., 2012). These VLM can manifest in two primary ways. First, they may contribute to rapid subsidence, coupled with a high regional sea level rise, resulting in increased coastal inundation, and necessitating the relocation of coastal communities. Conversely, observed VLM can primarily be attributed to glacial isostatic adjustment (GIA), leading to a net sea level retreat due to the crust uplifting faster than the RSL rise (Steffen and Wu, 2011). To gain a comprehensive understanding of the sea level fluctuations in coastal regions, it is crucial to quantitatively assess both the crustal and marine influences. VLM introduces additional spatial heterogeneity, typically within the range of ±10 mm/year (Ostanciaux et al., 2012; Santamaría-Gómez et al., 2012).

The use of direct GPS measurements provides an advantageous approach to VLM modelling as it accounts for all sources of VLM (Santamaría-Gómez et al., 2012).

However, collocated GPS observations are only available for a small subset, less than 5%, of tide gauges. Geodetic measurements offer another means of detecting VLM using SA and TG data. Understanding VLM is essential for comprehending long-term relative sea-level changes, with GIA playing a dominant role in Fennoscandia (Kuo et al., 2004).

1.2.2.2 Geoid model

The geoid heights (N) are needed to retrieve DT from the SA-derived SSH estimates. Typically, the geoid model relies on a Global Gravitational Model (GGM), a mathematical representation of Earth's external gravitational potential (like EGM2000). Despite recent advancements in remote geodetic techniques, like geopotential mapping satellite missions, which have facilitated the development of higher-resolution GGMs, obtaining reliable terrestrial data remains a challenge. However, in certain areas with access to more accurate and densely distributed sets of gravity and terrain data, the creation of Regional Gravimetric Models (RGMs) has become feasible. This localized or regional "densification" of data allows for the construction of specific RGMs that improve significantly the resolution and accuracy while remaining consistent with the reference GGM (Pavlis 2012). RGMs are particularly valuable for addressing local applications, including extracting DT from SA data efficiently. In this study, two high-resolution RGMs including EST-GEOID2017 and NKG2015 have been utilized which are specifically developed for the study area (details in **Section 3.1.2**).

1.2.2.3 Permanent Tide System

Tidal acceleration arises from the disparity between the gravitational forces exerted by the Moon and the Sun and the orbital accelerations resulting from the Earth's motion (centrifugal accelerations). The apparent movement of the Moon and the Sun is referred to as the permanent tide effect. The analysis of this permanent deformation defines the concept of tide systems. In terms of the Earth's gravitational field, tide systems have effects on water levels.

Remote sensing 3D positioning such as SA is in a tide-free system where the permanent part of the tidal deformation is not restored. For TG stations, tide systems used for potential differences determined with precise levelling are mixed so-called mean-tide, although there are some TG observations also available in zero-tide systems depending on the data provider. Hence, tidal corrections are necessary to be applied to improve the precision of geodetic measurements. The differences of these gravity fields can be described in terms of spherical harmonics. Because the permanent tidal effects change the gravity field globally, it sufficiently can be described as the flattening of the equipotential surfaces of the Earth's gravity field. Conceptually, the mean-tide, zero-tide, and tide-free ellipsoids have different flattening and equatorial radius.

In remote sensing, 3D positioning, such as SA, is conducted in a tide-free environment where the permanent component of tidal deformation remains uncompensated. When it comes to TG stations, the tide systems utilized for determining potential differences via precise levelling are typically a combination referred to as the mean-tide, although, depending on the data provider, there might also be TG observations available in the zero-tide system (e.g., in Denmark). Consequently, the application of tidal corrections becomes essential to enhance the precision of geodetic measurements. These variations can be expressed using spherical harmonics. Because the permanent tidal effects alter the gravity field on a global scale, it is adequate to describe them in terms of the flattening of the equipotential surfaces of the Earth's gravity field using the conversion

(units in m) introduced by (Ekman 1989). The geoid undulation (N) changes due to the permanent tide systems, from mean tide system to zero tide and vice versa are:

$$N_{zero-tide}(\varphi) = -N_{mean-tide}(\varphi) + 0.09940 - 0.29541(\sin^2(\varphi)) \tag{5}$$

$$\begin{aligned} H_{zero-tide}(\varphi) \\ = H_{mean-tide}(\varphi) + 0.09940 - 0.29541(\sin^2(\varphi) - 0.00042\sin^4(\varphi)) \end{aligned} \tag{6}$$

1.3 Sea Level Trend

Accurately determination of sea level trends is crucial for preparing coastal communities and predicting future projections (Prandi et al., 2021). Detecting these trends is challenging on a regional scale due to greater oceanic variability caused by redistribution effects like winds, making regional estimations more sensitive and error-prone compared to global scale assessments. **Publication III** explores the estimation of both ASL and RSL trends over various time frames using TG and SA data. SA stands as one of the primary sources for generating ASL data and has been extensively utilized in understanding variations in sea level trend estimations for studying climate change.

Estimating sea level trends from various sources involve anticipated uncertainties due to various systematic effects. Including the drifts within the ITRF realizations, errors in geophysical corrections (like tropospheric and ionospheric corrections), and corrections related to VLM, which can generate linear drifts. For instance, the uncertainty in ITRF realization drift can contribute to an uncertainty of approximately ±0.1 mm/yr (Couhert et al., 2015), while VLM correction uncertainties can exceed 0.05 mm/yr (Ablain et al., 2019) in global sea level trend estimation. These uncertainties are closely tied to the length of the time series and significantly escalate when factors such as VLM, reference frame variations, and geoid changes aren't factored in (Ablain et al., 2019).

2 Methodology

It is important to recognize that sea level variations, including Dynamic Topography (DT), can be derived through both geodetic and oceanographic approaches. Although both approaches aim to derive DT, they fundamentally utilize different methods, resulting in inherent differences. The methodology developed in this thesis uses these differences to enhance the validation phase, showcasing the efficiency and reliability of satellite altimetry (SA). Furthermore, it innovatively highlights necessary improvements in datasets and identifies geographical areas where these issues persist. Such utilization of SA data represents a novel approach not previously explored. Below, we outline the methodology of the geodetic approach (**Section 2.1**) and the synergized geodetic and oceanographic approach (**Section 2.2**)

2.1 Dynamic Topography Derivation by Geodetic Approach

The geodetic approach for determining DT consists of utilizing (i) SA and (ii) TG data-sets which are described below. Both sensors derive DT differently, for SA uses remote sensing and TG directly measures the water level.

2.1.1 Geodetic Approach Using SA

Recall that SA can remotely measure the sea level by calculating the time, it takes for the radar pulse to travel to the liquid surface and back to the altimeter by which the satellite's range (R) can be determined. Once the satellite's altitude (h_{SA}) relative to a reference ellipsoid is known, corrections (ΔR) are applied to this range measurement to obtain the SSH_{SA} through the process of satellite altimetry using Equation (7). Because various SA missions may use distinct reference ellipsoids, it becomes necessary to introduce an ellipsoidal correction (ΔE) for each data point (Jekeli, 2006). This correction accounts for the variations in parameters related to each reference ellipsoid, such as the semi-major and minor axes, flattening, and eccentricity. Through the application of ΔE (refer to Equation 2 in **Publication I**, different SA datasets can be aligned with respect to the same reference ellipsoid.

$$SSH_{SA} = h_{SA} - (R + \Delta R) + \Delta E \qquad (7)$$

where ΔR represents a comprehensive correction factor encompassing adjustments for the atmospheric, sea state effects and tidal effects on the SA signal (Equation 10 in **Publication III**). The accuracy of h_{SA} measurement is achieved at a level of 1–2 cm, thanks to the advantages of POD, while the precision of R derivation is within a range of a few centimetres (Normandin et al., 2018). A more accurate representation of sea level can be obtained through the DT, which can be calculated by referencing a geoid surface. To determine along-track $DT_{SA}(\varphi, \lambda, t_{cycle})$ the geoidal height (N) is subtracted from the SSH_{SA} at each data point (φ, λ) and at the time of SA cycle (t_{cycle}) using the Equation (8).

$$DT_{SA}(\varphi, \lambda, t_{cycle}) = SSH_{SA}(\varphi, \lambda, t_{cycle}) - N(\varphi, \lambda) \qquad (8)$$

2.1.2 Geodetic Approach using TG

Another reliable source of the DT variable is provided by land-bounded TG stations that measure directly and accurately the liquid surface by means of pressure sensors or floats. Since TG are usually coast bounded, they usually measure RSL, capturing the movement of the sea surface relative to the land. These observations inherently encompass the contribution of VLM while SA measures ASL and is less sensitive to VLM changes. Over time, variations in the geoid also need to be factored into TG observations. Moreover, TG measurements are closely tied to a national vertical datum, which is different from the SA international terrestrial reference frame. Furthermore, different TGs may reference distinct local vertical datums, necessitating a process of datum unification when comparing TG observations from various data providers. Additionally, TG and SA estimates may be obtained in different permanent tide treatment systems, so a harmonization process is essential for comparing these measurements. Therefore, it is imperative to consider the VLM correction ($VLM(\varphi_G, \lambda_{TG})$) from the reference time epoch (t_0) to the TG observation time record (t_i) and the geoid changes ($\Delta N(\varphi_{TG}, \lambda_{TG})$) corrections to address these discrepancies and enable the use of instantaneous SA data alongside TG observations ($DT_{observation}$).

$$
\begin{aligned}
DT_{TG}&(\varphi_{TG}, \lambda_{TG}, t_i) \\
&= DT_{observation}(\varphi_{TG}, \lambda_{TG}, t_i) + VLM(\varphi_{TG}, \lambda_{TG}).(t_i - t_0) \\
&\quad + \Delta N(\varphi_{TG}, \lambda_{TG}).(t_i - t_0)
\end{aligned} \quad (9)
$$

To compare TG-derived data with the SA, the DT_{TG} can be approximated at the time of SA cycles ($DT_{TG@SA\ cycle}$) within a predefined time window of SA overfly (t_{cycle}). To do this the DT_{TG} have been interpolated linearly before and after the t_{cycle} within a time window (w). Note that the TG could have gap exactly at t_{cycle}, for the TGs with data gap during this period the $DT_{TG@SA\ cycle}$ remains as nan values. $DT_{TG@SA\ cycle}$ is representing the suitable TG derived DT at the t_{cycle} considering low fluctuations of DT within w.

$$
DT_{TG@SA\ cycle}(\varphi_{TG}, \lambda_{TG}, t_i) = interp(DT_{TG}(\varphi_{TG}, \lambda_{TG}, t_{cycle} \pm w)) \quad (10)
$$

2.2 Dynamic Topography Derivation by Oceanographic Approach

Hydrodynamic models (HDM) are considered one of the most reliable sources of sea level data, due to their spatiotemporal resolutions. These models derive sea level by employing a series of Navier-Stokes mathematical equations, coupled with atmospheric, hydrological, and bathymetric driving forces. Essentially, the oceanographic approach involves simulating expected sea level behaviour, termed DT, even though the vertical datum remains unknown. In contrast, the geodetic approach directly measures sea level, either remotely through SA or in-situ via TG. However, two major limitations of HDM are notable: (i) its vertical reference datum is often unknown or undisclosed, and (ii) HDM expected to have modelling errors due to underlying assumptions and approximations. This presents a challenge when comparing HDM data with SA. On the other hand, TG data are known for their reliability. In this study the assumption is that that by comparing the difference between HDM data at coastal areas and TG data, the necessary corrections can be applied to the HDM.

So, in this study we have developed several approaches to address related limitations and rectify the HDM's discrepancies, a correction method needs to be applied to correct

the HDM in order to homogenise the DT_{HDM} with the reality which is referred to here as bias correction method.

The "HDM bias" functions as a corrective measure with the capability to address a variety of issues, such as the spatio-temporal changes in both vertical reference shifts and model errors. This bias correction can be determined by comparing the DT_{HDM} with another reliable and well-defined geodetic reference source of DT i.e. TG data. In this study, two approaches have been applied to correct HDM compared to DT_{TG}. The first method (**Section 2.2.1**) involves only a simplified shift of HDM compared to the closest TG station which is described in **Publication I**. The second method (**Section 2.2.2**), on the other hand, provides a more detailed treatment of the one-dimensional aspect that has been used in **Publication II**. In this study, the objective of correcting the HDM was to facilitate a comparison with SA. Consequently, HDM bias corrections were exclusively implemented at the specific time and location corresponding to SA (at the SA cycle and SA pass).

2.2.1 Simplified Bias Removal Method; Linear Interpolation (Single TG)

The hourly gridded HDM provides an estimation of DT (DT_{HDM}) over its domain for a specific period. Since DT_{HDM} grid points locations may not coincide exactly with the TG locations, thus a linear interpolated method can be utilized to coincide with the TG location ($\varphi_{TG}, \lambda_{TG}$) and approximate at the time (t) of TG record (closest). This variation could be compared with the TG observation in order to estimate a one-dimensional bias ($Bias_{HDM}$) of HDM:

$$Bias_{HDM}(\varphi_{TG}, \lambda_{TG}, t) = DT_{HDM}(\varphi_{TG}, \lambda_{TG}, t) - DT_{TG}(\varphi_{TG}, \lambda_{TG}, t) \qquad (11)$$

where DT_{HDM} and DT_{TG} are DT of each dataset at the location of TG ($\varphi_{TG}, \lambda_{TG}$) coordinates. The DT_{HDM} and DT_{TG} series include hourly observations, whilst the SA cycle occurs at a specific time. Hence, a temporal interpolation is required to estimate both DT_{HDM} and DT_{TG} values for the SA cycle. Then $Bias_{HDM}$ is applied as a constant value to each HDM cell node grid (at SA cycle and pass) to obtain the bias-corrected $DT_{HDM-corrected}$ by TG observation at each HDM grid point (g):

$$DT_{HDM-corrected}(\varphi_g, \lambda_g, t) = DT_{HDM}(\varphi_g, \lambda_g, t) - Bias_{HDM}(\varphi_{TG}, \lambda_{TG}, t) \qquad (12)$$

Finally, the HDM-derived SSH_{HDM} is available anywhere offshore by adding the N to $DT_{HDM-corrected}$:

$$SSH_{HDM}(\varphi_i, \lambda_i, t) = DT_{HDM-corrected}(\varphi_g, \lambda_g, t) + N(\varphi_i, \lambda_i) \qquad (13)$$

2.2.2 Complex HDM Bias Removal Method; IDW Interpolation (Multiple TGs)

One of the main aims is to compare the SA data with the HDM datapoints. So, it seems intuitive to compare SA data with respect to the offshore points than points located on land. In order to correct the HDM-derived DT by multiple TGs (rather than only one), the bias can be calculated at specific locations which are referred here to as "virtual station (VS)". By using the VS the following advantages:(i) the DT_{HDM} be obtained at the same data points as SA (i.e., over each pass and cycle) by selecting the VS at the beginning (and/or end) of the SA pass; (ii) correction of HDM seems to be more accurate at VSs rather than at the nearshore location of TGs, as the HDM could have more errors

near the coast and shallow waters (iii) utilizing multiple TGs advantages which could benefit not just one, but several of them. This multiplicity enhances the accuracy of bias estimation, particularly in regions equipped with extensive TG networks. The method outlined in **Publication II** involves computing the relative difference between the DT of HDM at the position of a TG and the VS location (cf. Figure 2, in **Publication II**). This, in turn, allows for the calculation of DT at the VS based on the TG's measurements. This calculation is executed by incorporating the relative DT difference.

The DT_{TG} may offer validity for offshore regions, particularly in areas equipped with a dense TG network. This validity extends across a valid domain encompassing the location of the VS. It is achieved by incorporating data from adjacent TGs and by adding the relative DT, which represents the DT difference between the HDM location of the VS to the TG observation. In such instances, the DT of the VS is computed through inverse distance weighted (IDW) interpolation of TG records, applied slightly seaward at the VS locations. In (Jahanmard et al. 2021), multiple interpolation methods, such as thin plate spline regression, linear interpolation, and IDW, were examined. The findings indicated an approximate 2 cm difference between these methods. Notably, the IDW method yielded slightly more realistic results. Consequently, a similar procedure was employed in this study for the bias correction. Consequently, VS is assumed to be an enhanced representative of duplicated TGs and is more consistent with HDM data. The bias correction method, which is both time and location-dependent, is introduced for the HDM at a VS through Equations (14)–(16) for each SA pass/cycle.

The determination of VS locations is a critical step and has been carried out by identifying the nearest location with good-quality SA data points close to the coastline. Any SA track includes at least two VSs, positioned at the beginning and end of the track, although some tracks (which cross lands) may have additional along-track VSs situated near the coast and in proximity to TG stations. A VS is intended to represent the k-nearest TGs during a SA pass. To compute the DT at the VS location ($DT_{TG@VS}$), the nearest hourly TG records are linearly interpolated at the SA cycle (t_{cycle}). Subsequently, the relative DT ($DT_{Relative}$) is added to this interpolated value, allowing for the retrieval of DT at the VS location (cf. Figure 2, in **Publication II**):

$$
\begin{aligned}
DT_{TG@VS}&(\varphi_j, \lambda_j, t_{cycle}) \\
&= interp\left(DT_{TG}\left(\varphi_j, \lambda_j, t_{cycle}\right)\right) + DT_{Relative}(\varphi_j, \lambda_j, t_{cycle})
\end{aligned}
\tag{14}
$$

The $DT_{Relative}$ is the difference between the HDM-derived DT (DT_{HDM}) at the location of the VS ($DT_{HDM}(\varphi_{VS}, \lambda_{VS}, t_{cycle})$) and that at the location of the TG ($DT_{HDM}(\varphi_{TG}, \lambda_{TG}, t_{cycle})$). The $DT_{Relative}$ offers a more realistic representation of TG-derived DT at the location of the VS compared to interpolation. This is because to consider the assumption that HDM can provide a reference surface for sea level, albeit not entirely precise.

$$
\begin{aligned}
DT_{Relative}&(\varphi_j, \lambda_j, t_{cycle}) \\
&= interp[DT_{HDM}(\varphi_{VS}, \lambda_{VS}, t_{cycle}) - DT_{HDM}(\varphi_{TG}, \lambda_{TG}, t_{cycle})]
\end{aligned}
\tag{15}
$$

the DT_{VS} is obtainable by adding the $DT_{Relative}$ to the timewise interpolated ($interp\left(DT_{TG}\left(\varphi_j, \lambda_j, t_{cycle}\right)\right)$). The $DT_{TG@VS}$ values adjacent to the VS are averaged using IDW, resulting in the determination of the DT at the VS location, denoted as $DT_{VS}(\varphi_{VS}, \lambda_{VS}, t_{cycle})$. This DT_{VS} value can now be employed to calculate the bias in

the HDM (cf. **Publication II**). The bias of HDM at the location of each VS ($Bias_{HDM}^{VS}(\varphi_{VS}, \lambda_{VS}, t_{cycle})$) can be determined by the difference between DT_{VS} and the initial HDM values DT_{HDM} by below equation:

$$
\begin{aligned}
Bias_{HDM}^{VS}&(\varphi_{VS}, \lambda_{VS}, t_{cycle}) \\
&= DT_{HDM}(\varphi_{VS}, \lambda_{VS}, t_{cycle}) - DT_{VS}(\varphi_{vs}, \lambda_{VS}, t_{cycle})
\end{aligned} \tag{16}
$$

The $Bias_{HDM}^{VS}$ serves to account for both discrepancies in vertical reference datums and errors in HDM modelling. Furthermore, since both HDM and TG data are available at hourly intervals, DT_{HDM} and DT_{TG} are linearly interpolated at the time of t_{cycle}. Additionally, because the spatial coordinates of HDM data points do not precisely align with SA points ($\varphi_{SA}, \lambda_{SA}$), a linear interpolation is employed to apply the $Bias_{HDM}^{VS}$ at SA data points situated between a pair of VSs along SA track. This is denoted as "$interp(Bias_{HDM}^{VS}(\varphi_{SA}, \lambda_{SA}, t_{cycle}))$". This value is then subtracted from the initial DT_{HDM}. Consequently, this process yields the corrected along-track HDM ($DT_{HDM-corrected}$), which is now in alignment and synchronized with SA data locations ($\varphi_{SA}, \lambda_{SA}$) at the SA cycle ($t_{cycle}$).

$$
\begin{aligned}
DT_{HDM-corrected}&(\varphi_{SA}, \lambda_{SA}, t_{cycle}) \\
&= DT_{HDM}(\varphi_{SA}, \lambda_{SA}, t_{cycle}) \\
&\quad - interp(Bias_{HDM}^{VS}(\varphi_{SA}, \lambda_{SA}, t_{cycle}))
\end{aligned} \tag{17}
$$

The $DT_{HDM-corr}$ can be assumed as the first approximation of "ground truth" and can be checked against the SA-derived DT.

2.2.3 Statistical Tests

The existing HDM bias examined using the mean and standard deviation (STD) of discrepancies between original HDM and TG readings denoted by ΔDT_{HDM-TG} at the TG station ($\varphi_{TG}, \lambda_{TG}$) using hourly data ($t_i$) during the whole study period by:

$$
\Delta DT_{HDM-TG}(\varphi_{TG}, \lambda_{TG}, t_i) = DT_{HDM}(\varphi_{TG}, \lambda_{TG}, t_i) - DT_{TG}(\varphi_{TG}, \lambda_{TG}, t_i) \tag{18}
$$

$$
MEAN_{HDM-TG}(\varphi_{TG}, \lambda_{TG}) = \frac{1}{y}\sum_{i=1}^{y}\Delta DT_{HDM-TG}(\varphi_{TG}, \lambda_{TG}, t_i) \tag{19}
$$

$$
\begin{aligned}
STD_{HDM-TG}&(\varphi_{TG}, \lambda_{TG}) \\
&= \sqrt{\frac{1}{y-1}\sum_{i=1}^{y}(\Delta DT_{HDM-TG}(\varphi_{TG}, \lambda_{TG}, t_i) - MEAN_{HDM-TG}(\varphi_{TG}, \lambda_{TG}))^2}
\end{aligned} \tag{20}
$$

where y is the total number of hourly DT records (same for both TG and HDM data) during the study period (i.e., y = years × days × hours).

After the correction of HDM derived sea level they can be considered as the ground truth and can be used for SA validation in term of discrepancies. The ΔDT_{SA-HDM} is the difference between DT_{SA} and ΔDT_{SA-HDM} which can be computed for each footprint point of each participating SA mission by:

$$
\begin{aligned}
\Delta DT_{SA-HDM}&(\varphi_s, \lambda_s, t_{cycle}) \\
&= DT_{SA}(\varphi_s, \lambda_s, t_{cycle}) - DT_{HDM-corr}(\varphi_s, \lambda_s, t_{cycle}) \\
&= SSH_{SA}(\varphi_s, \lambda_s, t_{cycle}) - SSH_{HDM}(\varphi_s, \lambda_s, t_{cycle})
\end{aligned} \tag{21}
$$

where the sub-index s is the SA data point after outlier elimination. The ΔDT_{SA-HDM} can be served as a representative the agreement between SA data and the ground truth within the SA track and for each SA mission. ΔDT_{SA-HDM} statistical analyses conducted by the root mean square error (RMSE), mean and standard deviation (STD).

2.3 Regional Sea Level Trend

Sea level trend can be computed using different data sources. In this study we have employed both TG and SA datasets. The TG based trends are simpler for calculating for they are located at defined locations over time span. However, there may be gaps in data due to sensor malfunction, technological improvements etc. Contrastingly, the SA data exact locations vary however it has been known for spatial and temporal consistency.

2.3.1 Trend Computation

The sea level trend can be determined using both TG and SA dataset. to compare the SA-derived trend with the TG-derived trend, the DT_{SA} close the TG station for each mission and at each pass and cycle have been averaged ($DT_{SA@TG}(\varphi_{TG}, \lambda_{TG}, t_{cycle})$) using below equation:

$$DT_{SA@TG}(\varphi_{TG}, \lambda_{TG}, t_{cycle}) = \frac{1}{m}\sum_{j=1}^{m} DT_{SA}(\varphi_j, \lambda_j, t_{cycle}) \qquad (22)$$

where m is the number of $DT_{SA}(\varphi_j, \lambda_j, t_{cycle})$ data point within the track segment of SA which have been extracted by a certain radius from each TG station (. The sub-index j is the summation counter for m. $DT_{SA@TG}$ will be used to estimate For SA ($DT_{SA@TG}(\varphi_{TG}, \lambda_{TG}, t_{cycle})$) the DT time sample is the SA cycle (t_{cycle}) however for TG the DT are based on the hourly records. Hence, the trend of TG observation at the time of t_{cycle} has been also estimated by $DT_{TG@SA\ cycle}$.

By having DT_{TG}, $DT_{TG@SA\ cycle}$ and $DT_{SA@TG}$ time series, the linear trend rate and acceleration can be estimated using a linear regression method by the ordinary least squares (OLS) estimator (full details on **Publication III**).

The comparison between the estimated trend denoted by β_t^e (e.g., from SA data) and observed trend denoted by β_t^o (e.g., from TG data) has been done using RMSE by below equation:

$$RMSE = \sqrt{\frac{1}{n}\sum_{t=1}^{n}(\beta_t^o - \beta_t^e)^2} \qquad (23)$$

where n is the total number of estimated trends during the study period, the β^e and β^o respective estimated (e.g., by SA) and observed (e.g., by TG) trend values at time t (at different time windows including long-short terms.

2.3.2 SA Optimality Regarding the Distance to TG

The computed trend using along-track SA data provides an opportunity to investigate how sea level trend estimates change regarding the distances from the coastline. Hence, the SA-derived sea level trend results within different distance to the TG can be averaged, to determine the SA sea level trend within that distance away from the TG. These trends can then be compared with the TG-derived trend to provide an insight into the expected sea level validity away from the coast. This comparison aims to

potentially explore scenarios where the TG might not consistently offer the optimal location for determining precise sea level trend estimates. To do this the SA-derived sea level data at different distances away from the TG has been averaged and the estimated trend from each group distance has been compared with the TG-derived trends to find the optimal distance. Detailed results are shown in (**Publication III**).

3 Experiments and Results

This chapter presents the results from all three publications, focusing on different methods employed to determine and validate SA-derived DT. **Publication I** examines various satellite altimetry (SA) missions that utilized different retrackers to assess the performance of coastal retrackers and their advantages. The identification of this retracker is important for precision in monitoring coastal sea level dynamics. A simple method for synergizing the geodetic (TG) and oceanographic approaches (HDM) is developed and presented in **Section 3.1**.

Publication II builds upon the synergized geodetic and oceanographic approach, expanding its scope to a wider geographic area while also identifying problematic areas. This evaluation reveals the reliability and applicability of the chosen retracker methodology, guiding the interpretation of sea level data over diverse geographical features. The findings of this publication are detailed in **Section 3.2**.

Publication III utilizes the insights gained from **Publication I** and **II** to explore sea level trend estimates in the complex marine area of the Baltic Sea. These analyses can contribute to a comprehensive understanding of the regional sea level dynamics and its underlying determinants which is introduced in **Section 3.3**. Each publication contributes unique insights to our understanding of SA-derived DT and its applications in diverse geographic regions. The limitations associated with each utilized dataset have been summarized in Table 2.

Table 2: Limitations and characteristic of used sea level data sources.

Dataset / Characteristic	TG	SA	HDM
Vertical datum	TG zero level	Geoid/MSS	undisclosed
Relative/Absolute	RSL	ASL	unknown
Tide system	Zero Tide	Mean Tide	Mean Tide
Reference frame	local TRFs	ITRFs	unknown
Temporal resolution	hourly	10–35 day	hourly
Spatial resolution	single point	along-track	gridded
Uncertainties	0.005 m	0.01 m	unknown
Availability	permanent stations	worldwide	worldwide
Coastal Data	good quality	problematic	good quality

3.1 Study Area and Datasets

3.1.1 Region of Interest; Baltic Sea

The Baltic Sea is a semi-enclosed, microtidal, marginal sea with geographical boundaries extending from 53°N to 66°N and 10°E to 30°E. It has an average depth of approximately 54 meters and covers a total surface area of 393,000 km^2. Geographically, the Baltic Sea ranks as the world's second-largest brackish water body, following the Caspian Sea, and is bordered by nine countries. The Baltic Sea is further divided into several sub-basins, each delineated by the sea's geomorphology and bathymetry.

The Baltic Sea is connected to the open ocean exclusively through a narrow passage that links it to the North Sea via the Danish Straits. This signifies that there are salt

and fresh water sources present. As a result, it displays a two-layer stratification, characterized by a seasonal thermocline during the summer and a persistent, well-defined halocline throughout the year. The halocline, situated at a depth of approximately 60–80 meters, separates the brackish surface water with a salinity of about 7 psu from the deeper water, which has a salinity of 12 psu. Surface salinity varies from 32 psu in the Kattegat to 1–2 psu in the northern regions (Gräwe et al., 2019).

Long-term sea level fluctuations in the Baltic Sea can be broadly classified into external variations, (Samuelsson and Stigebrandt, 1996). These variations are primarily driven by global factors, such as the expansion of sea level due to the thermal expansion of seawater and changes in the sea level of the surrounding basins. These global effects are transmitted into the Baltic Sea through the shallow and narrow Danish Straits, ultimately influenced by the North Sea. Consequently, these changes in the North Sea have a cascading impact on the sea level in the Kattegat and the freshwater budget of the basins within the Baltic Sea.

As a result, different factors affect the Baltic Sea level based on long- and short-term time scales. In general, on a decadal timescale, the sea level is influenced by a combination of meteorological and oceanographic factors (winds, pressure, temperature, salinity, precipitation, and evaporation). So given the limited exchange with the open ocean, the salinity of the Baltic Sea is particularly sensitive to the cumulative freshwater input it receives (e.g., Meier and Kauker, 2003).

Over shorter timeframes, such as weekly, daily, and hourly intervals, the sea level in the Baltic Sea is influenced by various localized events, many of which are meteorologically driven (Ekman 2009). Winds play a significant role in these short-term fluctuations, and it's worth noting that wind patterns in the Baltic Sea can exhibit strong anisotropic characteristics, as identified (Soomere 2003). Although the prevailing wind direction in the area is typically southwest, northerly winds can also be common. Storm surges (Suursaar et al., 2007) and coastal upwellings (Delpeche-Ellmann et al., 2017) exhibit seasonal trends in the Baltic Sea, with the most intense winds and waves generally occurring during the winter and autumn seasons (Jakimavičius et al., 2017). Moreover, temperature and precipitation variations contribute to a significant portion of the sea level variability between winter and summer (Hünicke et al., 2006).

One distinctive feature of the Baltic Sea region is its susceptibility to VLM due to GIA. In the Gulf of Bothnia, at the centre of the former ice sheet, GIA currently exerts effects of up to 10 mm/yr, gradually decreasing to nearly zero at the edges of the ice sheet, see Figure 3. The ongoing viscoelastic response of the Earth to the last deglaciation is also a significant factor contributes to the sea level variation in the Baltic Sea. This response, along with other effects such as changes in the North Atlantic and GMSL, as well as the influence of wind and waves on erosion and sediment transport, plays a crucial role in shaping the Baltic Sea's sea level dynamics (Weisse et al., 2021).
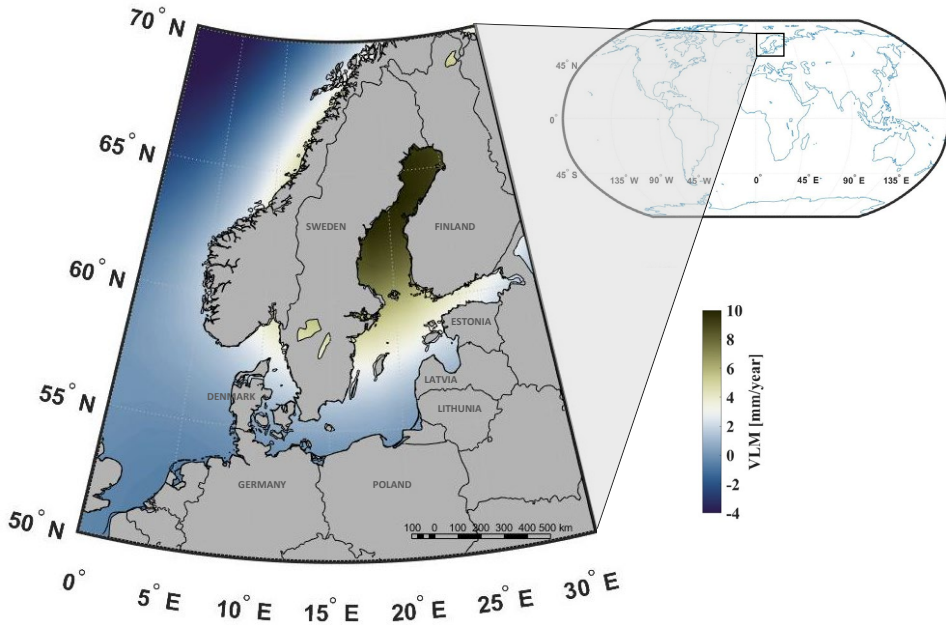
*Figure 3: Location of the study area. The background represents VLM value from NKG2016LU (Vestøl et al., 2019) over Baltic Sea (modified from **Publication III**).*

Over the past five decades, the ASL in the Baltic Sea has exhibited a slighter increase than the GMSL (Gräwe et. al., 2019, Weisse et. al., 2021). This trend is primarily attributed to a corresponding rise in ASL in the North Atlantic Ocean. Notably, the estimated ASL rates for the Baltic Sea are notably higher, averaging around 6 mm/yr. This disparity can be attributed to the unique characteristics of the Baltic Sea.

Sea level extremes also influence the sea level dynamics and are influenced by a multitude of factors, including storm surges and wave-breaking processes, which can have devastating impacts on small islands and their inhabitants (Tadesse et al., 2020 and Scicchitano et al., 2021). Consequently, the cumulative effect of sea level rise poses a significant threat to the Baltic Sea regions, where numerous archipelagos and small islands are found.

During winter months ice coverage is common over the Baltic Sea, especially in the northern part of the sea (62.1°–65.8°N) and the number of sea ice days can influence the sea level dynamics (Rosentau et al., 2017). For instance, during the winter–spring seasons the Gulf of Bothnia is covered by sea ice between 110 to 190 days of the year (Müller et al., 1982).

The Gulf of Finland is a geographically unique marine area situated at the easternmost end of the Baltic Sea studied in **Publication I**. The Gulf of Finland is bordered by Finland to the north, Estonia to the south, and Russia to the east. Its coastline exhibits diverse geomorphology, featuring both cliff-like and low-lying areas with indented coastlines and peninsulas. The coastal region is further characterized by the presence of numerous archipelagos, small islands, and rocks within 10 km of the coastline. It is characterized by its narrow and elongated shape, spanning approximately 400 km in length, and varying in width from 48 to 135 km. The average water depth in the Gulf of Finland is approximately 37 m, with its deepest point reaching 123 m. The gulf's short-term sea level dynamics are influenced by various factors, including

changes in the water balance originating from atmospheric conditions (such as wind direction), the presence of sea ice, and river runoff. Localized events, such as storm surges and coastal upwellings, also contribute to short-term and seasonal variations. Notably, due to prevailing southwest winds, increased storminess, and significant river discharge, particularly from the Neva and Narva rivers, the eastern section of the gulf experiences higher MSS and extreme water levels. For instance, the MSS, averaging from 2014 to 2019, increases eastward within the gulf, ranging from 20 to 29 centimeters (Kollo and Ellmann, 2019). The typical significant wave height in the gulf falls within the range of 0.5 to 0.8 meters, with a maximum significant wave height recorded at 5.2 meters (Soomere et al., 2008).

3.1.2 Datasets

The Baltic+SEAL project introduces an advanced multi-mission sea level data product tailored for the Baltic Sea which has been used as the main source of SA data for **Publication I–III**. This dataset has been meticulously developed and validated, leveraging updated advances in coastal altimetry and data processing techniques. The key component of this data product involves the utilization of two distinct retrackers: ALES+ for the LRM altimeters (such as Jason missions) and ALES+SAR for the delayed Doppler altimeters (such as Sentinel-3 missions), as described by Passaro et al., (2020).

ALES+SAR is tailored for delayed Doppler altimeters and adopts a simplified version of the Brown-Hayne functional form as an empirical retracker, aimed at accurately tracking the leading edge of the waveform. A Pulse Peakiness (PP) index is also employed; however, for S3A data, a PP threshold of less than 3 is used, with additional checks conducted to precisely determine the leading edge. The PP threshold may slightly differ from that used in ALES+. This difference is attributed to variations in the signal-to-noise ratio between the SAR mode and the LRM mode. In contrast to ALES+, the computation of sea state bias in ALES+SAR relies on models (Passaro et al., 2020). This approach offers a distinct methodology for correcting sea state-induced biases. Apart from the Baltic+SEAL dataset, the standard Level-2 data from AVISO and EUMETSAT has been used in **Publication I** (to compare with the Baltic+SEAL data) and **Publication III** (to extend the study period). A consistent set of range corrections has been applied for all SA datasets although the models may be different for some missions (more details in publications). These datasets have been assessed and validated against two HDM models (HBM-EST for **Publication I** and Nemo-Nordic NS01 for **Publication II** and **III**) which have been corrected by the TG data. The main constraint of the HDM data (even after correction) is their spatial resolutions (with 1 NM) compared to the SA data. Hence, the SA data can capture more details of the sea level dynamics (with a resolution of 300 m along its track).

The Baltic Sea region benefits from a dense TG data network with long-term and high-quality local sea level records which is illustrated in Figure 4. The figure background is the NKG2015 geoid model which has been utilized in this study, also in **Publication II** and **Publication III**. In this study, two different geoid models which have been locally developed for the study area have been utilized. Specifically, in **Publication I** the Estonian official geoid model EST-GEOID2017 (Ellmann et al., 2019) and for **Publication II** and **Publication III** the NKG2015 model (Ågren et al., 2016) has been used. For all publications the hourly data has been utilized also for **Publication III** the TG data at the time of SA cycles have been used for trend estimation.
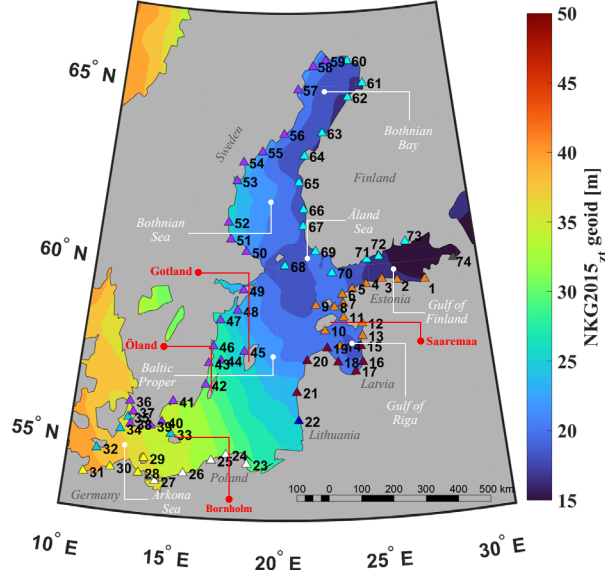
*Figure 4: Available TG network over the Baltic Sea, the background color represent the NKG2015 geoid model (source **Publication II**).*

Figure 4 represents the available TG network over the Baltic Sea with the summarized specifications of each national TG network in Table 3. For this study, TGs are unified by the EVRS-based national height systems i.e. BSCD2000 (Schwabe et al., 2020) which uses the zero-tide permanent tide system. However, the zero-tide system is not typically preferred for oceanographic approaches as it is a latitude-dependent tilt for the sea level variables. Hence the heights relative to BSCD2000 converted to the mean-tide concept for TG observations. Since TG records in the Baltic Sea region refer to NAP, the corresponding relations are written (Varbla et al., 2022):

$$H_{mean-tide}(\varphi) = H_{zero-tide}(\varphi) + 0.2954(\sin^2(\varphi) - \sin^2(\varphi_{NAP})) \qquad (24)$$

$$H_{mean-tide}(\varphi) = H_{free-tide}(\varphi) + 0.2954\gamma(\sin^2(\varphi) - \sin^2(\varphi_{NAP})), \qquad (25)$$
$$\text{where } \gamma = 0.7$$

$$N_{mean-tide}(\varphi) = N_{zero-tide}(\varphi) - 0.2954(\sin^2(\varphi) - \sin^2(\varphi_{NAP})) \qquad (26)$$

where φ_{NAP} is the latitude of NAP (52°22' 53").

Table 3: Specification of TG network based on the country across the Baltic Sea (the triangle colours represent the TGs from Figure 4).

Country	National height realisation	National geoid model	National ETRS89 realisation	Permanent tide system
▲ Denmark	DRV90	DKgeoid12/DVR90G2013	EUREF-DK94	tide-free
▲ Estonia	EH2000	EST-GEOID2017	EURF-EST97	zero-tide
▲ Finland	N2000	FIN2005N00	EURF-FIN	zero-tide
▲ Germany	DHHN2016	GCG2016	ETRS89/DREF91/R2016	mean-tide
▲ Latvia	LHS2000,5	LV14		zero-tide
▲ Lithuania	LAS07	LIT20G	LKS-94	zero-tide
△ Poland	PL-EVRS2007-NH	PL-geoid-2011	EURF89 PL-ETRF200	zero-tide
▲ Sweden	RH2000	SWEN17_RH2000	SWEREF99	zero-tide
▲ Russia	BHS77 (Kronstadt)	--		mean-tide

3.1.3 Auxiliary and Third-Party Data

In addition to the primary dataset detailed in **Section 3.1.2**, this study incorporates additional relevant auxiliary data to enhance clarity and gain insights into the dynamics and primary drivers of sea level variations. The supplementary datasets encompass both physical parameters of the sea and other sea level data sources explained below. This broader scope of data allows for a more comprehensive and nuanced understanding of the intricate factors influencing sea level behaviour in the study area.

1- Sea ice concentration over Baltic Sea by gridded ice chart model available from Copernicus Marine Service Information, www.resources.marine.copernicus.eu

2- Globally gridded SA-derived SLA (https://doi.org/10.48670/moi-00148) computed with respect to a twenty-year (1993–2012) mean from Copernicus Marine Data Store (www.data.marine.copernicus.eu). This SLA is estimated by optimal Interpolation method by merging the Level-3 along-track data from the multiple SA missions. This product is developed by the DUACS (Data Unification and Altimeter Combination System) system. This data has been used **in Section 3.4** (**Publication III**).

3- Baltic Sea Physical Reanalysis product (https://doi.org/10.48670/moi-00013) which include a reanalysis model of the physical conditions for the entire Baltic Sea. This product is developed using the Nemo ice-ocean model. This model is available at the native model resolution (with horizontal resolution of 1 nautical mile and 56 vertical layers). This data has been used **in Section 3.4** (**Publication III**).

4- Baltic+SEAL gridded SA data over the Baltic Sea region. This product provides SSH after the cross-calibrated multi-mission (Passaro et al. 2020). In this products' the SA observations are interpolated on an unstructured triangular grid (i.e., geodesic polyhedron) by 6–7 km spatial resolution. The monthly gridded sea level data are developed by fitting an inclined plane to each grid node using the weighted least square interpolation by considering along-track SSH within a radius of 100 km around the grid node centre (Tuomi et al., 2020). This data has been used **in Section 3.4** (**Publication III**).

All the utilized dataset in this study have been summarized in Table 4.

Table 4: Summary of used data by multiple sources for Thesis sections.

Data source	Section 3.3 Publication I	Section 3.4 Publication II	Section 3.5 Publication III
TG	4 stations	73 stations	13 stations
SA	2 missions	3 missions	10 missions
HDM	HBM-EST	Nemo-Nordic NS01	-
RGM	EST-GEOID2017	NKG2015	NKG2015
VLM	-	NKG2016LU	NKG2016LU
Auxiliary data	NO	YES	YES
Study Period	2017	2017-2019	1989-2022
Study Area	Gulf of Finland	Baltic Sea	Baltic Sea

3.2 Multi-mission SA Retrackers Validation

The first part of this study focuses on the analysis of along-track SA data by comparison between the standard retracking algorithms (Ocean and MLE4) and the Baltic+SEAL project adopted retracker for the Baltic Sea region (ALES+ and ALES+SAR). This analysis was conducted using data from both Sentinel-3A (S3A) and Jason-3 (JA3) satellites, covering a time-span of one year in 2017 over the Gulf of Finland. The details of this comparison are discussed in **Publication I** and are elaborated in three subsections presented here. In **Section 3.2.1**, the examination of the quality and quantity of SA data points as the satellites approach the near-coast regions has been conducted. This examination aims to assess the performance of SA data when transitioning from open ocean to coastal areas. **Section 3.2.2** focuses on investigating the consistency or inconsistency of SA data. This analysis provides insights into the potential biases in the SA data and its accuracy at different TG stations. To determine the most accurate retracker and the overall accuracy of the SA data. This analysis considers various factors and indicators, ultimately aiding in the selection of the most suitable retracker over a limited time (i.e. 2017). These examinations and comparisons are essential steps in ensuring the reliability and precision of SA data, particularly in coastal and near-coastal areas, and contribute to the broader understanding of SA applications in the Baltic Sea region by selecting the best retracker.

3.2.1 Along-track Performance of SSH_{SA}

This study explored the variations in the proximity to the coast at which valuable SSH data can be effectively obtained, considering the different satellite cycles along-track and various retracking. In pursuit of the highest data quantity and quality over near-coastal regions for each dataset, all data points up to the coastline were included, regardless the coastal QC flag, which typically excludes data points near the coast. Subsequently, a further step was taken to enhance data quality by eliminating clear outliers. This was accomplished by implementing a predefined threshold, which considered the difference between $SSH_{SA-corrected}$ and SSH_{HDM}, and any values exceeding a 30 cm difference were identified and removed from the dataset.

An illustrative example can be seen for the Paldiski station, as depicted in Figure 5 on the left side, marked at locations A and B. The focus here is on the quantity of data points that approach the coast. For Figure 5-B, pertaining to JA3 (pass#16 cycle#34), the ALES+ retracker provides 12 additional data points, covering a 4 km longer stretch

than those obtained with the MLE4 retracker. This signifies that the ALES+ retracker significantly enhances the coverage of data points closer to the coast. In the case of the Finnish archipelago, as displayed on the right side of Figure 5-A, it's evident that a considerable number of MLE4 data points (approximately 47 points) have been identified as outliers and subsequently removed. Conversely, in the ALES+ retracker more data points are available near the coastline. This observation underscores that the ALES+ retracker is the more reliable option for obtaining data up to the coast, especially for JA3, as it outperforms the MLE4 retracker by effectively retaining valuable data points after the removal of obvious outliers.
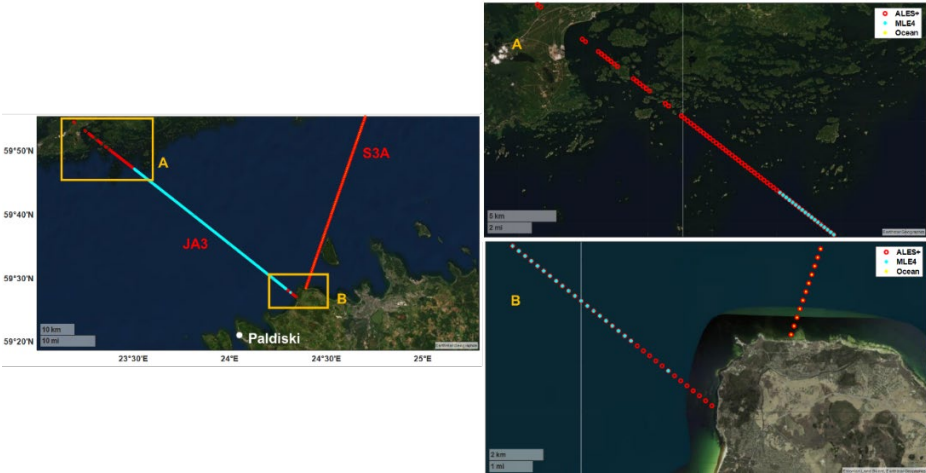
Figure 5: Distribution of near-coast Sentinel-3A (S3A) and Jason-3 (JA3) satellite tracks at the Paldiski station. On the left-hand side, performance of the JA3 track (A) is shown near the Finnish coast using ALES+ (red) and MLE4 (blue) retrackers, while on the right-hand side (B), the performance of JA3 and S3A tracks near the Estonian coast is depicted using ALES+ and ALES+SAR (red), Ocean (yellow), and MLE4 (blue) retrackers. The coastline source is Google Earth (from Publication I).

In Table 5, the average distance from the first available data point to the nearest coastline is provided after removing outliers which vary for each SA cycle. To offer a more comprehensive view, the minimum distance for each cycle at each TG and SA pass is also included. This information provides valuable insights into the proximity of data points to the coastline for each cycle and allows for a detailed examination of the variations in distance between the SA and the coastline.

Table 5: *Average and minimum distances from the first valid SA data point to the nearest coastline (km) after removing outlier data, for each satellite track (from **Publication I**).*

Pass Number	Average Distance [km]		Minimum Distance [km]		Average no. of Outliers	
S3A	**Ocean**	**ALES+ SAR**	**Ocean**	**ALES+ SAR**	**Ocean**	**ALES+ SAR**
Kunda#083	2.77	2.95	2.02	2.02	17	13
Kunda#414	2.07	2.07	1.73	1.73	7	5
Loksa#300	2.32	2.57	1.93	1.93	9	4
Narva-Jõesuu #197	2.74	2.74	2.47	2.47	12	12
JA3	**MLE4**	**ALES+**	**MLE4**	**ALES+**	**MLE4**	**ALES+**
Kunda#092	9.87	8.99	3.29	3.58	8	3
Paldiski#016	6.62	6.72	2.99	2.54	4	3

The results indicate that, on average, valid MLE4 retracker (JA3) data points were obtained at 7 to 10 km from the coastline. For S3A, regardless of the retrackers used (Ocean or ALES+SAR), consistently provided data points, on average, at 2 to 3 km from the coast, with very little difference observed between the two retrackers. This similarity in performance between Ocean and ALES+ SAR retrackers may explain the consistent results for S3A. In comparison between JA3 and S3A, it is evident that a more significant difference was observed with the JA3 satellite. The ALES+ retracker in JA3 demonstrated a higher number of data points located closer to the coast. These findings underscore the influence of the retracker choice on the proximity of data points to the coastline and highlight the potential advantages of specific retracking algorithms for near-coastal observations. Therefore, the choice of satellite and its specific characteristics can significantly impact the performance of coastal observations in satellite altimetry studies. This has been investigated more in **Publication II** which compared three SA data over the entire Baltic Sea.

The remaining question is whether the increased number of data points provided by the retracker algorithms translates into valid and reliable data. Figure 6 illustrates the along-track discrepancies at the Kunda station for each retracker/mission, utilizing all available cycles from 2017, without any outlier removal for an example. In general, a more coherent dataset is observed with the ALES+ and ALES+SAR retrackers when compared to the Ocean and MLE4 retrackers. However, the noisiest section appears to be within the first 10 km due the presence of numerous small islands and archipelagos. In this near-coast area, various marine processes such as breaking surface waves and upwellings, among others, can have a significant impact not only on the sea state but also on atmospheric conditions. An illustrative example is S3A cycle 18 for both the ALES+ SAR and Ocean retrackers at the Kunda station (pass#083) on May 21, 2017, as depicted in Figure 6. The occurrence of such discrepancies throughout the entire track for specific cycles could be attributed to a variety of factors including the degradation in range and geophysical corrections applied, contamination of the waveform by land or bright targets, or potentially influenced by the sea state prevailing at that specific time. These complex and dynamic factors can have an impact on the accuracy and reliability of the SA data for certain cycles, leading to discrepancies observed not only near the coast but also extending along the entire track.
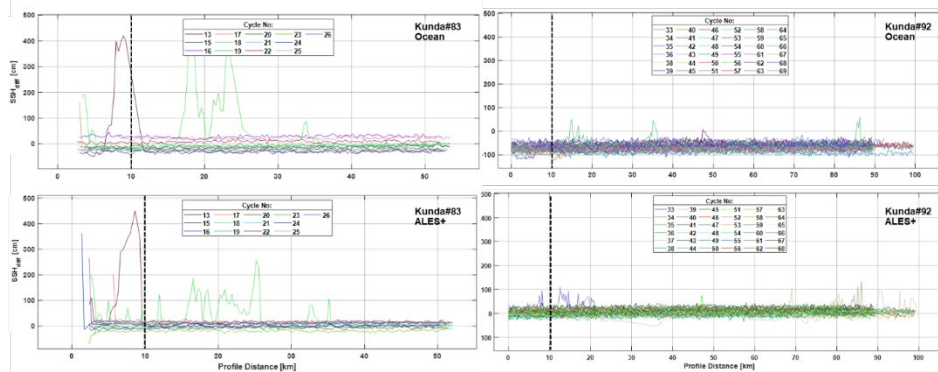
*Figure 6: Discrepancies in Sea Surface Height difference per cycle for Kunda-083 Sentinel-3A (S3A) (left) and Kunda-092 Jason-3 (JA3) (right) tracks. Top panels show results using Ocean retrackers, while bottom panels show results using ALES+ SAR retrackers. The zero value on the horizontal axis indicates the coastline position (from **Publication I**).*

3.2.2 Accuracy of Satellites and Retrackers

An examination of the yearly RMSE between SA and HDM across all stations is presented in Table 6. The comparison between the S3A Ocean and ALES+ SAR retrackers reveals a slight improvement of approximately 0.5 to 1 cm in terms of RMSE when using the ALES+ SAR retracker. In the case of the JA3 satellite, an improvement of 1 cm is observed with the ALES+ retracker compared to MLE4. Overall, the results indicate that the S3A ALES+ SAR retracker performs the best among the examined stations, meeting the target accuracy requirement of better than 5 cm, which is a significant achievement in SA applications.

*Table 6: Statistical estimates of post-fit residuals ΔSSH [cm] for along-tracks SSH from both S3A and JA3, comparing with HBM. Superior performances are highlighted in bold digits (from **Publication I**).*

Pass Number	Max Bias	Mean abs. bias	RMSE	Max Bias	Mean abs. bias	RMSE	No. used cycles
Sentinel-3A	**Ocean**			**ALES+ SAR**			
Kunda#083	-30.15	18.57	4.98	-19.25	9.28	**4.05**	12
Kunda#414	46.27	16.74	5.00	27.79	11.34	**3.95**	13
Loksa#300	-70.2	19.87	4.89	28.07	11.22	**4.25**	12
Narva-Jõesuu #197	49.15	20.65	5.55	39.35	13.37	**5.04**	11
Jason-3	**MLE4**			**ALES+**			
Kunda#092	31.80	10.47	7.75	28.17	9.32	**6.73**	35
Paldiski#016	-26.12	7.50	8.46	32.53	9.60	**7.40**	36

Table 6 clearly demonstrates that the Baltic+SEAL datasets lead to smaller RMSE estimates than the standard Level-2 SA products, which underscores the significant impact of the retracking algorithms and associated corrections utilized in the datasets. It becomes evident that the adoption of a coastal retracker is highly relevant and applicable for the Baltic Sea area. These results emphasize the importance of selecting

appropriate retracking algorithms and correction models, especially when dealing with coastal and near-coastal observations, as they can significantly enhance the accuracy and reliability of the SSH data. Consequently, the Baltic+SEAL data has been selected for further analysis to retrieve accurate sea level variation over the entire Baltic Sea which has been investigated in **Publication II** and briefly here in **Section 3.3**.

3.3 Determining Accurate DT by SA and Geoid Model

Following the selection of the best retracker, the next step is to derive SA-derived DT from multiple SA missions covering the entire Baltic Sea which has been discussed further in **Publication II**. The objective is to evaluate this SA-derived DT against corrected HDM data, both near the coast and offshore. This evaluation is achieved by examining the SA performance along the satellite tracks, focusing on the discrepancies, denoted as ΔDT_{SA-HDM}. Additionally, this study benefits from the synergy of multiple datasets, allowing for the investigation of the spatial patterns of ΔDT_{SA-HDM}. This approach helps in identifying problematic areas or regions with notable discrepancies between the SA-derived DT and the corrected HDM. Such analysis contributes to a comprehensive assessment of the performance of SA data in the Baltic Sea and aids in recognizing areas where further refinement or validation may be necessary. This process ultimately leads to the selection of suitable locations where reliable sea level trend estimation can be conducted. The details of this study have been discussed in **Publication III** and are further elaborated upon in **Section 3.4**.

3.3.1 HDM Validation Against In-situ Observations

The initial step in deriving DT from SA data offshore involves the validation of HDM data (Nemo-Nordic NS01) as an independent data source for sea level, both onshore and offshore throughout the entire Baltic Sea, using 74 TG stations observation. The results of this validation have been visualized in Figure 7, which depicts the mean and STD of HDM data residuals relative to TG observations for a three-year period spanning from 2017 to 2019. In Figure 7, each TG location in the Baltic Sea is represented, with the size of the circle denoting the mean value, while the colour indicates the STD. This presentation allows for a comprehensive view of the accuracy and variability of HDM data relative to TG observations at different locations, aiding in the validation of the HDM data for sea level estimation.
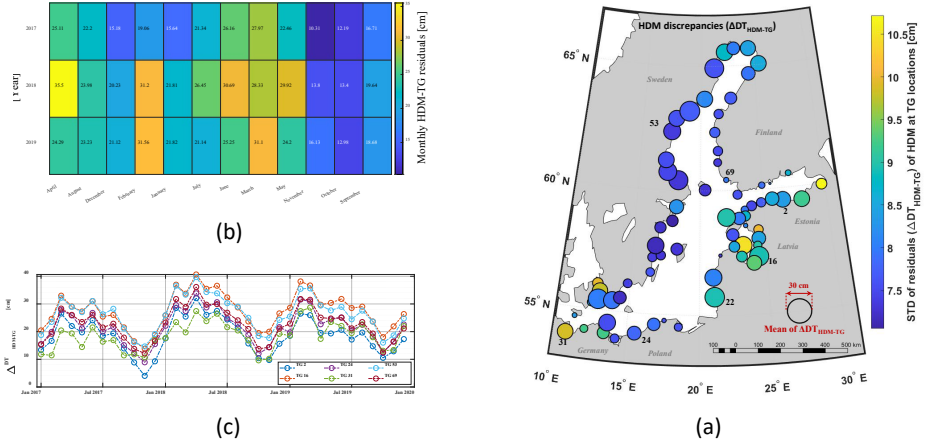
*Figure 7: Statistical analysis of HDM discrepancies in comparison with TGs. (a) Depicts the means (indicated by circle size) and STD (indicated by colours) of discrepancies between Nemo-Nordic HDM and 74 TGs across the Baltic Sea from 2017 to 2019. (b) Shows the monthly average of HDM discrepancies over a three-year period. (c) Displays the monthly average of HDM discrepancies at six selected TG locations (Kunda from Estonia, Skulte from Latvia, Leba from Poland, Travemünde from Germany, Spikarna from Sweden, and Turku from Finland), representing one station from each country with the highest STD or mean discrepancy (from **Publication II**).*

Figure 7-c highlights that the most significant discrepancies in the HDM, reaching approximately 30 cm, are observed during the period from February to March, corresponding to the winter-spring season. In contrast, the smallest discrepancies are evident during the autumn and summer seasons, where they are less than 20 cm. This observed variation can be attributed to a range of factors, including river runoff, snow melting, and other seasonal effects, such as the steric effect. It is possible that some of these seasonal effects may not have been initially incorporated into the HDM data, which explains the need for correction of the HDM data. It's important to note that, for the purpose of this study, the HDM was only corrected at the time instants of the SA cycles, highlighting the importance of accounting for these seasonal variations to improve the accuracy and reliability of sea level data.

3.3.2 SA Along-Track Performance

To assess the performance of DT_{SA} along the satellite track, Figure 8 presents the comparison of three cycles (18, 21, and 26 in 2017) of DT_{SA} with $DT_{HDM-corr}$ (green line) for the S3A pass #272. This pass extends from the southwest to the northern Baltic Sea and serves as a representative example of the HDM and SA data (location indicated in Figure 8-b). This comparison helps evaluate the consistency and accuracy of DT_{SA} data relative to the corrected HDM along this specific satellite track.
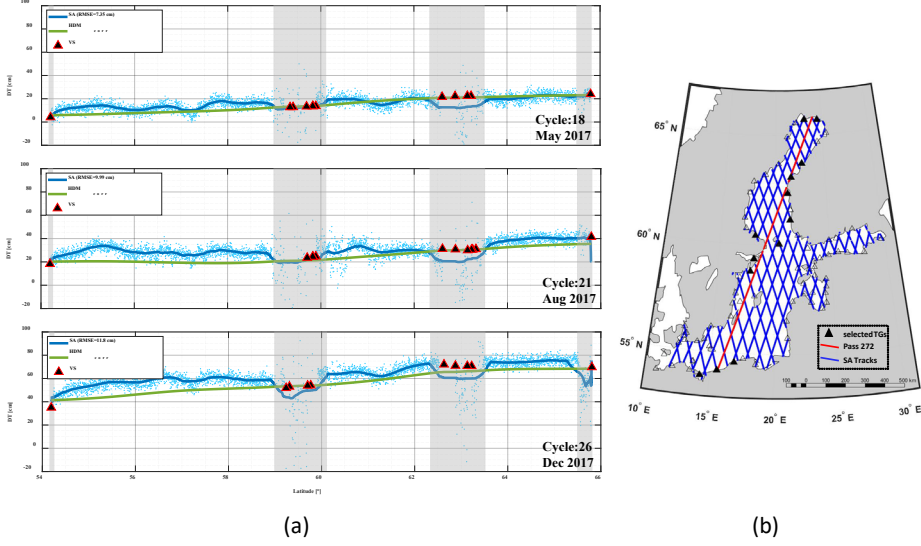
(a)	(b)

*Figure 8: (a) Comparative analysis between Sentinel-3A pass #272 DT (blue dots) and TG-corrected HDM ($DT_{HDM-corr}$) data (green line) for three cycles in 2017. The blue solid line represents the moving average of DT_{SA}, grey zones indicate masked near-coast and land areas, and triangles denote the locations of virtual stations. (b) Depicts the geographical location of Sentinel-3A pass #272 in the Baltic Sea (from **Publication II**).*

Figure 8 presents the actual data points of DT_{SA} (blue dots) with the blue solid line representing the smoothed DT_{SA}. The smoothing was calculated using a Moving Average (MA) over a sliding window of 0.5° latitude length across adjacent DT_{SA} data points. Along-track RMSE values between DT_{SA} and $DT_{HDM-corr}$ were estimated for each cycle. Several key observations can be made from Figure 8 and the accompanying data: (i) seasonal variations in DT are evident. For example, in May 2017, DT varies within the range of 5 to 20 cm, while in August 2017, it varies within 20 to 40 cm, and in December 2017, it varies within 40 to 60 cm; (ii) the SA data exhibit more detailed variation in DT compared to the HDM data, which represent a relatively smooth surface; (iii) as the SA data approach coastal areas, particularly within the vicinity of the virtual stations, they appear more scattered (latitude 59° to 60° and 66°); (iv) most of the $DT_{HDM-corr}$ values appear to be slightly lower than DT_{SA}. It's important to note that $DT_{HDM-corr}$ provides long-wavelength estimates of sea level with hourly temporal resolution and 1 NM spatial resolution, resulting in a smoother profile. However, DT_{SA} provides instantaneous estimates of sea level with approximately 300 m spatial resolution, offering more detailed and higher-frequency sea level features. Further investigation of these locations was carried out via $MEAN_{SA-HDM}$, considering each mission for the entire Baltic Sea.

3.3.3 Evaluation of DT Accuracy and Identification of Problematic Areas
Comparing the differences ΔDT_{SA-HDM} serves not only to assess the accuracy of DT_{SA} but also provides intuitive insights into persistent or semi-persistent patterns at locations that may be questionable. This comparison enables the identification of potential problematic areas through the synergy of SA, corrected HDM, TG, or geoid datasets, or any combination of these data sources. Accurate sea level variability can

be achieved by utilizing a high-resolution quasi-geoid model. The geoid plays a crucial role in determining precise DT through SA and can be instrumental in validating various SA missions and identifying problematic areas through multi-mission comparisons. This approach enhances the overall understanding of sea level variability and aids in addressing discrepancies or challenges in specific regions.

Figure 9 displays $MEAN_{SA-HDM}$ statistics for four selected passes of S3A (pass #158, #169) and JA3 (pass#111, #16) from 2017 to 2019 which provides insights into possible discrepancies and hints at their potential sources. These passes represent diverse SA data coverage in terms of direction (ascending and descending passes) and geographic orientation (north–south and east–west passes). Passes 158 (S3A) and 111 (JA3) are descending, while passes 169 (S3A) and 16 (JA3) are ascending.

(a)   (b)   (c)   (d)

(e)   (f)   (g)   (h)
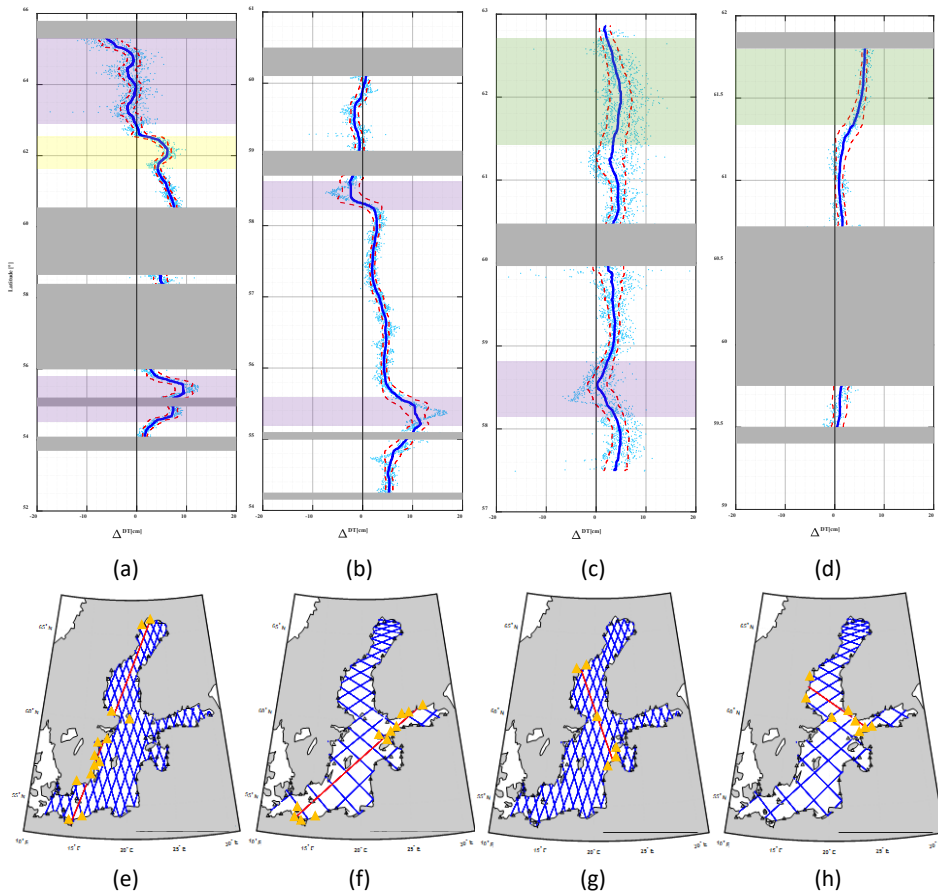
Figure 9: Along-track $MEAN_{SA-HDM}$for four SA passes ((a): S3A#158, (b): S3A#169, (c): JA3#111, and (d): JA3#16), considering all available cycles during the period of 2017–2019. The blue line represents the moving median of $MEAN_{SA-HDM}$, while the dashed red lines depict the moving standard deviation "envelope." Additionally, the average of $MEAN_{SA-HDM}$is indicated. The bottom row (e–h) showcases the location of each pass in the Baltic Sea, with grey zones denoting masked land areas. Potential problematic areas are classified into three types: Yellow shaded regions indicate suspected geoid model problems, green shade represents TG records problems (or the HDM problem), and purple shade suggests SA problems, possibly due to sea ice presence or land contamination (modified from **Publication II**).

48

The figure includes the whole-track average of $MEAN_{SA-HDM}$ and the pass locations over the Baltic Sea (red line) with associated TGs (yellow triangles) in the bottom row (Figure 9-e-h). This analysis aims to (i) illustrate persistent spatial areas of discrepancies, (ii) quantify discrepancies, and (iii) tentatively identify their sources. The examination reveals that SA exhibits more detailed variation compared to corrected HDM suggesting some expected level of discrepancy. However, when discrepancies exceed ±5 cm and display abnormal shapes (e.g., steep jumps), it indicates potential problematic areas related to data sources. The STD (dashed red line) aids in identifying persistent and semi-persistent patterns.

Upon analysing these tracks, a general difference (mean ΔDT_{SA-HDM}) of approximately ±10 cm is observed. The purple masked areas presents the SA related issues, the green area present the TG/HDM related problematic areas and the yellow masked areas in Figure 9-a highlight persistent locations with abrupt jumps (2–7 cm compared to nearby values) of ΔDT_{SA-HDM} around 62° latitude. In this highlighted area, the smaller STD indicates greater persistence, suggesting possible causes like geoid or HDM/TG deficiencies. Further investigation of five S3A passes across the Gulf of Bothnia in **Publication II** supports this observation. Additional evidence of the issue is presented in Figure 10, where examination of all SA cycles reveals identifiable problematic areas.
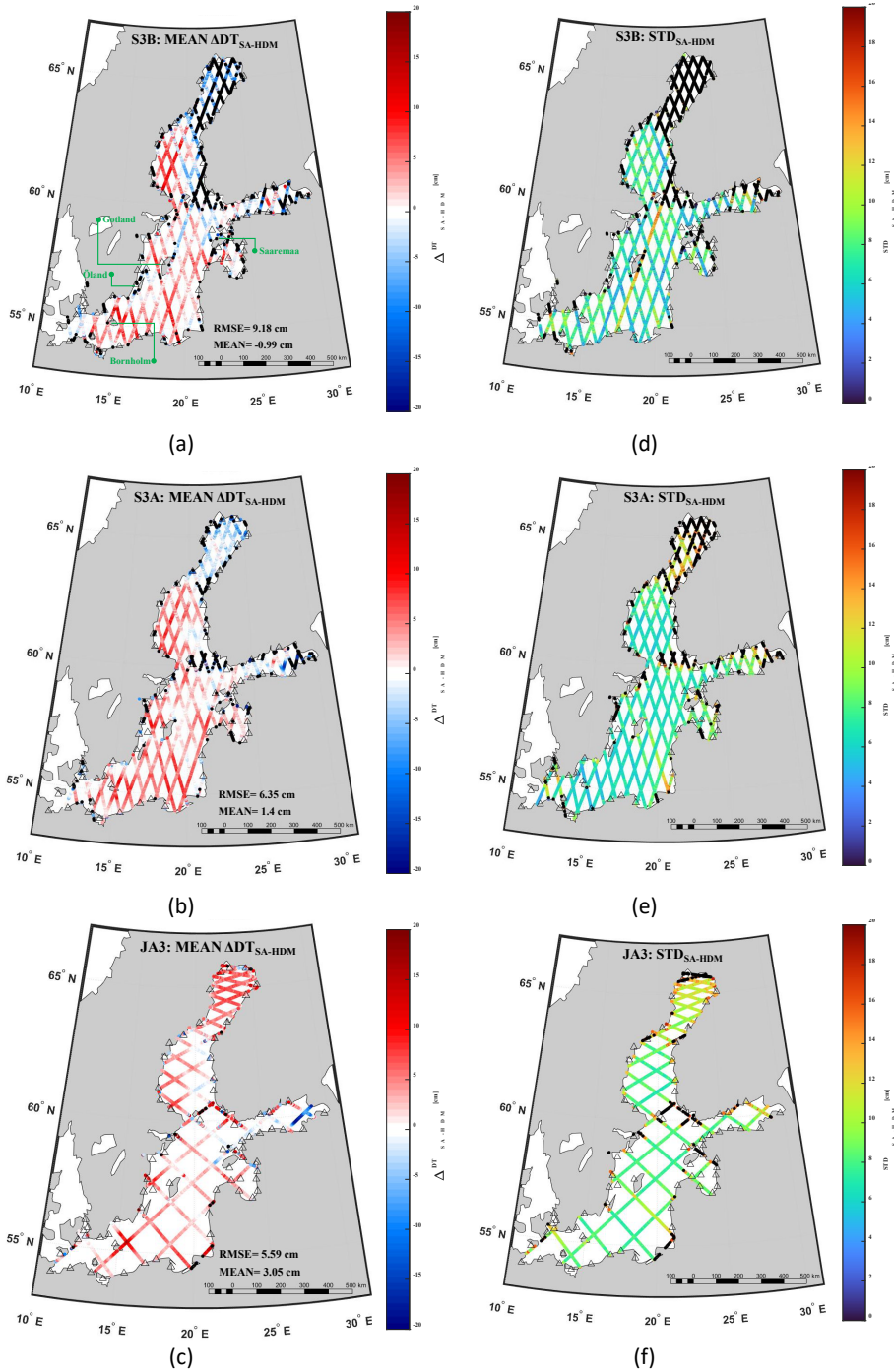
*Figure 10: Statistics of the along-track SA examination. In the top row, the discrepancies $MEAN_{SA-HDM}$ are depicted for the years 2017–2019 for missions (a) S3B, (b) S3A, and (c) JA3. For the $MEAN_{SA-HDM}$ plots, black dots represent $|\Delta DT_{SA-HDM}| > 20$ cm, which are excluded from the calculation of the RMSE values. Additionally, the associated STDs of ΔDT_{SA-HDM} larger than 20 cm are denoted in black dots in the bottom row (d–f) (from **Publication II**).*

Deteriorations in ΔDT_{SA-HDM} are evident around the latitude of 54°–55.5° (Figure 10-a,b), showing a deviation from 5 to 10 cm. The variable STD suggests a semi-persistent pattern. In Figure 10-a, Bornholm Island, located in the purple-highlighted area in Figure 9-a, contains several large rocks within the near-coast data corridor of the SA pass, potentially influencing the observations. Furthermore, in Figure 10-d,f, a substantial deviation (~3 cm) above latitude 61° near the Swedish coast is observed, potentially attributed to TG-corrected HDM (green masked area). The higher STD in Figure 10-c suggests semi-persistent patterns, possibly influenced by seasonal effects, while Figure 10-d indicates a small STD, hinting at a more persistent pattern. It is worth noting that the employed method for HDM correction is robust, yet not error-free. Consequently, some differences may arise due to errors in the TG/HDM correction method. Additionally, the Swedish TGs in this region exhibit issues compared to other TGs in the Baltic Sea, as illustrated in Figure 7. Additionally, around latitude 58.5° (Figure 10-b,c), SA passes closely align with the eastern coast of Saaremaa Island, Estonia, hinting at possible land contamination. At sub-arctic latitudes 63°–66°, a negative deviation from the zero line of approximately 0 to −8 cm occurs, with a large STD, indicating semi-persistent patterns and potential seasonal trends. This suggests issues with HDM modelling or SA. One possibility is SA's failure to accurately track sea level due to sea ice presence (purple-masked area) during winter months.

A comprehensive evaluation of along-track DT$_{SA}$ accuracy across multi-missions (S3B, S3A, and JA3) was conducted by comparing the entire along-track DT$_{SA}$ with DT$_{HDM-corr}$ over the Baltic Sea. This analysis aimed to identify potential problematic areas, accounting for land contamination, sea ice, geoid issues, or HDM problems, as detailed in **Publication II**. Figure 11 visually represents these areas affecting SA data quality in which the normalized $MEAN_{SA-HDM}$ for S3A and JA3 mission data throughout the Baltic Sea in 2017 (a full cycle to mitigate seasonal effects) is presented, employing standard score (Z-score) normalization (Freedman et al., 2020). This normalization indicates the deviation of $MEAN_{SA-HDM}$ values from the standard deviation of the entire Baltic Sea. To enhance clarity, areas with large STD_{SA-HDM} (black dots in Figure 10e-f), primarily resulting from land contamination at coastal regions, were excluded. Coloured rectangles in Figure 11 highlight problematic areas with persistent large $MEAN_{SA-HDM}$ estimates, categorized into three groups. Yellow rectangles identify persistent discrepancies in both S3A and JA3, possibly linked to geoid deficiencies in the Gulf of Finland and potentially the Bothnian Sea. In Figure 10-a–c, substantial discrepancies (ΔDT_{SA-HDM}) of approximately 30 cm are evident at latitudes around 59.6°, encompassing the western coast of Finland and the eastern Gulf of Finland. The small STD values in these areas suggest a persistent pattern.
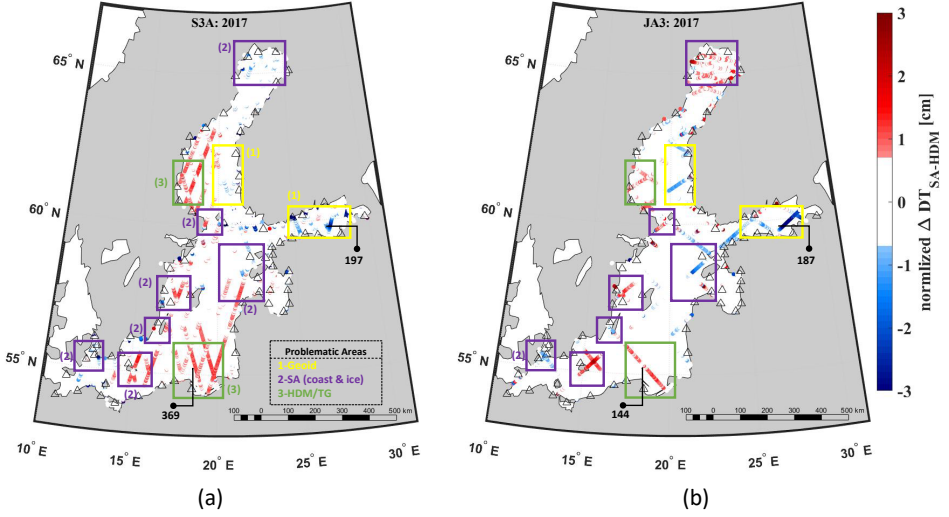
*Figure 11: Problematic areas in determining DT over the Baltic Sea. (a) shows the normalized mean of ΔDT_{SA-HDM} of S3A data, (b) depicts the same for JA3 data, both for the year 2017. The problematic areas are enclosed by coloured rectangles, each labelled with numbers to classify the possible reasons. Yellow rectangles represent geoid-related issues, purple rectangles indicate SA problems, and green rectangles suggest HDM or TG problems (from **Publication II**).*

3.4 Regional Sea Level Trend Estimation

This section presents the results of the reginal sea level trend over the 13 selected TG stations over the Baltic Sea using both TG and SA data. These TGs have been selected due to their suitable data coverage over 1995–2022 which overlap with the available SA data. Also based on their location (mainly over Baltic Proper) to avoid the problematic area which has been identified in **Publication II**. Details of these TG station's per country can be found in Table 7. Each TG contains hourly data between 1995–2022 except for some TGs with data gap, The data gap of each TG is also presented by percentage of missing hourly data in Table 7.

*Table 7: TGs specifications including latitude and longitude (in degrees) number of data points (i) along with the hourly data gap percentage January 1, 1995, and the end date is December 31, 2022, together with the VLM and ΔN[mm/yr] values (from **Publication III**).*

ID	Station	Latitude	Longitude	Country	VLM	ΔN	i	Gap
1	Dirhami	59.21	23.50	Estonia	3.09	0.4	117,833	51.99[1]
2	Ristna	58.92	22.06	Estonia	3.46	0.4	244,427	0.42
3	Ventspils	57.40	21.53	Latvia	1.56	0.3	200,199	18.41
4	Ustka	54.59	16.85	Poland	0.13	0.1	175,622	28.45
5	Kolobrzeg	54.19	15.55	Poland	-0.06	0.1	170,399	30.58
6	Swinoujscie	53.91	14.25	Poland	-0.18	0.1	175,157	28.64
7	Sassnitz	54.51	13.64	Germany	0.09	0.1	237,694	2.58
8	Rodvig	55.25	12.37	Denmark	0.62	0.2	226,479	7.73
9	Simrishamn	55.56	14.36	Sweden	0.89	0.2	234,745	0.00
10	Kungsholmsfort	56.11	15.59	Sweden	1.36	0.2	245,439	0.00
11	Marviken/Arkö[2]	58.55	16.84	Sweden	4.46	0.4	245,448	0.00
12	Hanko	59.82	22.98	Finland	4.16	0.4	245,448	0.00
13	Pori	61.59	21.46	Finland	7.44	0.7	244,728	0.29

[1] This station includes manually recorded historical data twice a day up to 2010, from 2011 onward the hourly observation by sensor is available, hence, the data gap is high in hourly time frame.
[2] The tide gauge Marviken has the data up to 10-01-2019 hence another station close (~10 km) to this TG has been used for more updated data: Arkö station with latitude: 58.4843° and longitude: 16.9607°.

To study the ASL trend from SA dataset, 10 SA missions' data including European Remote-Sensing Satellite-2 (ERS2), Envisat (ENV), Jason-1(JA1), Jason-2 (JA2), Cryosat-2 (CS2), SARAL/AltiKa (SRL), Sentinel-3A (S3A), Jason-3 (JA3), Sentinel-3B (S3B) and Sentinel-6A Michael Freilich Jason-CS (S6A have been utilized. This dataset is mainly containing data from the Baltic+SEAL project however, this dataset includes the data up to 2019. Hence, the standard data from 2019 to 2022 have been used to cover the whole study period. The standard data is originated from the European Organisation for the Exploitation of Meteorological Satellites (EUMETSAT) which can be downloaded from EUMETSAT Earth Observation Portal https://eoportal.eumetsat.int/. The details of SA data temporal coverage for each mission have been mentioned in Table 8 also more details in **Publication III**.

*Table 8: SA mission and related data (from **Publication III**).*

ID	SA	Data Period (Baltic+SEAL)		Data Period (Standard data)	
1	ERS2	16-May-1995	01-Jul-2003	-	-
2	ENV	18-Jun-2002	18-Oct-2010	-	-
3	JA1	15-Jan-2002	20-Jun-2013	-	-
4	JA2	12-Jul-2008	17-May-2017	-	-
5	CS2	19-Jul-2010	04-May-2019	-	-
6	SRL	14-Mar-2013	04-Jul-2016	-	-
7	S3A	04-Jan-2017	13-Jun-2019	13-Jun-2019	31-Dec-2022
8	JA3	17-Feb-2016	31-May-2019	31-May-2019	31-Dec-2022
9	S3B	01-Nov-2018	19-May-2019	19-May-2019	31-Dec-2022
10	S6A	-	-	1-Apr-2022	31-Dec-2022

Three main aspects of sea level trend have been examined in **Publication III** which include: (i) examination of the RSL and ASL trend estimates using the TG data (**Section 3.5.2**); (ii) comparison of the along track instantaneous SA data with the TG data for both long- and short-term trends (**Section 3.4.1** and **3.4.2**); (iii) inter-comparison of estimated trend by SA data (**Section 3.4.3**).

3.4.1 Long-term (1995-2022) Regional ASL Trend

The ASL trend is computed separately for each TG station and from multi-mission instantaneous SA data. It includes trends from SA, hourly TG trends (DT_{TG}), and TG readings during satellite passes ($DT_{TG@SA\ cycle}$). The resulting estimated trend, using both DT_{TG} and $DT_{TG@SA\ cycle}$, is shown in Figure 12, along with the RMSE for all stations. Overall, all three methods generally calculate the trend within a 2 mm/yr range. In most stations, the sea level trend ranges from 2 to 6 mm/yr when using both hourly TG and SA data (Figure 12-b). However, employing $DT_{TG@SA\ cycle}$ and SA data, the values range from 1 mm/yr to 6 mm/yr (Figure 12-c). Notably, stations in the northeastern section (like Pori, Hanko, Ristna, and Marviken) exhibit higher trend values, around 4 to 5 mm/yr. Comparing the datasets across all stations, the RMSE between SA-derived rates and $DT_{TG@SA\ cycle}$ rates, is lower (RMSE = 1.2 mm/yr). In Figure 12-a, the SA-derived DT (red bars) align closely with the TG-derived sea level trend, except for 5 stations (Dirhami, Ventspils, Ustka, Kolobrzeg, and Swinoujscie), where there's a significant observational gap. On average, the ASL trend across 13 stations stands at 3.9 mm/yr for hourly TG and 4.8 mm/yr for SA data in the Baltic Sea. The RMSE between these datasets is 1.5 mm/yr.
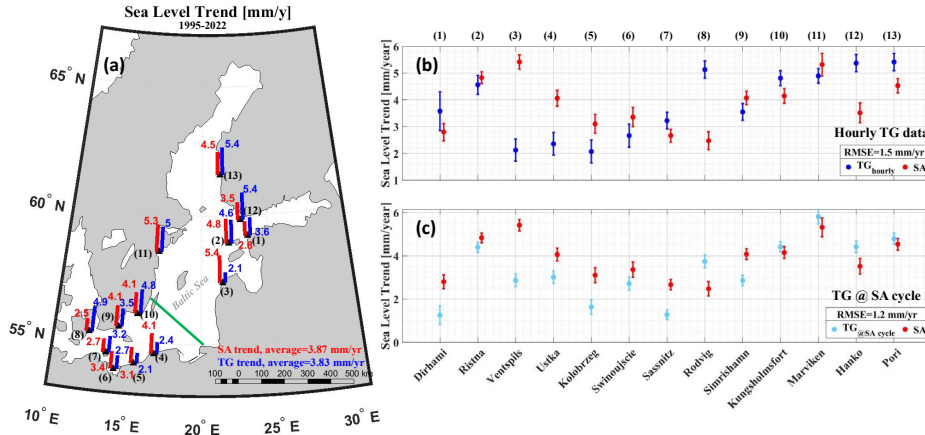
*Figure 12: ASL trend by SA and TG data for the period 1995 to 2022 over the Baltic Sea. (b) the rates obtained using both SA (red) and hourly TG data (dark blue). (c) rates using TG data only at SA cycles (light blue) compared with the instantaneous SA (red). The whiskers represent the estimated rate uncertainties within the 95% confidence interval of each dataset, and the RMSE between the estimated rates are also provided (modified from **Publication III**).*

Figure 12-b and Figure 12-c shows the limitations of TG data in estimating sea level trends, especially for stations with data gaps. These gaps and outliers in TG observations can distort regional-scale sea level trend estimates. As a result, SA data emerges as a reliable resource for determining these trends at a regional level. However, while

instantaneous SA data offers a more realistic trend compared to $DT_{TG@SA\,cycle}$, discrepancies between the SA-derived trend and TG data (DT_{TG}) likely stem from the gaps in TG observations.

3.4.2 Decadal Regional Trend

Decadal changes in both ASL and RSL trends were analysed for two periods: January 2000 to December 2009, and January 2010, to December 2019. Figure 13 illustrates the comparison of decadal sea level trends between SA and TG for three different periods: 2000–2019, 2000–2009, and 2010–2019, utilizing instantaneous SA data ($DT_{SA@TG}$), hourly TG data (DT_{TG}), and TG data during SA cycles ($DT_{TG@SA\,cycle}$). This figure showcases a spatial pattern in trend rates similar to that seen in Figure 12. For the SA during both periods (2000–2009 and 2010–2019), trend rates remained within the range of approximately 3 to 10 mm/yr. However, the TG-derived trends, using both $DT_{TG@SA\,cycle}$ and DT_{TG}, exhibited a varied trend range from −2 to 16 mm/yr.

The reliance on TG data for sea level trend estimation is common, but its reliability is often hindered by data gaps, resolution limitations, and missing data. Table 9 shows that despite SA data representing singular values at specific times each month (depending on the SA cycle), they still capture a realistic trend comparable to TG data. For instance, the average sea level rates between 2000–2009 were around 2.7 mm/yr for TG data and 3.9 mm/yr for SA data. Similarly, for the period of 2010–2019, these rates were 8.1 mm/yr and 7.6 mm/yr, respectively. These findings prove valuable, particularly in areas lacking TG stations, highlighting that TG data might not always provide accurate information due to varying data resolutions. The RMSE between instantaneous SA rates, $DT_{TG@SA\,cycle}$, and DT_{TG} rates, considering all stations, is also depicted in Figure 13. The maximum RMSE occurs during 2000–2009 (at 4.7 mm/yr), correlating with a larger number of data gaps (945 in total across all stations) during this period compared to the period of 2010–2019 (with 182 data gaps).
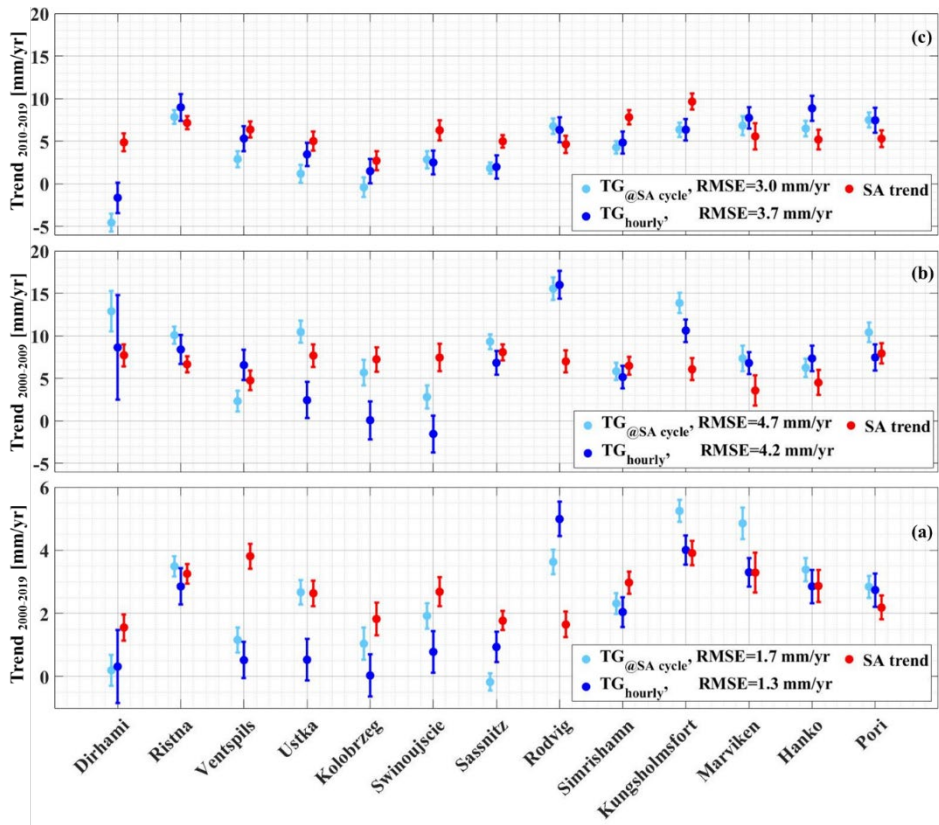
Figure 13: Decadal sea level trend by hourly TG records (dark blue), TG data at the time of SA cycles (light blue) and SA data (red) over the period of (a) 2000–2019, (b) the 2000–2009 decade (c) and 2010–2019 decade (from **Publication III**).

*Table 9: The estimated sea level trend from SA data ($DT_{SA@TG}$), hourly TG data (DT_{TG}) and TG data at the time of SA cycle ($DT_{TG@SA\ cycle}$) over different decades and during the whole study period (From **Publication III**).*

ID	$DT_{SA@TG}$ Jan 2000-Dec 2009	$DT_{SA@TG}$ Jan 2010-Dec 2019	DT_{TG} Jan 2000-Dec 2009	DT_{TG} Jan 2010-Dec 2019	$DT_{TG@SA\ cycle}$ Jan 2000-Dec 2009	$DT_{TG@SA\ cycle}$ Jan 2010-Dec 2019	$DT_{SA@TG}$ 1995-2022	DT_T 1995-2022
1	7.7±0.04	4.9±0.04	8.6±0.20	-1.7±0.06	12.9±0.08	-4.6±0.03	2.8±0.01	3.6±0
2	6.7±0.03	7.1±0.03	8.4±0.06	9.0±0.05	10.1±0.03	7.8±0.03	4.8±0.01	4.6±0
3	4.8±0.04	6.4±0.03	6.6±0.06	5.3±0.05	2.3±0.04	2.9±0.03	5.4±0.01	2.1±0
4	7.7±0.04	5.0±0.04	2.4±0.07	3.4±0.05	10.5±0.04	1.2±0.04	4.1±0.01	2.4±0
5	7.2±0.05	2.7±0.04	0.1±0.07	1.5±0.05	5.7±0.05	-0.4±0.04	3.1±0.01	2.1±0
6	7.4±0.05	6.3±0.04	-1.5±0.07	2.5±0.05	2.8±0.05	2.8±0.03	3.4±0.01	2.7±0
7	8.1±0.03	5.0±0.02	6.8±0.05	2.0±0.05	9.3±0.03	1.8±0.02	2.7±0.01	3.2±0
8	7.0±0.04	4.6±0.03	16.0±0.05	6.3±0.05	15.6±0.04	6.7±0.03	2.5±0.01	5.1±0
9	6.5±0.04	7.8±0.03	5.1±0.04	4.8±0.04	5.8±0.03	4.3±0.03	4.1±0.01	3.5±0
10	6.1±0.04	9.6±0.03	10.6±0.04	6.3±0.04	13.9±0.04	6.4±0.03	4.1±0.01	4.8±0
11	3.6±0.06	5.6±0.05	6.8±0.04	7.7±0.04	7.3±0.05	6.8±0.04	5.3±0.01	4.9±0
12	4.5±0.05	5.2±0.04	7.3±0.05	8.9±0.05	6.2±0.04	6.5±0.03	3.5±0.01	5.4±0
13	7.9±0.04	5.3±0.03	7.5±0.05	7.5±0.05	10.4±0.04	7.5±0.03	4.5±0.01	5.4±0
Mean							**3.87**	**3.83**

3.4.3 Inter-comparison SA trend

3.4.3.1 SA Data Optimality Regarding the Distance to TG

The use of along-track SA data allows for an examination of how sea level trend estimates vary with distance from the coastline. Figure 14 illustrates SA-derived sea level trend results at distances ranging from 5 to 50 km from the coast. Each distance range is averaged to determine the SA sea level trend within that range. The TG-derived trend is also included for comparison, offering insights into expected sea level changes at the coast. This comparison demonstrates the variability in sea level trends away from the TG station and explores scenarios where the TG may not consistently provide the most precise sea level trend estimates, depending on the specific context.
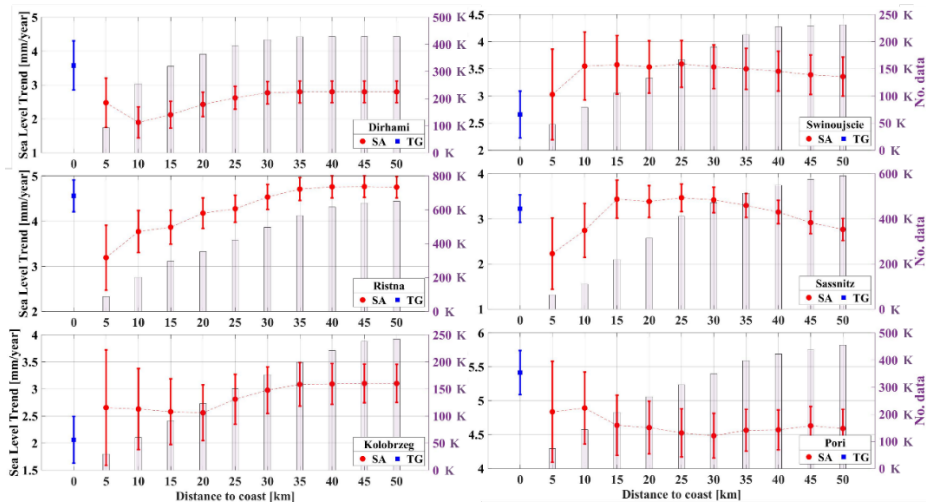
*Figure 14: Along-track SA-derived sea level trend (red) away from the coast compared to the TG trend (blue). The number of SA data points within the distance are denoted in the right-hand side vertical axis with numbers in thousand (K) format (from **Publication III**).*

In the figure the largest RMSEs are observed within SA-derived trend for the 10–15 km distance from the coast. Also, different trend values for the nearby stations (e.g., Ristna and Dirhami) may be attributed to the marine dynamics influencing the sea level variables over coastal areas, including the surface waves causing wave set-up and set-down.

3.4.3.2 Sea level Trend of Different SA Category

In this study, SA missions were categorized into two groups based on their constellation: high-inclination orbit satellites (SA1) and low-inclination orbit satellites (SA2). This categorization aimed to explore potential impacts of these distinctions on derived sea level trends from SA data. The sea level trends for each category were estimated during the period of 2003–2022 (where overlapping data existed) and compared with TG-derived trends over the same period. The results are depicted in Figure 15. Generally, the low-inclination SA data align better with TG trends, although exceptions exist at eight stations (Ristna, Ustka, Kolobrzeg, Swinoujscie, Sassnitz, Rodvig, Simrishamn, and Pori). Most SA missions exhibit agreement with TG, showcasing an average difference of 2.8 mm/yr for both group missions compared to all TG data.
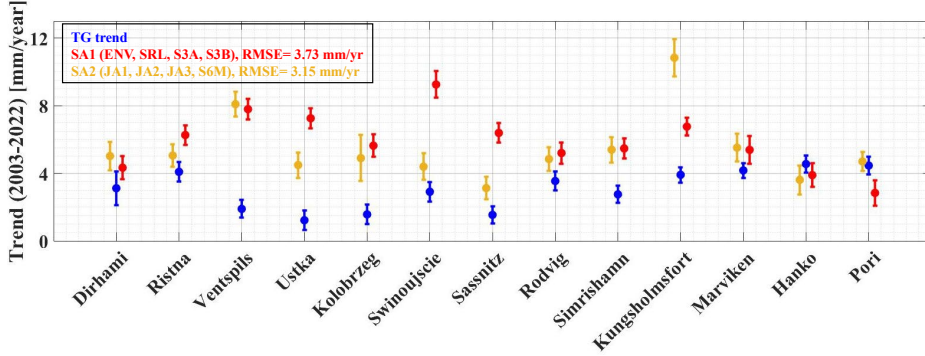
*Figure 15: ASL for the period of 2003–2022 (overlapped data time) for two categories of SA missions compared to the TG trend (blue). The high inclination (red) and low inclination (yellow) SA have been estimated different trends over different TG locations. The bars are representing uncertainties using 95% CI (from **Publication III**).*

Overall, the SA2 group (low inclination) demonstrated a closer alignment with TG data, boasting an RMSE of 3.15 compared to the SA1 group, which exhibited an RMSE of 3.73 mm/yr. Across 13 stations, the average discrepancy for the SA2 group stood at 2.5 mm/yr, with the largest difference reaching 6.9 mm/yr at Kungsholmsfort (10) station. Meanwhile, the SA1 group showcased an average discrepancy of 3.2 mm/yr compared to TG trends, with the maximum difference of 6.3 mm/yr observed at Swinoujscie (6) station.

3.4.3.3 Gridded vs instantaneous SA trend

Gridded SA data, a method frequently employed in various studies (Madsen 2019, Passaro 2021, Kapsi 2023, etc.), proves advantageous for estimating sea level trends. This method amalgamates data from different missions, bridging temporal gaps and allowing mutual complementation. In this study, a comparison was conducted between sea level trends derived from instantaneous SA data and three available gridded datasets within the region (explained in **Section 3.1.3**). These findings were examined against trends derived from both instantaneous SA data and TG methods. The investigation covers the data period from 1995–2019, as data from the Baltic+SEAL project were available up to June 2019. The comparison results are illustrated in Figure 16. This figure also illustrates the long-term trend variations (from Figure 12 and Table 9) derived from TG (DT_{TG}) and SA ($DT_{SA@TG}$) methods for a 28-year period, marked by triangle markers, for comparison purposes. The inter-comparison results indicate a strong agreement between most of the gridded products and the instantaneous SA calculated in this study. However, notable differences arise, particularly with the Baltic+SEAL gridded data, showing a discrepancy of 4.7 mm/yr for Ventspils (#3) station, and the global gridded SLA for Dirhami (#1) station, displaying a difference of 3.3 mm/yr. While TG data also exhibited some discrepancies compared to other products, these issues were addressed earlier in this study.
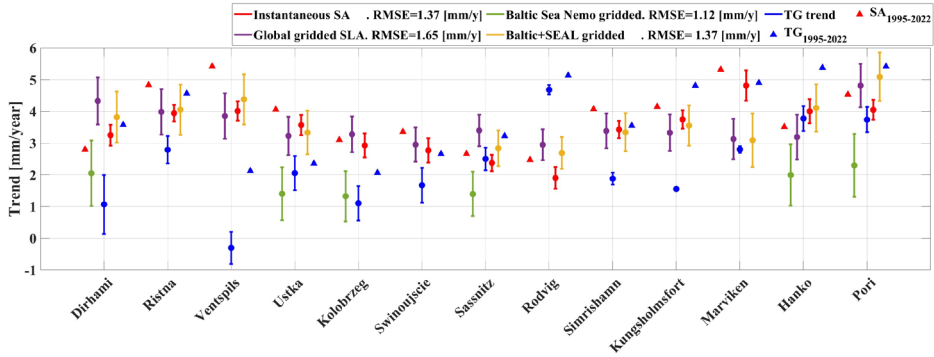
*Figure 16: Comparison of ASL trend derived from instantaneous SA data (red) and three gridded datasets including SA global SLA data by Copernicus (purple), gridded Nemo model SLA by Copernicus (green) and Baltic+SEAL gridded SA data (yellow) together with the TG (blue) data in the period of 1995–2019. The bars are representing uncertainties using 95% CI (from **Publication III**).*

In this figure the RMSE between estimated trend of each dataset and the TG related trend have been mentioned for the 6 stations out of 13 stations. From this figure the instantaneous SA data results are matching with the gridded data however with better RMSE compared to the TG data. Although the instantaneous SA and gridded data from Baltic+SEAL have same RMSE, but this gridded data also could not get close to 2 TG stations (Kolobrzeg and Swinoujscie) for a proper trend estimate. This emphasises the advantage of using the instantaneous SA-derived DT rather than gridded and SLA data for a realistic estimate of sea level trend. The rate of each dataset is mentioned in Table 10. This table also include the long-term trend from 1995 to 2022 (28 years) estimations of both SA and TG. From this table, the instantaneous SA data has better match with TG (bold fonts) for 5 stations more than the other datasets.

The figure illustrates the RMSE between the estimated trend of each dataset and the corresponding TG-related trend for 6 out of the 13 stations. The results show that the instantaneous SA data aligns closely with the gridded data, demonstrating a superior RMSE compared to the TG data. Although the RMSE between the instantaneous SA data and the Baltic+SEAL gridded data is similar, the Baltic+SEAL dataset fails to accurately estimate trends at two TG stations (Kolobrzeg and Swinoujscie). This underscores the advantage of using instantaneously derived SA trends over gridded and SLA data for realistic sea level trend estimates. The rates of each dataset are detailed in Table 10, where the long-term trend (28 years) estimations of both SA and TG are provided. It's evident from this table that the instantaneous SA data (highlighted in bold fonts) exhibit a better match with TG data for five stations compared to other datasets

*Table 10: ASL trend during 1995–2019 using hourly TG observations, instantaneous SA and three gridded products (show as circle in Figure 16 with associated RMSE) together with the long-term trend (triangles). Better performance compared to TG observations are in bold font (from **Publication III**).*

ID	TG (●) 1995-2019	SA (●) 1995-2019	Global$_{SLA}$ (●) 1995-2019	Nemo (●) 1995-2019	SEAL (●) 1995-2019	TG (▲) 1995-2022	SA (▲) 1995-2022
1	1.07±0.31	3.25±0.11	4.33±0.0	**2.05±0.0**	3.82±0.03	3.6±0.02	2.8±0.01
2	2.79±0.14	**3.94±0.09**	3.98±0.0	NaN	4.05±0.03	4.6±0.01	4.8±0.01
3	-0.3±0.17	4.01±0.10	**3.85±0.0**	NaN	4.38±0.03	2.1±0.01	5.4±0.01
4	2.06±0.18	3.57±0.11	3.23±0.0	**1.40±0.0**	3.33±0.02	2.4±0.01	4.1±0.01
5	1.11±0.18	2.92±0.13	3.28±0.0	**1.33±0.0**	NaN	2.1±0.01	3.1±0.01
6	1.67±0.18	**2.77±0.13**	2.95±0.0	NaN	NaN	2.7±0.01	3.4±0.01
7	2.50±0.12	**2.37±0.09**	3.40±0.0	1.40±0.0	2.84±0.02	3.2±0.01	2.7±0.01
8	4.68±0.05	1.90±0.11	**2.95±0.0**	NaN	2.69±0.02	5.1±0.01	2.5±0.01
9	1.88±0.06	3.43±0.09	3.38±0.0	NaN	**3.34±0.02**	3.5±0.01	4.1±0.01
10	1.55±0.01	3.75±0.10	**3.33±0.0**	NaN	3.55±0.02	4.8±0.01	4.1±0.01
11	2.80±0.03	4.82±0.16	3.13±0.0	1.85±0.0	**3.09±0.03**	4.9±0.01	5.3±0.01
12	3.78±0.13	**4.00±0.13**	3.19±0.0	1.99±0.0	4.11±0.02	5.4±0.01	3.5±0.01
13	3.74±0.13	**4.05±0.10**	4.82±0.0	2.30±0.0	5.09±0.03	5.4±0.01	4.5±0.01
					RMSE	1.78	0.64

4 Discussion and Concluding Remarks

The research performed for this thesis demonstrates that for marine sciences the important contribution of utilizing along-track satellite altimetry sea level data, especially when employed with a high-resolution geoid. Utilization of the geoid is a key component that allows the derivation of dynamic topography (DT). The developed methods for determination DT was an essential part of this thesis for it allowed a compatible comparison with other sea level data sources so that: (i) validation and accuracy determination could be effectively performed and (ii) considering the advantages and disadvantages of SA and that of other data sources, the utilized approaches showed that by combining various sources it was possible to identify problematic sources and their geographic locations. Such methods/approaches utilized in this study is considered to be novel in that it has not been performed before in such detail.

4.1 Summary of Results

In **Publication I** it was shown that 'several versions' of satellite altimetry sea level data exist and a major difference with them was the type of coastal retracker that was utilized. This in effect could affect the final sea level computed especially in the coastal area. As a result, we investigated in **Publication I** whether these coastal retrackers methods (ALES+ SAR for S3A and ALES+ for JA3) that were expected to give better results, especially in the coastal areas (that are often contaminated by land, ice, etc.) made a difference when compared to more generalized retrackers, often utilized for the open sea areas (Ocean for S3A and MLE4 for JA3). This was explored in the Gulf of Finland, Baltic Sea.

To compare the different SA missions and retrackers a ground truth is required for comparison. Both tide gauges (TG) and hydrodynamic models (HDM) were utilized for this. A simple method was developed that made the HDM vertical datum comparable to that of the TG and SA. So, a simple Bias correction (shift) was applied to HDM data, and this was assumed to be constant for that particular SA track however it would change for each cycle. Note that in this **Publication I** whilst the geoid was utilized, it was not explicitly used to determine DT but instead, all sources were made to refer to sea surface height (SSH). This was so for the purpose of validating different SA missions and it was not that important to derive to DT, however, the utilization of geoid was still implemented.

The results showed that in terms of retrackers the S3A in SAR mode provided more good data points within a range of 2–3 km to the coastline. However, such JA3 measurements that utilized LRM good data points were typically located further from the coastline, within a range of 7–10 km. So overall it was found that the specialized ALES+ and ALES+SAR retracking methods notably improved the coherence of both SA datasets. This was one of the first studies to examine the ALES+ and ALES+SAR retracking methods in the Gulf of Finland where the method utilized the marine geoid. Consequently, the Baltic+SEAL dataset that utilized these improved retrackers was chosen for further investigation in **Publication II** due to its enhanced spatial-temporal coverage across the entire Baltic Sea for a three-year period.

Based on the limitations of the method utilized in **Publication I** (especially computation of Bias correction) and our realization that it was essential to now derive sea level data, DT versus SSH. **Publication II** examined a more meticulous approach of determining DT for the entire Baltic Sea. As result a comprehensive and improved method was developed that utilized a virtual station. These virtual base stations were

more representative of the ground truth whilst still utilizing the TG and HDM data. **Publication II** was innovative from other SA studies in that it not only validated SA data with ground truth data but was also able to identify the problematic areas associated with each dataset' error sources.

The statistical results of **Publication II** showed discrepancies between corrected HDM and SA across all missions were within ±20 cm. The RMSE ranged from 5–9 cm (9.2 cm for S3B, 6.4 cm for S3A, and 5.6 cm for JA6), and STD between 2 to 16 cm across the entire Baltic Sea. Notably, areas with complex geographical features, like coastal regions, archipelagos, and small islands, exhibited larger mean and STD values of these discrepancies.

The most revealing outcome of the inter-comparison of data sources however was identification of the problematic regions and sources of this. This was found by identifying persistent and semi-persistent discrepancies amongst the data sources. For instance, semi-persistent patterns revealed from SA data problematic issues notably in sub-arctic areas (e.g., Gulf of Bothnia) that were most likely affected by sea ice and land contamination. Persistent problems were also found in the TG data. For the assumption in our studies so far assumed 'TG' to be more or less the ground truth in our method developed, however particular problematic TG stations were identified (e.g., correction inadequacies, TG zero problems), and also HDM issues were observed in areas such as the eastern Swedish coast and the Southern Baltic. Also, for persistent discrepancies geoid-related problems were identified in the eastern Gulf of Finland and this region was also confirmed by Varbla et al., (2020). This proved that the method developed was reliable in identifying problematic areas and sources. Consequently, these problematic areas were avoided in **Publication III**, where sea level trend estimation was performed using multi-mission along track SA data. Another revealing observation was that the SA data tended to reveal more realistic sea level variation i.e. high frequency and low frequency signals compared to the HDM which tended to display a smoother sea surface. This implies the potential in future studies for SA data to be investigated and utilized further for ocean dynamic processes.

Publication III explored another aspect of DT by evaluating sea level trends for the Baltic Proper that were computed using multi-mission satellite altimetry data for the period 28 years (1995–2022). In this paper, both long-term decadal trends were calculated using an ordinary least squares (OLS) estimator (Cazenave and Llovel, 2010). The emphasis in this study was on the coastal areas so a comparison of the SA-derived trend was made in the coastal area with respect to 13 TG stations. The long-term trend for the Baltic Proper showed a range that varied from 3.83 mm/yr for TG hourly data, 3.87 mm/yr for instantaneous SA data, and 3.32 mm/yr for TG at the time of SA pass. So, in essence, all three sources more or less agreed with each other. Thus, proving that SA was a reliable source. These results also were similar to other studies in the study areas (e.g., Passaro et al., 2021; Kapsi et al., 2023). Note however for these other sea level trend sources different periods and data sources were utilized. Also, when compared to the global mean sea level of around 3 mm/yr sourced from TG and SA data (Oppenheimer et al., 2019), the long-term sea-level trend calculated for the Baltic Sea appears similar.

The Baltic Sea is also affected by vertical land motion and results between relative sea level and absolute sea level showed a major difference in the areas affected by VLM. Thus, it is important to consider this when accessing sea level trends. For instance, in the northern and eastern Baltic Sea regions, ASL showed an increasing trend from south to north, contrasting with RSL's decreasing trend from north to south.

Decadal trend estimates revealed higher estimates with some decades being higher than others. For instance, 2000–2009, most stations (9 out of 13) showed higher trends compared to 2010–2019, although some stations may have had data gaps during this period. Factors such as increased westerly winds, augmented precipitation, and air pressure fluctuations, as indicated by studies like Reißmann et al. (2009) and Gräwe et al. (2019), could contribute to these trends. The analysis also revealed spatial variations in sea level trends across the Baltic Sea, with higher values (4 to 5 mm/yr) in the northeast compared to stations in the southwest (2 to 4 mm/yr) which could be mainly attributed to increased frequency and intensity of westerly winds Gräwe et al. (2019). These observations highlighted the varied influences shaping decadal sea level trends across the Baltic Sea.

Interestingly a more detailed investigation was made with respect to the comparison of sea level trends computed with SA for different distances from the coast (0–50 km range) compared with TG data. The results showed that at some TG stations, the differences were higher or lower than the SA data. Thus, showing the possible influence of coastal processes e.g. in terms of wave setup and wave setdown (Soomere et al., 2020). This however requires further examination for future studies. Overall, the results suggest that for sea level estimates the utilization of SA data may be a better alternative and can be utilized alone. A comparison of multi-SA missions with different orbit constellations analysis found that low-inclination satellites yielded slightly better trend estimation results across the Baltic Sea. It also revealed the superiority of instantaneous SA-derived DT for sea level trend estimates over gridded datasets.

Thus, in summary **Publication III** showed that along track can be a utilized as validated source of sea level trend estimates and that derivation of DT allowed a more reliable approach especially for complex sea areas affected by vertical land motion.

4.2 Key Conclusions Presented for Defence

- Recent advancements in SA coastal retrackers (ALES+ and ALES+SAR) in SA demonstrate improvement in coastal areas.
- For satellite altimetry development of methods that consider a consistent vertical datum (e.g. high-resolution geoid), and standardization of corrections is essential for comparison of other sea level data sources.
- Hydrodynamic models serve as valuable tools for understanding offshore sea level variations, aiding in the validation and assessment of along-track satellite altimetry data, albeit with inherent limitations leading to errors.
- Hydrodynamic model errors and biases can be mitigated using multinational unified data from tide gauge networks, with these errors manifesting spatially and temporally within a range of 10–35 cm.
- Comparison of along-track satellite altimetry with corrected hydrodynamic model data underscores the superiority of altimetry-derived data in capturing mesoscale and sub-mesoscale sea level dynamics, facilitating more reliable estimates of climate change variables, including sea level trends.
- The synergy of data from multi-mission satellite altimetry allows for deeper insights into the quantification of dynamic topography, enabling the identification of persistent and semi-persistent problematic areas associated with each dataset. This includes detecting tide gauge stations with poor data quality and identifying distortions in geoid undulations.

- Satellite altimetry-derived sea level variations offer a reliable method for estimating sea level trends at coastal areas compared to tide gauge data. Long-term time series of satellite altimetry can also be utilized for validating or developing vertical land uplift models.

4.3 Perspective of Future Work

Future research can explore various aspects of this study, including:

- Spatio-temporal analysis of sea level trend: Future studies could investigate deeper the primary drivers of trends in sea level by exploring sea level patterns across various time frames and over other regions benefiting from this methodology. This could include analysing annual and inter-decadal cycles to unravel the intricate involvement of key physical parameters influencing these trends. By examining sea level variations over different temporal scales, a more nuanced understanding of the underlying mechanisms driving sea level change can be attained.

- Acceleration of Sea Level Rise: Expanding the scope of this study to include an examination of the acceleration of sea level rise could yield valuable insights into critical phenomena shaping sea level behaviour in the. This can help to better understand the underlying processes driving these changes and could involve investigating the role of factors such as climate change, ocean circulation patterns, and glacial melting in contributing to the observed acceleration in sea level rise.

- Integration of Multi-Source Data: Integrating data from multiple sources, including satellite altimetry, hydrodynamic models, and in-situ observations, could enhance the comprehensiveness of future studies. By combining datasets from different sources, researchers can gain a more holistic understanding of sea level dynamics and improve the accuracy of their analyses. This integrated approach could provide valuable insights into the complex interactions between various factors influencing sea level variability and help refine future projections of sea level change in the region.

- Regional Climate Modelling: Utilizing regional climate models to simulate future sea level scenarios could provide valuable projections for assessing potential impacts and planning adaptation strategies. By incorporating projections of future climate scenarios, including changes in temperature, precipitation, and atmospheric circulation patterns, a better anticipation for future sea level trends can be determined. This could support a better understanding of decision-making and proactive measures to mitigate the impacts of sea level rise in the region.

List of Figures

List of Tables

References

1   Ablain, M.; Legeais, J.F.; Prandi, P.; Marcos, M.; Fenoglio-Marc, L.; Dieng, H.B.; Benveniste, J. and Cazenave, A.; 2017. Satellite altimetry-based sea level at global and regional scales. In Integrative study of the mean sea level and its components (pp. 9–33). Cham: Springer International Publishing. https://doi.org/10.1007/s10712-016-9389-8

2   Ablain, M.; Meyssignac, B.; Zawadzki, L.; Jugier, R.; Ribes, A.; Spada, G.; Benveniste, J.; Cazenave, A. and Picot, N.; 2019. Uncertainty in satellite estimates of global mean sea-level changes, trend and acceleration. Earth System Science Data, 11(3), pp. 1189–1202. https://doi.org/10.5194/essd-11-1189-2019

3   Andersen, O. B. and Knudsen, P.; 2009. DNSC08 mean sea surface and mean dynamic topography models. J. Geophys. Res.-Oceans, 114, 327–343, https://doi.org/10.1029/2008JC005179

4   Ågren, J.; Strykowski, G.; Bilker-Koivula, M.; Omang, O.; Märdla, S.; Forsberg, R.; Ellmann, A.; Oja, T.; Liepins, I.; Parseliunas, E.; et al. 2016. The NKG2015 gravimetric geoid model for the Nordic-Baltic region. In Proceedings of the 1st Joint Commission 2 and IGFS Meeting International Symposium on Gravity, Geoid and Height Systems, Thessaloniki, Greece 19–23 September 2016; pp. 19–23. Available online: https://www.isgeoid.polimi.it/Geoid/Europe/NordicCountries/GGHS2016_paper_143.pdf

5   Becker, S.; Losch, M.; Brockmann, J.M.; Freiwald, G. and Schuh, W.D.; 2014. A tailored computation of the mean dynamic topography for a consistent integration into ocean circulation models. Surveys in Geophysics, 35, pp. 1507–1525. https://doi.org/10.1007/s10712-013-9272-9

6   Brown G. S.; 1977. The Average Impulse Response of a Rough Surface and Its Applications. IEEE Transactions on Antennas and Propagation, 25(1), 67–74. https://doi.org/10.1109/TAP.1977.1141536

7   Cazenave, A.; Dieng, H.B.; Meyssignac, B.; Von Schuckmann, K.; Decharme, B. and Berthier, E.; 2014. The rate of sea-level rise. Nature Climate Change, 4(5), pp. 358–361. https://doi.org/10.1038/NCLIMATE2159

8   Cipollini, P.; Calafat, F.M.; Jevrejeva, S.; Melet, A. and Prandi, P.; 2017. Monitoring sea level in the coastal zone with satellite altimetry and tide gauges. Integrative study of the mean sea level and its components, pp. 35–59. https://doi.org/10.1007/978-3-319-56490-6_3

9   Challenor, P.G. and Srokosz, M.A.; 1989. The extraction of geophysical parameters from radar altimeter return from a non-linear sea surface. Mathematics in remote sensing, pp. 257–268.

10 Chen, X.; Zhang, X.; Church, J. et al. 2017. The increasing rate of global mean sea-level rise during 1993–2014. Nature Clim Change 7, 492–495. https://doi.org/10.1038/nclimate3325

11 Church, J.A.; White, N.J.; Konikow, L.F.; Domingues, C.M.; Cogley, J.G.; Rignot, E.; Gregory, J.M.; van den Broeke, M.R.; Monaghan, A.J. and Velicogna, I.; 2011. Revisiting the Earth's sea-level and energy budgets from 1961 to 2008. Geophysical Research Letters, 38(18). https://doi.org/10.1029/2011gl048794

12 Couhert, A.; Cerri, L.; Legeais, J.F.; Ablain, M.; Zelensky, N.P.; Haines, B.J.; Lemoine, F.G.; Bertiger, W.I.; Desai, S.D. and Otten, M.; 2015. Towards the 1 mm/y stability of the radial orbit error at regional scales. Advances in Space Research, 55(1), pp. 2–23. https://doi.org/10.1016/j.asr.2014.06.041

13 Delpeche-Ellmann, N.; Mingelaitė, T.; Soomere, T.; 2017. Examining Lagrangian surface transport during a coastal upwelling in the Gulf of Finland, Baltic Sea. J. Mar. Syst., 171, 21–30. https://doi.org/10.1016/j.jmarsys.2016.10.007

14 Ekman, M.; 1989. Impacts of geodynamic phenomena on systems for height and gravity. Bulletin Géodésique, 63, pp. 281–296.

15 Ekman, M.; 2009 The Changing Level of the Baltic Sea during 300 Years: A Clue to Understanding the Earth. Summer Institute for Historical Geophysics Åland Islands. Logotipas. 158 p. Available online: https://www.baltex-research.eu/publications/Books%20and%20articles/The%20Changing%20Level%20of%20the%20Baltic%20Sea.pdf

16 Ellmann, A.; and Vaníček P; 2007. "UNB application of Stokes–Helmert's approach to geoid computation." Journal of Geodynamics, Vol. 23, pp. 200–213. https://doi.org/10.1016/j.jog.2006.09.019

17 Ellmann, A.; Märdla, S. and Oja, T.; 2019. The 5 mm geoid model for Estonia computed by the least squares modified Stokes's formula. Survey review. https://doi.org/10.1080/00396265.2019.1583848

18 Featherstone, W.; 2000. Towards the unification of the Australian height datum between mainland and Tasmania using GPS and AUSGeoid98. Geomatics Research Australasia, 73, pp. 33–54. http://hdl.handle.net/20.500.11937/3275

19 Featherstone, W.E. and Filmer, M.S.; 2012. The north-south tilt in the Australian Height Datum is explained by the ocean's mean dynamic topography. Journal of Geophysical Research: Oceans, 117(C8). https://doi.org/10.1029/2012JC007974

20 Filmer, M.S.; Hughes, C.W.; Woodworth, P.L.; Featherstone, W.E. and Bingham, R.J.; 2018. Comparison between geodetic and oceanographic approaches to estimate mean dynamic topography for vertical datum unification: evaluation at Australian tide gauges. Journal of Geodesy, 92(12), pp. 1413–1437. https://doi.org/10.1007/s00190-018-1131-5

21 Filmer, M.S. and Featherstone, W.E.; 2012. A re-evaluation of the offset in the Australian Height Datum between mainland Australia and Tasmania. Marine Geodesy, 35(1), pp. 107–119. https://doi.org/10.1080/01490419.2011.634961

22 Freedman, D.; Pisani, R.; Purves, R.; 2020. Statistics: Fourth International Student Edition. W Norton & Company. p. 22. Available online: https://www.amazon.com/Statistics-Fourth-International-Student-Freedman/dp/0393930432

23 Fu, L.L. and Cheney, R.E.; 1995. Application of satellite altimetry to ocean circulation studies: 1987–1994. Reviews of Geophysics, 33(S1), pp. 213–223. https://doi.org/10.1029/95RG00187

24 Gräwe U.; Klingbeil K.; Kelln J.; Dangendorf S.; 2019. Decomposing mean sea level rise in a semi-enclosed basin, the Baltic Sea. Journal of Climate. Jun 1;32(11): 3089–3108. https://doi.org/10.1175/JCLI-D-18-0174.1

25 Guo, J.; Hwang, C.; and Deng, X.; 2022. Editorial: Application of satellite altimetry in marine geodesy and geophysics, Front. Environ. Sci., 10, 910562, https://doi.org/10.3389/feart.2022.910562

26 Hay, C.C.; Morrow, E.; Kopp, R.E. and Mitrovica, J.X.; 2015. Probabilistic reanalysis of twentieth-century sea-level rise. Nature, 517(7535), pp. 481–484. https://doi.org/10.1038/nature14093

27 Hayne, G.; 1980. Radar altimeter mean return waveforms from near-normal-incidence ocean surface scattering. IEEE Transactions on Antennas and Propagation, 28(5), pp. 687–692. https://doi.org/10.1109/TAP.1980.1142398

28 Hünicke, B.; Zorita, E.; 2006. Influence of temperature and precipitation on decadal Baltic Sea level variations in the 20th century. Tellus A Dyn. Meteorol. Oceanogr. 58, 141–153. https://doi.org/10.1111/j.1600-0870.2006.00157.x

29 Jahanmard, V.; Delpeche-Ellmann, N. and Ellmann, A.; 2021. Realistic dynamic topography through coupling geoid and hydrodynamic models of the Baltic Sea. Continental Shelf Research, 222, p. 104421. https://doi.org/10.1016/j.csr.2021.104421

30 Jakimavičius, D.; Kriaučiūnienė, J.; Šarauskienė, D.; 2018. Assessment of wave climate and energy resources in the Baltic Sea nearshore (Lithuanian territorial water). Oceanologia, 60, 207–218. https://doi.org/10.1016/j.oceano.2017.10.004

31 Jekeli C.; 2006. Geometric Reference System in Geodesy. Ohio State University: Columbus, Division of Geodesy and Geospatial Science School of Earth. https://kb.osu.edu/bitstream/handle/1811/77986/Geom_Ref_Sys_Geodesy_2016.pdf?sequence=1&isAllowed=y

32 Jevrejeva, S.; Moore, J.C.; Grinsted, A. and Woodworth, P.L.; 2008. Recent global sea level acceleration started over 200 years ago?. Geophysical Research Letters, 35(8). https://doi.org/10.1029/2008GL033611

33 Kapsi, I.; Kall, T. and Liibusk, A.; 2023. Sea Level Rise and Future Projections in the Baltic Sea. Journal of Marine Science and Engineering, 11(8), p. 1514. https://doi.org/10.3390/jmse11081514.

34 Kollo K. and Ellmann A.; 2019. Geodetic Reconciliation of Tide Gauge Network in Estonia. Geophysica, 54(1), 27–38. http://www.geophysica.fi/pdf/geophysica_2019_54_kollo.pdf

35 Knudsen, P.; Bingham, R.; Andersen, O. and Rio, M.H.; 2011. A global mean dynamic topography and ocean circulation estimation using a preliminary GOCE gravity model. Journal of Geodesy, 85, pp. 861–879. https://doi.org/10.1007/s00190-011-0485-8

36 Kuo, C.Y.; Shum, C.K.; Braun, A.; Mitrovica, J.X.; 2004. Vertical crustal motion determined by satellite altimetry and tide gauge data in Fennoscandia. Geophys. Res. Lett., 31. https://doi.org/10.1029/2003GL019106.

37 Lehmann, A.; 1995. A three-dimensional baroclinic eddy-resolving model of the Baltic Sea. Tellus A 47, 1013–1031. https://doi.org/10.1034/j.1600-0870.1995.00206.x

38 Madsen, K.S.; Høyer, J.L.; Suursaar, Ü.; She, J. and Knudsen, P.; 2019. Sea level trends and variability of the Baltic Sea from 2D statistical reconstruction and altimetry. Frontiers in Earth Science, 7, p. 243. https://doi.org/10.3389/feart.2019.00243

39 Maus S.; Green C.M.; Fairhead J.D.; 1998. Improved ocean-geoid resolution from retracked ERS-1 satellite altimeter waveforms. Geophys J Int 134(N1):243–253. https://doi.org/10.1046/j.1365-246x.1998.00552.x

40 Meier, H.M. and Kauker, F.; 2003. Sensitivity of the Baltic Sea salinity to the freshwater supply. Climate research, 24(3), pp. 231–242. https://doi.org/10.3354/cr02423

41 Müller, K.; 1982. Coastal Research in the Gulf of Bothnia; Springer Science & Business Media: Berlin/Heidelberg, Germany, Volume 45. Available online: https://link.springer.com/book/9789061930983

42 Ophaug, V.; Breili, K.; Gerlach, C.; 2015. A comparative assessment of coastal mean dynamic topography in Norway by geodetic and ocean approaches. Journal of Geophysical Research: Oceans 120, 7807–7826. https://doi.org/10.1002/2015JC011145

43 Oppenheimer, M.; Glavovic, B.; Hinkel, J.; Van de Wal, R.; Magnan, A.K.; Abd-Elgawad, A.; Cai, R.; Cifuentes-Jara, M.; Deconto, R.M.; Ghosh, T. and Hay, J.; 2019. Sea level rise and implications for low lying islands, coasts and communities. https://doi.org/10.1017/9781009157964.006

44 Ostanciaux, E.; Husson, L.; Choblet, G.; Robin, C. and Pedoja, K.; 2012. Present-day trends of vertical ground motion along the coast lines. Earth-Science Reviews, 110(1-4), pp. 74–92. https://doi.org/10.1016/j.earscirev.2011.10.004

45 Pajak, K. and Blaszczak-Bak, W.; 2019. Baltic sea level changes from satellite altimetry data based on the OptD method. Acta Geodyn. Geomater, 16, pp. 235–244. https://doi.org/10.13168/AGG.2019.0019

46 Passaro, M.; Mueller, F., and Dettmering, D.; 2020. Baltic+ SEAL: Algorithm Theoretical Baseline Document (ATBD). Technical report delivered under the Baltic+ SEAL project, European Space Agency. https://doi.org/10.5270/esa.BalticSEAL.ATBDV1.1

47 Passaro, M.; Müller, F.L.; Oelsmann, J.; Rautiainen, L.; Dettmering, D.; Hart-Davis, M.G.; Abulaitijiang, A.; Andersen, O.B.; Høyer, J.L.; Madsen, K.S. and Ringgaard, I.M.; 2021. Absolute Baltic Sea level trends in the satellite altimetry era: A revisit. Frontiers in Marine Science, 8, p. 647607. https://doi.org/10.3389/fmars.2021.647607

48 Pavlis, N.K.; 2012. Global gravitational models. In Geoid determination: theory and methods (pp. 261–310). Berlin, Heidelberg: Springer Berlin Heidelberg. https://doi.org/10.1007/978-3-540-74700-0_6.

49 Prandi, P.; Meyssignac, B.; Ablain, M.; Spada, G.; Ribes, A. and Benveniste, J.; 2021. Local sea level trends, accelerations and uncertainties over 1993–2019. Scientific Data, 8(1), p. 1. https://doi.org/10.1038/s41597-020-00786-7

50 Pujol, M.-I.; Schaeffer, P.; Faugère, Y.; Raynal, M.; Dibarboure, G.; and Picot, N.; 2018. Gauging the improvement of recent mean sea surface models: a new approach for identifying and quantifying their errors. J. Geophys. Res.-Oceans, 123, 5889–5911, https://doi.org/10.1029/2017JC013503

51 Ray, C.; Roca, M.; Martin-Puig, C.; Escolà, R. and Garcia, A.; 2015. Amplitude and dilation compensation of the SAR altimeter backscattered power. IEEE Geoscience and Remote Sensing Letters, 12(12), pp. 2473–2476. https://doi.org/10.1109/LGRS.2015.2485119

52 Reißmann, J.H.; Burchard, H.; Feistel, R.; Hagen, E.; Lass, H.U.; Mohrholz, V.; Nausch, G.; Umlauf, L.; Wieczorek, G.; 2009. Vertical mixing in the Baltic Sea and consequences for eutrophication–A review. Prog. Oceanogr., 82, 47–80, https://doi.org/10.1016/j.pocean.2007.10.004

53 Rosentau, A.; Muru, M.; Gauk, M.; Oja, T.; Liibusk, A.; Kall, T.; Karro, E.; Roose, A.; Sepp, M.; Tammepuu, A.; et al.l 2017. Sea-level change and flood risks at Estonian coastal zone. In Coastline Changes of the Baltic Sea from South to East; Springer: Berlin/Heidelberg, Germany, pp. 363–388. https://doi.org/10.1007/978-3-319-49894-2_16

54 Rulent J.; Calafat FM.; Banks CJ.; Bricheno LM.; Gommenginger C.; Green JAM.; Haigh ID.; Lewis H.; and Martin ACH.; 2020. Comparing Water Level Estimation in Coastal and Shelf Seas From Satellite Altimetry and Numerical Models. Front. Mar. Sci. 7:549467. https://doi.org/10.3389/fmars.2020.549467

55 Santamaría-Gómez, A.; Gravelle, M.; Collilieux, X.; Guichard, M.; Míguez, B.M.; Tiphaneau, P. and Wöppelmann, G.; 2012. Mitigating the effects of vertical land motion in tide gauge records using a state-of-the-art GPS velocity field. Global and Planetary Change, 98, pp. 6–17. https://doi.org/10.1016/j.gloplacha.2012.07.007

56 Samuelsson, M. and Stigebrandt, A.; 1996. Main characteristics of the long-term sea level variability in the Baltic sea. Tellus a, 48(5), pp. 672–683. https://doi.org/10.1034/j.1600-0870.1996.t01-4-00006.x

57 Sandwell, D.T. and Smith, W.H.; 2005. Retracking ERS-1 altimeter waveforms for optimal gravity field recovery. Geophysical Journal International, 163(1), pp. 79–89. https://doi.org/10.1111/j.1365-246X.2005.02724.x

58 Schaeffer, P.; Faugére, Y.; Legeais, J.F.; Ollivier, A.; Guinle, T. and Picot, N.; 2012. The CNES_CLS11 global mean sea surface computed from 16 years of satellite altimeter data. Marine Geodesy, 35(sup1), pp. 3–19. https://doi.org/10.1080/01490419.2012.718231.

59 Schwabe, J.; Ågren, J.; Liebsch, G.; Westfeld, P.; Hammarklint, T.; Mononen, J.; Andersen, O.B.; 2020. The Baltic Sea Chart Datum 2000 (BSCD2000): Implementation of a common reference level in the Baltic Sea. Int. Hydrogr. Rev., 23, 63–83. Available online: https://digitale-bibliothek.bsh.de/viewer/api/v1/records/184272/files/source/Westfeld_Baltic_Sea_Chart_2020.pdf

60 Scicchitano, G.; Scardino, G.; Monaco, C.; Piscitelli, A.; Milella, M.; De Giosa, F. and Mastronuzzi, G.; 2021. Comparing impact effects of common storms and Medicanes along the coast of south-eastern Sicily. Marine Geology, 439, p. 106556. https://doi.org/10.1016/j.margeo.2021.106556

61 Schreiner, P.; König, R.; Neumayer, K.H. and Reinhold, A.; 2023. On precise orbit determination based on DORIS, GPS and SLR using Sentinel-3A/B and-6A and subsequent reference frame determination based on DORIS-only. Advances in Space Research, 72(1), pp. 47–64. https://doi.org/10.1016/j.asr.2023.04.002

62 Soomere, T.; 2003. Anisotropy of wind and wave regimes in the Baltic proper. J. Sea Res., 49, 305–316. https://doi.org/10.1016/S1385-1101(03)00034-0

63 Soomere, T.; Pindsoo, K.; Kudryavtseva, N. and Eelsalu, M.; 2020. Variability of distributions of wave set-up heights along a shoreline with complicated geometry. Ocean Science, 16(5), pp.1047-1065. https://doi.org/10.5194/os-16-1047-2020

64 Soomere T.; Behrens A.; Tuomi L.; Nielsen JW.; 2008. Wave conditions in the Baltic Proper and in the Gulf of Finland during windstorm Gudrun. Nat Hazards Earth Syst. Sci 8(1), 37–46. https://doi.org/10.5194/nhess-8-37-2008

65 Slobbe D. C.; Klees R.; and Gunter B. C.; 2014. Realization of a consistent set of vertical reference surfaces in coastal areas. Journal of Geodesy, 88(6), 601–615. https://doi.org/10.1007/s00190-014-0709-9

66 Steffen, H. and Wu, P.; 2011. Glacial isostatic adjustment in Fennoscandia—a review of data and modeling. Journal of geodynamics, 52(3-4), pp. 169–204. https://doi.org/10.1016/j.jog.2011.03.002

67 Suursaar, Ü.; Sooäär, J.; 2007. Decadal variations in mean and extreme sea level values along the Estonian coast of the Baltic Sea. Tellus A Dyn. Meteorol. Oceanogr., 59, 249–260. https://doi.org/10.1111/j.1600-0870.2006.00220.x.

68 Tadesse, M.; Wahl, T. and Cid, A.; 2020. Data-driven modeling of global storm surges. Frontiers in Marine Science, 7, p. 260. https://doi.org/10.3389/fmars.2020.00260

69 Tokmakian, R.T.; Challenor, P.G.; Guymer, T.H. and Srokosz, M.A.; 1994. The UK EODC ERS-1 altimeter oceans processing scheme. International Journal of Remote Sensing, 15(4), pp. 939–962.

70 Tuomi, L.; Rautiainen, L.; Passaro, M.; 2023. User Manual Along-Track Data Baltic+SEAL; Project: ESA AO/1-9172/17/I-BG-BALTIC+ BALTIC+ Theme 3 Baltic+ SEAL (Sea Level) Requirements Baseline Document/BG-BALTIC+ SEAL (Sea Level) Category: ESA Express Procurement Plus-EXPRO+ Deliverable: D1.1 Code: TUM_BSEAL_RBD; Baltic SEAL: München, Germany.

71 Vaníček P.; Huang J.; Novák P.; Pagiatakis S.D.; Véronneau M.; Martinec Z.; Featherstone W.E.; 1999: Determination of the boundary values for the Stokes-Helmert problem, Journal of Geodesy, Vol. 73, Springer. https://doi.org/10.1007/s001900050235

72 Varbla, S.; Ellmann, A.; Delpeche-Ellmann, N.; 2020. Validation of Marine Geoid Models by Utilizing Hydrodynamic Model and Shipborne GNSS Profiles. Mar. Geod., 43, 134–162. https://doi.org/10.1080/01490419.2019.1701153

73 Varbla, S.; Ågren, J.; Ellmann, A.; Poutanen, M.; 2022. Treatment of Tide Gauge Time Series and Marine GNSS Measurements for Vertical Land Motion with Relevance to the Implementation of the Baltic Sea Chart Datum 2000. Remote Sens., 14, 920. https://doi.org/10.3390/rs14040920

74 Vestøl, O.; Ågren, J.; Steffen, H.; Kierulf, H.; Tarasov, L.; 2019. NKG2016LU: A new land uplift model for Fennoscandia and the Baltic Region. J. Geod., 93, 1759–1779. https://doi.org/10.1007/s00190-019-01280-8

75 Weisse R.; Dailidienė I.; Hünicke B.; Kahma K.; Madsen K.; Omstedt A.; Parnell K.; Schöne T.; Soomere T.; Zhang W.; Zorita E.; 2021. Sea level dynamics and coastal erosion in the Baltic Sea region. Earth System Dynamics. Aug 17;12(3):871–898. https://doi.org/10.5194/esd-12-871-2021

76 Wingham, D.J. and Rapley, C.G.; 1986. The saturation of the SEASAT altimeter, paper submitted to lnt. J. Remote Sensing.

77 Wöppelmann, G.; Letetrel, C.; Santamaria, A.; Bouin, M.N.; Collilieux, X.; Altamimi, Z.; Williams, S.D.P. and Miguez, B.M.; 2009. Rates of sea-level change over the past century in a geocentric reference frame. Geophysical Research Letters, 36(12). https://doi.org/10.1029/2009gl038720

Acknowledgements

Abstract

Along-Track Satellite Altimetry to Identify Coastal Sea Level Dynamics using a Synergized Geodetic-Oceanographic Approach

Satellite Altimetry (SA) is recognized as a valuable technique for determining sea level variation. However, there are some limitations in its performance especially with respect to the coastal areas and determining proper validation methods in the offshore areas. As a result, this study explores a method for deriving dynamic topography (DT) using SA in conjunction with a high-resolution marine geoid model, hydrodynamic models (HDMs), tide gauges (TGs). The method developed is expected to allow accurate determination of satellite altimetry sea level performance from coastal to offshore areas.

The first objective of this study examines whether the different satellite data products and their different retrackers actually improve sea level results in the coastal areas. The method consisted of utilizing along-track SA data from Sentinel-3A (S3A) and Jason-3 (JA3) data in the eastern Baltic Sea. Specific standard SA retracking algorithms (Ocean and MLE4) versus advanced coastal and sea ice retrackers (ALES+ SAR for S3A and ALES+ for JA3) were investigated. These SA data are compared with TG-corrected HDM-derived DT over the Baltic Sea. Results showed that the adapted retrackers (ALES+ and ALES+ SAR) provide more reliable SSH data within 2–3 km from the coastline for S3A and 7–10 km for JA3. The root mean square errors (RMSE) for S3A ALES+ SAR and Ocean retrackers range from 4–5 cm, while for JA3 ALES+ and MLE4, RMSE range from 6–7 cm, representing improvements of 0.5–1 cm over standard retrackers.

The second objective was the development of a synergized method using more expansive sea level datasets for the entire Baltic Seas and to determine the problematic geographic areas and data sources. Comparison of SA discrepancies between SA-derived DT and corrected HDM had the average of 20 cm, with RMSE of 9 cm (S3B) and 6 cm (S3A and JA3). SA data offer a more detailed variation of DT compared to HDM, which tends to generate only a smooth surface and underestimate DT. The synergy of multi-mission SA data also revealed the problematic areas with persistent issues associated with each data including the geoid model.

Finally, we analyse long-term (1995–2022) and decadal (2000–2009 and 2010–2019) sea level trends in the Baltic Sea using 13 tide gauge stations and multi-mission along-track SA. Both absolute sea level (ASL) and relative sea level (RSL) trends are examined, considering the influence of vertical land motion (VLM). Long-term ASL trends show agreement between TG and SA data, with estimates of 3.3 mm/yr and 3.9 mm/yr, respectively. Decadal trends exhibit higher rates, particularly during 2000–2009. Our study demonstrates the reliability of SA in determining regional sea level trends compared to TG data, providing valuable insights for understanding sea level variability in the Baltic Sea.

Lühikokkuvõte

Satelliitaltimeetria pikiorbiitse andmestikuga rannikumere veetaseme dünaamika tuvastamine kasutades sünergilist geodeetilis-okeanograafilist meetodit

Satelliitaltimeetriat (SA) kasutatakse merepinna taseme määramisel. Siiski on sellel tehnikal mõned kitsaskohad, eriti rannikualadel, aga ka avamerealadel sobivate valideerimismeetodite rakendamisel. Seetõttu on käesolevas teadustöös tuletatud meetod meretaseme dünaamilise topograafia (DT) määramiseks, kasutades SA- andmeid koos kõrge ruumilise lahutusega meregeoidi mudeli, hüdrodünaamiliste mudelite ja veemõõdujaamade tulemustega. Eeldatakse, et väljatöötatud meetod võimaldab adekvaatselt tuvastada satelliitaltimeetria täpsust ja võimalusi nii ranniku- kui ka avamerealadel.

Käesoleva töö esimese eesmärgina uuritakse, et kas erinevad SA andmetooted ja nende erinevad reträkkerid parendavad rannikualade meretaseme määramise tulemusi. Meetodis kasutatakse Läänemere idaosas Sentinel-3A (S3A) ja Jason-3 (JA3) pikiorbiitseid andmeid. Spetsiifiliselt uuriti standardseid SA reträkkimise algoritme (Ocean ja MLE4) võrrelduna täiustatud ranniku- ja merejää reträkkeritega (ALES+ SAR S3A jaoks ja ALES+ JA3 jaoks). Neid SA-andmeid võrreldi Läänemere veemõõdujaamade andmetega korrigeeritud hüdrodünaamilise mudelist (HDM) tuletatud DT-ga. Tulemused näitasid, et kohandatud reträkkerid (ALES+ ja ALES+ SAR) pakuvad usaldusväärsemaid SSH-andmeid 2–3 km ja 7–10 km raadiuses rannajoonest vastavalt S3A ja JA3 puhul. Ruutkeskmised vead (RMSE) JA3 ALES+ ja MLE4 reträkkerite puhul jäävad vahemikku 6–7 cm, samas kui S3A ALES+ SAR-i ja Oceani puhul saavutatakse 4–5 cm, seega RMSE on 0,5–1 cm võrra täpsem võrreldes algsete reträkkeritega.

Teiseks eesmärgiks oli sünergilise meetodi väljatöötamine, millega tuvastati probleemsed geograafilised piirkonnad ja andmeallikad, kasutades ulatuslikumaid Läänemere meretaseme andmestikke. SA-st tuletatud DT ja korrigeeritud HDM-i võrdlusest saadi keskmiselt 20 cm suurune erinevus, kusjuures S3B saavutati RMSE 9 cm ning S3A ja JA3 puhul 6 cm. SA andmetest saadakse detailsem DT võrreldes HDM-iga, mis kipub tekitama ainult sileda pinna ja alahindama DT-d. Mitmeinstrumendilise SA andmete sünergia võimaldas tuvastada ka probleemseid geoidi modelleerimise piirkondi.

Kolmandaks analüüsiti pikaajalisi (1995-2022) ja dekaadilisi (2000–2009 ja 2010–2019) meretaseme muutuste trende Läänemerel, kasutades 13 veemõõdujaama ja mitmeinstrumendiliste SA satelliitide pikiorbiitseid andmeid. Käsitleti nii absoluutse merepinna (ASL) kui ka suhtelise meretaseme (RSL) muutuste trende, võttes ka arvesse maa vertikaalliikumise (VLM) mõju. Pikaajalised ASL-i muutuste trendid tunnistavad TG ja SA andmete põhiste arvutuste sarnasust, vastavalt 3,3 mm/a ja 3,9 mm/a. Dekaadiliste muutuste trendid on mõnevõrra suuremad, eriti aastatel 2000–2009. Üldkokkuvõttes näitavad tulemused SA andmestiku usaldusväärsust Läänemere meretaseme trendide määramisel.

Appendix 1

Publication I

Mostafavi, M., Delpeche-Ellmann, N. and Ellmann, A., 2021. Accurate sea surface heights from Sentinel-3A and Jason-3 retrackers by incorporating high-resolution marine geoid and hydrodynamic models. Journal of Geodetic Science, 11(1), pp. 58–74. https://doi.org/10.1515/jogs-2020-0120

Research Article

M. Mostafavi, N. Delpeche-Ellmann, and A. Ellmann*

Accurate Sea Surface heights from Sentinel-3A and Jason-3 retrackers by incorporating High-Resolution Marine Geoid and Hydrodynamic Models

Abstract: One of the major challenges of satellite altimetry (SA) is to produce accurate sea surface heights data up to the shoreline, especially in geomorphologically complex sea areas. New advanced re-tracking methods are expected to deliver better results. This study examines the achievable accuracy of Sentinel-3A (S3A) and Jason-3 (JA3) standard retrackers (Ocean and MLE4) with that of improved retrackers adapted for coastal and sea ice conditions (ALES+ SAR for S3A and ALES+ for JA3). The validation of SA data was performed by the integration of tide gauges, hydrodynamic model and high-resolution geoid model. The geoid being a key component that links the vertical reference datum of the SA with other utilized sources. The method is tested in the eastern section of Baltic Sea. The results indicate that on average reliable sea surface height (SSH) data can be obtained 2–3 km from the coastline for S3A (for both Ocean and ALES+SAR) whilst an average distance of 7–10 km for JA3 (MLE4 and ALES+) with a minimum distance of 3–4 km. In terms of accuracy, the RMSE (with respect to a corrected hydrodynamic model) of S3A ALES+ SAR and Ocean retrackers based SSH were 4–5 cm respectively, whereas with the JA3 ALES+ and MLE4 associated SSH RMSE of 6–7 cm can be achieved. The ALES+ and ALES+ SAR retrackers show SSH improvement within a range of 0.5–1 cm compared to the standard retrackers. This assessment showed that the adaptation of localized retrackers for the Baltic Sea (ALES+ and ALES+SAR) produced more valid observation closer to the coast than the standard retrackers and also improved the accuracy of SSH data.

1 Introduction

Satellite altimetry (SA) is a well-known technique that is used to derive sea surface heights (SSH) both in the off-shore and coastal areas. There are however some uncertainties in its' performance and obtainable SSH accuracy in near-coastal areas. The reasons for these uncertainties are mostly due to: (*i*) the data capture parameters (e.g. resolution, incidence angle, pulse transmission and reception techniques etc.) of different satellite missions are configured differently; (*ii*) specifics in retracking algorithm to determine the derived range; (*iii*) satellite related errors (instrumental and geophysical) that are sometimes inadequately defined and location dependent and (*iv*) differences that exist between the vertical reference datum of SA and other sources that is required for the accurate validation, (Slobbe et al., 2014; and Vignudelli et al., 2006).

Given that there is an increasing need for sub-decimetre accuracy in SSH, especially in the near-shore area (e.g., navigation, shipping, engineering, and climate change studies) it is necessary to explore the accuracy of SA techniques especially in the coastal areas (Omstedt and Hansson, 2006). To accomplish this, data sources that serve as a reliable 'ground truth' are required. As a result,

M. Mostafavi: Department of Civil Engineering and Architecture, Tallinn University of Technology, Tallinn, Estonia, Ehitajate tee 5, Tallinn, 19086, Estonia
N. Delpeche-Ellmann: Department of Cybernetics, Tallinn University of Technology, Tallinn, Estonia
***Corresponding Author: A. Ellmann:** Department of Civil Engineering and Architecture, Tallinn University of Technology, Tallinn, Estonia, Ehitajate tee 5, Tallinn, 19086, Estonia, E-mail: artu.ellmann@taltech.ee

the perspective of this study is based on validating SA accuracy using different sources and ensuring that all these data sets utilize similar vertical reference datum. Essentially the key component that enables comparison of SA data with other sources is the geoid (equipotential surface of the earth). The question now arises on the ideal source that can be used to quality control the accuracy of SA.

Traditionally SA data are validated with tide gauge (TG) records (Gomez-Enri et al., 2016; Passaro et al., 2014; Cipollini et al., 2017). Whilst this is a reasonable method, there exist two aspects that should be considered when comparing SA with TG. Firstly, TG data are mostly land bounded, as a result it represents sea level data within a particular spatial boundary of the TG location, indicating that it does not necessarily represent conditions offshore (Roemmich et al., 2017). Secondly, very often the zero level of the TG vertical reference refer to some navigational Chart Datum (e.g., mean sea level-MSL or lowest astronomic tide-LAT). These vertical datums can change from one country to another, which causes inaccuracy and compatibility issues. Given that currently many countries have implemented and are in development of a gravity-based height reference system, where the definition of vertical datum is realized through geoid modelling (e.g., NGS 2013; Véronneau and Huang 2016; Ellmann et al., 2019) it is reasonable to take advantage of such equipotential surface of the earth system. Thus, in this study we investigate the SSH accuracy that can realistically be achieved with SA through the development of a method that utilizes the geoid based vertical datum, hydrodynamic models (HDM) and TG.

Essentially, HDM-s can complement the spatial limitations of TG measurements, for they provide a reasonable estimate of sea level anywhere in the coastal and offshore areas. The only limitation is that the vertical reference used, can be with respect to their own (arbitrary) vertical reference surface, that varies both spatially and temporarily (Slobbe et al., 2014; Rulent et al., 2020; Jahanmard et al., 2021). In addition, HDM are based on a mathematical approximation that may not always be capable of simulating the exact reality of marine conditions. To overcome such limitations a solution that derives the difference between the TG and HDM at similar locations allows a vertical reference shift correction to be introduced to the HDM and thus referring to a geoid model.

Such a method has previously been explored in terms of validation of the SA derived SSH by comparison of geoid related SSH (e.g., Slobbe et al., 2014; Birgiel et al., 2018, and 2019). A similar approach is undertaken in this study, henceforth two recent satellite missions Sentinel-3A (S3A) and Jason-3 (JA3) and their associated retrackers are ex-

amined in the complex coastal area of the Baltic Sea. The main difference of these two satellite altimeters is the way the transmitted and received signals are configured. For S3A can operate on both a Low-Resolution Mode (LRM) and Synthetic Aperture Radar (SAR) mode (Dinardo et al., 2020), whilst JA3 operates only at conventional pulse limited LRM. In this study the S3A SAR mode is used.

It is a common knowledge that SA measurements yield reasonable SSH results in the open sea area. The challenges remain in the coastal areas, where due to contamination of the SA signal there may be a gap (that can vary between 0–10 km) on approaching the coastline (Passaro et al., 2014; Idris et al., 2020). These near coast data points are often flagged as unreliable. The gaps are located in the section of the coastal area that is commercially active and the marine dynamics are energetic and prominent. For instance, data from these gaps are of essential importance for navigation (keel clearance), marine process (breaking waves, wave set up) and marine engineering (pipeline layout, renewable energy infrastructure). One of the main reasons for this inaccurate or absence of data approaching the coastline lies in the techniques used in processing the received signal and the determination of the actual water surface level. For often on approaching the coastline the SA signals may not only be influenced by water surfaces but also by land contamination, infrastructure, turbulent waters etc.

From the return echo of the altimeter, the range ('tracking range') is usually calculated by an onboard tracker. This 'tracking range' is only a first approximation, due to noise contamination a slight misinterpretation of the actual sea surface occurs. Thus, the tracker range is usually in error and this may especially occur in coastal areas that are influenced by land, archipelagos, infrastructures etc. To compensate this error, a retracking process is utilized in a post-processing stage which attempts to fit a model response to the real waveform (Passaro et al., 2014). Implementation of the retracker results in a more accurate range determination that represents the sea surface. Altimetry however was originally designed for the open sea, thus many of these retrackers are developed (especially in the waveform modelling) for a global implementation usage that normally follow a Brown model (Brown, 1977).

In coastal areas however, where there may be other targets (e.g., land, small rocks, offshore structures, sea ice etc.) errors can be introduced that distort the shape of the received waveforms (i.e., they do not exactly conform to the Brown model). This is more prevalent to occur in the coastal areas, thus resulting in inaccuracies in the range determination. Each coastal area can also be different, thus more advanced retrackers that are specifically tuned

to local conditions are developed (Andersen et al., 2010; Freeman and Smith, 2010). Instead, coastal waveforms have been developed based on different methods (e.g., waveform shape, multiple waveforms to detect brightest target prior to retracking, retracking of sub-waveform etc.). These advanced coastal retrackers are expected to provide better and more accurate near-coast SSH (Passaro et al., 2014; Dinardo et al., 2014; Roblou et al., 2007).

Newly developed retracking methods are expected to perform better than the standard retrackers. Monitoring their performance in coastal area is essential, as these retrackers are based on algorithms that are globally or locally tuned and may not always be applicable to a specific site. As a result, this study examines and compares standard retrackers including Ocean (for S3A) and MLE4 (for JA3) with ALES+ (for JA3) (Passaro et al., 2018) and ALES+ SAR (for S3A) (Passaro et al., 2020a and 2020b), which were developed in the framework of the European Space Agency's Sea Level Climate Change Initiative and Baltic+ SEAL projects. The intention of this study is not only to examine the overall achievable accuracy of retrackers but to take a closer examination of the retrackers' performance in the near-coastal area (i.e., <10 km from the coastline).

The study site is in the Gulf of Finland located in the eastern section of the Baltic Sea. This study area is quite dynamic with its numerous archipelagos, varying coastal morphology and dynamic coastal processes. This site is exceptionally equipped with a high-density network of tide gauges that is referred to the geoid based national vertical datum. This makes an ideal study area to examine the method with assigned satellites and their retrackers. Previous studies have also examined and compared the accuracy of Sentinel-3A satellite (Birgiel et al., 2018, and 2019; Liibusk et al. 2020). In Birgiel et al., (2018) for the Sentinel-3A SSH data an accuracy (root mean square error of 115 and 99 mm) was achieved for the SAMOSA2 (also known as Ocean) and SAMOSA+ retrieved SSH. These retrackers however were not specifically tuned to the Baltic Sea.

Instead, one of the new aspects of this study is the utilization of a newly tuned retracker (ALES+ and ALES+ SAR) that is compared to the standard retrackers (Ocean and MLE4, the SAMOSA+ dataset could also be an obvious choice to be examined, however, for brevity of this study it was excluded). The main aspects explored are: (*i*) quantification of how close to the coast the SA data with their different retrackers (stand alone and newly modified for the site) are able to reach the coast and the quality of these data, (*ii*) a closer examination of the SA derived SSH after removing a bias and (*iii*) examination of the accuracy of the satellites and their retrackers respect to corrected HDM.

The outline of the study is as follows. In Section 2 the developed methodology is described, whereas Section 3 contains a description of the utilized data set and study area. Section 4 describes the processing of the satellite data. In Section 5 the results are presented. A discussion of the results is presented in Section 6. A brief summary concludes the paper.

2 Methodology

First, interrelations between the observables and the reference surfaces used in this study are reviewed. The basic concept of satellite measurement encompasses that the satellite altimeter transmits a pulse of known power towards the sea surface. On interacting with the sea surface, the pulse is reflected to altimeter where the two-way travel time is determined, yielding the range R_{obs} of the satellite. Given the satellite altitude h_{SA} with respect to reference ellipsoid (could be different for different satellite missions) the SA derived SSH is obtained (cf. Fig. 1):

$$SSH_{SA} = h_{SA} - (R_{obs} + \Delta R) - dh \tag{1}$$

where ΔR denotes a combined correction terms (to be explained in Section 4) for the influence of the atmosphere and sea state to the SA signal. The h_{SA} measurement accuracy is 1–2 cm benefiting from Precise Orbit Determination (POD), whereas R_{obs} is derived with a precision of a few centimetres (Normandin et al., 2018). The term dh accounts for the differences of parameters in the involved reference ellipsoids, since the different SA missions and terrestrial datasets may refer to different reference ellipsoids, see Fig. 1. All terrestrial and SA datasets need to be referenced to the same reference ellipsoid using the ellipsoidal correction (dh) and a local geoid model. If the SA reference ellipsoid (ellipsoid 2) differs from the one (ellipsoid 1) for terrestrial or another SA datasets, a datum conversion from different ellipsoid should be considered by using approach in (Jekeli, 2006):

$$dh = \frac{a'(1 - e'^2)}{\sqrt{1 - e'^2\sin^2\varphi}} - \frac{a(1 - e^2)}{\sqrt{1 - e^2\sin^2\varphi}} \tag{2}$$

where a and a' are lengths of the semi-major axis of participating ellipsoids, e and e' are their corresponding eccentricity values and φ is the latitude of the point of interest.

TG records and HDM data have been used to validate the SSH_{SA} in this study. The TG measurements commonly refer to the zero of the national vertical datum. If the vertical datum is coinciding with an appropriate geoid model,
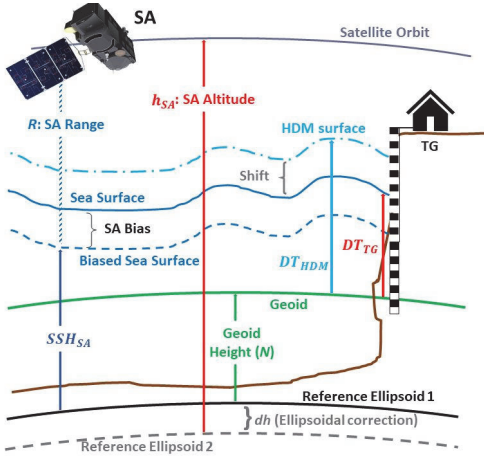
Figure 1: Interrelations between observations, data models and reference surfaces. Consult the main text body for the used symbols and abbreviations.

then the TG readings reflect the dynamic topography (DT), see Fig. 1. TG records are valid only at near-shore and may not represent adequately the offshore SSH. Conversely, a regionally computed HDM (even though referred to arbitrary vertical datum) is an independent source of offshore sea level variation. Essentially, these are equivalent to DT, but not referred to the geoid. Due to this similarity we denote the HDM derived sea level variations as DT_{HDM}. The HDM usually provides hourly estimation of gridded DT for a time period. DT_{HDM} is a spatio-temporal function with respect to a vertical reference datum that may or may not be disclosed (idealistically it would be best to refer HDM to a regional geoid model). Due to this difference in vertical datum between TG and HDM there is a need to estimate a shift ($Shift_{HDM}$) at nearby (say, within distance of 1–2 km, depending on the spatial resolution of HDM) TG location using:

$$Shift_{HDM}(\varphi_{TG}, \lambda_{TG}, t) = DT_{HDM}(\varphi_{TG}, \lambda_{TG}, t)$$
$$- DT_{TG}(\varphi_{TG}, \lambda_{TG}, t) \quad (3)$$

where DT_{HDM} and DT_{TG} are measured dynamic topography of each dataset at the location of tide gauge with ($\varphi_{TG}, \lambda_{TG}$) coordinates. The DT_{HDM} and DT_{TG} series contain hourly records, whilst the SA satellite flyover occurs at a specific time. Therefore, a temporal interpolation and an approximation to the closest value is required to estimate the DT_{TG} and DT_{HDM} values respectively for the exact time instant t of SA flyover. The $Shift_{HDM}$ assumed to be constant spatially (along the track) and would be changed temporarily (in different cycles). This $Shift_{HDM}$ is applied as a constant

to each cell node of the HDM grid at the time of the particular SA pass. So, the TG corrected $DT_{HDM-corrected}$ at each HDM grid (g) point could then be expressed as:

$$DT_{HDM-corrected}(\varphi_g, \lambda_g, t) = DT_{HDM}(\varphi_g, \lambda_g, t)$$
$$- Shift_{HDM}(\varphi_{TG}, \lambda_{TG}, t) \quad (4)$$

The HDM derived SSH can now be computed anywhere offshore by adding the geoidal height N:

$$SSH_{HDM}(\varphi_i, \lambda_i, t_i) = N(\varphi_i, \lambda_i) + DT_{HDM-corrected}(\varphi_i, \lambda_i, t_i) \quad (5)$$

where (φ_i, λ_i) denotes the coordinates of an i-th SA track-point at the time (t) of SA satellite flyover. For comparisons $DT_{HDM-corrected}$ values are interpolated both spatially and temporally to coincide with SA track locations and simultaneous with the satellite cycles. Note that geoid models are static, i.e. lacking the time variable component. The systematic and random differences SSH_{diff} of the tide gauge corrected HDM and the SSH_{SA} in along-track locations (φ_i, λ_i) can be determined as:

$$SSH_{diff}(\varphi_i, \lambda_i, t) = SSH_{SA}(\varphi_i, \lambda_i, t) - SSH_{HDM}(\varphi_i, \lambda_i, t) \quad (6)$$

This provides a tentative idea of SSH_{SA} accuracy, agreement to the in-situ gauge and the quality of initial SA data within the studied portion of the SA track. Here the SSH_{HDM} represents ground truth in near and offshore areas. Ideally SSH_{diff} should be a minimum value, still there may be outliers that can be identified by large SSH_{diff} values. Usually SSH_{SA} values also contain a bias (associated with each satellite track). It is of interest to investigate and eliminate such biases from SSH_{SA} data-series. Thus, SSH_{diff} is averaged along each track taking into consideration the number of track-points m for estimating the bias

$$bias_{SA-HDM}(track\#, t) = \frac{1}{m} \sum_{i=1}^{m} SSH_{diff}(\varphi_i, \lambda_i, t) \quad (7)$$

where t shows the time of each cycle at each track number ($track\#$). The time instant t varies (within a few seconds) in the above summation, but it can be taken as a constant for practical considerations, since SSH_{HDM} has low temporal resolution (hourly estimates) and the comparisons are also spatially limited to the vicinity of the selected tide gauge. Therefore, for the sake of the brevity symbol t will be used hitherto. There is an assumption that within limited spatial domain the bias is more or less constant for each cycle, whereas the $bias_{SA-HDM}$ estimates may vary (e.g. due to varying atmosphere and sea state) for different cycles and tracks. Hence the $bias_{SA-HDM}$ estimates need to be determined for each cycle and track. The above bias correction is implemented in the SSH_{SA}, yielding the corrected

SSH estimates

$$SSH_{SA-corrected}(\varphi_i, \lambda_i, t) = SSH_{SA}(\varphi_i, \lambda_i, t)$$
$$- bias_{SA-HDM}(track\#, t) \qquad (8)$$

Caused by various interferences of the radar pulses gross errors and outliers are expected in the SA datasets, which should be corrected. Exceptional outliers at the SA along-track locations (φ_i, λ_i) are removed, using a threshold of $|SSH_{diff} - bias_{SA-HDM}| > 30$ cm (see e.g., Birgiel et al., 2019).

To evaluate the performance of the corrected $SSH_{SA-corrected}$ in each cycle the post-fit residuals of the remaining $SSH_{SA-corrected}$ values and the reference SSH_{HDM} data are determined by:

$$\Delta SSH(\varphi_i, \lambda_i, t) = SSH_{SA-corrected}(\varphi_i, \lambda_i, t)$$
$$- SSH_{HDM}(\varphi_i, \lambda_i, t) \qquad (9)$$

The root mean square error (RMSE) of post-fit residuals at each track and cycle is then estimated by:

$$RMSE(track\#, t) = \sqrt{\frac{1}{n} \sum_{j=1}^{n} \left(\Delta SSH_j (\varphi_i, \lambda_i) \right)^2} \qquad (10)$$

where n is the number of good quality SA points of at each cycle within the studied track portion, the sub-index j is summation counter. Eq. (10) provides a statistically meaningful estimate of the accuracy of SSH_{SA} within the studied track portion in the given cycle.

These *RMSE (track#,t)* values can be used for computing annual RMSE using all available cycles for the given track portion by:

$$RMSE_{yearly}(track\#) = \sqrt{\frac{1}{k} \sum_{i=1}^{k} (RMSE (track\#, i = t))^2} \qquad (11)$$

where k is the number of available cycles per year (poor quality cycles with large number of outliers have been excluded). Along the coast these steps were repeated for all available tracks that a tide gauge station existed close to the satellite pass for each SA mission. Similarly, seasonal statistical estimates can be computed which could help to understand the behavior of bias during different meteorological conditions and to model the bias during different seasons e.g., for the sea-ice conditions. The developed method is tested and applied at 4 stations (for 6 different tracks) in the Gulf of Finland study area.

3 Study area and used datasets

3.1 Study area

The Baltic Sea (BS) is a semi-enclosed brackish water body located in northern Europe (see Fig. 2). This sea area is surrounded by nine countries, there exists a high density of marine traffic and coastal activities. The sea area is further subdivided into several sub-basins. The study site is the Gulf of Finland which is located in the easternmost section of the BS, it is a narrow and elongated marine area with a length of approximately 400 km and width varying from 48–135 km. The mean water depth is around 37 m (maximum depth is 123 m).

The short-term sea level dynamics in the gulf are affected by changes in the water balance that are mostly driven by atmospheric conditions (e.g. winds direction), river runoff and the presence of sea ice. Localised events (e.g. storm surges, coastal upwellings, see e.g. Delpeche-Ellmann et al., 2017 etc.) shall also affect the short term and seasonal variability. Due to the prevailing south-west wind direction, storminess and river discharge (the Neva river, located on the eastern end is the largest contributor of fresh water in the Baltic Sea) a higher MSL and extreme water levels tends to occur on the eastern section. For instance, the mean sea surface topography (averaged from 2014–2019) increases eastwards in the gulf from 20 to 29 cm (Kollo and Ellmann, 2019). The typical significant wave height is within the range of 0.5–0.8 m, with a maximum significant wave height of 5.2 m (Soomere et al., 2008).

The gulf is surrounded by Finland to the north, Estonia to the south and Russia to the east. The geomorphology of the coastline can be cliff like or low-lying with indented coastlines and peninsulas present. The coastal area is characterised by several archipelagos, small islands, and rocks within 10 km from the coastline. The gulf is equipped with the presence of precise and dense TG network and high quality geodetic infrastructure. The above characteristics make the gulf an ideal site to evaluate the performance of SA in the coastal area.

Two recent satellite missions S3A, JA3 and their associated retrackers are examined in this complex coastal area. For this, the along-track SSH_{SA} data are examined and compared with the SSH_{HDM} data at four operational tide gauge stations including: Narva-Jõesuu, Kunda, Loksa and Paldiski, see Fig. 2. The selected data period of all available cycles is one year, from January to December 2017, considering that 2017 is the first full year period for both examined satellites. The presence of sea ice tends to be a challenge for SA in determining accurate SSH. For 2017 sea ice

conditions were mild with most of the fast ice concentrated on the extreme eastern section of the gulf and around the western large islands (Hiiumaa and Saaremaa) off the Estonian coast.

3.2 Geoid model: EST-GEOID2017

This study uses a recent high-resolution Estonian quasi-geoid EST-GEOID2017 model (Ellmann et al., 2019), which covers the region from 57°N to 60°N latitude and from 20°E to 30°E longitude, with a spatial resolution of 0.01° × 0.02° (1.8 × 1.8 km). The extent of the model also sets geographical limitations to other datasets. Hence no SA data were examined beyond the northern boundary (60°N) of the geoid model. Additional input data (gravity data and elevation models from neighboring countries) were obtained through participating in the Nordic-Baltic joint geoid modelling project NKG2015 (Ågren et al., 2016; Märdla et al., 2017). Using a set of high-precise GNSS levelling points the geoid model is fitted to the Estonian vertical datum EH2000, which is the national realization of the European Vertical Reference System-EVRS (the zero of which is the Normaal Amsterdams Peil - NAP). The EST-GEOID2017 geoid model is an official part of the Estonian vertical datum, hence the model is used to convert GNSS-derived ellipsoidal heights to EH2000 heights and vice versa. Also the tide gauge records yield the DT_{TG} values that are referred to the EST-GEOID2017 model. The geoid model accuracy on land is estimated to be 5 mm (Ellmann et al., 2019), the geoidal heights are given with respect to the GRS80 ellipsoid.

3.3 Hydrodynamic Model: HBM-EST

The three-dimensional baroclinic eddy-resolving circulation model HIROMB-Boost Hydrodynamic Model (HBM-EST) developed by the Marine Systems Institute (Lagemaa et al., 2011) and specially tuned to the Estonian waters was implemented in this study for evaluating along-track performance of SA data. The horizontal resolution of the model is of 0.5 nautical miles. This model is divided into 50 vertical layers, with the thickness of each layer 4 m in the upper 80 m. The temporal resolution of the model is one hour. The open boundary of the HBM-EST model is located at the Danish Straits, i.e. the western edge of the Baltic Sea. The atmospheric forcings are sourced by the high-resolution limited area model (HIRLAM) and the daily data from the river runoff model HBV (Hydrologiska Byråns Vattenbalansavdelning) is used for freshwater inflow. Sea ice

data was obtained from Louvain-la-Neuve sea ice model (LIM3). The HBM-EST model is currently used mostly for operational sea level forecast in Estonia and plays a crucial role in the short-term prediction of the sea level. The model data provides DT_{HDM} and could be used as an independent source for the offshore. The HDM vertical reference datum is undisclosed thus there is a need to obtain the $Shift_{HDM}$ (Eq. 3) by using tide gauge measurements to derive DT_{HDM} from the HDM sea level. This model covers a region from 57°N to 60°N latitude and from 21°E to 30°E longitude, spatial resolution of 0.008° × 0.016° (529 × 455 horizontal grid points) (Lagemaa, 2012). The HBM-EST data was retrieved from http://emis.msi.ttu.ee.

3.4 Tide gauge data and nearby SA tracks

Within the study area there are four Estonian TG stations which have suitable location nearby satellites' tracks (see Fig. 2 and Table 1). The tide gauge network is operated by the Estonian Environment Agency. Sea level data (DT_{TG}) are recorded hourly and the measurements are referred (following methodology in Kollo and Ellmann, 2019) to the geoid based vertical datum EH2000. The zero of the utilized Estonian TG stations coincide with a recent high-resolution geoid model EST-GEOID2017 (Ellmann et al., 2019) and necessary corrections applied including vertical land motion and TG sensor drift correction (Kollo and Ellmann, 2019).

The first full year cycle after launch of the Sentinel-3A and Jason-3 satellites occurred in 2017, so the first 2017 cycle for the S3A and JA3 satellites is numbered 13 and 33, respectively. Table 1 contains the used TG stations and their related SA track number (both **asc**ending and **desc**ending passes) of each SA mission.

3.5 Satellite altimetry missions

Two satellite missions are examined in this study: Sentinel- 3A operating in Synthetic-aperture radar (SAR) mode and Jason 3 that operates in Low Resolution Mode (LRM). In SAR mode the transmit signals are sent in bursts that exploits an inter burst interval to receive the reflected pulses, whilst in the LRM the transmit and receive signals are processed incoherently. In SAR mode it is expected that a noise reduction and a finer along track resolution due to the acquisition of the high-rate digitized burst pulses (Dinardo, 2020). The main SA elements are explained below.
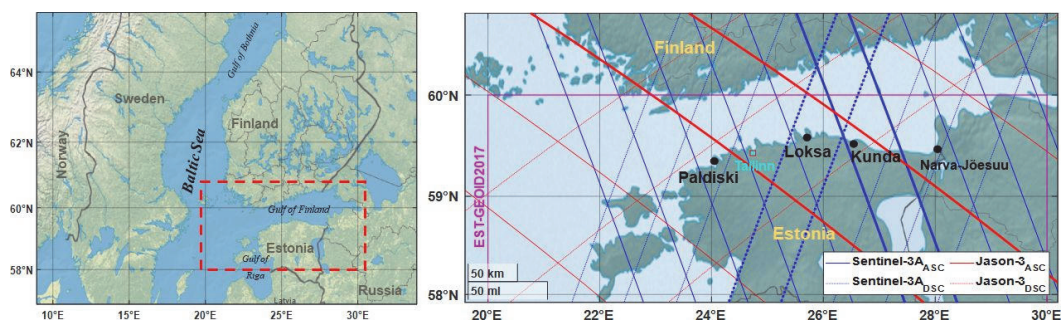
Figure 2: Location of the study area in Baltic Sea (left) and the JA3 (red) and S3A (blue) satellite tracks (used tracks are in bold) and location of tide gauge stations (black dots) in Gulf of Finland (right).

Table 1: List of TG used stations and nearby SA tracks, see Fig. 2 for their exact locations.

TG station Name	LAT [°]	LON [°]	Satellite	Pass# (asc/desc)	Cycles (2017)	Distance to TG [KM]
Kunda	59.521	26.542		083* / **414**	13-26	9 / 14
Loksa	59.584	25.707	S3A	739 / **300**	13-25	- / 17
Narva-Jõesuu	59.469	28.042		**197** /528	13-25	38 / -
Paldiski	59.351	24.049	JA3	**16** / -	34-69	19 / -
Kunda	59.521	26.542		**92** / -	33-68	15 / -

3.5.1 Sentinel-3A

Sentinel-3A was launched in February 2016 and apart from a Synthetic Aperture Radar Altimeter (SRAL), it is also equipped some other sensors (e.g., ocean and land color instrument, DORIS system, laser retroreflector, microwave radiometer amongst others). SRAL is the first dual frequency (Ku/C-bands, 13.575 and 5.41 GHz, respectively) near-nadir radar altimeter that operates fully in SAR mode. To achieve correlated pulses, the SAR altimeter emits 64 pulses towards the sea surface at a pulse repetition frequency of 17.8 kHz. A fast Fourier transform is performed on the received pulses in the along-track dimension, generating 64 Doppler footprints. The corresponding footprint shape is more rectangular shape than a round shape, for more details see Table 1. The echoes reflected from these Doppler footprints are averaged to generate multi-looked SAR waveforms. The European Organisation for the Exploitation of Meteorological Satellites (EUMETSAT) processes and distributes marine data. Reprocessed standard data can be downloaded from EUMETSAT Earth Observation Portal https://eoportal.eumetsat.int/. The Non-Time Critical (NTC) 20 Hz range values containing standard "Ocean" retracker with geophysical and environmental correction estimates were extracted to compute the SSH_{SA}.

3.5.2 Jason-3

The satellite was launched in January 2016, is a follow-on altimetry mission of TOPEX/Poseidon (T/P), Jason-1 and Jason-2, with the same repeat orbit (9.9156 days) as its predecessors. The Jason-3 onboard nadir-looking Posideon-3B altimeter is a dual-frequency (Ku/C bands, 13.575 and 5.3 GHz, respectively), which is capable to mapping the sea surface topography with high reliability. This pulse-limited altimeter operates in LRM over the global ocean. The along track horizontal resolution of ~300 m is attainable, and the footprint shape is circle like. In this study, we use the official Geophysical Data Record (GDR) 20Hz data product containing standard "MLE4" retracker, which can be accessed from a dedicated AVISO+ FTP server on ftp://ftp-access.aviso.altimetry.fr/.

3.6 Satellite Altimetry Retrackers

Many of the developed SA retrackers represent a global implementation with the reflected waveform normally following a Brown model (Brown, 1977) that conforms to the open ocean. The waveform for this model is usually characterized by fast-rising leading edge and a slowly decaying trailing edge. The echo's leading edge signifies the parameters of importance for the re-tracking (epoch, significant

Table 2: The used SA mission's specifications

Mission	Altimeter	Mode	Altitude [km]	Inclination	Cycle period [Days]	Along-track resolution	Across-track resolution
Sentinel-3A	SRAL	SAR	814.5	98.65°	27	~300 m	1.64 km
Jason-3	Poseidon-3B	LRM	1336	66.04°	9.91	~300 m	10 km*

*Source: Desjonquères et al., (2010)

wave height, backscatter coefficient). A specific point on the leading edge, known as the retracking point, is used to mark the point of measurement of altimeter vertical range to surface. In non-ocean areas though, altimetry suffers the distortion in waveforms, consequently, the waveform deviates from its standard shape. Therefore, there is a need to correct the distorted waveform. The difference of mid-point on the leading-edge respect to the nominal gate (in terms of gate number) represents an estimate of the retracking correction. New coastal SA retrackers are expected to improve the quality SA data by considering all these aspects.

As a result, this study compares the JA3 and S3A standard products using "MLE-4" and "Ocean" retrackers with that of improved retrackers (ALES+ for JA3 and ALES+SAR for S3A) that are specifically adjusted for coastal and sea ice conditions of the Baltic Sea. The retrackers data have been assessed for time period of 2017 in this study.

3.6.1 Ocean Standard Retracker

The SAMOSA (SAR Altimetry MOde Studies and Applications) is a physical, full SAR (Synthetic Aperture Radar) waveform retracker that was developed for open-ocean waters (Dinardo et al., 2014). It extracts from the return power waveform (echo) the ocean geophysical information in a non-linear curve best scheme, based on a bounded Levenberg-Marquardt Least-Squares Estimation Model (LEVMAR-LSE). SAMOSA retracker provides a closed-analytical expression of the waveform and exists in different versions. Improved "Ocean like" (Ocean) retracker (SAMOSA V2.5) is one of the standard retracker available in level-2 datasets of Sentinel-3A SRAL altimeter (Ray et al., 2015).

3.6.2 MLE4 Standard Retracker

The MLE4 retracker is based on a 2nd order Brown analytical model and is based on the Hayne model (Hayne, 1980). It estimates the four parameters (range, significant wave height, power of the trailing edge Sigma0) by determin-

ing the value that maximizes the probability of obtaining the recorded waveform shape in the presence of noise of a given statistical distribution (Thibaut et al., 2006). The MLE4 algorithm performing very well for mispointing angles up to 0.8 degrees and significantly improved in range estimation especially in areas where altimeter waveforms present a typical trailing edge slopes comparing to MLE3 retracker (Thibaut et al., 2010). In this study we used the GDR product 20Hz available in level 2 products which can be accessed from a dedicated AVISO+ (Archiving Validation and Interpretation of Satellite Oceanographic) FTP server on ftp://ftp-access.aviso.altimetry.fr/.

3.6.3 Baltic Sea Adapted Retracker ALES+ and ALES+SAR

The Baltic+SEAL consists of a novel improved multi-mission sea level data product for the Baltic Sea (BS). The retrackers employed for the data products consists of ALES+ which was utilized for the LRM altimeter and ALES+SAR for the delayed Doppler altimeters (Passaro et al., 2020a). In this study the high frequency along-track altimetry SSH of Baltic+SEAL data have been utilized.

ALES+ is a modification of ALES (Adaptive Leading Edge Sub-waveform) which is based on the Brown-Hayne functional form that models the radar returns from the ocean to the satellite. It is based on a sub-waveform retracker that adapts the fitting of the signal depending on the sea state and on the slope of its trailing edge (Passaro et al., 2018; 2020a). The sea state bias correction is deduced by means of statistical techniques based on the observations using high frequency wind speed and significant wave height (SWH) estimates from ALES+ (refer to Passaro et al., 2020a for more details). ALES+SAR is utilized for the delayed Doppler altimeters and this adopts a simplified version of the Brown-Hayne functional form as an empirical retracker to track the leading edge of the waveform. The different values between ALES+ and ALES+SAR is due to the different signal to noise ratio of the LRM mode vs SAR (refer to Passaro et al., 2020a for more details).

In this study the SSH data has been extracted from the Baltic+SEAL Sentinel-3A (ALES+SAR) and Jason-3

(ALES+) 20 Hz products. The data was obtained from http://balticseal.eu/data-access/.

4 Data processing

The SSH_{SA} data for S3A Ocean and JA3 MLE4 retrackers were directly derived by Eq. 1. Where the standard atmospheric and geophysical corrections applied for the Ocean and MLE4 retrackers are displayed below:

$$\Delta R = ionospheric\ correction$$
$$+\ dry\ tropospheric\ correction$$
$$+\ wet\ tropospheric\ correction + sea\ state\ bias$$
$$+\ ocean\ tide + load\ tide + pole\ tide + solid\ earth\ tide \tag{12}$$

$$\Delta R_{ALES+} = ionospheric\ correction$$
$$+\ dry\ tropospheric\ correction$$
$$+\ wet\ tropospheric\ correction + sea\ state\ bias$$
$$+\ ocean\ tide + load\ tide + pole\ tide + solid\ earth\ tide$$
$$+\ dynamic\ atmosphere\ correction$$
$$+\ radial\ orbit\ correction \tag{13}$$

For Baltic+SEAL datasets (ALES+ and ALES+SAR) the SSH_{SA} data were directly extracted from the database. Whilst the basic formulae for SSH_{SA} remains the same (Eq. 1) the standard atmospheric and geophysical corrections utilized slightly varied. Eq. 13 displays two additional corrections, Dynamic Atmosphere Correction (DAC) and Radial Orbit Errors (ROC) that were applied to the Baltic+SEAL dataset. Note that the ocean tide and load tide (summarized and stored as one value) is not included in the extracted Baltic+SEAL SSH but was applied afterwards in our calculations.

The SSH_{SA} from Baltic+SEAL products and the Jason-3 standard products refer to the T/P reference ellipsoid, while SSH_{HDM} model data refers to GRS80. The vertical height difference between two ellipsoids need to be applied to SA dataset to relate them to the same ellipsoid. Therefore, a difference between the ellipsoids of T/P and GRS80 in Baltic Sea needs to be accounted for. The corresponding ellipsoidal correction was determined by inserting into Eq. 2, where $a_{T/P}$= 6378136.3 m, $e_{T/P}$= 0.081819221456 m and a_{GRS80}= 6378137.0 m, e_{GRS80}= 0.081819190842621, yielding dh= 72.6 cm. This correction was applied to SSH_{SA} derived by MLE4, ALES+ and ALES+SAR retrackers. The Sentinel-3A derived SSH_{SA} (standard product) reference ellipsoid is WGS84. The sub-

mm range difference between GRS80 and WGS84 geometry can be neglected in this exercise. The different datasets were processed using the developed method to validate the retrackers performance against the ground truth. As TG and HDM provide hourly data, the closest data to the satellite overfly time have been selected which could represent the best sea condition at that time. For S3A the standard Ocean retracker for cycle 13–26 and MLE4 retracker of JA3 was employed for cycles 33–69 in the year 2017. Figure 3 shows the flowchart of the entire data processing.

5 Results

Examination of both Sentinel-3A and Jason-3 SA along-track data cycles using the various retrackers (Ocean, MLE4, ALES+, ALES+SAR) for 2017 represented some interesting characteristics with respect to: (i) along-track performance in terms of quantity and quality of satellite data on approaching the near-coast, (ii) bias consistency/inconsistency and (iii) the overall accuracy of the satellite and their retrackers.

5.1 Along-track performance of SSH_{SA}

Investigation of the satellites' cycles along track data points using the different retrackers showed disparity with respect to how close to coast useful SSH_{SA} data was retrievable (cf. Table 3).

To obtain the best quality and quantity of data points in the near-coast areas for each dataset all the data points up to the coastline were first examined. This was followed by the removal of obvious outliers by using a predefined threshold of a difference between $SSH_{SA-corrected}$ and SSH_{HDM} larger than 30 cm (see Sec 2). Baltic+SEAL official quality flags are also available, which in future studies is an option to be explored further.

Table 3 shows the average distance from the first available data point to the nearest coastline (after the removal of obvious outliers). As both datasets (Level-2 and Baltic+SEAL) provide same points location along a track, distance to the coast is measured respect to a single point to the coast. Since the distance varies for each cycle the minimum distance that was observed is also shown. Note that this distance does not necessarily represent minimum along track distance to the coast. Instead it depends on the shape and configuration of the coastline and its closeness to the satellite track.
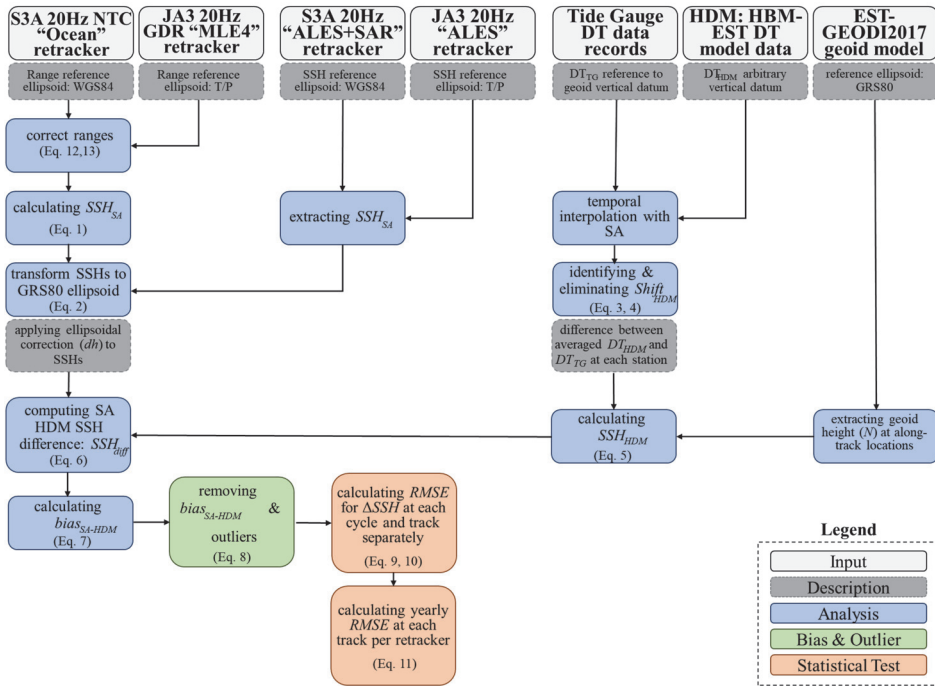
Figure 3: Flowchart of different stages of the developed method for validating the satellite altimetry retracker.
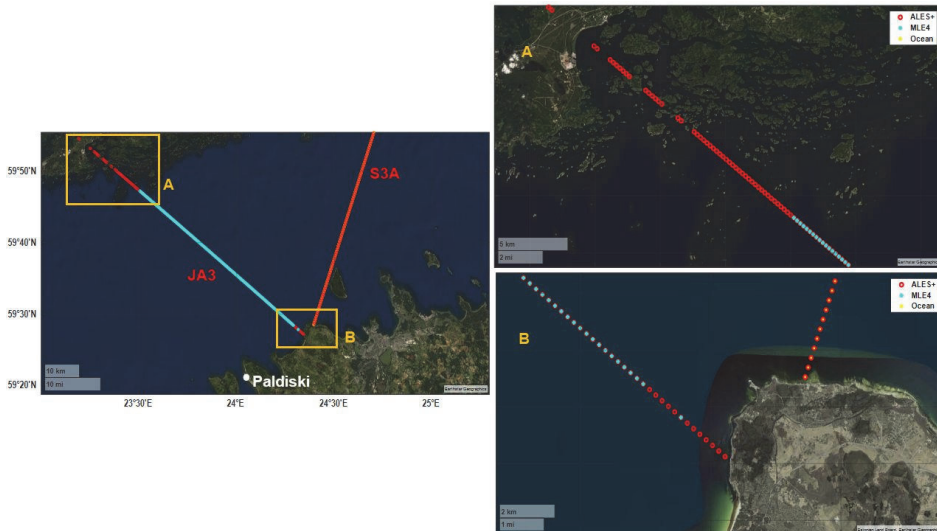
Figure 4: Locations of the near-coast SA tracks: the S3A (pass#186 cycle 13) and JA3 (pass#016 cycle 34) tracks performance near the shoreline at Paldiski station (left hand side). The JA3 track (A) performance using ALES+ (red) and MLE4 (blue) retrackers, zoom in near the Finnish coast; and the JA3 and S3A tracks (B) performance using ALES+ and ALES+SAR (red), Ocean (yellow) and MLE4 (blue) retrackers near the Estonian coast (right hand side).
The coastline source is the Google Earth.

Table 3: Average and minimum distances from the first valid SA data point to the nearest coastline (km) after removing outlier data, for each satellite track.

Pass Number	Average Distance [km]		Minimum Distance [km]		Average no. of Outliers	
Sentinel-3A	Ocean	ALES+ SAR	Ocean	ALES+ SAR	Ocean	ALES+ SAR
Kunda#083	2.77	2.95	2.02	2.02	17	13
Kunda#414	2.07	2.07	1.73	1.73	7	5
Loksa#300	2.32	2.57	1.93	1.93	9	4
Narva-Jõesuu #197	2.74	2.74	2.47	2.47	12	12
Jason-3	**MLE4**	**ALES+**	**MLE4**	**ALES+**	**MLE4**	**ALES+**
Kunda#092	9.87	8.99	3.29	3.58	8	3
Paldiski#016	6.62	6.72	2.99	2.54	4	3

The results display that valid JA3-MLE4 retracker data points were obtained on average for 7–10 km from the coastline, with the minimum distance of data points reaching as close as 3–4 km from the coastline. An example of this is illustrated for the Paldiski station (Fig. 4 left hand side; at location A and B), in terms of quantity of data points that approached the coast. For in Fig. 4-B for JA3 (pass#16 cycle#34) ALES+ provide 12 more data points that accounted for the 4 km longer stretch than the MLE4 retracker. Also, in the Finnish archipelago (Fig. 4-A right hand side) it is obvious that many MLE4 data points (around 47 points) have been removed as they have been detected as outliers. Conversely, in the ALES+ retracker (in JA3 mission) they are available for possible examination, if required. Thus ALES+ provided the most reliable data up to the coast for JA3, as compared to the MLE4 retracker after removing obvious outliers.

On the contrary, the S3A (the Ocean and ALES+ SAR retrackers) consistently provided data points on average 2–3 km from the coast (see Fig. 5), with very little difference between retrackers. An example is illustrated in Table 3 and Fig. 4 (bottom) for Kunda station that shows whilst data points increased closer to the coast with ALES+ SAR, the actual distance to the coast was the same for the Ocean retracker. This may be due to the similarities that exist between the Ocean and ALES+ SAR retrackers. Thus, comparison between JA3 and S3A shows that a bigger difference was observed in the JA3 satellite using ALES+ (as compared with MLE4) which showed more data points closer to the coast.

Regarding the closeness to the coast S3A performed better than JA3. This may be due to the capabilities of S3A SAR mode where the pulses are transmitted and received with a higher PRF (pulse repetition frequency) and the inter-burst interval that allows a finer resolution and less noisier data (Dinardo, 2020) compared to the JA3 associated LRM. This highlights some of the essential benefits

Figure 5: The along track SSH_{SA} at Kunda station, pass #414 using Ocean (red) and ALES+ SAR (blue) retrackers and detected outliers (circles). Distance to the coast from first available good quality point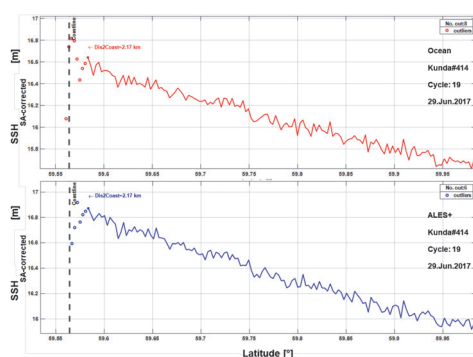 is measured. The vertical dashed line denotes the location of coastline. The colored circles denote near-coast SSH_{SA}.

of the SAR mode. Considering that the different satellites used different orbits and inclination, their ground track are expected to differ. Thus, the shape of the coastline and the presence of numerous small islands/archipelagos differ for individual satellites' track. This would influence the quality, number of data points retrieved and the distance to the coastline.

The question now remains on whether the increased amount of the retracker data points actually provided valid data points. Figure 6 shows for each retracker/mission using all available cycles in 2017 at Kunda station the along-track discrepancies (before any obvious outlier removal). In general it is obvious that better coherence was provided by the ALES+ and ALES+SAR retracker (compared to the Ocean and MLE4 ones). This is also reflected in Table 4 which showed smaller RMSE estimates for the ALES+ and ALES+ SAR retracker. Thus

the retracking algorithms and corrections used in the Baltic+SEAL datasets makes a difference in the quality and quantity of data on the near coast area. As a result, the usage of a coastal retracker appears relevant and applicable for the Baltic Sea area.

Closer examination of the critical areas (approaching the near-coast/shoreline) shows that for some cycles within the 0–10 km zone a larger SSH_{diff} are present. For example, in Fig. 6 for S3A SSH_{SA} data at Kunda station, the noisiest section appears to be within the first 10 km. On most occasions these larger values occur for particular cycles, this suggest that problems may not only be related to land contamination. Instead it is highly likely to be due to the marine dynamics, atmospheric and geophysical corrections applied, at these locations for particular instances in time. In this section of the near coast area various marine processes (e.g. breaking surface waves, upwellings etc.) may affect not only the sea state but also the atmosphere.

Interestingly for some cycles largest differences were not confined only to the nearshore but instead in some problematic cycles the entire track was affected. For instance, S3A cycle 18 of both ALES+ SAR and Ocean retrackers at Kunda station (pass#083) on 21st May 2017 (Fig. 6). This may be due to degradation of range/geophysical corrections, waveform contamination by land and bright targets, or perhaps sea state at this particular time.

5.2 Bias correction

By utilising DT_{HDM} and the geoid model the SSH_{HDM} estimates were computed by Eq. (5). SSH_{HDM} is considered as the 'approximate true' value. This calculation allows us to validate the SSH_{SA} data with the SSH_{HDM}. Note that all the relevant data sources are now referenced to the same reference ellipsoid of GRS80. Figure 7 displays an example of these results at the Kunda and Narva-Jõesuu stations. Figure 7 reveals that between the SSH_{SA} and SSH_{HDM} datasets a SSH_{diff} exist and this SSH_{diff} changes with time and location. The quantification of SSH_{diff} allows a bias estimate (Eq. 7) to be applied to the SSH_{SA}. Once the $bias_{SA-HDM}$ is implemented a reasonable agreement between the SSH_{SA} and the SSH_{HDM} is present. In Fig. 7 the red markers representing $SSH_{SA-corrected}$ which are more comparable to SSH_{HDM}.

The $bias_{SA-HDM}$ are presented for each station using the different missions and their retrackers (Fig. 8). In theory the bias is expected to be at a minimum, however, from Fig. 6 to 8 it is quite obvious that the bias changes randomly. Inspection of the bias with respect to the ground

truth (Table 4) shows that with the S3A Ocean data, the bias can vary maximum from -70.2 to +49.3 cm (a mean of 18.6 to 20.6 cm) whilst for S3A-ALES+SAR data it varied from -19.2 to 39.4 cm (a mean of 9.3 to 13.4 cm). For S3A Ocean the bias changes randomly and for particular seasons they are out of sync (i.e. in opposite phases) with the other stations, especially from January to March. For the ALES+SAR retracker the bias at most stations (the exception being Narva-Jõesuu station), are synchronized with each other. This is a remarkable improvement compared to the Ocean retracker. This could be due to the retracking algorithm and/or additional corrections (e.g., Radial Orbit correction, refer to Section 4) which was used in the Baltic+SEAL data product. Whilst for Ocean and MLE4 retrackers only the standard corrections are applied. This once more proves that the method made by the ALES+SAR retracker improves the quality of results and the importance of the additional corrections. It should be noted that the bias calculated represents a combination of different corrections and errors associated with the SA results, in order to comply to the corrected HDM results.

With respect to the Jason-3 satellite the MLE4 showed that the $bias_{SA-HDM}$ varied on a more somewhat seasonal pattern, with a maximum $bias_{SA-HDM}$ of between -26.1 to 31.8 cm (mean 7.5 to 10.5 cm) which is much less than the S3A Ocean retracker. In most cases the $bias_{SA-HDM}$ at the stations were synchronized, with exceptions in some months. With the JA3 ALES+ retracker the maximum bias of 28.2 to 32.5 cm (with a mean of 9.3 to 9.6 cm), see Fig. 7. With respect to the bias correction, JA3 the ALES+ retracker showed some differences in coherence between two stations. Considering that the JA3-ALES+ provided more data points close to the coast compared to JA3-MLE4 data. Also, once the $bias_{SA-HDM}$ correction is implemented it improves the overall accuracy of the satellite data (Section 5.3).

5.3 Retrackers Accuracy Assessment

Once the $bias_{SA-HDM}$ have been implemented, $SSH_{SA-corrected}$ is obtained by Eq. 8. A better agreement between SSH_{HDM} and $SSH_{SA-corrected}$ was obtained (cf. Fig. 7, Fig. 9). Examination of the yearly RMSE (Eq. 11) amongst all stations is reflected in Table 4. Comparison of the S3A Ocean and ALES+ SAR retrackers shows a slight improvement of the order of approximately of 0.5–1 cm in terms of RMSE. An accuracy within the range of 4.9–5.5 cm for the Ocean retracker and 3.9–5.0 cm ALES+ SAR retracker have been achieved. Thus with respect to the JA3 satellite an improvement of 1 cm is observed with the
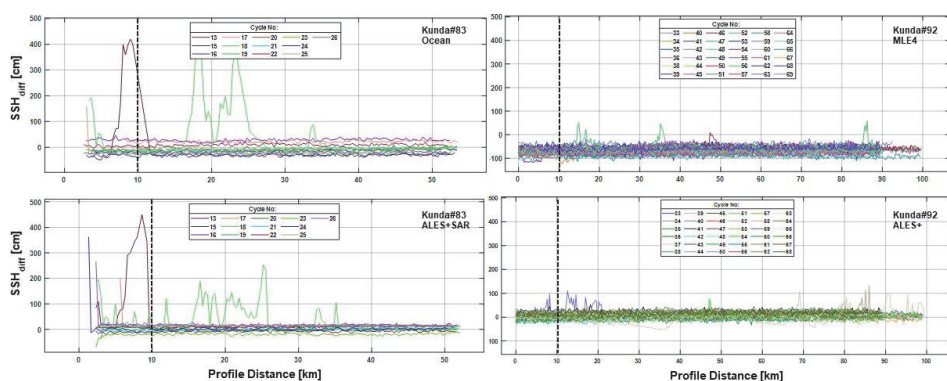
Figure 6: Discrepancies SSH_{diff} per each cycle in Kunda-083 S3A (left hand side) and Kunda-092 JA3 (right hand side) using Ocean and MLE4 (top) and ALES+ SAR and ALES+ (bottom) retrackers. The zero value in the horizontal axis denotes the location of the coastline.
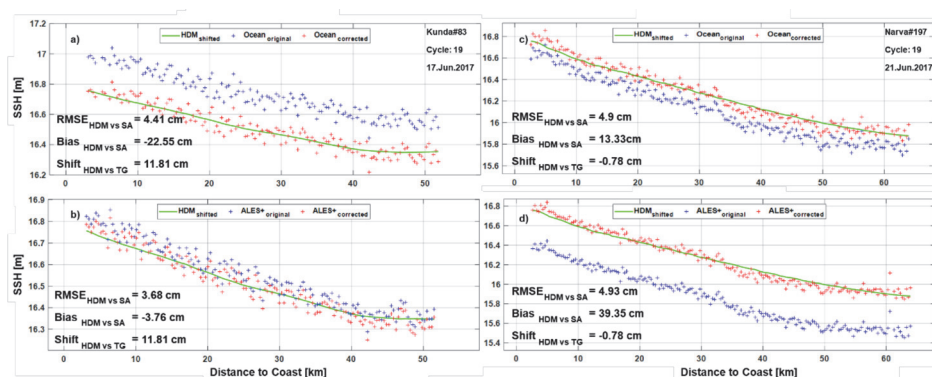
Figure 7: The along track bias per Kunda-083 (a) and Narva-Jõesuu 197 (b) stations in cycle 19 using both Ocean (top) and ALES+ SAR (bottom) retrackers. In this figure red crosses show the SA data points after removing the bias from initial data (blue crosses). The green line represents HDM_{SSH} – the ground truth.
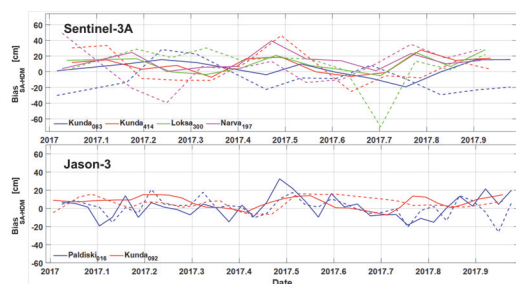
Figure 8: The Sentinel-3A (top) and Jason-3 (bottom) associated $bias_{SA-HDM}$ using standard (dash lines) and ALES+ (lines) retrackers at the used TG station.

ALES+ retracker. The MLE4 retracker had an accuracy of 8.5–7.7 cm and the ALES+ 6.7–7.4 cm. Overall, the resulting

RMSE was larger for the JA3. These results show that the S3A ALES+ SAR retracker performs the best amongst the examined stations, which meets the required target accuracy of better than 5 cm.

Note that for JA3 satellite a larger number of cycles were considered (35–36 cycles) compared to S3A (12–13 cycles) thus JA3 provide more data points in the gulf along its more inclined track and shorter revisit time (10 days). In the study area S3A provide between 130–190 data points along track for each cycle, whilst JA3 could provide between 200–330 points. The number of data points examined also influences the statistics.

Table 4 shows the yearly RMSEs of SA and HDM derived SSH comparison at each station in 2017 using both Jason-3 and Sentinel-3A datasets after $bias_{SA-HDM}$ removal. Maximum and absolute (abs.) of $bias_{SA-HDM}$ together with number of used cycles at each

station is also computed. Cycles (e.g. cycles 14 and 18 for Kunda#083, cycles 14 and 26 for Loksa#300) with large number of unacceptable outliers were excluded from the calculation from both datasets.

6 Discussion

In this study two satellite altimetry missions (Sentinel-3A and Jason-3) using their standard retrackers (Ocean and MLE4, respectively) and a specially improved retracker for the Baltic Sea (ALES+, ALES+ SAR) have been examined in Gulf of Finland. One of the key components of this study is the comparison of the SA data with more realistic ground truth data. This was obtained by incorporating hydrodynamic model (HDM) with tide gauge (TG) data and utilization of a high-resolution geoid model. This method allows us to not only obtain the accuracy of the SA at the coast (not only in the vicinity of the TG) but also to realistically assess the accuracy of data points in offshore via the HDM usage.

First, the performance of the retrackers was explored. The results showed that S3A in SAR mode allows more data points to be consistently obtained closer to the coastline. Obtaining a closeness of 2–3 km from the coastline, as compared to JA3 associated LRM which produces an average distance of 7–10 km. Studies performed in Spain using S3A 80 Hz data also found that a reliable distance of good quality was reached at a minimum distance of 3 km (Aldarias et al., 2020). Also a study that compared several retrackers in the archipelagos of Southeast Asia found that the coastal retracker SAMOSA+ performed superior to others within < 2 km from coastline (Idris et al., 2020). Thus, future studies can also explore the capabilities of SAMOSA+ and the S3A 80 Hz.

With the JA3 ALES+ retracker showed on some occasions the inclusion of more data points closer to the coast especially at the Paldiski station (Fig. 4) and the Finnish coast (to be explored in future studies). Thus, a minimum distance of around 3 km can be reached on some occasions. In general, the ALES+ and ALES+SAR retracker improved the coherence of both satellite mission's data. Whether, this was due to the additional corrections, for instance the Radial Orbit error that have been corrected with a multi-mission cross calibration or the retracking algorithm utilised, its effect is quite noticeable. It should be noted that JA3 could provide more data points at each track in Gulf of Finland compare to S3A due to the ground track's orientation (Fig. 2). JA3 passes over the gulf with 5 tracks with ~10 days repeat cycles whilst S3A passes over

with 16 tracks and 27 days repeat cycle in the east-westerly elongated shape of the study area.

After the $bias_{SA-HDM}$ correction was applied, the ΔSSH (Eq. 9) allows an even deeper insight into the performance of SA data source. The results surprisingly show for S3A-Ocean retracker a bias (mean 18.6–20.7 cm) that varies randomly with time. However, for S3A-ALES+SAR bias magnitude decreases (mean 9.3–13.4 cm) with most stations being synchronized. The Kunda station had different corrections than the other (ascending) tracks, taking into consideration the pass 414 is descending. For JA3 the ALES+ retracker showed a better synchronization than the MLE4 for the examined stations. The magnitude of the bias correction was about the same for the ALES+ (mean 9.3–9.6 cm) and the MLE4 (mean 7.5–10.5 cm). Overall these results emphasize the importance of this $bias_{SA-HDM}$ correction. The bias correction indirectly accounts for any correction that is required to obtain closeness to the true value. The obtained accuracy for S3A "Ocean" products and ALES+SAR achieving a RMSE of 4–5 cm shows better results than previous studies (RMSE of 11.5 and 9.9 cm in Birgel et al., 2018) in the Gulf of Finland, The results of our study in the Gulf of Finland agree well with that of the Baltic+SEAL validation report (where different stations were examined) for S3A, which obtained a RMSE of 4–7 cm and for the JA3 a RMSE of 7–14 cm (Rautiainen et al., 2020). Thus, in general the study shows promising results that utilization of a method to that incorporates the geoid, HDM and TG along with an improved retracker for the Baltic Sea (ALES+ and ALES+ SAR) enhanced the accuracy of both the S3A and JA3 data.

7 Conclusion

Accuracy assessment of two different satellite missions (Sentinel-3A and Jason-3) with their standard retrackers (Ocean and MLE4), and improved retrackers for the Baltic Sea (ALES+, ALES+SAR) is examined in this study. Results show that the ALES+ and ALES+SAR retrackers improves the accuracy of SSH by of the order of 0.5–1 cm for both missions. With S3A "Ocean" products and ALES+SAR obtaining a root mean square error of 4–5 cm can be achieved. Whilst with the JA3 ALES+ a root mean square error of 6–7 cm can be achieved. The ALES+ SAR retrackers allowed a consistent distance to the coast of 2–3 km for S3A whilst a distance of 7–10 km can be mostly achieved with JA3 ALES+ satellite. The developed method in this study incorporates the use of the geoid, tide gauge and hydrodynamic model that allowed the determination of comparable SSH. The method developed in this study can

Table 4: Statistical estimates of post-fit residuals ΔSSH [cm] for SA and HBM along track SSH for both S3A and JA3 (better performances are emphasised in the bold digits)

Pass Number	Max Bias	Mean abs. bias	RMSE	Max Bias	Mean abs. bias	RMSE	No. used cycles
Sentinel-3A		Ocean			ALES+ SAR		
Kunda#083	-30.15	18.57	4.98	-19.25	9.28	**4.05**	12
Kunda#414	46.27	16.74	5.00	27.79	11.34	**3.95**	13
Loksa#300	-70.2	19.87	4.89	28.07	11.22	**4.25**	12
Narva-Jõesuu #197	49.15	20.65	5.55	39.35	13.37	**5.04**	11
Jason-3		MLE4			ALES+		
Kunda#092	31.80	10.47	7.75	28.17	9.32	**6.73**	35
Paldiski#016	-26.12	7.50	8.46	32.53	9.60	**7.40**	36

Figure 9: The along track $SSH_{SA-corrected}$ versus SSH_{HDM} at two TG stations: Left: Kunda-083 Sentinel-3A using Ocean (red) and ALES+ SAR (blue) retrackers Right: Paldiski-016 Jason-3 using MLE4 (red) and ALES+ (blue) retrackers. The bottom plots show differences ΔSSH between $SSH_{SA-corrected}$ and SSH_{HDM} (green).

be applied for other satellite missions and sea areas that require accurate sea level data.

References

Ågren J., Strykowski G., Bilker-Koivula M., Omang O., Märdla S., Forsberg R., Ellmann A., Oja T., Liepiņš I., Paršeliūnas E., Kaminskis J., Sjöberg L. E., and Valsson G., 2016. The NKG2015 gravimetric geoid model for the Nordic-Baltic region. 1st Joint Commission 2 and IGFS Meeting International Symposium on Gravity, Geoid and Height Systems.

Aldarias A., Gómez-Enri J., Laiz I., Tejedor B., Vignudelli S., and Cipollini P., 2020. Validation of Sentinel-3A SRAL Coastal Sea Level Data at High Posting Rate: 80 Hz. IEEE Trans Geosci Remote Sens.

58 (6): 3809–3821.

Andersen O. B., Knudsen P., and Berry P. A. M., 2010. The DNSC08GRA global marine gravity field from double retracked satellite altimetry. J. Geod., 84(3), 191–199. https://doi.org/10.1007/s00190-009-0355-9

Birgiel E., Ellmann A., and Delpeche-Ellmann N., 2018. Examining the Performance of the Sentinel-3 Coastal Altimetry in the Baltic Sea Using a Regional High-Resolution Geoid Model. Proceedings - 2018 Baltic Geodetic Congress, BGC-Geomatics 2018, 196–201. https://doi.org/10.1109/BGC-Geomatics.2018.00043

Birgiel E., Ellmann A., and Delpeche-Ellmann N., 2019. Performance of sentinel-3A SAR altimetry retrackers: The SAMOSA coastal sea surface heights for the Baltic sea. International Association of Geodesy Symposia, 150, 23–32. https://doi.org/10.1007/1345_2019_59

Bosch W., Dettmering D., and Schwatke C., 2014. Multi-Mission Cross-Calibration of Satellite Altimeters: Constructing a Long-Term Data Record for Global and Regional Sea Level Change Studies. Remote Sens., 6(3), 2255–2281. https://doi.org/10.3390/rs6032255

Brown G. S., 1977. The Average Impulse Response of a Rough Surface and Its Applications. IEEE Trans. Antennas Propag , 25(1), 67–74. https://doi.org/10.1109/TAP.1977.1141536

Carrere L., Lyard F., Cancet M., Guillot A., Carrere L., Lyard F., Cancet M., and Guillot, A., 2015. FES 2014, a new tidal model on the global ocean with enhanced accuracy in shallow seas and in the Arctic region. EGUGA, 5481. https://ui.adsabs.harvard.edu/abs/2015EGUGA..17.5481C/abstract

Cipollini P., Calafat F. M., Jevrejeva S., Melet A., and Prandi P., 2017. Monitoring Sea Level in the Coastal Zone with Satellite Altimetry and Tide Gauges (Vol. 38, pp. 35–59). Springer, Cham. https://doi.org/10.1007/978-3-319-56490-6_3

Delpeche-Ellmann, N., Mingelaitė, T., Soomere, T., 2017. Examining Lagrangian surface transport during a coastal upwelling in the Gulf of Finland, Baltic Sea. Journal of Marine Systems 171, 21–30. https://doi.org/10.1016/j.jmarsys.2016.10.007

Desjonquères J. D., Carayon G., Steunou N., and Lambin J., 2010. Poseidon-3 Radar Altimeter: New Modes and In-Flight Performances. Mar. Geod., 33(sup1), 53–79. https://doi.org/10.1080/01490419.2010.488970

Dinardo S., 2020. Techniques and Applications for Satellite SAR Altimetry over water, land and ice - TUprints. https://doi.org/10.25534/tuprints-00011343

Dinardo S., Bruno L., Ambrózio A., and Jerome B., 2014. SAR Altimetry Processing on Demand Service for CryoSat-2 and Sentinel-3 at ESA G-POD. Conference on Big Data from Space (BiDS'14). https://doi.org/10.1109/MGRS.2014.2345997

Ellmann A., Märdla S., and Oja T., 2019. The 5 mm geoid model for Estonia computed by the least squares modified Stokes's formula. Surv. Rev., 52(373), 352–372. https://doi.org/10.1080/00396265.2019.1583848

Gomez-Enri J., Cipollini P., Passaro M., Vignudelli S., Tejedor B., and Coca J., 2016. Coastal Altimetry Products in the Strait of Gibraltar. IEEE Trans Geosci Remote Sens, 54(9), 5455–5466. https://doi.org/10.1109/TGRS.2016.2565472

Hayne G. S., 1980. Radar Altimeter Mean Return Waveforms from Near-Normal-Incidence Ocean Surface Scattering. IEEE Trans. Antennas Propag, 28(5), 687–692. https://doi.org/10.1109/TAP.1980.1142398.

Idris N.H., Vignudelli S., and Xiaoli D., 2021. Assessment of retracked sea levels from Sentinel-3A Synthetic Aperture Radar (SAR) mode altimetry over the marginal seas at Southeast Asia. Int. J. Remote Sens, 42:4, 1535-1555, DOI: 10.1080/01431161.2020.1836427.

Jahanmard V., Delpeche-Ellmann N., and Ellmann A. Realistic dynamic topography through coupling geoid and hydrodynamic models of the Baltic Sea. Cont. Shelf Res., 222, 104421. https://doi.org/10.1016/j.csr.2021.104421

Jekeli C., 2006. Geometric Reference System in Geodesy. Ohio State University: Columbus, Division of Geodesy and Geospatial Science School of Earth. https://kb.osu.edu/bitstream/handle/1811/77986/Geom_Ref_Sys_Geodesy_2016.pdf?sequence=1&isAllowed=y

Kollo K., and Ellmann A., 2019. Geodetic Reconciliation of Tide Gauge Network in Estonia. Geophysica, 54(1), 27–38. http://www.geophysica.fi/pdf/geophysica_2019_54_kollo.pdf

Lagemaa P., 2012. Operational Forecasting in Estonian Marine Waters. TUT Press, 128.

Lagemaa P., Elken J., and Kõuts T., 2011. Operational sea level forecasting in Estonia. Estonian J. Eng., 17(4), 301–331. https://doi.org/10.3176/eng.2011.4.03

Liibusk A., Kall T., Rikka S., Uiboupin R., Suursaar Ü., and Tseng K.-H., (2020). Validation of Copernicus Sea Level Altimetry Products in the Baltic Sea and Estonian Lakes. Remote Sens., 12 (24), 4062. DOI: 10.3390/rs12244062

Märdla S., Ågren J., Strykowski G., Oja T., Ellmann A., Forsberg R., Bilker-Koivula M., Omang O., Parseliūnas E., Liepinš I., and Kaminskis J., 2017. From Discrete Gravity Survey Data to a High-resolution Gravity Field Representation in the Nordic-Baltic Region. Mar. Geod., 40(6), 416–453. https://doi.org/10.1080/01490419.2017.1326428

Müller F., Dettmering D., Bosch W., and Seitz F., 2017. Monitoring the Arctic Seas: How Satellite Altimetry Can Be Used to Detect Open Water in Sea-Ice Regions. Remote Sens., 9(6), 551. https://doi.org/10.3390/rs9060551

Müller F. L., 2020. User Manual Along-Track Data Baltic+ SEAL Project: ESA AO/1-9172/17/I-BG-BALTIC+ (Sea Level) Internal Dataset 2 (Update).

National Geodetic Survey (NGS)., 2013. The National Geodetic Survey Ten Year Strategic Plan, 2013-2023: Positioning America for the Future. https://www.ngs.noaa.gov/INFO/TenYearPlanpublicreview.pdf

Normandin C., Frappart F., Diepkilé A. T., Marieu V., Mougin E., Blarel F., Lubac B., Braquet N., and Ba A., 2018. Evolution of the Performances of Radar Altimetry Missions from ERS-2 to Sentinel-3A over the Inner Niger Delta. Remote Sens., 10(6), 833. https://doi.org/10.3390/rs10060833

Omstedt A., and Hansson D., 2006. The Baltic Sea ocean climate system memory and response to changes in the water and heat balance components. Cont. Shelf Res., 26(2), 236–251. https://doi.org/10.1016/j.csr.2005.11.003

Passaro M., Cipollini P., Vignudelli S., Quartly G. D., and Snaith H. M, 2014. ALES: A multi-mission adaptive subwaveform retracker for coastal and open ocean altimetry. Remote Sens. Environ., 145, 173–189. https://doi.org/10.1016/j.rse.2014.02.008

Passaro M., Rose S. K., Andersen O. B., Boergens E., Calafat F. M., Dettmering D., and Benveniste J., 2018. ALES+: Adapting a homogenous ocean retracker for satellite altimetry to sea ice leads, coastal and inland waters. Remote Sens. Environ., 211, 456–471. https://doi.org/10.1016/j.rse.2018.02.074

Passaro M., Müller F., and Dettmering D., 2020a. Baltic+ SEAL:

Algorithm Theoretical Baseline Document (ATBD), Version 2.1. Technical report delivered under the Baltic+ SEAL project. http://doi.org/10.5270/esa.BalticSEAL.ATBDV2.1.

Passaro et al. 2020b. Baltic+ SEAL: Product Handbook, Version X.X. User manual delivered under the Baltic+ SEAL project. [Available in February, 2021].

Rautiainen L., Särkkä J., Tuomi L., Müller F., and Passaro M., 2020. Baltic+ SEAL: Validation Report, Version 2.2 Technical report delivered under the Baltic+ SEAL project. http://doi.org/10.5270/esa.BalticSEAL.VRV2.2

Ray C., Martin-Puig C., Clarizia M. P., Ruffini G., Dinardo S., Gommenginger C., and Benveniste J., 2015. SAR altimeter backscattered waveform model. IEEE Trans Geosci Remote Sens, 53(2), 911–919. https://doi.org/10.1109/TGRS.2014.2330423

Roblou L., Lyard F., le Henaff M., and Maraldi C., 2007. X-track, a new processing tool for altimetry in coastal oceans. International Geoscience and Remote Sensing Symposium (IGARSS), 5129–5133. https://doi.org/10.1109/IGARSS.2007.4424016

Roemmich D., Woodworth P., Jevrejeva S., Purkey S., Lankhorst M, Send U, and Nikolai Maximenko N., 2017. In situ observations needed to complement, validate, and interpret satellite altimetry. In Stammer D., and Cazenave A., (Eds.), Satellite altimetry over oceans and land surfaces (pp. 113–148). CRC Press. http://nora.nerc.ac.uk/id/eprint/518392/.

Rulent J., Calafat FM., Banks CJ., Bricheno LM., Gommenginger C., Green JAM., Haigh ID., Lewis H., and Martin ACH., 2020. Comparing Water Level Estimation in Coastal and Shelf Seas From Satellite Altimetry and Numerical Models. Front. Mar. Sci. 7:549467. doi: 10.3389/fmars.2020.549467.

Slobbe D. C., Klees R., and Gunter B. C., 2014. Realization of a consistent set of vertical reference surfaces in coastal areas. J. Geod, 88(6), 601–615. https://doi.org/10.1007/s00190-014-0709-9

Soomere T., Behrens A., Tuomi L., Nielsen JW., 2008. Wave conditions in the Baltic Proper and in the Gulf of Finland during windstorm Gudrun. Nat Hazards Earth Syst. Sci 8(1), 37–46. https://doi.org/10.5194/nhess-8-37-2008

Thibaut P., Labroue S., Ablain M., Faugere Y., and Zanife O.-Z., 2006. Evaluation of the Jason-1 ground retracking algorithm. Ocean Surface Topography Science Team (OSTST) Meeting. https://www.aviso.altimetry.fr/fileadmin/documents/OSTST/2006/thibaut.pdf

Thibaut P., Poisson J. C., Bronner E., and Picot N., 2010. Relative Performance of the MLE3 and MLE4 Retracking Algorithms on Jason-2 Altimeter Waveforms. Mar. Geod., 33(sup1), 317–335. https://doi.org/10.1080/01490419.2010.491033

Véronneau M., and Huang J., 2016. The Canadian geodetic vertical datum of 2013 (CGVD2013). Geomatica, 70(1), 9–19. https://doi.org/10.5623/cig2016-101

Vignudelli S., Snaith H. M., Lyard F., Cipollini P., Venuti F., Birol F., Bouffard J., and Roblou L., 2006. Satellite radar altimetry from open ocean to coasts: challenges and perspectives. In Frouin R. J., Agarwal V. K., Kawamura H., Nayak S., and Pan D., (Eds.), Proceedings of 5th Society of Photo-Optical Instrumentation Engineers (SPIE) Asia-Pacific remote sensing symposium (Vol. 6406, pp. 1–12). SPIE Asia-Pacific Remote Sensing. https://doi.org/10.1117/12.694024

Appendix 2

Publication II

Mostafavi, M., Delpeche-Ellmann, N., Ellmann, A. and Jahanmard, V., 2023. Determination of Accurate Dynamic Topography for the Baltic Sea Using Satellite Altimetry and a Marine Geoid Model. Remote Sensing, 15(8), p. 2189. https://doi.org/10.3390/rs15082189

Article

Determination of Accurate Dynamic Topography for the Baltic Sea Using Satellite Altimetry and a Marine Geoid Model

Majid Mostafavi [1,*], Nicole Delpeche-Ellmann [2], Artu Ellmann [1] and Vahidreza Jahanmard [1]

1   Department of Civil Engineering and Architecture, Tallinn University of Technology, 19086 Tallinn, Estonia
2   Department of Cybernetics, School of Science, Tallinn University of Technology, 19086 Tallinn, Estonia
*   Correspondence: majid.mostafavi@taltech.ee

Abstract: Accurate determination of dynamic topography (DT) is expected to quantify a realistic sea surface with respect to its vertical datum and in identifying sub-mesoscale features of ocean dynamics. This study explores a method that derives DT by using satellite altimetry (SA) in conjunction with a high-resolution marine geoid model. To assess the method, DT was computed using along-track SA from Sentinel- 3A (S3A), Sentinel-3B (S3B), and Jason-3 (JA3), then compared with DT derived from a tide-gauge-corrected hydrodynamic model (HDM) for the period 2017–2019 over the Baltic Sea. Comparison of SA-derived DT and corrected HDM showed average discrepancies in the range of ±20 cm, with root mean square errors of 9 cm (for S3B) and 6 cm (for S3A and JA6) and a standard deviation between 2 and 16 cm. Inter-comparisons between data sources and multi-mission SA over the Baltic Sea also potentially identified certain persistent and semi-persistent problematic areas that are either associated with deficiencies in the geoid, tide gauge, HDM, and SA or a combination of all of these. In addition, it was observed that SA data have the potential to show a more realistic (detailed) variation of DT compared to HDM, which tended to generate only a smooth (low-pass) surface and underestimate DT.

Keywords: satellite altimetry; Baltic Sea; absolute sea level; dynamic topography; geoid model; hydrodynamic model; hydrogeodesy; tide gauge

1. Introduction

Accurate and consistent absolute sea level determination is a fundamental indicator of changes in our climate and is applicable in many research disciplines, including hydrogeodesy and oceanography. It is well known that sea level can be deduced from different sources, including tide gauge (TG) stations, hydrodynamic models (HDMs), and satellite altimetry (SA) [1]. These data sources, whilst capable, often refer to different vertical datums with different spatio-temporal resolutions [1]. For instance, for SA derived sea surface heights (SSH), the vertical reference is the ellipsoid, whereas TG data may refer to a geoid (equipotential surface of the earth) or mean sea level (MSL), and the vertical datum of HDM can often be undisclosed (Figure 1) and generally may have a bias that varies both spatially and temporally with respect to the records of nearby TG stations [1,2]. These differences often make it challenging for comparison and consistency among the sources. Consequently, this hinders the full understanding of continuous sea level variations from coast to offshore.

Instead, a useful component that reasonably represents sea level dynamics, capturing both mean and sub-mesoscale dynamics (i.e., <10 km ocean features), is dynamic topography (DT), which dynamically varies in a spatio-temporal domain in intricate patterns [3]. DT can be derived using two methods. Firstly, via an oceanographic approach, DT is calculated by using sea level data from ocean models. However, in many cases, the vertical datum often is unknown or undisclosed. Secondly, DT is calculated by using the difference between the SA-determined SSH and a suitable geoid model (i.e., DT = SSH-geoid).

Note that DT is a more realistic component than the sea level anomaly (SLA = SSH-MSL). Instead of mean sea level (MSL), using a geoid allows for the determining of both mean and time-varying dynamics that exist so that sub-mesoscale dynamics can potentially be determined. Thus, the main intention of this study is to describe in detail a methodology that computes DT obtained from SA. A secondary aspect that this study examines is a quantitative comparison of the differences between the DT obtained from SA and the TG corrected HDM (i.e., biases accounted for) and a provisional investigation into the causes of these differences.
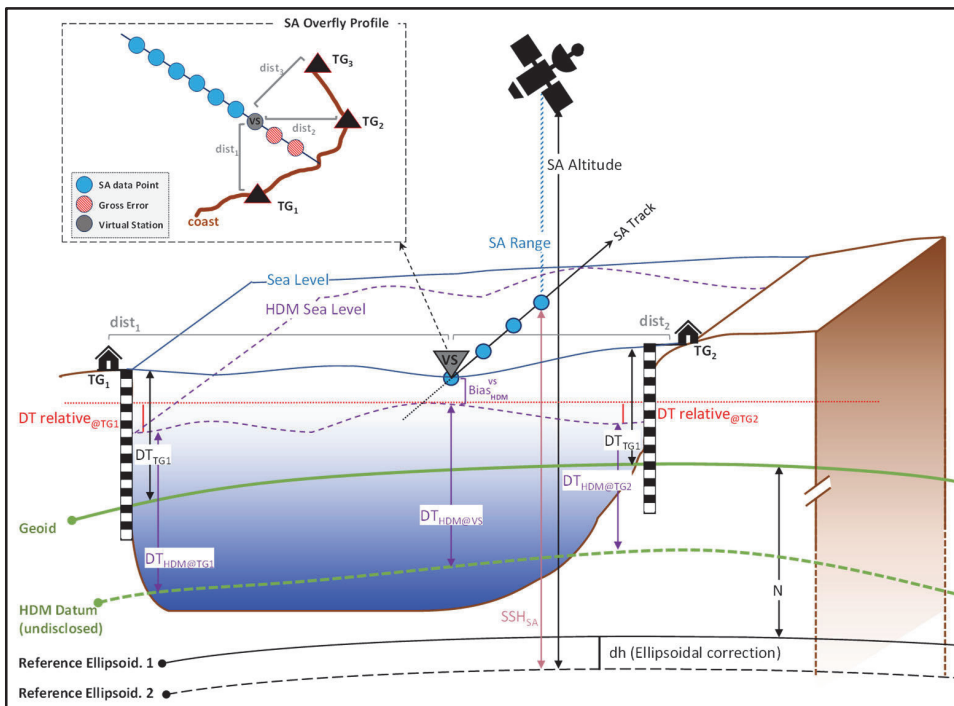
Figure 1. Inter-relations between the participating datasets (hydrodynamic model, tide gauges, and satellite altimetry data), geoid model, and different reference ellipsoids. Virtual Station (VS) is used to correct the HDM near the TG. The top inset illustrates the VS selection principles along the SA tracks.

Even though multiple global geoid models are available (such as the Earth Gravitational Model EGM08 [4]), they are not sufficient in terms of accuracy and spatial resolution. For DT to make a difference, one requires the utilization of high-resolution regional geoid models [1,5] that can be obtained by in situ gravity and remote sensing measurements (using SA-derived gravity data products and ship- or airborne gravity measurements) along with robust and intricate modeling techniques [6]. Most study areas are limited in developing high-resolution geoid models due to a lack of vital technical expertise and equipment (which can be expensive). Many countries, however, are moving forward in computing accurate geoid models for their land–sea areas (e.g., the Baltic Sea region, Canada, Australia, etc.). An example is illustrated with respect to the Baltic Sea countries of pursuing a collaboration amongst nations, which has now resulted in a regionally calculated high-resolution geoid model (NKG2015) [6]. This effort now paves the way for further developments in marine studies that were not possible before.

Historically, TG stations provide a reliable measurement of relative sea level, i.e., relative to land-bound benchmarks. However, in some areas (such as the Baltic Sea region) it is necessary for TG records to be corrected for vertical land motion (VLM) to acquire

absolute sea level (i.e., refer to the Earth's center of mass) [7]. In addition, the major limitation of TG observations is that they are not representative for offshore sea level variability. Meanwhile, SA and HDM data are quite capable of representing absolute sea level both in coastal and offshore areas; once a HDM is corrected for the bias and tilts that exist, a realistic comparison with other sources is possible. Note that HDM compilations are based on mathematical models whereas the actual marine areas are unpredictable and turbulent. Thus, it is expected that the comparison of SA (which remotely measures the real sea surface) with corrected HDM (which is the only available source of DT offshore) can reveal the actual sea surface topography and possible modeling imperfections. In addition, the present study hints at problematic issues either with the geoid, HDM, TG, or SA datasets. Recently developed high-resolution regional HDMs can reproduce the best spatio-temporal resolution sea level variations nearshore and offshore. Therefore, it will be more effective to use SA data in conjunction with HDM to validate the retrieval of accurate absolute sea level variations offshore, with TG data providing realistic quality control at the coast [8,9].

The perspective undertaken in this study is to show that SA-derived DT can be accurately calculated both at the coast and offshore. It should be noted that SA data have some limitations, especially in coastal areas and sub-arctic sea ice regions. The SA data are affected by the vicinity to the coast of a few kilometers, where the radar echo interacts with the nearby land surface, leading to corrupted waveforms [10]. Moreover, SA data are aligned to the International Terrestrial Reference Frame (ITRF), which may not necessarily coincide with the reference frame of the coordinates of land-bounded TG stations. TG stations normally refer to other pan-continental or national reference datums, such as the European Terrestrial Reference System (ETRS) and its national realizations. Another difficulty is related to the tidal effects and altimeter observation corrections (including geophysical and media corrections) that often become inaccurate close to the coast [11]. Furthermore, seasonal sea ice coverage, irregular coastlines, and the presence of numerous archipelagos, small islands, and rocks within 10 km from the coastline would affect SA data quality in many areas [10,12–16].

The potential of SA for monitoring coastal sea level variations and many oceanographic fields has motivated the development of coastal altimetry studies. Hence, several projects (e.g., PISTACH [17]; PEACHI [18]; COASTALT [19]; X-TRACK [20], Baltic+SEAL [21]) have been developed to improve the retrieval of sea level parameters from coastal waveforms of SA. In particular, the European Space Agency's Baltic+ Sea Level (ESA Baltic+SEAL) Project, launched in April 2019, is generating enhanced multi-mission sea level products that are specifically developed for the Baltic Sea. To attain a consistent description of sea level variability, a new re-tracking algorithm was developed and applied. This yields a homogeneous SSH determination that is particularly adapted for the complex areas of the Baltic Sea and North Sea, especially with respect to the presence of seasonal sea ice and complex coastal geomorphology [21].

As mentioned earlier, the focus of this study is to explore a developed methodology to estimate accurate DT in the Baltic Sea using a synergy of SA, corrected HDM, a dense TG network, and a high-resolution geoid model. The Baltic Sea is a semi-enclosed shallow sea in northern Europe that is heavily influenced by a massive density of marine traffic, coastal activities, port development, and sub-mesoscale marine dynamics [10]. Thus, knowledge of accurate DT variations in the Baltic Sea is critical for many reasons (e.g., consistency amongst data sources, sea level trends estimate, derivation of currents, etc.). In addition, since no sea level source is perfect (mentioned above with respect to the limitation of HDM and SA), but given that they all refer to the same vertical datum, this now allows a logical inter-comparison to be performed. By performing statistical analysis, this comparison has the potential to identify the problematic areas of the sea level sources utilized. Note that the sources of these problematic areas are only provisionally explored in this study to demonstrate the usefulness of DT and the benefits that the synergy of different sources of sea level data can indirectly reveal. For a more detailed understanding of these sources,

more resources are required that are out of the scope of this study but can be pursued for future studies. Note that the other sources of sea level from which DT can also be derived consist of shipborne GNSSs (global navigation satellite systems) and airborne laser scanning profiles. For instance, Ref [22] used airborne laser scanning profiles for determining DT. In addition, Ref [23,24] used shipborne GNSS profiles for determining DT over the Baltic Sea. Usage of these other sources are, however, restricted by their spatial and temporal resolution.

The method developed and described in this study was possible for the Baltic Sea region, which is fortunate to have a dense multi-national TG network, a high-resolution geoid model, a land uplift model, and access to data-assimilated HDM and SA data specifically tuned to the sea conditions. In particular, HDM bias with respect to the TG readings has been eliminated along the SA track, so the corrected HDM provides accurate DT estimates both near- and offshore. Such a combination can assist in retrieving accurate DT from relatively short altimetry time series [25]. This method to our knowledge has not been performed before, especially from the point of view of utilizing multi-mission along-track SA data and a high-resolution geoid model. It also can be applied to other sea areas.

Previous studies have examined the performance of SA data in the Baltic Sea [10,12–16,26–28], but these studies mostly examined the sea surface in terms of SSH and were limited to mostly validation of SA data. In addition, many of these studies examined only a section of the Baltic Sea.

Thus, the focus of this study is (i) development and demonstration of a detailed method for determining accurate DT using along-track SA, derived for multiple satellite missions in the entire Baltic Sea, and (ii) by statistically and qualitatively comparing the discrepancy between SA and corrected HDM to identify the persistent and semi-persistent patterns that could potentially reveal problematic areas of the various sources utilized (e.g., geoid model, TG, HDM, and SA). The time period examined for all data sources was between 2017 and 2019; this was based on the availability of all the data sources, since the SA data were sourced from the Baltic+SEAL project and these data were up to 2019 (at the time of the study). This three-year long-term period, however, is considered to be representative enough for our objectives to describe the method and to show its potential.

This paper is organized in a format such that the developed methodology is described in Section 2 and the study area and utilized datasets are described in Section 3. Section 4 presents the results of the obtainable DT accuracy and identifies the areas with persistent and semi-persistent patterns by comparing the different sources of sea level data and multi-mission SA. The results of this study are discussed in Section 5, whereas Section 6 contains a brief summary of this study.

2. Methodology

This section describes the method employed to achieve accurate DT using two approaches: the first approach utilizes HDM, and the second approach uses SA. The first approach involves extracting the HDM data points that coincide with the SA along-track data points. Once this is performed, the HDM data points are corrected via TG observations by means of utilizing virtual stations (Section 2.1). The second approach requires a geoid model and some other vital auxiliary corrections for obtaining DT from the SA-computed sea surface heights (Section 2.2). This original HDM provides high-correlation estimates of TG-observed sea levels along the Baltic coastline. However, the original HDM also contains some biases due to the undisclosed actual vertical datum used [2]. Hence, for further computational steps, it is vital to retrieve reliable DT values in a stable vertical reference datum by correcting the HDM. For this purpose, the HDM correction method with respect to the TG observations by means of utilizing virtual stations (VS) was applied (cf. Section 2.1), to consider these biases as well as unify the vertical reference of the HDM to the same reference surface as the TG and SA data. The second approach requires a geoid model and some other vital auxiliary corrections for obtaining DT from the SA-computed sea surface

heights (Section 2.2). The difference between SA-derived DT (DT_{SA}) and HDM-derived DT (DT_{HDM}) is then calculated both spatially and temporally using VSs. It is expected that the HDM may appear to be somewhat insensitive in terms of fully capturing the short-wavelength marine surface variations; this is mainly due to the fact that it is a model with limitations (e.g., parametrization, approximations model forcings, etc.). The HDM, however, is still a key source because it is capable of simulating both coastal and offshore sea level data. The assumption in the present study is that once the HDM is corrected for this bias and tilts, it can be compared to the SA data. Utilization of the geoid allows the comparison of the corrected HDM and SA to be performed; otherwise, the two datasets would be incomparable in an absolute sense.

In this study, it was essential that the HDM was corrected and considered as the ground truth during examination of the DT_{SA} estimates. Note, however, that in the comparisons, one of the sources had to be assumed to be the ground truth (in this case the corrected HDM via TGs) to obtain the discrepancies. So, the comparison of appropriately corrected HDM (which was always the case in the further comparisons) versus DT_{SA} provides a good quantification of the accuracy of the latter.

2.1. TG/HDM Based DT Estimates
2.1.1. General Overview of the Method

This section describes the method used to correct the HDM derived DT (DT_{HDM}) at specific locations that are referred to as virtual stations (VSs). The concept of utilizing VSs originates from the following characteristics: (i) it is important that DT_{HDM} be calculated at the same data points as SA (i.e., in space and time); (ii) correction of HDM is assumed to be more accurate at VSs rather than at the near-shore location of TGs, and (iii) the study area is equipped with numerous TGs that may lie in proximity to SA data points.

It is commonly known that TG records are valid nearshore and may not adequately represent offshore DT. Instead, a regional HDM is an independent data source that can provide sea level data both at the coast and offshore. The method proposed is that by calculating the relative difference between DTs of HDM at the location of a TG and the location of the proposed VS, it is possible to calculate the DT at the VS via the TG's readings. This is performed by simply adding this relative difference in DTs (Equations (1)–(3)). Different interpolation methods (linear interpolation, thin plate spline regression, and inverse distance weighted (IDW)) were explored in [2] and the results show a difference of around 2 cm. However, the IDW showed slightly more realistic results, so in this study, a similar procedure was implemented.

In addition, the vertical reference datum of HDM is often unknown/undisclosed and may contain some errors and discrepancies from the exact reality of sea level. To overcome such limitations, a bias correction solution needs to be introduced to correct the HDM by a one-dimensional vertical shift at a single time instant (which changes during the time of the SA cycle). This correction represents the difference between the TG and the HDM data at a VS. The correction values (i.e., bias) change over time, and we computed this correction at the time of SA. The reason why it changes is due to two components: (i) The fact that the TG measures in situ data (i.e., the actual situation) whilst the HDM is based on a mathematical model that attempts to model the sea surface based on the input forces, models, etc. So, it is expected that the HDM may have an error when compared to reality. (ii) The HDM vertical reference is often undisclosed and can vary both spatially and temporally. Basically, the error between the HDM and the tide gauges can be separated into two parts: constant and time-variable. For simplicity, we express the "HDM bias" as a combination of all errors. In Ref. [2], a detailed examination was made into the bias and the study showed that the HDM bias can be spatially interpolated at each time instant in order to correct the HDM, and since the bias was interpolated (not the sea level), IDW interpolation can be a good choice. This bias correction method between a TG and HDM at a VS is explained in more detail below in Equations (1)–(5) for each SA cycle. Note that in the used equations, the HDM correction values (Equation (5)) are both time- and location-dependent.

2.1.2. Detailed Method

Determination of the VS locations is the first step of HDM correction. A VS is selected as the closest location of a good-quality SA data point approaching the coastline (Figure 1). Each SA track has at least two VSs (at the beginning and the end of the track), though many tracks have more along-track VSs, close-to-coast, and nearby TG stations (cf. Figure 2a).
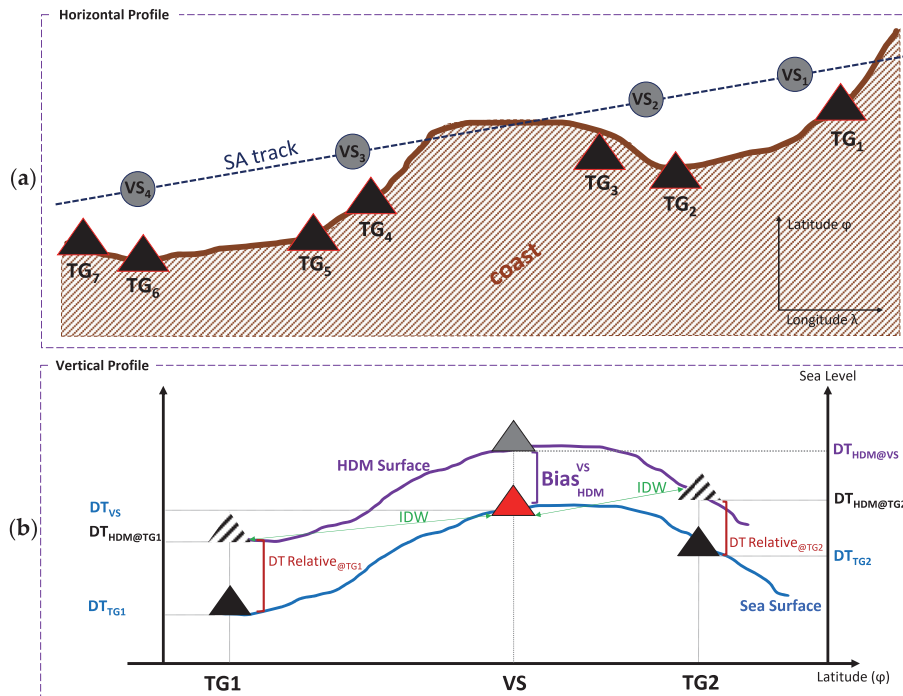
Figure 2. Determination of the HDM bias and selection principles of virtual stations (VSs). (**a**) The horizontal profile of a single SA pass and selection of VSs along the SA track near TG locations. (**b**) Determination of the HDM bias at the location of VS ($Bias_{HDM}^{VS}$) using the DT_{TG} by adding the relative DT.

Note that the coastline-located TGs may not exactly coincide with the HDM data grid nodes. In addition, the available HDM data near TG locations are expected to have some errors due to the limitations of HDM in nearshore and shallow waters. In addition, given the dense network of TG stations in the study area, the TG-derived DT may be valid toward offshore within a valid domain (including the VS's location) using adjacent TGs and by adding the relative DT, i.e., the difference in DT at the HDM location of the VS and the location of the TG (cf. Figure 2b). In such cases, the DT of the VS is determined using inverse distance weighted (IDW) interpolation slightly seaward at the VS locations. Hence, VS is assumed to represent an enhanced duplicate of the TGs and is consistent with HDM data.

A VS intends to represent the *k*-nearest TG stations at a SA pass. The nearest TG (hourly, *t*) readings are interpolated (*interp*) linearly at the time of SA overfly cycle time (t_{cycle}), whereas the relative DT ($DT_{Relative}$) is added to this to retrieve DT at the location of the VS ($DT_{TG@VS}$). The $DT_{Relative}$ is the difference between the HDM-based DT at the location of the VS ($DT_{HDM}\left(\varphi_{VS}, \lambda_{VS}, t_{cycle}\right)$ and that at the location of the TG ($DT_{HDM}\left(\varphi_{TG}, \lambda_{TG}, t_{cycle}\right)$). The $DT_{Relative}$ could provide more realistic DT of TG readings at the location of the VS rather than simple interpolation (cf. Figure 2b) since the assump-

tion is that the HDM is providing a reference base surface sea level, not a precise one. By adding the $DT_{Relative}$ to the timewise-interpolated DT_{TG} $interp\left(DT_{TG}\left(\varphi_j, \lambda_j, t_{cycle}\right)\right)$, the DT_{VS} is obtainable. The adjacent $DT_{TG@VS}$ (Figure 2b red triangle) to the VS are averaged using IDW [29] to yield the DT at the VS location ($DT_{VS}(\varphi_{VS}, \lambda_{VS})$), which now can be used to determine the bias of the HDM.

$$DT_{TG@VS}\left(\varphi_j, \lambda_j, t_{cycle}\right)$$
$$= interp\left(DT_{TG}\left(\varphi_j, \lambda_j, t_{cycle}\right)\right) + DT_{Relative}\left(\varphi_j, \lambda_j, t_{cycle}\right) \tag{1}$$

where

$$DT_{Relative}\left(\varphi_j, \lambda_j, t_{cycle}\right)$$
$$= interp[DT_{HDM}\left(\varphi_{VS}, \lambda_{VS}, t_{cycle}\right) - DT_{HDM}\left(\varphi_{TG}, \lambda_{TG}, t_{cycle}\right)] \tag{2}$$

and

$$DT_{VS}\left(\varphi_{VS}, \lambda_{VS}, t_{cycle}\right) = \frac{1}{\sum_{j=1}^{k} p_j} \sum_{j=1}^{k} p_j \cdot DT_{TG@VS}\left(\varphi_j, \lambda_j, t_{cycle}\right) \tag{3}$$

Note that k is the total number of available TG stations reasonably close to the VS. Hence, a 130 km radius was selected based on empirical experience in the study area to guarantee the availability of at least one TG station within this radius and exclude farther TGs. The symbol p_j is the assigned IDW weight for the j-th TG station with coordinates $\left(\varphi_j, \lambda_j\right)$, which is computed as follows:

$$p_j = \frac{c_0}{dist_j} \tag{4}$$

where c_0 is the minimum distance of the associated TGs to the VS and $dist_j$ is the distance of the j-th participating TG to the VS. Using the IDW, the TG station with the minimum distance (~3 km) to the VS has the maximum effect on DT_{VS}. In addition, distant TGs would be neglected (TGs exceeding 130 km distance). The DT_{VS} is expected to represent a more truthful condition of the sea level (in contrast to DT_{TG}) that can be compared to the SA data point. For the SA passes that are near only a single ($k = 1$) TG at each side of the coast, only one TG reading is selected to obtain the DT_{VS} (i.e., $DT_{VS}\left(t_{cycle}\right) = interp(DT_{TG}(t))$, interpolated time-wise only) with maximum weight ($p = 1$).

DT_{VS} is compared with DT_{HDM} to remove any possible bias of the HDM. The HDM bias at the location of each VS ($Bias_{HDM}^{VS}(\varphi_{VS}, \lambda_{VS})$) is determined by the difference between DT_{VS} and the initial HDM values DT_{HDM}:

$$Bias_{HDM}^{VS}\left(\varphi_{VS}, \lambda_{VS}, t_{cycle}\right) = DT_{HDM}\left(\varphi_{VS}, \lambda_{VS}, t_{cycle}\right) - DT_{VS}\left(\varphi_{vs}, \lambda_{VS}, t_{cycle}\right) \tag{5}$$

Recall that the assumption made in this study is that the VS tends to represent TG observations and is more or less a reliable ground truth that better reflects nearshore sea dynamics. The $Bias_{HDM}^{VS}$ represents both vertical reference datum discrepancies and HDM modeling errors. In addition, both HDM and TG data have hourly records, so the DT_{HDM} and DT_{TG} are temporally (and linearly) interpolated at the SA overfly time instant (t_{cycle}). In addition, since HDM data points spatially do not exactly coincide with SA along-track points ($\varphi_{SA}, \lambda_{SA}$), a bilinear interpolation of HDM is applied at the SA data points (including VS location). The $Bias_{HDM}^{VS}$ is interpolated linearly between a pair of VSs along each SA ground track denoted by "$interp(Bias_{HDM}^{VS}\left(\varphi_{SA}, \lambda_{SA}, t_{cycle}\right))$" and then subtracted from the initial DT_{HDM}. As a result, the corrected along-track HDM

$(DT_{HDM-corr})$ is obtained, which now coincides and is simultaneous with SA data locations $(\varphi_{SA}, \lambda_{SA})$ at the SA overfly time instant $\left(t_{cycle}\right)$:

$$
\begin{aligned}
DT_{HDM-corr}&\left(\varphi_{SA}, \lambda_{SA}, t_{cycle}\right) \\
&= DT_{HDM}\left(\varphi_{SA}, \lambda_{SA}, t_{cycle}\right) - interp(Bias_{HDM}^{VS}\left(\varphi_{SA}, \lambda_{SA}, t_{cycle}\right))
\end{aligned}
\tag{6}
$$

This along-track $DT_{HDM-corr}$ is assumed as the "first approximation ground truth" and will be checked against the SA derived DT (Section 2.2).

2.2. Estimation of DT from Satellite Altimetry and Statistical Examinations

The general concept of SA measurement includes the satellite's altimeter transmitting a pulse of known power toward the sea surface. On interacting with the sea surface, the pulse is then reflected to the altimeter. The two-way travel time is determined, yielding the range of the satellite after applying range correction (including geophysical and media corrections). Given the known SA orbit, SA-derived SSH is then obtainable with respect to the reference ellipsoid (cf. Figure 1).

However, a more realistic reference surface to be employed would be that of a geoid to retrieve the DT. For this purpose, along-track $DT_{SA}(\varphi_i, \lambda_i)$ is determined by subtracting the geoidal height (N) from the SSH_{SA} using the following expression:

$$
DT_{SA}\left(\varphi_i, \lambda_i, t_{cycle}\right) = SSH_{SA}\left(\varphi_i, \lambda_i, t_{cycle}\right) - dh(\varphi_i) - N(\varphi_i, \lambda_i)
\tag{7}
$$

Since original datasets of different SA missions and geoids may refer to different reference ellipsoids, the ellipsoidal correction ($dh(\varphi_i)$) of each data point is required. The ellipsoidal correction is due to the differences in parameters that are associated with each reference ellipsoid (including semi-major and minor axes, flattening, and eccentricity). By applying dh, both datasets (SA and geoid) will refer to the same reference ellipsoid (see also [10]).

$$
dh(\varphi_i) = \frac{\acute{a}\left(1 - \acute{e}^2\right)}{\sqrt{1 - \acute{e}^2 \sin^2(\varphi_i)}} - \frac{a\left(1 - e^2\right)}{\sqrt{1 - e^2 \sin^2(\varphi_i)}}
\tag{8}
$$

where a and a' are lengths of the semi-major axes of the participating ellipsoids, e and e' are their corresponding eccentricity values, and φ_i is the latitude of the point of interest. The discrepancies between the DT_{SA} and $DT_{HDM-corr}$ will be examined statistically. In addition, unqualified SA data points (which could be different for each SA cycle) need to be excluded from further data processing.

Errors and outliers of the SA dataset occur due to many reasons such as land-contaminated areas, extreme sea events (e.g., storms, surges, etc.) and waveform retracking sampling problems [10]. To remove these outliers from each SA track/cycle, a sequential approach for data screening is applied. The steps involved:

1. DT_{SA} values larger than a specific predefined threshold ($|DT_{SA}| >$ threshold) are considered as gross errors and removed from the data points. This threshold value (here selected as 1.5 m) corresponds to the study area characteristics that depend on historical extrema of the DT occurring in the study area (which is ~1.3 m in the Baltic Sea);

2. The erratic DT_{SA} are identified as those three times larger than the standard deviation (STD) of the mean value of the whole track in a cycle (the longer tracks are divided into sub-tracks to obtain more homogeneous selections);

3. The outliers are detected as elements more than three local scaled moving medians (MADs) from the median DT_{SA} over the 0.5° latitude (~55 km) window length along the track to have a smooth low-pass DT_{SA} behavior.

This approach assists in filtering unqualified data, which allows a more accurate determination of DT_{SA}. After excluding the gross errors and outliers from all SA along-

track data points, the remaining good-quality data points (their locations are denoted by sub-index *s*, e.g., φ_s, λ_s) are used for further steps.

The difference between DT_{SA} and $DT_{HDM-corr}$ is the discrepancy (ΔDT_{SA-HDM}), which is computed for each footprint point of each participating satellite mission by

$$\Delta DT_{SA-HDM}\left(\varphi_s, \lambda_s, t_{cycle}\right) = DT_{SA}\left(\varphi_s, \lambda_s, t_{cycle}\right) - DT_{HDM-corr}\left(\varphi_s, \lambda_s, t_{cycle}\right) \quad (9)$$

These discrepancies provide a tentative idea of SA agreement to the ground truth within the studied portion of each SA track for each SA mission separately. Statistical analyses of the discrepancies are conducted in terms of the root mean square error (RMSE), standard deviation (STD), and mean of ΔDT_{SA-HDM} by the equations below:

$$MEAN_{SA-HDM}\left(\varphi_s, \lambda_s\right) = \frac{1}{m}\sum_{cycle=1}^{m}\Delta DT_{SA-HDM}\left(\varphi_s, \lambda_s, t_{cycle}\right) \quad (10)$$

$$STD_{SA-HDM}(\varphi_s, \lambda_s)$$
$$= \sqrt{\frac{1}{m-1}\sum_{cycle=1}^{m}\left(\Delta DT_{SA-HDM}\left(\varphi_s, \lambda_s, t_{cycle}\right) - MEAN_{SA-HDM}(\varphi_s, \lambda_s)\right)^2} \quad (11)$$

Equations (10) and (11) potentially represent the validation of SA versus the corrected HDM over a single location considering all cycles of the SA mission (minor deviations in data points' locations from each other at sequential cycles is negligible). The *m* symbol is the number of qualified SA cycles on each location (φ_s, λ_s). The threshold of *m* can be selected as 90% of the total number of available cycles of each SA mission during the study period over the study area. The locations (φ_s, λ_s) containing datapoints less than this threshold are excluded. By having the along-track mean of the discrepancies at each location ($MEAN_{SA-HDM}\left(\varphi_s, \lambda_s\right)$), the performance of the individual SA mission over the entire sea (or any selected basin) can be evaluated by:

$$MEAN_{SA-HDM}\left(mission/Basin\right) = \frac{1}{b}\sum_{s=1}^{b} MEAN_{SA-HDM}(\varphi_s, \lambda_s) \quad (12)$$

$$STD_{SA-HDM}(mission/Basin)$$
$$= \sqrt{\frac{1}{b-1}\sum_{s=1}^{b}(MEAN_{SA-HDM}(\varphi_s, \lambda_s) - MEAN_{SA-HDM}\left(mission/Basin\right))^2} \quad (13)$$

$$RMSE(mission/Basin) = \sqrt{\frac{1}{b}\sum_{s=1}^{b}(MEAN_{SA-HDM}\left(\varphi_s, \lambda_s\right))^2} \quad (14)$$

where *b* is the total number of (φ_s, λ_s) locations (along-track locations of all passes, separately for each SA mission).

Equations (12)–(14) provide statistics for each SA mission. The RMSE and STD are commonly used to examine both along-track and mission/basin SA data quality. They provide statistically meaningful estimates of DT_{SA} accuracy at a given location or the whole basin via different SA missions. Different SA missions' data were not merged in this study; therefore, the range of *m* varies for each mission. The particulars of the used datasets are explained in Section 3. Figure 3 shows the flowchart of the applied methodology and data processing steps.
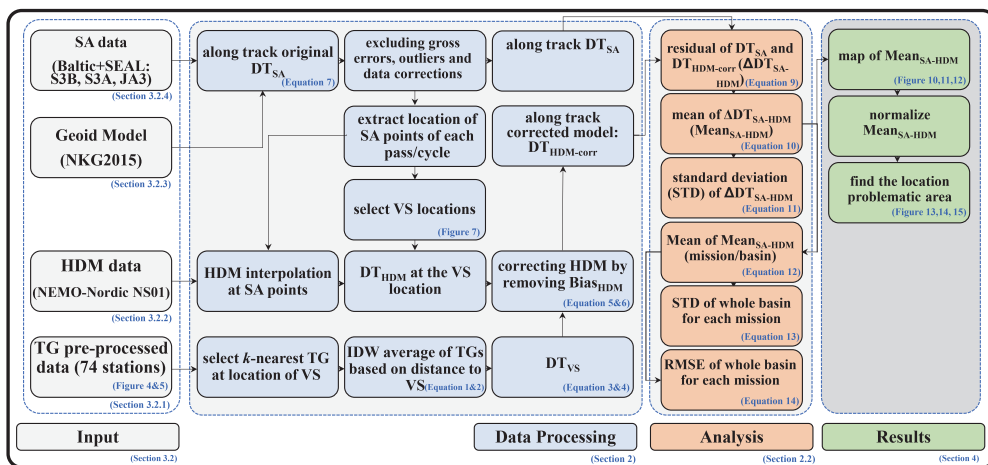
Figure 3. Workflow of different stages of developed methodology and analysis for validation and assessment process (the corresponding section, table, or figure of each stage is denoted by blue font). The used data products (in brackets) refer to the case study.

3. Study Area and Datasets

3.1. Baltic Sea

The Baltic Sea is the world's second-largest brackish water body (after the Caspian Sea) that has limited water exchange with the North Sea via narrow and shallow Danish straits. This estuarine-type water body's main source of freshwater originates from the numerous rivers that flow into it. The Baltic Sea is surrounded by nine countries and subdivided into several sub-basins that are based on the geomorphology and bathymetry of the sea area. Due to glacial isostatic adjustment, the Baltic Sea region is also strongly affected by vertical land motion (VLM) [30]. Due to the numerous countries surrounding the Baltic Sea, it has a high density of marine traffic and coastal activities. These attributes make it vital to have a common and realistic vertical datum (e.g., a geoid) that sea level can be referenced against, especially with the marine engineering and navigation activities performed for the Baltic Sea.

Several components based on different time frames affect the sea level dynamics in the Baltic Sea. With respect to the long term, the global sea level change (due to thermal sea water expansion and the melting of glaciers) will influence the Baltic Sea's level, whilst the variation in temperature, precipitation, and evaporation is expected to mostly exert influence on a decadal time scale [7]. For short-term influences (yearly, seasonally, daily, etc.), variations in the water balance caused by water exchange in the Danish Straits (e.g., saltwater intrusions from the Atlantic (Major Baltic inflow)) that are driven by atmospheric conditions may cause drastic sea level changes. River runoff also affects the water balance, with the biggest freshwater contributor being the Neva River located on the eastern side of the Baltic Sea [31]. It is common in winter months for the Baltic Sea to become ice-covered; the number of sea ice days also changes the dynamics of the sea level [32]. Ice coverage is common in the winter months for the Baltic Sea, especially in the northern (Gulf of Bothnia) and eastern sections (Gulf of Finland). This also has been a challenge for SA in determining the sea surface. However, improved SA coastal retrackers are expected to provide better data products over this region, e.g., Baltic+SEAL [10].

In much shorter time frames (e.g., weekly, daily, and hourly), other localized events also affect the sea level. Most of these events tend to be influenced by meteorological factors [33], especially the winds, which can be strongly anisotropic in the Baltic Sea [34]. However, the dominant wind direction in this area is southwest, but it is common for northerly winds to also be prevalent. Storm surges [35] and coastal upwellings [36] are also quite prevalent in the Baltic Sea, with a more or less seasonal trend. The strongest winds and highest waves are highly expected in the winter and autumn seasons [37]. In addition, temperature and precipitation may contribute to 15–35% of the sea level variability between winter and summer [38]. It is somewhat expected that HDMs may have difficulty reproducing some of these localized events. In addition, the internal Rossby radius can be relatively small, usually within the range of 1–2 km [39]. This makes it very challenging for the numerical models to replicate the (sub)-mesoscale dynamics in this water body. However, with SA, if the satellite flies over at the correct time and its measurement is represented as DT, the SA data may be able to capture some evidence of these small-scale dynamics.

3.2. Datasets

3.2.1. Tide Gauge Stations

The Baltic Sea has one of the world's densest observational tide gauge networks with remarkably long-term and high-quality local sea level records [40]. Within the study area, 74 TG stations (Figure 4a) were selected to have suitable locations near satellite tracks. The details of each TG station per country can be found in Table 1. An identification number (ID) was assigned to each TG station; the relevant details are given in Appendix A Table A1 as well.

(**a**) (**b**)
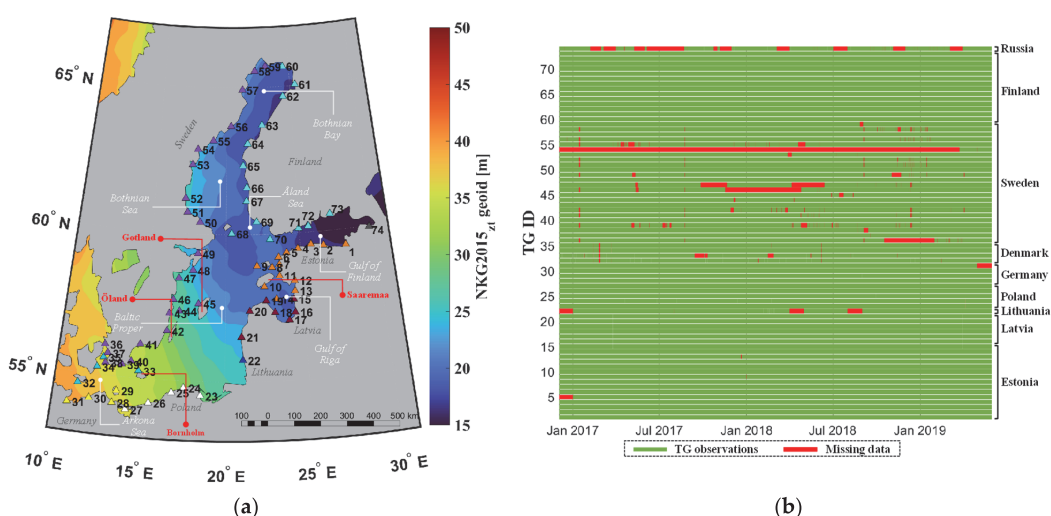
Figure 4. Characteristics of the study area: (**a**) Location of the Baltic Sea (the background represents the NKG2015 geoid model) together with the location of the tide gauges (triangle symbols). The names of sub-basins and main islands are denoted in white and red, respectively. (**b**) TG data availability between December 2016 to April 2019 of each TG ID (**b**). The TG numbering is clockwise, starting from the eastmost Estonian TG station and finishing with the Russian Kronstadt TG station (No. 74), which is located at the eastmost end of the Gulf of Finland.
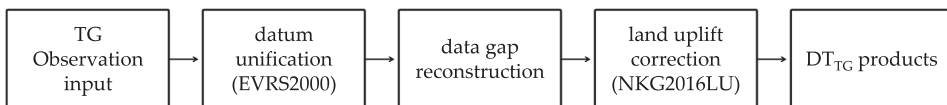
Table 1. Used TG stations of each country, their vertical datums, and the data agency.

ID	Country [1]	Vertical Datum [2]	No. TGs	No. of Data Gaps [3] [h]	Data Provider
1–14	▲Estonia	EH2000	14	1128	www.ilmateenistus.ee, accessed on 18 February 2020
15–21	▲Latvia	LAS2000,5	7	56	www.meteo.lv, accessed on 25 February 2020
22	▲Lithuania	LAS07	1	2163	www.aaa.am.lt, accessed on 2 February 2020
23–27	Poland	PL-EVRF2007-NH	5	100	www.imgw.pl, accessed on 11 April 2020
28–31	▲Germany	DHHN92	4	4419	www.bsh.de, accessed on 23 October 2020
32–35	▲Denmark	DVR90	4	1861	www.emodnet-physics.eu, accessed on 12 October 2020
36–59	▲Sweden	RH2000	24	37,567	www.smhi.se, accessed on 31 March 2020
60–73	▲Finland	N2000	14	0	www.ilmatieteenlaitos.fi, accessed on 28 March 2020
74	▲Russia	BHS77 (+15 cm)	1	9125	www.emodnet-physics.eu, accessed on 15 February 2020

[1]: Note that the TGs are distinguishable country-wise by the corresponding triangle color in Figure 4. [2]: A national realization of EVRS. [3]: Between 2017 and 2020.

These TG networks are operated by national tide gauge agencies and refer to the corresponding national realization of the EVRS2000 (European Vertical Reference System 2000) vertical datum, the zero level of which is the Normaal Amsterdams Peil (NAP). Hence, all data record vertical datums are harmonized with EVRS2000 using the Baltic Sea Chart Datum 2000 (BSCD2000). In addition, in BSCD2000, land uplift was modeled according to the NKG2016LU model at the epoch 2000.0 [41].

Since TGs measure relative sea level with respect to land, their measurements are required to be corrected for VLM in order to obtain absolute sea level. In the Baltic Sea region, vertical land motion is due to geophysical GIA and varies from -1 mm/year in the Arkona Sea to 10 mm/year in the Gulf of Bothnia [42]. In this study, the land uplift effect was removed from TG observations using the NKG2016LU model. This model includes the latest GIA land uplift model for the Baltic Sea region developed by the Nordic Commission of Geodesy (NKG, www.nordicgeodeticcommission.com, accessed on 26 August 2021). It covers an area from 49° to 75°N and 0° to 50°E [30]. The VLM corrections (from the reference time epoch, i.e., 2000.0) were applied from the model (linearly interpolated at the location of TG) by adding it to the TG readings (to the observation time epoch) [6]. During the selected time span of 2017–2019, some TG hourly data gaps exist, as can be seen in Table 1 and Figure 3b. These gaps were filled using highly correlated adjacent TG stations to reconstruct gap-free TG data, cf. [43]. Figure 5 shows the steps for the TG observation reconstructions. In further steps, TG#33 was excluded from the dataset due to data inconsistency with the other TGs.

TG Observation input → datum unification (EVRS2000) → data gap reconstruction → land uplift correction (NKG2016LU) → DT$_{TG}$ products

Figure 5. Steps for TG observation data reconstructions and corrections.

3.2.2. Hydrodynamic Model

Nemo-Nordic is a three-dimensional coupled ocean–sea ice model of the Baltic and North Sea based on the NEMO-3.6 (Nucleus for European Modeling of the Ocean) ocean engine, which was developed by the Swedish Meteorological and Hydrological Institutes (SMHI) [44]. In this study, a data-assimilated version (NS01) of the Nemo-Nordic model with an hourly temporal resolution and a spatial resolution of 1 nautical mile (~2 × 2 km) was utilized for the period 2017–2019 (www.smhi.se, accessed on 14 April 2020). The

bathymetry of the model was obtained from the General Bathymetric Chart of the Oceans Grid (GEBCO-2014). This HDM provides high-correlation estimates with the TGs along the Baltic coastline. However, this model also contains some errors, which are limited to a standard deviation of around 10 cm due to the undisclosed actual vertical datum used [2]. More details on the possible deficiencies of this particular HDM can be found in [2]. Hence, for further computational steps, it is vital to retrieve reliable DT values in a stable vertical reference datum by applying HDM correction. In this study, the applied methodology to identify and eliminate the above-mentioned HDM errors (for more details see [2]) using geoid-referenced TG-corrected HDM is described, which can be now used for deriving instantaneous and realistic sea level data near- and offshore. Then, the corrected HDM can be used to validate the SA derived DT. For this purpose, the HDM correction method with respect to the TGs was applied (cf. Section 2.1) to consider these biases, as well as unify the vertical reference of the HDM to the same reference surface as for the TG and SA data.

HDM correction (cf. Section 2.1) is basically a shift due to the biased vertical datum of the HDM (with respect to the zero level of the national vertical datum) that can also be due to HDM modeling errors. In this study, the TG was not only used to correct the HDM, but also for examining the discrepancies between HDM data and TG observations at each TG station $(\varphi_{TG}, \lambda_{TG})$ using hourly data (t_i) by:

$$\Delta DT_{HDM-TG}(\varphi_{TG}, \lambda_{TG}, t_i) = DT_{HDM}(\varphi_{TG}, \lambda_{TG}, t_i) - DT_{TG}(\varphi_{TG}, \lambda_{TG}, t_i) \quad (15)$$

The mean and standard deviation (STD) of HDM data discrepancies at each TG station (here 73 stations, TG#33 excluded) during the whole study period can be estimated as:

$$MEAN_{HDM-TG}(\varphi_{TG}, \lambda_{TG}) = \frac{1}{y}\sum_{i=1}^{y} \Delta DT_{HDM-TG}(\varphi_{TG}, \lambda_{TG}, t_i) \quad (16)$$

$$STD_{HDM-TG}(\varphi_{TG}, \lambda_{TG}) \\ = \sqrt{\frac{1}{y-1}\sum_{i=1}^{y}(\Delta DT_{HDM-TG}(\varphi_{TG}, \lambda_{TG}, t_i) - MEAN_{HDM-TG}(\varphi_{TG}, \lambda_{TG}))^2} \quad (17)$$

where y represents the total number of hourly DT records during 2017–2019 (y = years × days × hours) for Figure 6a or amount of data for each month during 2017–2019 (for Figure 6b). Figure 6 shows the mean and STD of HDM data residuals relative to TG observations during 2017–2019. In the figure, the circle size represents the mean (Equation (16)), whereas the color shows the STD at each TG location over entire Baltic Sea.

From Figure 6b,c, a seasonal pattern of HDM discrepancies is observed. Figure 6c indicates that the maximum discrepancies in the HDM (~30 cm) occur from February to March (winter–spring) and are the smallest during the autumn and summer seasons (less than 20 cm). This could be due to river runoff, snow melting, and other effects (e.g., steric effect) that may not be included in the original HDM (also cf. Section 3.1). Note that for the purpose of this study, the HDM was only corrected at the time instants of the SA cycles. In addition, from Figure 6a, the Swedish TGs (from TG#50 to TG#59) have larger $MEAN_{HDM-TG}(\varphi_{TG}, \lambda_{TG})$ (~25 cm). This indicates that either the HDMs are overestimating the DT more than usual or that there may be a problem with TG corrections in this part of the study area. Compared to other stations in the Baltic Sea, the Latvian and Estonian TGs (e.g., TG ID 12–19) have the largest STD_{HDM-TG} (more than 9 cm), as well as some Danish and German TGs (e.g., ID#31, 36, and 37) in Arkona Sea. The TGs with larger STD_{HDM-TG} may indicate problematic issues that require further examination for future studies. For instance, some of these issues could be due to TG data inconsistencies (including the TG zero level).
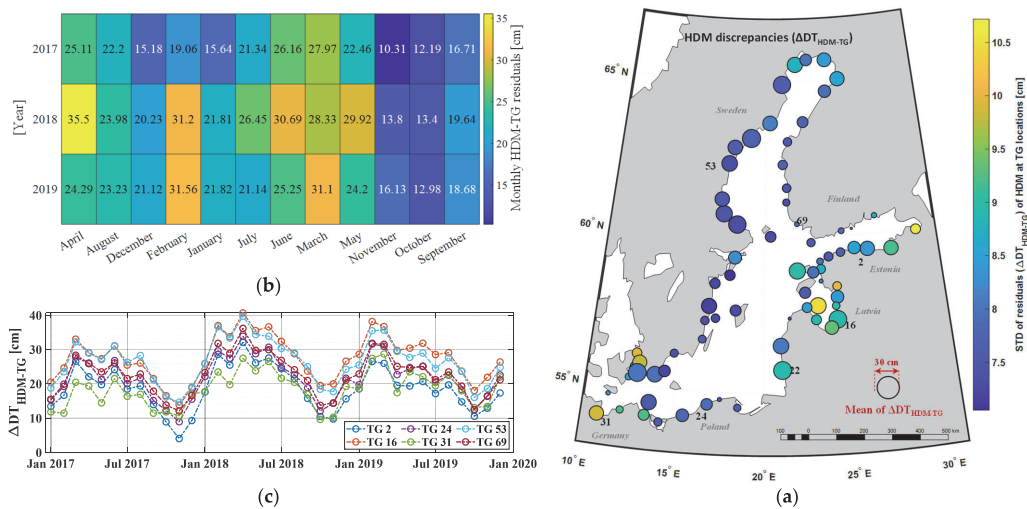
Figure 6. Statistics of HDM discrepancies with respect to participating TG stations. (**a**) Means (characterized by the circle size) and standard deviations (characterized by the colors) of discrepancies between HDM and TGs (Equations (16) and (17)) during 2017–2019 over the Baltic Sea. (**b**) Monthly average of HDM discrepancies over three years (Equation (16)). (**c**) Monthly average of HDM discrepancies at six selected TG locations (one station in each country with the largest STD or mean). TG IDs are explained in Figure 4a as well as in Table A1 (Appendix A).

3.2.3. Geoid Model

The NKG2015 gravimetric quasi-geoid model for the Nordic–Baltic countries was developed by the NKG in 2016 [6]. It is referred to the Geodetic Reference System GRS80 ellipsoid and extends from 53° to 73°N and from 0° to 34°E with a grid spacing 0.01° × 0.02°. The NKG2015 quasi-geoid determination is based on the least-squares modification of Stokes' formula with additive corrections and using the GOCE/GRACE geopotential model and corrected with a one-parameter fit to the national realizations of the EVRS and has a good agreement with GNSS/levelling control points with a STD of 3.0 cm, whilst the EGM2008 (global model) STD is 4.4 cm [6]. The NKG2015 model was used to retrieve DT_{SA} from satellite derived SSH data (i.e., DT = SSH-geoid). Various studies have estimated the NKG2015 geoid error [24] that could reach up to 15 cm over certain marine areas. Such deficient geoid modeling areas were associated with the poor coverage of marine gravity data. Contrastingly, the global geoid models that are customarily used by the satellite altimetry community are less accurate and with a poorer spatial resolution (typically 0.1° × 0.1°). The availability of such a high-resolution regional geoid model is clearly advantageous for the SA-based DT determination in the present study.

3.2.4. Satellite Altimetry

In this study three satellite missions including Sentinel-3A (S3A), Sentinel-3B (S3B) and Jason-3 (JA3) are examined to determine the DT. These missions have different characteristics (Table 2) and track geometry (Figure 7). S3A and S3B have almost the same track patterns and observed the same place on the Earth within 30 s. The main difference is that S3B orbit flies ±140° out of phase with S3A. In addition, S3A/S3B uses SAR (synthetic aperture radar) mode (by SRAL: Synthetic Aperture Radar Altimeter) whilst JA3 uses LRM (low-resolution mode) over the global ocean (by Poseidon-3B altimeter). The characteristics of the missions are summarized in Table 2.

Table 2. The used SA missions and their main specifications.

Mission	Altimeter	Mode	Altitude [km]	Inclination [°]	Cycle [Days]	Used Retracker	Launch Date
Sentinel-3B	SRAL	SAR	814.5	98.65	27	ALES+SAR	Apr'18
Sentinel-3A	SRAL	SAR	814.5	98.65	27	ALES+SAR	Feb'16
Jason-3	Poseidon-3B	LRM	1336	66.04	9.91	ALES+	Feb'16
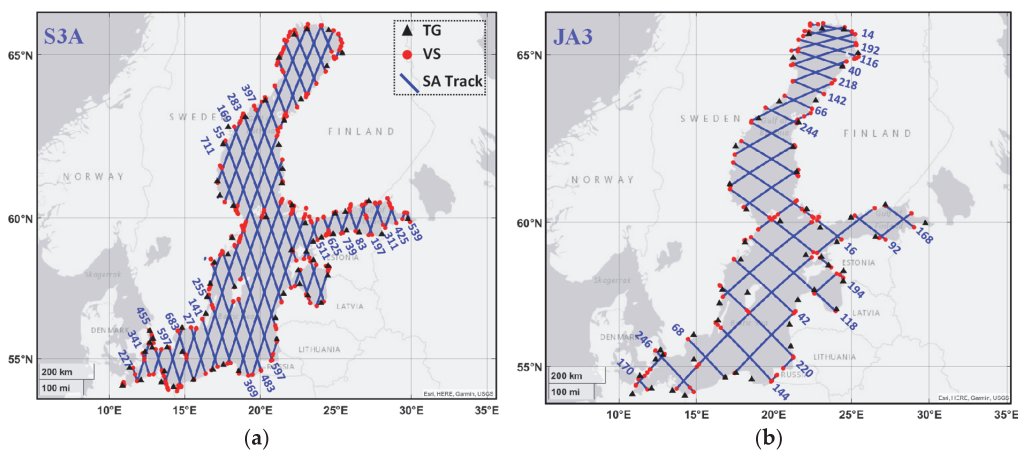
Figure 7. Coverage of SA passes within the study area. (**a**) Sentinel 3A (note that S3B has almost the same track patterns) and (**b**) Jason-3 missions. For each mission ascending pass numbers are shown. The locations of VS and TG stations are denoted by red circles and black triangles, respectively.

Recent coastal SA retrackers including ALES+ and ALES+SAR appear to improve the SA data quality [10]. In this study, the ALES+ retracker SA data products for the JA3 data and ALES+SAR for S3A and S3B [21] are used. The difference between ALES+ and ALES+SAR is due to the different signal-to-noise ratios of the SAR mode VS LRM. ALES+ is a modification of ALES (Adaptive Leading-Edge Sub-waveform), which is based on the Brown-Hayne functional form that models the radar returns from the ocean to the satellite. This retracker uses sub-waveforms and adapts the fitting of the signal depending on the sea state also on the slope of its trailing edge [21,45]. Based on ocean and coastal waveform characteristics, it uses leading-edge detection for peaky waveforms. These data are produced by the Baltic+SEAL team project (www.balticseal.eu, accessed on 23 March 2021). The Baltic+SEAL consists of a novel improved multi-mission sea level data product (necessary corrections are applied) for the Baltic Sea, that has been created and validated using the latest innovations in coastal altimetry and data processing. The data products are based on the use of retrackers for both LRM (JA3) and delayed Doppler altimeters (including S3A and S3B) [21].

Compared to the open ocean, SA data are degraded near the shoreline due to land contamination on the radar echo, seasonal sea ice conditions, and corrections effect (e.g., wet tropospheric correction). This yields the altimeter measurements close to the coast (~3 km away) to be flagged as poor data in the Baltic+SEAL dataset. In this study, quality flagging has not been applied in order to assess all available data in the region. Instead, this study applies an iterative data screening approach (cf. Section 2.1) for the removal of the gross errors ($|DT_{SA}| > 1.5$ m) and outliers (using STD and MAD filters, cf. Section 2.2). However, some other corrections are still needed prior to further investigation to make the SA data compatible with terrestrial data.

SA data in Baltic+SEAL products are not directly compatible with TG data (instantaneous sea level data) as the former dataset is corrected for atmospheric pressure effect using Dynamic Atmosphere Correction (DAC). Since the instantaneous DT is examined in this study, the SA data needs to be de-corrected by adding the DAC back to the SSH before the comparison [27]. In addition, these SA data are referenced to TOPEX/Poseidon (T/P) ellipsoid and ITRF (realization 2008), while the TG observations are referred to NAP and ETRF (European Terrestrial Reference Frame). Also recall that the NKG2015 geoid model refers to the GRS-80 reference ellipsoid. The height difference between the ETRF and ITRF in terms of ellipsoidal heights was applied to the SA data. Moreover, SA data are in the mean tide system while TG readings adopt the zero-tide system [46]. Therefore, the effect of these permanent tide systems is accounted for using [47] conversion into the zero-tide system. In addition, the SA terrestrial reference frame needs to be transferred from $ITRF_{2008}$ to $ETRF_{YYYY}$, which is an ETRF realization of the year "YYYY" related to TG observations (in this study: 2017–2019), using the method described by [48]. The aforementioned corrections are necessary to be accounted for to enable using SA data with the modified HDM for retrieving absolute instantaneous DT. These steps are illustrated in Figure 8.
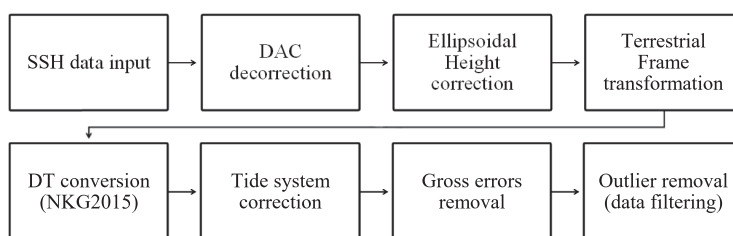
Figure 8. SA data preprocessing steps diagram including data filtering, harmonization, and corrections.

In this study, more than 4 million S3A/3B and JA3 data points (Table 3) along 116 passes during 2017–2019 (131 cycles) were extracted from Baltic+SEAL 20 Hz data products. These SA passes cross 74 nearby TGs; see Tables A2 and A3 in the Appendix A. The numbers of used TGs are at maximum 16, at minimum 2, and 6 stations on average for Jason-3 tracks and 13, 2, and 6 for Sentinel-3 tracks, respectively (cf. Table A2 in the Appendix A). Table 3 shows the main statistics of these datasets. The SA data points out of the HDM coverage (near the coastline) were excluded (cf. the number of outliers in Table 3) for the consistency of the datasets. The number of locations represents the persistent locations of SA data points in the cycles. The used different SA data periods are also summarized in Table 3. Although the S3B mission was launched in April 2018, the start of usable data is in November 2018. Thus, the S3B data before November 2018 were excluded in this study. Accordingly, in statistical evaluations (by Equations (10)–(12)), 92 cycles of JA3 (whereas the number of qualified cycles *m* = 82), 33 cycles of S3A (*m* = 29), and 7 cycles of S3B (*m* = 6) over 3 years (2017–2019) were investigated.

Table 3. SA data details including total number of passes, observations, and outliers for the study area within 2017–2019.

Mission	Passes	Footprint Locations (φ_s, λ_s)	VS $(\varphi_{VS}, \lambda_{VS})$	Observations	Outliers	Cycle No.	Data Period
S3A	42	42,536	6595	1,459,334	101,422	13–45	January 2017–May 2019
S3B	41	41,277	1396	267,084	19,767	19–25	November 2018–May 2019
JA3	33	20,483	9493	2,473,488	212,386	30–121	December 2016–May 2019
Total	116	104,296	17,484	4,199,906	333,575	131 cycles	-

4. Results

This section presents the statistical results of the method described in Section 2. The main focus is on SA derived DT (from multiple missions) and its evaluation against a corrected HDM both near- and offshore. The results and analysis are presented in the following sequence: (i) examination of the SA along-track performance in terms of ΔDT_{SA-HDM} (using selected SA tracks) and (ii) spatial evaluation of DT accuracy in terms of $MEAN_{SA-HDM} (\varphi_s, \lambda_s)$ and $STD_{SA-HDM} (\varphi_s, \lambda_s)$; in addition, (iii) the spatial pattern of ΔDT_{SA-HDM} where problematic (in terms of larger $MEAN_{SA-HDM}$) areas are identified.

4.1. SA Along-Track Performance

Figure 9 displays an example of the along-track DT_{SA} for the S3A pass #272, which stretches from the southwest to the northern Baltic Sea and represents a reasonable example of the HDM and SA data quality and values (Figure 9b). In this figure, three cycles (18, 21, and 26 in 2017) of DT_{SA} for this pass are compared with the $DT_{HDM-corr}$ (green line).
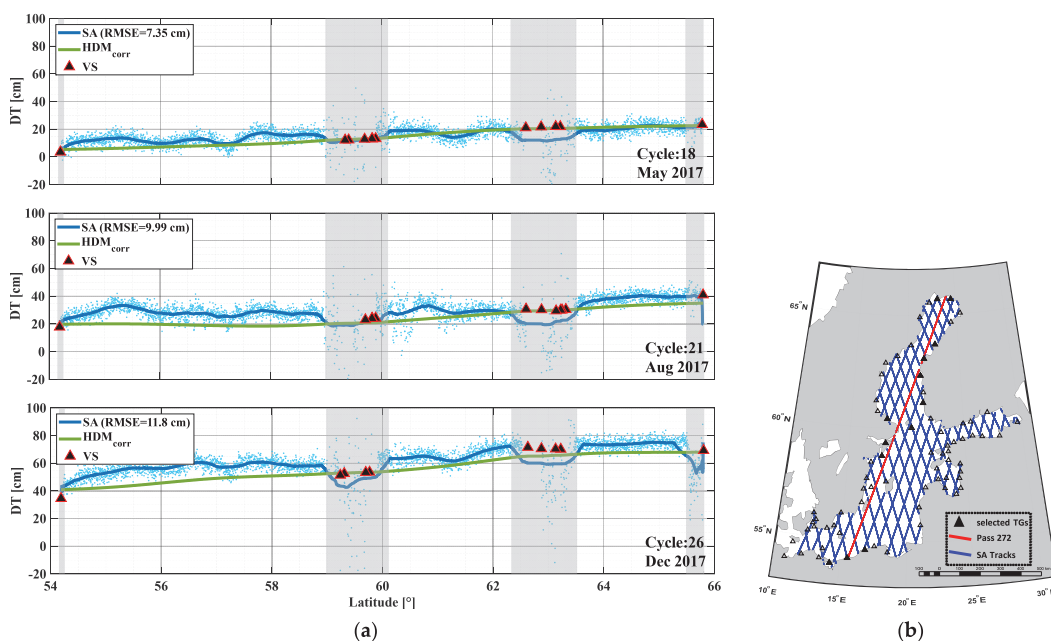
Figure 9. (**a**) Comparison of S3A pass #272 DT_{SA} (blue dots) with the TG-corrected HDM ($DT_{HDM-corr}$) (green line) for 3 cycles (representing different seasons) in 2017. The DT_{SA} moving average is denoted by the blue solid line, the grey zones showing masked near coast and land areas, and the triangles denote locations of virtual stations; (**b**) the location of the S3A pass #272 in the Baltic Sea.

The actual data points of DT_{SA} are displayed (blue dots). The blue solid line shows smoothed DT_{SA} that was calculated as a moving average over a sliding window of $0.5°$ latitude length across adjacent DT_{SA}. The along-track RMSE between DT_{SA} and $DT_{HDM-corr}$ was estimated for each cycle.

From Figure 9a it can be observed that: (i) Seasonal variations in DT (e.g., May 2017 varied within 5–20 cm, August 2017 within 20–40 cm, and December 2017 within 40–60 cm); (ii) the SA data (blue solid line and blue dots) reveal more variation in DT compared to the HDM data, which represents a fairly smooth surface; (iii) on approaching the coastal areas (i.e., within the vicinity of the virtual stations), the SA data appear more scattered (e.g., latitude 59–60° and 66°). Most of the $DT_{HDM-corr}$ values appear to be slightly lower than DT_{SA} (e.g., latitude 54–56°). In addition, $DT_{HDM-corr}$ provides long-wavelength estimates of sea level by hourly temporal resolution and one nautical spatial resolution (hence yielding a smooth profile). Contrastingly, DT_{SA} provides instantaneous estimates of sea level with ~300 m spatial resolution and consequently provides more detailed (higher frequency) sea level features. Further investigation via $MEAN_{SA-HDM}(\varphi_s, \lambda_s)$ about these locations was performed with respect to each mission for the whole Baltic Sea and can be found in Sections 4.2 and 4.3.

### 4.2. Evaluation of DT Accuracy and Identification of Problematic Areas

Comparing the differences ΔDT_{SA-HDM} not only allows the DT accuracy to be determined but also intuitively (by using statistics from Equations (10) and (11)) hints at persistent or semi-persistent patterns at questionable locations that may exist. This comparison allows for the identification of potential problem areas via the synergy of SA, corrected HDM, TG, or geoid datasets (or any combination of those). Accurate sea level variability is obtainable by utilizing a high-resolution quasi-geoid model (rather than the mean sea surface). The geoid is the key component in determining accurate DT by SA and can be used to validate different SA missions and determine the problematic area by multi-mission comparison. This is examined in Section 4.2.2 in terms of the $MEAN_{SA-HDM}(\varphi_s, \lambda_s)$ and $STD_{SA-HDM}(\varphi_s, \lambda_s)$.

4.2.1. Along-Track $MEAN_{SA-HDM}(\varphi_s, \lambda_s)$ over Baltic Sea

Figure 10 shows an example of statistics in terms of $MEAN_{SA-HDM}(\varphi_s, \lambda_s)$ (Equation (10)) for four tracks of S3A (pass #158, #169) and JA3 (pass#111, #16) using all available cycles during 2017–2019. These tracks were specially selected to represent an example of the satellite data coverage from north–south and east–west of the Baltic Sea for both ascending and descending passes. The pass numbers 158 (S3A) and 111 (JA3) are descending while 169 (S3A) and 16 (JA3) are ascending passes to represent a reasonable example of SA pass coverage area in the Baltic Sea. The whole-track average of the $MEAN_{SA-HDM}(\varphi_s, \lambda_s)$ was also calculated and referred to (Equation (12)). The figure also includes the location of each pass over the Baltic Sea (red line) and associated TGs (black triangles) in the bottom row (Figure 10e–f). This examination allows for: (i) illustrating the spatially persistent areas where discrepancies may exist; (ii) quantifying the discrepancy; and (iii) provisionally identifying the source of the discrepancies. The previous section revealed that SA shows more detailed variation than the corrected HDM, so some level of discrepancy is expected. When, however, the discrepancy appears to be larger than expected (e.g., >±5 cm) and its shape appears to be abnormal (e.g., steep jumps), it can reveal the location of problematic areas that may possibly be related to the data sources. Examination of the standard deviation (dashed red line) assists with the identification of the persistent and semi-persistent patterns that may exist. Figure 10 shows the possible discrepancy and hints to the possible sources that may be the reason.
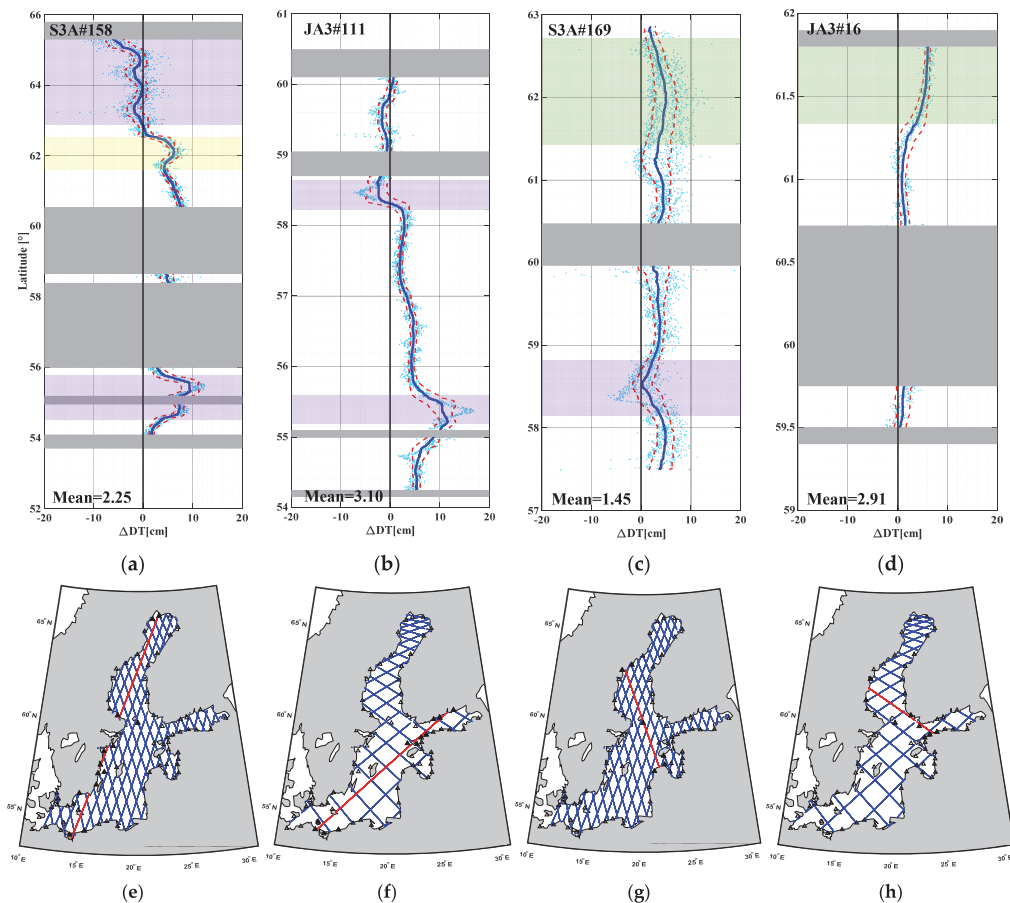
Figure 10. Along-track $MEAN_{SA-HDM}$ (φ_s, λ_s) for 4 SA passes ((**a**): S3A#158, (**b**): S3A#169, (**c**): JA3#111, and (**d**): JA3#16) considering all available cycles during 2017–2019. The blue line represents the moving median of $MEAN_{SA-HDM}$ (φ_s, λ_s) and the dashed red lines represent the moving standard deviation "envelope". The average of $MEAN_{SA-HDM}$ (φ_s, λ_s) is also denoted. The bottom row (**e**–**h**) represents each pass location in the Baltic Sea. The grey zone denotes masked land areas. The potential problematic areas are classified into three types. Yellow shaded regions: the suspected geoid model problems; green shade: TG records problem (or the HDM problem); purple shade: SA problem, possibly due to sea ice presence or land contamination.

Examination of these tracks shows that, in general, a difference (mean ΔDT_{SA-HDM}) of ±10 cm exists. The yellow masked areas in Figure 10a show the persistent locations with sudden jumps (2–7 cm with respect to the nearby values) of ΔDT_{SA-HDM} around 62° latitude. The standard deviation is smaller in this highlighted area, which verifies it is more or less persistent. This hints that it could be probably due to geoid or HDM/TG deficiencies. Further examination of five S3A passes that are present in this section of the Baltic Sea (two descending (passes #158, #272) and three ascending (passes #169, #283, #37)) and cross the Gulf of Bothnia hints that the problem is most likely due to the geoid (see Figure 11). Figure 11 shows the $MEAN_{SA-HDM}$ during 2017–2019, whereas the geoidal heights reveal a suddenly decreasing slope from 20 to 17.5 m around the latitude 63°. Note that the identification of the geoid model as the potential source of the problem is representative of the SA data since Equation (7) includes the geoid component. Further evidence of the geoid model being the potential problem is also shown in Section 4.2.2, where all the SA

cycles are examined (see Figure 12) as well as in Section 4.3, where the key problematic areas are identified. Further future exploration is required for the final verification of the possible sources since the intention of this study was to a develop method for SA-derived DT and provisionally hint at problematic areas and their possible sources.
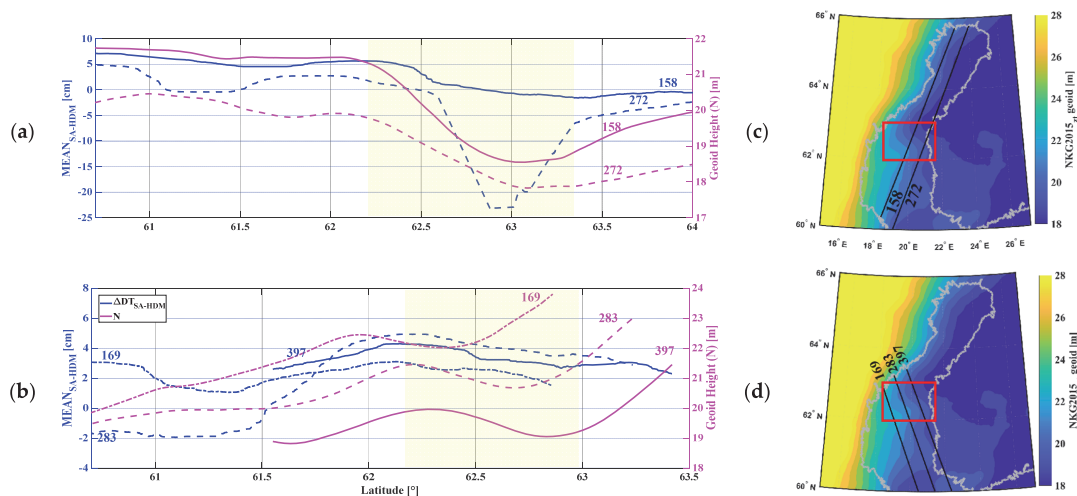
Figure 11. The averaged $MEAN_{SA-HDM}$ during 2017–2019 over the Gulf of Bothnia of S3A for two descending (**a**) and three ascending passes (**b**), denoted in blue lines. The geoid undulations along the passes are denoted in magenta-color lines (the different line styles represent each pass). The yellow masked area is the location of steep geoid slopes, which may cause deteriorations in ΔDT_{SA-HDM}. The locations of yellow masked areas in the left-hand-side profiles are denoted by red rectangles in the right-hand-side maps (**c**,**d**), whereas the NKG2015 geoid model is in the background. Note that for pass#272 the drastic drop at 63° is most likely due to land contamination.

Figure 12. *Cont.*

(**d**)　　　　　　　　　　　　　　(**e**)　　　　　　　　　　　　　　(**f**)
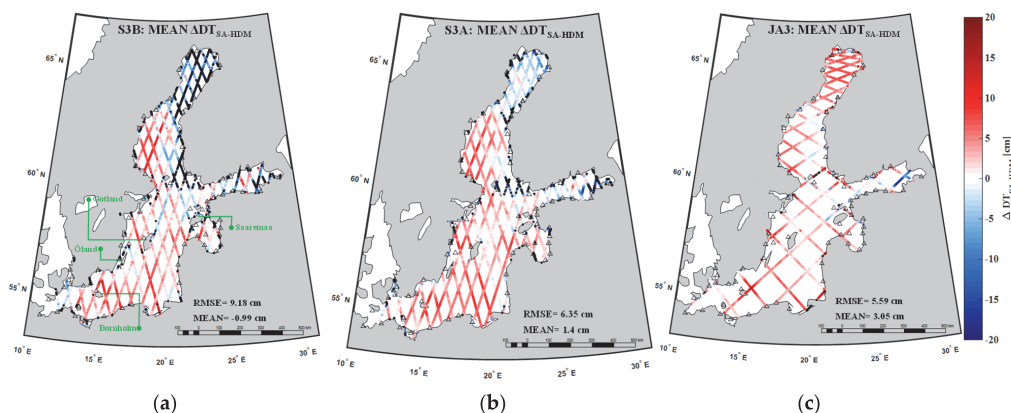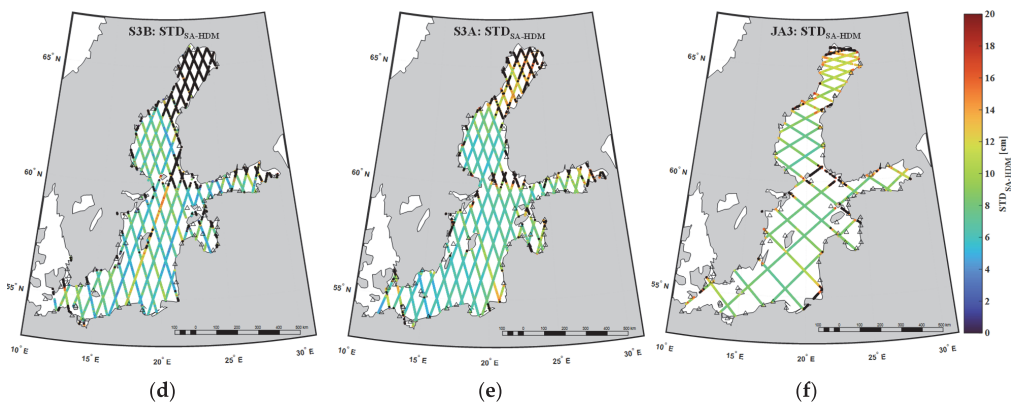
Figure 12. Statistics of the along-track SA examination. (top row) Mean ΔDT_{SA-HDM}, discrepancies between SA along-track DT data (DT_{SA}) and $DT_{HDM-corr}$ ($MEAN_{SA-HDM}$) during 2017–2019 for (**a**) S3B, (**b**) S3A and (**c**) JA3 missions (Equation (10)). The $|\Delta DT_{SA-HDM}| > 20\ cm$ are represented as black dots in the $MEAN_{SA-HDM}$ plots and this is excluded from the calculation of the RMSE value of the whole basin per each mission (Equations (12) and (14)). In addition, (bottom row; (**d–f**)) associated STDs of ΔDT_{SA-HDM} (Equation (11)) larger than 20 cm are denoted in black dots.

Deteriorations in ΔDT_{SA-HDM} also occur around the latitude of 54–55.5° (Figure 10a,b) with a deviation from 5 to 10 cm. The standard deviation varies and can be interpreted as large, thus hinting at a semi-persistent pattern. However, in Figure 10a, Bornholm Island is located in the purple highlighted area, where several large rocks exist within the near-coast data corridor of the SA pass. In addition, around latitude 58.5° (Figure 10b,c), the SA passes are located very close to the eastern coast of Saaremaa Island (cf. Figure 4 for its location), Estonia. This could also hint at possible land contamination. Further examination into these areas is also performed in Section 4.2.2 and Section 4.3.

At sub-arctic latitudes 63–66°, (Figure 10a,c) a negative deviation from the zero line of around 0 to −8 cm occurs. Notice that the standard deviation tends to be large at times, thus hinting at semi-persistent patterns and possible seasonal trends. This suggests HDM modeling or SA problems. One possibility for this may be due to SA not correctly tracking the sea level due to sea ice presence (purple-masked area) during the winter months. Similar observations are also made later on when examination of all the multi-mission SA passes is performed in Section 4.2.2 (Figure 12). Sea ice charts were examined along with the SA DT along-track data (Figure 13). The investigation strongly hints at this possibility being due to the presence of seasonal sea ice in this area.

In addition, in Figure 10c,d, a large deviation (~3 cm) above latitude 61° near the Swedish coast could be due to TG-corrected HDM (green masked area). The standard deviation in Figure 10c is higher, thus hinting at semi-persistent patterns (e.g., seasonal effects), whilst Figure 12d shows the standard deviation to be small, hinting at a persistent pattern. Note that the employed method for HDM correction is quite robust. Nevertheless, this method is still not errorless, so it is expected that some differences could also be due to errors in the TG/HDM correction method applied. In addition, the Swedish TGs in this area seem to have some problems compared to the other TGs in the Baltic Sea (cf. Figure 6). These observations are also further examined in Section 4.3.
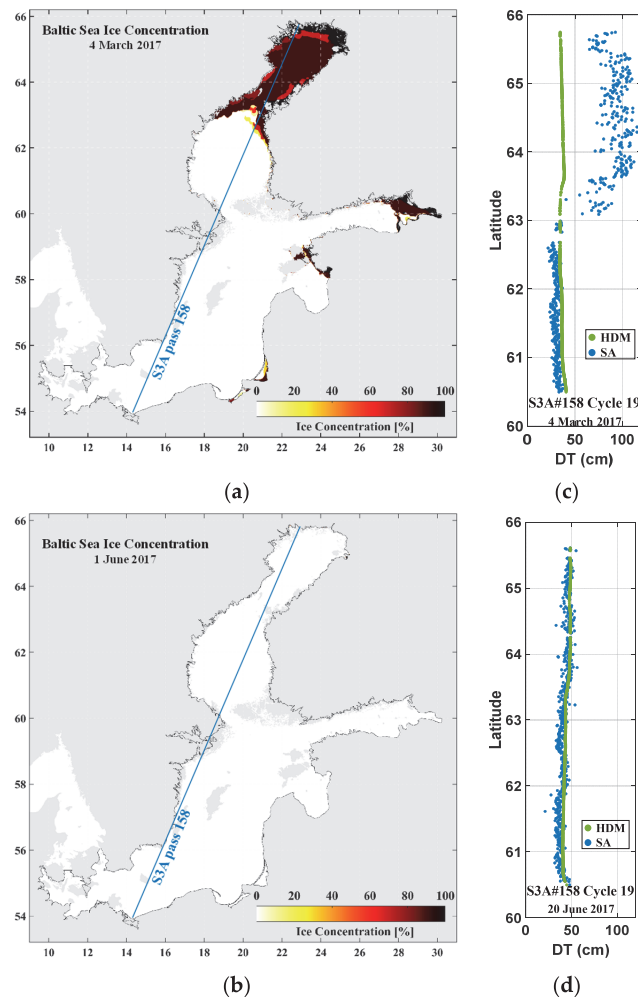
Figure 13. Sea ice concentration over Baltic Sea for March (**a**) and June (**b**) 2017 (source: gridded ice chart model available from Copernicus Marine Service Information) and the comparison between $DT_{HDM-corr}$ (green) and DT_{SA} (blue) over pass#158 in two cycles, cycle 15, March (**c**) and cycle 19, June (**d**) 2017.

Note that whilst some of these discrepancies, especially the large and steep values, were possibly identified to be related to limitations in SA (e.g., land contamination or sea ice) and/or HDM/TG problems), it is more useful to examine all the SA track discrepancies, which are explored further in Section 4.2.2. It is quite obvious from the examples shown in Figure 10a–d that the along-track SA captures more realistic (detailed) variability in the sea level than the HDM. This is due to the fact that the HDM is computed based on a mathematical model that attempts to simulate the sea surface [2], whilst the SA measures the actual instantaneous sea surface. Thus, the SA may be capturing more realistic small-scale dynamics than the HDM (which provides a low-frequency smooth surface only). Using this ability of SA, the SA data can lead to obtaining more information about sea level behavior for future studies. This favorable SA ability can also contribute to exploring some of the meso-scale dynamics that exist in the Baltic Sea (and other basins).

4.2.2. DT Examination over the Entire Baltic Sea

Deeper examination of the accuracy of the along-track DT_{SA} via multi-mission (S3B, S3A, and JA3) was conducted by comparing the entire along-track DT_{SA} with $DT_{HDM-corr}$ at specific locations (φ_s, λ_s) in terms of $MEAN_{SA-HDM}$ (φ_s, λ_s) and STD_{SA-HDM} (φ_s, λ_s). The key component in this comparison is that the HDM is now corrected via the TG observations near the coast, so that $DT_{HDM-corr}$ represents accurate estimates along the SA track. The DT_{SA} and $DT_{HDM-corr}$ inter-comparison is illustrated in Figure 12, where the top row shows the spatially averaged ΔDT_{SA-HDM} along each SA mission track (Equation (10)) together with the mean and RMSE (Equation (14)) of these ΔDT_{SA-HDM} over the entire Baltic Sea for each mission, 2017–2019. The figure (bottom row) also indicates the along-track STDs (Equation (11)) of these ΔDT_{SA-HDM} for each mission.

Similarities and differences between JA3 with SA3/S3B in Figure 12 may help identify the source of the problem. For example, differences between missions may indicate that the problem may not be with the geoid or TG but most likely due to SA mission specifics (e.g., some deficiencies in data capture or environment). This can be observed in the Bay of Bothnia (above 63° latitude), which was identified as one of the areas with a large ΔDT_{SA-HDM} (less than −20 cm) in Figure 12a,c for S3B and JA3. However, for S3A (Figure 12b), the large values appear to mostly occur at the coast. This inconsistency amongst the different SA missions suggests that the problem was not due to the geoid or HDM/TG (for geoid and HDM/TG problems would show a consistent pattern). Instead, it hints at a possible seasonal pattern and an association with this particular area of the Baltic Sea. One possible reason could be sea ice. The northern part of the sea (62.1–65.8°N) is covered by sea ice during the winter–spring seasons (110–190 days of the year) [49]. The Gulf of Bothnia is known for having seasonal sea ice; therefore, it may be challenging for SA to track the sea surface correctly in the winter months. Figure 13 shows maps of sea ice concentration obtained for the months of March and June 2017 (model by Copernicus Marine Service Information, www.resources.marine.copernicus.eu) and the S3A pass#158 of cycle 15 (March) and cycle 19 (June) in 2017 of DT_{SA} (blue dots) compared with DT_{HDM}, which shows for March that the ice extent covers these same areas with a high discrepancy, whilst for the month of June, when no ice was present, the discrepancy was small.

In the Gulf of Bothnia, S3A appears to perform the best, whereas S3B performance in this region was much poorer. However, it should be noted that the S3B data span covers only 7 months during the winter/spring seasons (cf. Table 3), which makes for poorer compatibility with SA derived DT (rather than S3A/JA3). In the figure, generally the JA3 associated $MEAN_{SA-HDM}$ shows larger ΔDT_{SA-HDM} due to the satellite constellation (including orbit inclination), especially at sub-arctic latitude areas where the Jason mission could not provide much reliable data (rather than the Sentinel series). Another reason could be attributed to the SAR mode advantage (Sentinel-3) compared to the LRM mode (Jason-3) in terms of retrieving more precise DT_{SA} estimates. The SAR mode SA data reaches closer to the coast [13], which also yields more scattered data. This is confirmed by Figure 11e,f, where the S3A has more large errors (denoted by the black dots) near the coast than JA3.

Examining Figure 12 also shows that, within latitudes 60–63° (especially on the Swedish shores), with all satellite missions, large differences ΔDT_{SA-HDM} (7–20 cm) consistently occur. This could potentially hint at HDM/TG related issues. For this particular area, a similar problem was also identified in Section 3.2.2 for Figure 6a, where comparison of uncorrected HDM-TG showed the largest residuals of around 25 cm for the Swedish western coast and a seasonal trend, where it was at a maximum from February to March. Given the observation that a seasonal pattern occurs, and that the standard deviation was high, around 8–10 cm (Figure 12 d–f), there hints of issues with the HDM model itself, but it is also possible that there may be an issue with the corrected HDM (due to the poor TG data records).

For the southern Baltic Sea around Bornholm Island and Öland Island, large discrepancies appear amongst all SA missions (10–20 cm). In addition, from Figure 12d–f (STD_{SA-HDM}), the standard deviation appears to be within the range of (4–6 cm). This

standard deviation is considered to be more or less reasonabl; thus, a persistent pattern (the black dots in Figure 12) shows the location of scattered SA data, which could be most likely related to SA performance due to environmental/meteorological effects including high land contamination and/or sea ice conditions over these regions, which cause certain challenges for the DT estimations [50]. A similar identification was also found upon the examination of the along-track data in Figure 12a–c (purple shaded areas). Moreover, large ΔDT_{SA-HDM} values are also located within the complex coastal environments of the Baltic Sea, such as the Åland Sea and the Archipelago Sea, where the geometric properties (e.g., presence of small islands) can significantly impact SA consistency. Over these areas, many archipelagos, several small islands, and rugged coastlines exist. This area contains one of the largest archipelagos in the world, having 30,500 islands and a 23 m average water depth [51]. Over the Åland Sea and the Archipelago Sea, SA passes cross narrow and shallow straits; therefore, land contamination may affect the SA results. Later in this study, Figure 14 also identifies these areas as potentially being affected by land contamination or sea ice in these areas and Figure 15c also shows SA along-track and how the SA data may have been influenced upon approaching land.
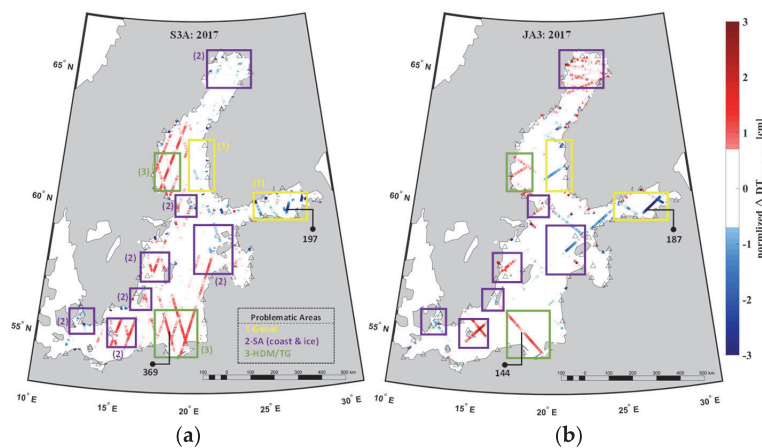
Figure 14. Problematic DT determination areas over the Baltic Sea. (**a**) Normalized mean of ΔDT_{SA-HDM} ($MEAN_{SA-HDM}$) of S3A data (**a**) and JA3 data (**b**) over the Baltic Sea in 2017. The problematic areas are enclosed by colored rectangles (and numbers) to classify the possible reasons. Geoid: yellow, SA: purple, and HDM or TG: green. Four selected passes (two passes for S3A and two passes for JA3) are specified to illustrate the possible reasons (cf. Figure 12).

In Figure 12a–c, large discrepancies ΔDT_{SA-HDM} within the range of 30 cm are observed at latitudes 59.6° around the western coast of Finland and in the eastern Gulf of Finland. The small standard deviation values in these areas hint at a persistent pattern. Thus, we assume that this may be due to possible geoid modeling problems for this area, which was also identified in Figures 10a and 11, which more closely examined the SA pass and the geoidal slopes. Later, Figure 15a,b (see Section 4.3) show that for both the S3A and JA3 missions, the mean DT from SA is considerably far from that of the HDM within latitudes 59.6° to 60°. For instance, with the S3A pass at latitude 59.9–60° [~10 km], a sudden difference in DT_{SA} around 10 cm occurs, and with JA3 from latitude 59.6° to 59.8° [~20 km] the difference decreases 20 cm, and from latitude 60° to 60.2° increases again by 15 cm (these areas are shaded in yellow). In addition, the standard deviation was smaller than 10 cm (see Figure 12e). This hints at a persistent problem and the evidence suggests that it may be a geoid modeling problem.
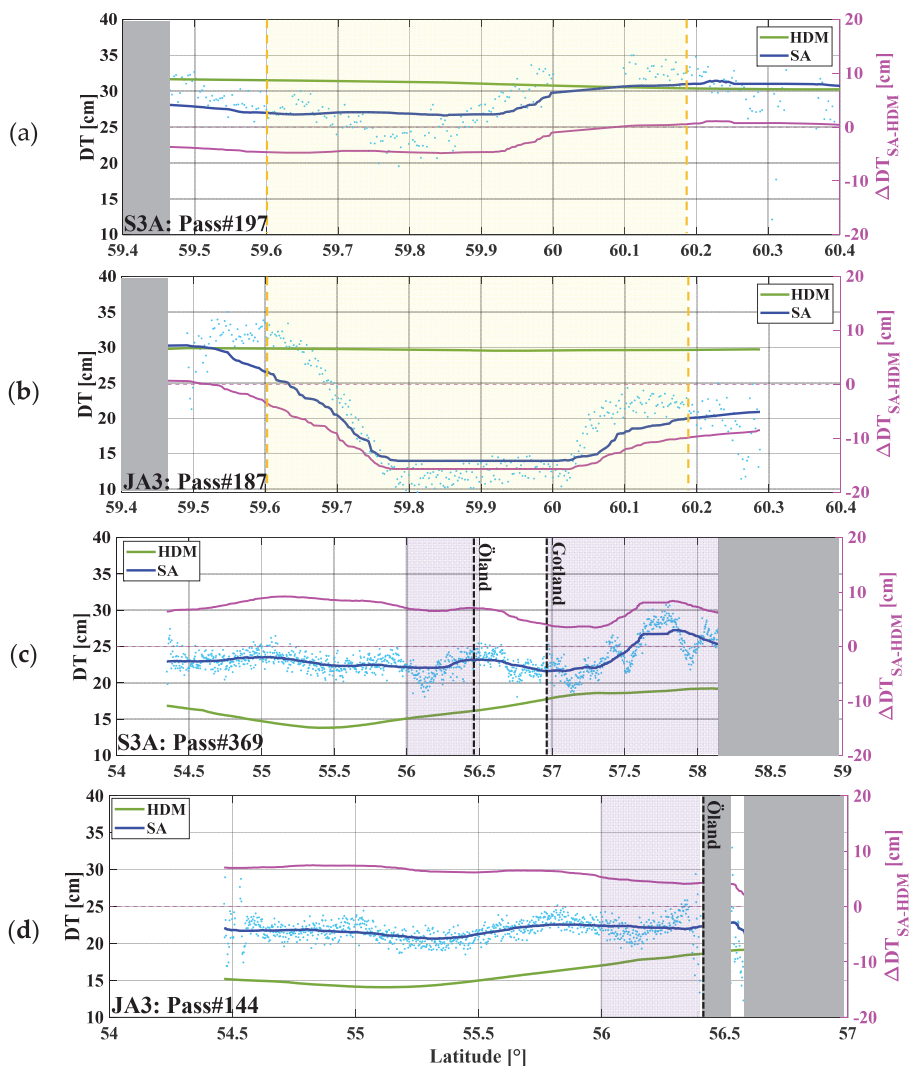
Figure 15. Along-track DT and $Mean_{SA-HDM}$ (Equation (10)) of four selected passes (cf., Figure 14). The along-track mean DT of SA is denoted in blue dots (whereas the blue solid line is the moving median of $0.5°$ latitude window) and HDM in green line (left axis). The $MEAN_{SA-HDM}$ is represented on the right axis by magenta color (**a**,**c**) for two S3A passes at almost the same locations as two JA3 passes (**b**,**d**). The problematic areas of possible geoid modeling are highlighted in yellow; the purple areas are due to poor quality of SA data near the land (vertical dashed lines represent the locations of islands). The grey zones mask land areas.

4.3. Spatial Pattern of ΔDT_{SA-HDM} Discrepancies

It is important to identify the key areas that may be problematic and require further attention. To accomplish this, the normalized $MEAN_{SA-HDM}$ of the S3A and JA3 mission for the entire Baltic Sea for the year 2017 (a full cycle to remove any seasonal effects) is presented in Figure 14. The normalization was performed based on standard score (Z-score) [52]. This indicates how much the $MEAN_{SA-HDM}$ (φ_s, λ_s) values differ from the whole Baltic Sea standard deviation ($STD_{SA-HDM}(mission/Basin)$). In this figure, the areas with large $STD_{SA-HDM}(\varphi_s, \lambda_s)$ (black dots locations in Figure 12e) are excluded, since they

are mostly due to land contamination at the coastal areas, which makes SA data more scattered. The Figure 14a,b identify highly affected areas (larger $MEAN_{SA-HDM}$ (φ_s, λ_s) values) that can be explored further. By comparing Figure 13 with Figure 12a,b, the larger discrepancies at the sub-arctic latitudes region are mostly due to the presence of sea ice in the winter–spring seasons (cf. Section 4.2).

Colored rectangles in Figure 14a,b identify problematic areas where persistent large $MEAN_{SA-HDM}$ (φ_s, λ_s) estimates exist. Recall that the extremely scattered SA data with STD_{SA-HDM} larger than 20 cm are excluded from such comparisons. To identify the source of the problems, a combination of site characteristics and previous knowledge is utilized. These areas are classified in three groups. The yellow rectangles identify persistent discrepancy areas in both S3A and JA3, which are due to the possible geoid deficiencies that occur in the Gulf of Finland and perhaps also in the Bothnian Sea. Note that geoid problems in the eastern part of the Gulf of Finland were identified earlier in [53]. The purple rectangles identify mostly coastal areas or locations within the vicinity of islands. Possible reasons for this could be poor SA performance near land and/or the environmental effects of sea ice at sub-arctic latitudes. The green rectangles are mostly located on the Swedish east coast and in the southern Baltic Sea. They are most likely related to HDM problems or TG-related issues. Recall also that a large residual (HDM-TG) within 20–30 cm was identified in these areas (Figure 6). In addition, frequent data gaps occur for TG#54 (Figure 4b) and the gap in TG stations between the Lithuanian and Polish coastline (Figure 4a).

To illustrate better these problematic areas, some examples of the along-track mean of DT from SA data and corrected HDM data over four selected passes are shown in Figure 15. These passes are selected to demonstrate the problematic areas almost at the same location for two different missions (S3A and JA3) during the study period (2017–2019).

Regarding Figure 15a,b, both the S3A and JA3 missions show that the mean DT from SA is considerably far from that of the HDM within latitudes 59.6° to 60°. For instance, with S3A, the difference increases from 0 to −10 cm from latitude 59.9–60° [~10 km], and with JA3 from latitude 59.6 to 60.2°, the difference increases from 0 to −20 cm (yellow-shaded areas). This drastic change in the middle of the sea is not reasonable in this section of the Gulf of Finland. It is suggested that this is most likely a geoid-related issue; see [53] also. In addition, Figure 15c,d show the scattering SA data (purple masked area) near the land for both missions when the SA tracks approach the islands (vertically dashed black lines) and the coast (gray masked area). However, the data for S3A are less scattered than JA3, and it also has more data points near the coast. Note that for Figure 15a,b, the moving average of 0.5° (blue line) appears to be large but still the dots show the SA pattern in this area. Note that by comparing the different sources of sea level data and also by using different multi-missions' SA, it was possible to hint at the problematic areas and problematic data source. This aspect, however, was not the main scope of the present study; it can be thoroughly examined in another future study.

5. Discussion

The focus of this study was on deriving accurate DT from multi-mission SA data and comparing its accuracy to a TG-corrected HDM ($DT_{HDM-corr}$). Comparison with different SA missions and different sources of data not only determined the accuracy of the SA assessment but also indirectly identified problematic areas with different sources of errors. According to our method, the TG-corrected HDM served as the "ground truth". Since DT_{SA} is comparable to DT_{TG} only at the coastline, there was a need for the along-track SA data to be validated offshore using the corrected HDM (Section 2.1).

It should be considered that often, systematic biases between DT_{HDM} and in situ data exist (see Section 2.1). By measuring the bias of HDM at VS locations ($Bias_{HDM}^{VS}$) using adjacent TGs (Equations (1)–(6) and Figure 2), the inconsistency between the geoid-referred TGs and HDM data (with undisclosed reference datum) was expected to be resolved, and can now be utilized for the comparison with DT_{SA} (Section 2.1). The average residuals (bias) between HDM and TG ($MEAN_{HDM-TG}$ ($\varphi_{TG}, \lambda_{TG}$)) varied from 10 cm to 35 cm,

whereas in most cases the HDM overestimated the DT (Section 3.2.2). The maximum residuals occurred in the Swedish east coast (TG ID 50–56) and some other locations on the southern Baltic Sea and Latvian coastal area, e.g., near TG#16, 22, and 31 (see Figure 6). The monthly average residuals of the HDM and TG over the Baltic Sea also displayed a seasonal pattern (cf. Figure 6b,c), with maximum bias occurring during February to March (winter–spring) and being the smallest during the autumn and summer seasons.

In the evaluations, the location-dependent discrepancies $MEAN_{SA-HDM}(\varphi_s, \lambda_s)$ were calculated after data filtering of each SA pass/cycle over the Baltic Sea (Equations (9) and (10)). Hence, the $MEAN_{SA-HDM}(\varphi_s, \lambda_s)$ represents the relative accuracy of the DT_{SA} with respect to $DT_{HDM-corr}$. The uncertainties of SA data for each mission were evaluated in terms of RMSE of the $MEAN_{SA-HDM}(\varphi_s, \lambda_s)$. The $RMSE(mission/Basin)$ estimates are 9 cm (for S3B) and 6 cm (S3A and JA6) in the entire Baltic Sea (cf. Figure 12b,c). Note that for the S3B mission, only seven months of SA data were available for this study, which may affect the reliability of statistics. Overall, the S3A dataset appears to be superior to the S3B and JA3 ones. Consequently, the SAR mode altimeters (especially for S3A) provide more accurate instantaneous DT estimates over the LRM-associated ones, which can be more affected by local geometric impacts. In addition, the Sentinel constellation and geometry of the orbits (due to the satellite orbit inclination and altitude) led to better results in the Baltic Sea rather than the Jason mission, especially over sub-arctic latitude areas (Figure 12a–c). The improved algorithms and additional corrections (especially for sea ice and land contamination) that were employed in the Baltic+SEAL data may have also improved the results compared to standard retrackers as in [10], although our analysis shows that there is still some space for improvements, especially within coastal areas.

The comparisons of DT_{SA} with $DT_{HDM-corr}$ (Equations (9)–(14)) were performed and evaluated spatially. The results of the mean and STD of the deleted discrepancies (Equations (10) and (11)) and Figure 11) showed larger values in the complex part of the Baltic Sea at the coastal areas, where the presence of the archipelagos and small islands affect the retrieval of DT_{SA} (cf. Section 4.2). This also demonstrates that our algorithms for removing the outliers can also be improved, as in this study a common method (see Section 2.2) was used for all the data both at the coast and offshore. However, it was observed that outliers remained, especially in the complex archipelago areas. An alternative would be to use smaller window lengths in the final stage of outlier removal. In addition, in the northern part of the Baltic Sea (Gulf of Bothnia), the presence of seasonal sea ice conditions caused poorer quality in SA data due to limited opportunities for SA beams to interact with the open water.

These problematic areas were extensively made better identifiable by performing the normalization of $MEAN_{SA-HDM}(\varphi_s, \lambda_s)$ by Z-score. These results indicate that sea ice may still be a major problem affecting the quality of SA data. Land contamination, especially in areas such as the Baltic Sea where numerous archipelagos exist, due to the deviation of returned radar waveforms is another source of errors. In addition, some other regions, e.g., part of the eastern Swedish coast, may reveal TG issues (such as inadequate/incorrect correction applied, gauge zero problems, also a lack of enough TG stations near the Russian coast) and HDM problems. Geoid-related problems were also identified, e.g., in the eastern part of the Gulf of Finland (Figures 12 and 14) cf. also [53].

It should be noted that in this study the corrected HDM was considered to represent the offshore "ground truth". Whilst this was necessary for the method to be implemented, it also has its limitations. The examination of the along-track SA data (Figure 9) shows that SA represents the sea surface more realistically than the HDM model. In fact, the SA data in the offshore areas show the actual variation of the sea surface compared to the HDM, which represents an unrealistically smooth sea surface. In addition, in most cases, the HDM data underestimates the DT compared to SA. The residuals ΔDT_{SA-HDM} (Equation (9)) also show that almost 95% of the data varied from −10 to +20 cm. These variations are a key component in examining mesoscale ocean dynamics. It can also lead to the need to improve the HDMs, which can be explored for future studies.

In general, the performance of all tested SA missions appears to be within their design requirements after data processing and corrections (cf. Figure 2). Furthermore, by comparison of retrieved DTs (ΔDT_{SA-HDM}) in the local regions, the problematic areas can be determined. These areas could have special characteristics that could lead to large discrepancies/inconsistencies. The reasons can be categorized as (i) environmental/meteorological effects including land contaminations and sea ice conditions; (ii) inconsistencies in TG readings (e.g., due to zero-level issues) that affect the correction of HDM; (iii) problems with HDM modeling; and (iv) problematic issues with geoid models. This study attempted to identify the reasoning for some of these problematic areas, but in many cases, further examination is required using other complementary data.

6. Conclusions

This study demonstrates a method for determining accurate dynamic topography (DT) by incorporating satellite altimetry (SA) data of Sentinel-3A (S3A), Sentinel-3B (S3B) and Jason-3 (JA3) missions in conjunction with a tide gauge (TG) corrected Nemo-Nordic Hydrodynamic Model (HDM). A core component in this study was the access to a high-resolution NKG2015 quasi-geoid model that allowed retrieval of accurate DT_{SA} over the entire Baltic Sea.

The method showed that, on average, the discrepancies between HDM and SA (i.e., Mean ΔDT_{SA-HDM}) were in the range of ± 20 cm (with an average of -1 to 3 cm and RMSE of 5–9 cm over entire Baltic Sea) with standard deviations within 2 cm and 16 cm, respectively. The SA data show more realistic sea level data compared to those of the HDM, which tend to underestimate the DT variations. A spatial assessment of these discrepancies showed critical areas that require further examination. For instance, the Gulf of Bothnia revealed areas of large discrepancies, which hints that SA possibly has challenges in determining the sea surface due to the seasonal presence of sea ice. In addition, on the Swedish east coast and the Southern Baltic Sea, possible TG problems may exist. In the eastern part of Gulf of Finland, it is possible that geoid-related problems exist.

The inter-comparison of SA missions confirmed that better DT_{SA} results are obtainable via SAR mode (S3A and S3B) rather than LRM mode SA missions (JA3), since much larger ΔDT_{SA-HDM} values were found with respect to those obtained for the JA3 mission. This fact emphasizes that the JA3 dataset is noisier than that of S3A, and also that the SRAL altimeter for Sentinel-3 missions better solves the signal in the coastal band. In addition, due to the Jason mission's orbit and inclination over sub-arctic areas, JA3 could not provide much reliable data. Hence, the Sentinel-3 missions provided more accurate results than Jason-3 over Baltic Sea.

The presented methodology is a promising solution that provides more realistic SA-based absolute sea level data. The method also allows identification of problematic areas due to the limitations of the data sources utilized. For future studies, an iterative approach can be implemented to identify and correct these problematic areas/sources. In addition, utilization of newly launched altimetry missions, for instance the Sentinel-6 Michael Freilich satellite (launched in 2020) and the Surface Water and Ocean Topography (SWOT) (launched in 2022), could lead to more precise and reliable estimates and enhance our knowledge about sea level heights.

Appendix A

Table A1. The used tide gauge stations.

ID	TG Station (Country)		Latitude (°N)	Longitude (°E)
1	Narva-jõesuu	EE	59.46905	28.04211
2	Kunda	EE	59.52100	26.54173
3	Loksa	EE	59.58447	25.70721
4	Pirita	EE	59.46887	24.82081
5	Paldiski	EE	59.35076	24.04932
6	Dirhami	EE	59.20843	23.49693
7	Haapsalu	EE	58.95801	23.52743
8	Heltermaa	EE	58.86555	23.04714
9	Ristna	EE	58.92121	22.05518
10	Roomassaare	EE	58.21725	22.50377
11	Virtsu	EE	58.57225	23.51126
12	Pärnu	EE	58.38747	24.48196
13	Häädemeeste	EE	58.03745	24.46360
14	Ruhnu	EE	57.78354	23.26350
15	Salacgrīva	LV	57.75528	24.35361
16	Skulte	LV	57.31583	24.40944
17	Daugavgrīva	LV	57.05944	24.02333

Table A1. *Cont.*

ID	TG Station (Country)		Latitude (°N)	Longitude (°E)
18	Mērsrags	LV	57.33472	23.13278
19	Kolka	LV	57.73722	22.59278
20	Ventspils	LV	57.39556	21.53444
21	Liepāja	LV	56.51556	20.99944
22	Klaipeda	LT	55.73024	21.08112
23	Gdynia	PL	54.51770	18.55520
24	Leba	PL	54.76340	17.55050
25	Ustka	PL	54.58800	16.85380
26	Kolobrzeg	PL	54.18660	15.55340
27	Swinoujscie	PL	53.90840	14.25430
28	Greifswald	DE	54.09280	13.44610
29	Sassnitz	DE	54.51080	13.64310
30	Warnemünde	DE	54.16972	12.10333
31	Travemünde	DE	53.95810	10.87220
32	Rodby	DK	54.65000	11.35000
33	Tejn	DK	55.25000	14.83330
34	Rodvig	DK	55.25420	12.37280
35	Dragor	DK	55.60000	12.68330
36	Helsingborg sjöv	SE	56.04460	12.68700
37	Barsebäck	SE	55.75640	12.90330
38	Skanör	SE	55.41670	12.82940
39	Ystad sjöv	SE	55.42270	13.82570
40	Simrishamn	SE	55.55750	14.35780
41	Karlshamn sjöv	SE	56.15420	14.82130
42	Kalmar sjöv	SE	56.67130	16.38880
43	Oskarshamn	SE	57.27500	16.47810
44	Ölands norra udde	SE	57.36610	17.09720
45	Visby	SE	57.63920	18.28440
46	Västervik sjöv	SE	57.74820	16.67470
47	Arkö	SE	58.48430	16.96070
48	Landsort norra	SE	58.76890	17.85890
49	Loudden sjöv	SE	59.34130	18.13730
50	Forsmark	SE	60.40860	18.21080
51	Bönan sjöv	SE	60.73840	17.31860
52	Ljusne sjöv	SE	61.20670	17.14520
53	Spikarna	SE	62.36330	17.53110
54	Lunde sjöv	SE	62.88650	17.87640
55	Skagsudde sjöv	SE	63.19060	19.01190

Table A1. *Cont.*

ID	TG Station (Country)		Latitude (°N)	Longitude (°E)
56	Holmsund sjöv	SE	63.68030	20.33310
57	Furuögrund	SE	64.91580	21.23060
58	Strömören sjöv	SE	65.54970	22.23830
59	Kalix-storön	SE	65.69690	23.09610
60	Kemi	FI	65.67337	24.51526
61	Oulu	FI	65.04030	25.41820
62	Raahe	FI	64.66630	24.40708
63	Pietarsaari	FI	63.70857	22.68958
64	Vaasa	FI	63.08150	21.57118
65	Kaskinen	FI	62.34395	21.21483
66	Mäntyluoto	FI	61.59438	21.46343
67	Rauma	FI	61.13353	21.42582
68	Föglö	FI	60.03188	20.38482
69	Turku	FI	60.42828	22.10053
70	Hanko	FI	59.82287	22.97658
71	Helsinki	FI	60.15363	24.95622
72	Porvoo	FI	60.20579	25.62509
73	Hamina	FI	60.56277	27.17920
74	Kronstadt	RU	59.96670	29.75000

Table A2. SA pass numbers nearby used TG stations.

TG ID	S3A	JA3	S3B [1]
1	72,197,311,425,528,642	92,168,187	83,197,311,425,528,642,756
2	83,197,411,528	72,187	83,197,311,414,528
3	83,300,414,739	-	83,300,414,739
4	186,311,625	16	186,300,625,739
5	72,186,511,625	16,111	186,511,625
6	72,511	16,111,194	72,397,511
7	72,511	194	72,397
8	397,72	111,194	72,283,397
9	283,683,728	111,194	728,283
10	72,169,283,728	118	72,169,186,283,397
11	72,186,397	187,194	72,186,397
12	186,300,511	187,194	186,300,511
13	300,511	187,194	300,511
14	186,283	187,194	72,169,186,283
15	300	118,187	397
16	300	118,194	397
17	397,283,300	118	283,300,397
18	300,186,283	118	283,300,397,186

Table A2. *Cont.*

TG ID	S3A	JA3	S3B [1]
19	72,169,186,283	118,187	283,72,169,186
20	55,169,728	187,118	55,72,169
21	55,597,711,728	187,42	55,72,597,711,728
22	369,483,597,711,728	187,220,9,144,187,220	72,369,483,597,711,728
23	369,500,597,614,728	144,187,68	141,255,369,483,500,597,614,728
24	255,369,386,500,614,27	187,68	141,255,369,386,500,614
25	27,141,255,272,386,500,683	68,187,246	141,255,272,386,500,683
26	27,158,272,386,569,683	246,68,11	27,158,272,386,569,683
27	44,158,272,455,569,683	246,111	44,158,199,272,455,569,683
28	44,455,700	246,111	44,158,199,272,455,569,683
29	44,227,341,455,700	35,111,170	44,158,199,341,455,569,700
30	113,227,244,341,472,586,655,700	35,170	85,113,216,227,341,541,558,586,672,700
31	113,227,244,358,472,586,655,769	35,170,213	85,113,216,227,358,472,541,558,586,655,672,769
32	113,227,244,341,358,472,586,655,769	35,170,213	85,102,113,216,227,244,341,358,472,541, 558,586,655,672,769
33	158,569,683,27,44,	68,111	569,683
34	341,586	246,35	85,199,216,341,455,586,672,700,769
35	455,586	246,35	199,216,455,586,672
36	16,130,244,341,358,455,472,586	137,213,246	16,102,130,199,216,227,244,302,341,358, 444,455,472,541,558,586,672,758
37	455,586	35,246	16,102,130,199,216,302,455,586,672,758
38	455,586,700	246,35	199,341,455,569,586,700
39	44,569,700	-	199,700
40	27,44,569,683,700	68	27,44,569,683
41	227,44,141,158,683	68,144	27,44,141,158,683
42	27,141,158,255	144	27,141,158,255
43	158,255,369,386,483,500	35,144,220	158,255
44	158,255,369,386,483,500	35,144,220	158,255,369,386,483
45	386,483,597	35,220	158,255,369,386,483
46	158,255,369,483,500	35,220	158,255,369,483
47	158,369,483,500	42,220	158,369,483,597
48	158,272,369,483,597	42,118,213	158,272,369,386,483,597
49	272,4,597,711	118,213	272,711
50	44,158,272,711	61,118,137,194,213	44,158,272,711
51	44,700,711	61,137,194	44,700
52	44,700,711	61,194,239,16	700,711
53	55,700,711	61,92,239,16	55,169,711
54	55,169,283,700	92,163,168,239,244	55,169,283,700
55	44,169,283,397,511,700	163,168,244	44,169,397,511,700

Table A2. *Cont.*

TG ID	S3A	JA3	S3B [1]
56	44,283,397,511,625,739	11,66,87,142,163,218,244	44,283,397,511,625,700,739
57	44,83,625,739	11,40,66,87,116,142,163,189,218	44,83,158,197,311
58	59,158,197,272,428	14,37,113,116,189,192	83,158,197,272,311,425
59	272,311,386,425,539	14,87,113,116,189,192	272,311,386,425,539
60	272,311,386,425,539	14,87,113,116,189,192	272,311,386,425,539
61	386,425,500,539	11,40,87,116,189,192	311,386,425,539
62	197,311,386,425,500	11,40,87,116,142,163,189,192,244	83,197,272,386,625,739
63	197,272,311,386,511,625,739	66,142,163,218,239,244	83,197,272,386,625,739
64	272,511,625,739	61,66,142,168,239,244	272,511,625,739
65	272,386,511	61,92,137,168,244	272,386,511
66	386,397	61,92,137,168	272,386,397
67	272,397,500	92,137,213	283,386,397,500
68	158,169,272,283,386,500,614	16,35,118,194,213	169,272,283,386,397,500,597,614
69	283,397,500,614,728	16,35,213	283,386,397,500,614,728
70	72,397,511,614,625,728	16,35	72,283,397,511,614,625,728
71	83,186,300,625,739	92,111	72,83,186,300,625,739
72	83,186,197,300,414	92,111,186	83,186,197,300,414,628,739
73	83,197,300,311,414,425,528,642,756	111,168,187	83,197,300,311,414,425,528,642
74	311,425,528,539,642,756	168,187	100,311,425,539,642,756

[1] Pass number before final phase (before Nov 2018) also mentioned in the table but were excluded from the analysis.

Table A3. TG stations near SA passes.

JA Pass#	TG ID	S3 Pass#	TG ID Crossed Over
9	21,22,23	16	36
11	56,57,58,60,61,62	27	24,41,25,26,40,42
14	58,59,60	44	27,28,40,41,51,56,57,58,55,50,52,29,39
16	4,5,6,70,69,68,52,53	55	20,53,21,54
35	29,30,31,32,34,35,38,37,43,44,45,46,70,69,68	72	6,8,10,19,7,11,5,70,1,22
37	58,59	83	2,72,63,58,3,71,73,57
40	57,58,61,62	113	30,31,32
42	20,21,48,47	130	36
61	50,51,52,53,64,65,66	141	24,42,25,41
66	63,64,56,57	158	59,50,47,46,43,26,27,41,42,44,48,68,58
68	23,24,25,40,41,26	169	20,68,54,19,10,55
87	56,57,60,61,62	186	18,14,5,71,4,72,11,12,19
92	1,2,71,72,65,66,67,53,54	197	58,62,73,1,2,72,63,59
111	26,27,28,9,8,6,5,72,73,71,29	227	29,31,30,32
113	58,59,60	244	30,32,36,31
116	57,58,59,60,61,62	255	23,43,44,24,25,42,46

Table A3. *Cont.*

JA Pass#	TG ID	S3 Pass#	TG ID Crossed Over
118	50,49,48,68,10,14,15,16,17,18,19	272	25,48,65,64,60,67,26,27,49,50,68,63,59
137	36,50,51,65,66,67	283	55,9,10,19,54,56,68,69,14,18,17
142	56,57,62,63,64	300	72,3,12,13,15,17,71,73,4,16,18
144	21,22,23,41,42,43,44	311	1,73,62,59,74,58,60,61
163	62,63,54,55,56,57	341	29,32,34,30,36
168	1,72,73,74,66,65,64,55,54	358	31,32,36
170	29,30,31,32	369	47,44,22,23,24,46,48,
187	73,74,1,11,12,13,14,18,2,19,20,21,22,23,24,25	386	24,45,68,63,66,60,61,62,65,25,26,44
189	57,58,59,60,61,62	397	55,67,69,8,11,17,66,56,70
192	58,59,60,61,62	414	2,73,3,72
194	50,51,52,68,15,13,12,11,9,8,7,6	425	60,62,74,1,73,61,59
213	31,36,48,49,50,67,68,69,32	455	27,28,38,37,36,29,35
218	62,63,57,56	472	30,31,36,32
220	21,22,45,44,43,46,47	483	48,45,22,49,47,44,46,23
239	52,53,54,63,64	500	23,67,68,61,62,69,24,25,47,44,46
244	54,55,56,63,64,65	511	6,12,70,56,5,13,7,64,65,63,55
246	25,26,27,28,34,35,36,37,38	528	2,73,1,74
		539	74,61,60
		569	39,26,27,40
		586	32,34,35,37,30,31,36,38
		597	21,49,22,23,45,48
		614	23,69,24,70,68
		625	4,71,64,56,5,70,63,57
		642	1,73,74
		655	30,31,32
		683	25,41,26,27,40,39
		700	28,39,52,55,51,53,54,40,38,29,30
		711	21,50,52,22,49,51,53
		728	9,20,21,22,70,23,69,10
		739	3,71,63,57,64,56,58
		756	74,73
		769	31,32

References

1. Jahanmard, V.; Delpeche-Ellmann, N.; Ellmann, A. Realistic dynamic topography through coupling geoid and hydrodynamic models of the Baltic Sea. *Cont. Shelf Res.* **2021**, *222*, 104421. [CrossRef]
2. Jahanmard, V.; Delpeche-Ellmann, N.; Ellmann, A. Towards realistic dynamic topography from coast to offshore by incorporating hydrodynamic and geoid models. *Ocean Model.* **2022**, *180*, 102124. [CrossRef]
3. Milne, G.A.; Gehrels, W.R.; Hughes, C.W.; Tamisiea, M.E. Identifying the causes of sea-level change. *Nat. Geosci.* **2009**, *2*, 471–478. [CrossRef]
4. Pavlis, N.K.; Holmes, S.A.; Kenyon, S.C.; Factor, J.K. The development and evaluation of the Earth Gravitational Model 2008 (EGM2008). *J. Geophys. Res. Solid Earth* **2012**, *117*, B04406. [CrossRef]

5. Ellmann, A.; Märdla, S.; Oja, T. The 5 mm geoid model for Estonia computed by the least squares modified Stokes's formula. *Surv. Rev.* **2019**, *52*, 352–372. [CrossRef]
6. Ågren, J.; Strykowski, G.; Bilker-Koivula, M.; Omang, O.; Märdla, S.; Forsberg, R.; Ellmann, A.; Oja, T.; Liepins, I.; Parseliunas, E.; et al. The NKG2015 gravimetric geoid model for the Nordic-Baltic region. In Proceedings of the 1st Joint Commission 2 and IGFS Meeting International Symposium on Gravity, Geoid and Height Systems, Thessaloniki, Greece, 19–23 September 2016; pp. 19–23. Available online: https://www.isgeoid.polimi.it/Geoid/Europe/NordicCountries/GGHS2016_paper_143.pdf (accessed on 26 August 2021).
7. Varbla, S.; Ågren, J.; Ellmann, A.; Poutanen, M. Treatment of Tide Gauge Time Series and Marine GNSS Measurements for Vertical Land Motion with Relevance to the Implementation of the Baltic Sea Chart Datum 2000. *Remote Sens.* **2022**, *14*, 920. [CrossRef]
8. Fu, W.; She, J.; Dobrynin, M. A 20-year reanalysis experiment in the Baltic Sea using three-dimensional variational (3DVAR) method. *Ocean Sci.* **2012**, *8*, 827–844. [CrossRef]
9. Xu, Q.; Cheng, Y.; Plag, H.-P.; Zhang, B. Investigation of sea level variability in the Baltic Sea from tide gauge, satellite altimeter data, and model reanalysis. *Int. J. Remote Sens.* **2015**, *36*, 2548–2568. [CrossRef]
10. Mostafavi, M.; Delpeche-Ellmann, N.; Ellmann, A. Accurate Sea Surface heights from Sentinel-3A and Jason-3 retrackers by incorporating High-Resolution Marine Geoid and Hydrodynamic Models. *J. Geod. Sci.* **2021**, *11*, 58–74. [CrossRef]
11. Andersen, O.B.; Scharroo, R. Range and geophysical corrections in coastal regions: And implications for mean sea surface determination. In *Coastal Altimetry*; Springer: Berlin/Heidelberg, Germany, 2011; pp. 103–146. [CrossRef]
12. Birgiel, E.; Ellmann, A.; Delpeche-Ellmann, N. Examining the Performance of the Sentinel-3 Coastal Altimetry in the Baltic Sea Using a Regional High-Resolution Geoid Model. In Proceedings of the 2018 Baltic Geodetic Congress (BGC Geomatics), Olsztyn, Poland, 21–23 June 2018; pp. 196–201. [CrossRef]
13. Birgiel, E.; Ellmann, A.; Delpeche-Ellmann, N. Performance of sentinel-3A SAR altimetry retrackers: The SAMOSA coastal sea surface heights for the Baltic Sea. In *International Association of Geodesy Symposia*; Springer: Berlin/Heidelberg, Germany, 2019; pp. 23–32. [CrossRef]
14. Liibusk, A.; Kall, T.; Rikka, S.; Uiboupin, R.; Suursaar, Ü.; Tseng, K.-H. Validation of Copernicus Sea Level Altimetry Products in the Baltic Sea and Estonian Lakes. *Remote Sens.* **2020**, *12*, 4062. [CrossRef]
15. Karimi, A.A.; Bagherbandi, M.; Horemuz, M. Multidecadal Sea Level Variability in the Baltic Sea and Its Impact on Acceleration Estimations. *Front. Mar. Sci.* **2021**, *8*, 702512. [CrossRef]
16. Madsen, K.S.; Høyer, J.L.; Tscherning, C.C. Near-coastal satellite altimetry: Sea surface height variability in the North Sea–Baltic Sea area. *Geophys. Res. Lett.* **2007**, *34*, L14601. [CrossRef]
17. Mercier, F.; Rosmorduc, V.; Carrere, L.; Thibaut, P. *Coastal and Hydrology Altimetry Product (PISTACH) Handbook*; Centre National d'Études Spatiales (CNES): Paris, France, 2010; p. 4. Available online: https://www.aviso.altimetry.fr/fileadmin/documents/data/tools/hdbk_Pistach.pdf (accessed on 23 March 2023).
18. Valladeau, G.; Thibaut, P.; Picard, B.; Poisson, J.C.; Tran, N.; Picot, N.; Guillot, A. Using SARAL/AltiKa to Improve Ka-band Altimeter Measurements for Coastal Zones, Hydrology and Ice: The PEACHI Prototype. *Mar. Geod.* **2015**, *38*, 124–142. Available online: https://www.tandfonline.com/action/journalInformation?journalCode=umgd20 (accessed on 23 March 2023). [CrossRef]
19. Vignudelli, S.; Cipollini, P.; Gommenginger, C.; Snaith, H.; Coelho, H.; Fernandes, J.; Gomez-Enri, J.; Martin-Puig, C.; Woodworth, P.; Dinardo, S.; et al. The COASTALT project: Towards an operational use of satellite altimetry in the coastal zone. In Proceedings of the Oceans 2009, Biloxi, MS, USA, 26–29 October 2009; IEEE: New York, NY, USA, 2009; pp. 1–6. [CrossRef]
20. Birol, F.; Fuller, N.; Lyard, F.; Cancet, M.; Niño, F.; Delebecque, C.; Fleury, S.; Toublanc, F.; Melet, A.; Saraceno, M.; et al. Coastal applications from nadir altimetry: Example of the X-TRACK regional products. *Adv. Space Res.* **2017**, *59*, 936–953. [CrossRef]
21. Tuomi, L.; Rautiainen, L.; Passaro, M. *User Manual Along-Track Data Baltic+SEAL*; Project: ESA AO/1-9172/17/I-BG-BALTIC+ BALTIC+ Theme 3 Baltic+ SEAL (Sea Level) Requirements Baseline Document/BG-BALTIC+ SEAL (Sea Level) Category: ESA Express Procurement Plus-EXPRO+ Deliverable: D1.1 Code: TUM_BSEAL_RBD; Baltic SEAL: München, Germany, 2020. [CrossRef]
22. Varbla, S.; Ellmann, A.; Delpeche-Ellmann, N. Applications of airborne laser scanning for determining marine geoid and surface waves properties. *Eur. J. Remote Sens.* **2021**, *54*, 558–568. [CrossRef]
23. Liibusk, A.; Varbla, S.; Ellmann, A.; Vahter, K.; Uiboupin, R.; Delpeche-Ellmann, N. Shipborne GNSS acquisition of sea surface heights in the Baltic Sea. *J. Geod. Sci.* **2022**, *12*, 1–21. [CrossRef]
24. Varbla, S.; Liibusk, A.; Ellmann, A. Shipborne GNSS-Determined Sea Surface Heights Using Geoid Model and Realistic Dynamic Topography. *Remote Sens.* **2022**, *14*, 2368. [CrossRef]
25. Novotny, K.; Liebsch, G.; Dietrich, R.; Lehmann, A. Combination of sea-level observations and an oceanographic model for geodetic applications in the Baltic Sea. In *A Window on the Future of Geodesy*; Springer Series of IAG Symposia; Springer: Berlin/Heidelberg, Germany, 2005; pp. 195–200. [CrossRef]
26. Passaro, M.; Müller, F.L.; Oelsmann, J.; Rautiainen, L.; Dettmering, D.; Hart-Davis, M.G.; Abulaitijiang, A.; Andersen, O.B.; Høyer, J.L.; Madsen, K.S.; et al. Absolute Baltic Sea Level Trends in the Satellite Altimetry Era: A Revisit. *Front. Mar. Sci.* **2021**, *8*, 647607. [CrossRef]
27. Rautiainen, L.; Särkkä, J.; Tuomi, L.; Müller, F.; Passaro, M. *Baltic+ SEAL: Validation Report*; Baltic SEAL: Frascati, Italy, 2020. [CrossRef]

28. Pajak, K.; Kowalczyk, K. A comparison of seasonal variations of sea level in the southern Baltic Sea from altimetry and tide gauge data. *Adv. Space Res.* **2018**, *63*, 1768–1780. [CrossRef]
29. Shepard, D. A Two-Dimensional Interpolation Function for Irregularly-Spaced Data. In Proceedings of the 23rd ACM National Conference, Las Vegas, NV, USA, 27–29 August 1968; ACM Press: New York, NY, USA, 1968; pp. 517–524. [CrossRef]
30. Vestøl, O.; Ågren, J.; Steffen, H.; Kierulf, H.; Tarasov, L. NKG2016LU: A new land uplift model for Fennoscandia and the Baltic Region. *J. Geod.* **2019**, *93*, 1759–1779. [CrossRef]
31. Myrberg, K.; Soomere, T. The Gulf of Finland, its hydrography and circulation dynamics. In *Preventive Methods for Coastal Protection*; Springer: Berlin/Heidelberg, Germany, 2013; pp. 181–222. [CrossRef]
32. Rosentau, A.; Muru, M.; Gauk, M.; Oja, T.; Liibusk, A.; Kall, T.; Karro, E.; Roose, A.; Sepp, M.; Tammepuu, A.; et al. Sea-level change and flood risks at Estonian coastal zone. In *Coastline Changes of the Baltic Sea from South to East*; Springer: Berlin/Heidelberg, Germany, 2017; pp. 363–388. [CrossRef]
33. Ekman, M. The Changing Level of the Baltic Sea during 300 Years: A Clue to Understanding the Earth. Summer Institute for Historical Geophysics Åland Islands. Logotipas. 2009. 158p. Available online: https://www.baltex-research.eu/publications/Books%20and%20articles/The%20Changing%20Level%20of%20the%20Baltic%20Sea.pdf (accessed on 23 March 2023).
34. Soomere, T. Anisotropy of wind and wave regimes in the Baltic proper. *J. Sea Res.* **2003**, *49*, 305–316. [CrossRef]
35. Suursaar, Ü.; Sooäär, J. Decadal variations in mean and extreme sea level values along the Estonian coast of the Baltic Sea. *Tellus A Dyn. Meteorol. Oceanogr.* **2007**, *59*, 249–260. [CrossRef]
36. Delpeche-Ellmann, N.; Mingelaitė, T.; Soomere, T. Examining Lagrangian surface transport during a coastal upwelling in the Gulf of Finland, Baltic Sea. *J. Mar. Syst.* **2017**, *171*, 21–30. [CrossRef]
37. Jakimavičius, D.; Kriaučiūnienė, J.; Šarauskienė, D. Assessment of wave climate and energy resources in the Baltic Sea nearshore (Lithuanian territorial water). *Oceanologia* **2018**, *60*, 207–218. [CrossRef]
38. Hünicke, B.; Zorita, E. Influence of temperature and precipitation on decadal Baltic Sea level variations in the 20th century. *Tellus A Dyn. Meteorol. Oceanogr.* **2006**, *58*, 141–153. [CrossRef]
39. Delpeche-Ellmann, N.; Giudici, A.; Rätsep, M.; Soomere, T. Observations of surface drift and effects induced by wind and surface waves in the Baltic Sea for the period 2011–2018. *Estuar. Coast. Shelf Sci.* **2020**, *249*, 107071. [CrossRef]
40. Barbosa, S.M. Quantile trends in Baltic sea level. *Geophys. Res. Lett.* **2008**, *35*. [CrossRef]
41. Schwabe, J.; Ågren, J.; Liebsch, G.; Westfeld, P.; Hammarklint, T.; Mononen, J.; Andersen, O.B. The Baltic Sea Chart Datum 2000 (BSCD2000): Implementation of a common reference level in the Baltic Sea. *Int. Hydrogr. Rev.* **2020**, *23*, 63–83. Available online: https://digitale-bibliothek.bsh.de/viewer/api/v1/records/184272/files/source/Westfeld_Baltic_Sea_Chart_2020.pdf (accessed on 23 March 2023).
42. Kuo, C.Y.; Shum, C.K.; Braun, A.; Mitrovica, J.X. Vertical crustal motion determined by satellite altimetry and tide gauge data in Fennoscandia. *Geophys. Res. Lett.* **2004**, *31*. [CrossRef]
43. Jahanmard, V.; Delpeche-Ellmann, N.; Ellmann, A. Machine learning prediction for filling the interruptions of tide gauge data using a least square estimation method from nearest stations. In *Geodesy for A Sustainable Earth, Scientific Assembly of the International Association of Geodesy, Abstract Book: Scientific Assembly of the International Association of Geodesy*; Chinese Society for Geodesy: Beijing, China, 2021.
44. Hordoir, R.; Axell, L.; Höglund, A.; Dieterich, C.; Fransner, F.; Gröger, M.; Liu, Y.; Pemberton, P.; Schimanke, S.; Andersson, H.; et al. Nemo-Nordic 1.0: A NEMO-based ocean model for the Baltic and North seas–research and operational applications. *Geosci. Model Dev.* **2019**, *12*, 363–386. [CrossRef]
45. Passaro, M.; Rose, S.K.; Andersen, O.B.; Boergens, E.; Calafat, F.M.; Dettmering, D.; Benveniste, J. ALES+: Adapting a homogenous ocean retracker for satellite altimetry to sea ice leads, coastal and inland waters. *Remote Sens. Environ.* **2018**, *211*, 456–471. [CrossRef]
46. Sacher, M. The European Vertical Reference System (EVRS)–Development and latest results. In *Geophysical Research Abstracts*; Federal Agency for Cartography and Geodesy: Frankfurt, Germany, 2019; Available online: https://meetingorganizer.copernicus.org/EGU2019/EGU2019-1811.pdf (accessed on 23 March 2023).
47. Ekman, M. Impacts of geodynamic phenomena on systems for height and gravity. *J. Geodesy* **1989**, *63*, 281–296. [CrossRef]
48. Boucher, C.; Altamimi, Z. Memo: Specifications for Reference Frame Fixing in the Analysis of a EUREF GPS Campaign (Version 8). 2011. Available online: http://etrs89.ensg.ign.fr/memo-V8.pdf (accessed on 23 March 2023).
49. Müller, K. *Coastal Research in the Gulf of Bothnia*; Springer Science & Business Media: Berlin/Heidelberg, Germany, 1982; Volume 45. Available online: https://link.springer.com/book/9789061930983 (accessed on 23 March 2023).
50. Mostafavi, M.; Delpeche-Ellmann, N.; Ellmann, A. Satellite Altimetry Performance Verified to Enhanced Hydrodynamic Model of the Baltic Sea. In *European Space Agency's 2022 Living Planet Symposium. Bonn, Germany: The electronical abstract book, session E3.04 Baltic Sea Regional Applications and Science: Living Planet Symposium (LPS22)*; European Space Agency: Paris, France, 2022. Available online: https://lps22.eu/scientific-session (accessed on 23 March 2023).
51. Bonsdorff, E.; Blomqvist, E.M.; Mattila, J.; Norkko, A. Long-term changes and coastal eutrophication. Examples from the Aland Islands and the Archipelago Sea, northern Baltic Sea. *Oceanolica Acta* **1997**, *20*, 319–329. Available online: https://archimer.ifremer.fr/doc/00093/20402/18069.pdf (accessed on 23 March 2023).

52. Freedman, D.; Pisani, R.; Purves, R.; Statistics: Fourth International Student Edition. W W Norton & Company. 2020, p. 22. Available online: https://www.amazon.com/Statistics-Fourth-International-Student-Freedman/dp/0393930432 (accessed on 23 March 2023).

53. Varbla, S.; Ellmann, A.; Delpeche-Ellmann, N. Validation of Marine Geoid Models by Utilizing Hydrodynamic Model and Shipborne GNSS Profiles. *Mar. Geod.* **2020**, *43*, 134–162. [CrossRef]

Appendix 3

Article

Long-Term and Decadal Sea-Level Trends of the Baltic Sea Using Along-Track Satellite Altimetry

Majid Mostafavi [1,*] , **Artu Ellmann** [1] **and Nicole Delpeche-Ellmann** [2]

1   Department of Civil Engineering and Architecture, Tallinn University of Technology, 19086 Tallinn, Estonia
2   Department of Cybernetics, School of Science, Tallinn University of Technology, 19086 Tallinn, Estonia
*   Correspondence: majid.mostafavi@taltech.ee

Abstract: One of the main effects of climate change is rising sea levels, which presents challenges due to its geographically heterogenous nature. Often, contradictory results arise from examining different sources of measurement and time spans. This study addresses these issues by analysing both long-term (1995–2022) and decadal (2000–2009 and 2010–2019) sea-level trends in the Baltic Sea. Two independent sources of data, which consist of 13 tide gauge (TG) stations and multi-mission along-track satellite altimetry (SA), are utilized to calculate sea-level trends using the ordinary least-squares method. Given that the Baltic Sea is influenced by geographically varying vertical land motion (VLM), both relative sea level (RSL) and absolute sea level (ASL) trends were examined for the long-term assessment. The results for the long-term ASL show estimates for TG and SA to be 3.3 mm/yr and 3.9 mm/yr, respectively, indicating agreement between sources. Additionally, the comparison of long-term RSL ranges from −2 to 4.5 mm/yr, while ASL varies between 2 and 5.4 mm/yr, as expected due to the VLM. Spatial variation in long-term ASL trends is observed, with higher rates in the northern and eastern regions. Decadal sea-level trends show higher rates, particularly the decade 2000–2009. Comparison with other available sea-level datasets (gridded models) yields comparable results. Therefore, this study evaluates the ability of SA as a reliable source for determining reginal sea-level trends in comparison with TG data.

Keywords: absolute sea level; sea-level trend; tide gauge; satellite altimetry; vertical land motion; relative; Baltic Sea; dynamic topography

1. Introduction

Sea-level variation stands as a crucial benchmark for assessing global climate change, with approximately 410 million individuals residing in areas lower than 2 m above sea level. Thus, there exists a looming risk of sea-level rise [1] and, as a consequence, accurate and reliable methods are required for determining these changes. One of the main reasons behind these sea-level changes is that, starting from the mid-1960s, the oceans absorbed more heat and expanded, leading to a noticeable acceleration in the rate of the sea-level rise [2]. This consistent ongoing global warming has been a primary driver behind the persistent rise in global sea levels [3–5]. Since the 1990s, the satellite altimetry (SA) technique [6] has enabled observations of the absolute sea level (ASL), i.e., relative to the Earth's centre of mass (CM). However, it is important to note that relative sea level (RSL) observations primarily rely on data series from land-bound tide gauges (TGs), which may be susceptible to uncertainties due to vertical land motion (VLM) and instrumental limitations (e.g., [7]). Both measurement techniques have unveiled a significant acceleration in the Earth's average sea-level rise over recent decades, primarily attributed to the increasingly rapid loss of ice in Greenland and Antarctica [2,8,9].

Therefore, the accurate detection of contemporary changes and trends in sea levels is essential for preparing coastal communities and forecasting future sea-level projections [10]. While many researchers have investigated the trends of sea levels, the precise scale of these

trends remains enshrouded in uncertainty. Most of the research conducted has focused on global mean sea level (GMSL) changes (e.g., [11–15]). The estimated GMSL trend varies between 2 and 4 mm/yr, thus depending on the data source and the time span of the datasets considered (e.g., [16–23]). Although these studies attribute sea-level changes as a response to global-scale climate variability, they are limited in providing regional insights.

Estimating regional sea-level changes seems more practical, but also, within a smaller domain, it may be challenging to decipher the noise compared to that of GMSL. This complexity arises from the fact that oceanic variability is typically larger on regional scales due to redistribution effects like wind. In addition, coastal regions are also more sensitive and more susceptible to errors that are frequently neglected when calculating the global average [24]. However, during the last decade, considering the advances in the more accurate estimation of sea levels, focus has shifted to regional sea-level trend assessments (e.g., [25–30]). Also, the currently achievable accuracy and stability in estimating sea-level changes at the regional scale enable the analysis and attribution of sea-level changes as a response to climate variability more precisely.

SA is one of the most widely used sources to study ASL and has been extensively used to understand sea-level variabilities. The SA working principle is to transmit short pulses of microwave radiation, which interact with the sea surface and return to the altimeter. From the two-way travel time of the pulses, the range between the satellite and the sea surface can be estimated. SA thus provides highly accurate spatiotemporal ASL measurements with respect to an earth-fixed geocentric coordinate system. Since October 1992, with the advent of the TOPEX/Poseidon mission, SA has provided repeated precise measurements of sea levels and continuously improved the observing system and associated data record over most of the world's oceans. Multiple SA missions have collected sea-level data with unprecedented coverage, resolution, accuracy, and stability. Hence, SA-derived sea-level estimates have become a needed reference for scientists, stakeholders, and decision-makers [5,15,28,31,32]. The question now arises on the ability of SA to be used independently, especially in complex coastal areas.

However, there are certain challenges in using SA data to retrieve spatiotemporal distribution of sea level data over coastal areas, closer than about 30 km to the land. In coastal zones, the quality of the range measurements is degraded because the radar pulses are reflected partly from land and partly from the sea. It is also more difficult to compute accurate range corrections, since the tidal patterns are more complex to model [33]. Therefore, SA observations closer than ~30 km to the coast are only seldom used in sea-level trend studies. Also, the majority of sea-level trend investigations use monthly gridded SA data based on regular grids with a spatial resolution of 6–25 km.

Furthermore, many studies use the sea-level anomaly (SLA, which is a deviation of the sea level from the mean sea surface) for studying the sea-level changes at the regional scale. MSS is not an equipotential surface due to semi-persistent external forces that affect the mean sea-level variability in a spatiotemporal domain [34]. In addition, MSS models possess uncertainties due to averaging conventions. SA-based MSS models also may contain error-modelling deficiencies, e.g., dynamic atmospheric correction (DAC), especially at sub-polar latitudes. In addition, temporal interpolation of SA data for the MSS determination is vague considering the SA revisiting cycle (varies from 10–35 days). An alternative to SLA is dynamic topography (DT), which is the separation of sea surface height (SSH), and a geoid model (a static equipotential of earth's surface). Accurate DT is the most reliable source to represent sea level dynamics which plays an important role in understanding the oceans and sea level changes. Utilizing the SA-determined DT enables representing both mean and time-varying dynamics of the ocean so that sub-mesoscale dynamics can potentially be captured [33,35–37].

Therefore, this study uses SA-determined instantaneous DT to represent more reliable sea level changes at a regional scale. Both TG and SA observations are employed for investigating various aspects of sea level trends (e.g., [38]). TG stations provide sea level records that are referred to geoid-based chart datums. These can serve for the validation

of SA data. Nevertheless, TG stations are predominantly located nearshore, and their measurements are relative to land-bounded benchmarks. Consequently, to acquire ASL from the TG observation within vertical land motion (VLM) regions it is necessary to correct the TG records, i.e., ASL = RSL + VLM.

Accordingly, the developed regional sea trend estimation methodology is tested in the Baltic Sea region, which is affected by the post-glacial rebound. The Baltic Sea is surrounded by nine countries with a high density of marine traffic and coastal activities where more than 84 million people live in the Baltic catchment area [39]. Therefore, predicting future sea level changes, forecasting ocean phenomena, and responding to marine disasters are needed to conduct research on sea level trends in the Baltic Sea. A realistic analysis of sea level trends and their uncertainty over the Baltic Sea region is very topical and highly important, which could help to make a reliable prediction of the long-term trend in sea level over this region. Previous studies have shown the Baltic Sea RSL trend between 1–3 mm/yr [40–46] and ASL rates between 3–6 mm/yr [29,44–47]. Thus, there is a wide range of variation amongst studies for different time spans and locations are utilized. Quantifying sea level trend uncertainties is also required to judge the reliability of sea level observations and prevent misinterpretations of artifacts arising from the limitations of the sea level observing systems [10].

The sea level trend estimate uncertainties may occur due to possible systematic effects such as inconsistencies in the international reference frame (ITRF) realizations, which can reach ±0.1 mm/yr for GMSL trend estimation [48]. The VLM correction uncertainty also can exceed 0.05 mm/yr [13]. In addition, the SA data may contain geophysical (tropospheric and ionospheric) correction errors. These sea level trend uncertainties are directly correlated with the length of the time series, and they increase considerably when the uncertainties of VLM, the reference frame, and geoid changes are not considered [13]. In this study, these effects are considered which are explained in detail in relevant sections below.

The time span examined for this study is from 1995 to 2022 and the study region is the section of the Baltic Sea where the best quality SA data (with lower land contamination and sea-ice concentration) is available (mainly over Baltic Proper area). The SA-derived sea level trend estimates are verified by using a larger amount of TG stations, as compared to previous studies (e.g., [41,43–45,49]). The aim of this study is to: (i) to develop a method for estimating the regional decadal and long-term (almost 3 decades) sea level linear trends from instantaneous SA measurements, (ii) compare the corresponding regional ASL and RSL trends, (iii) inter-comparison of various SA derived trend estimates from different approaches/datasets that consists of (a) investigating whether the distance to coast affects the SA trend estimation, (b) comparison of trend estimates of different SA mission orbit constellations, and (c) comparisons between the various existing gridded and averaged SA data-product (3 models) trends vs. instantaneous SA data (this study) derived sea level trend.

The main challenge with the Baltic Sea level trend estimation is the seasonal and annual dynamic variations of sea level, which exhibit behaviour distinct to the open oceans. In adjacent years the annual mean level of the Baltic Sea could often change by more than 2 dm (cf. Figure A1), which complicates the trend estimations, especially over short-term periods. The research also aims to determine whether SA can serve as a viable substitute for TG observations in estimating regional trends, especially for the areas with poor TG networks or TGs with long data gaps. Also, by comparing the SA-derived ASL trend estimates with the RSL trend by TG, the VLM rates can be validated or developed over other regions. In this study, the DT values have been used both for TG and SA data which is a more realistic than the SLA used representation of sea level variability [33,50,51]. Another novelty of the paper is using instantaneous along-track SA data rather than gridded products which could lead to a more realistic regional sea level trend estimate especially in areas closer to the coast.

This paper is organized such that the developed methodology is described in Section 2, whereas the specifics of the study area and utilized datasets are described in

Sections [3] and [4], respectively. Section [5] presents the results in following order (i) long-term ASL and RSL trends (ii) decadal ASL over the past two decades, i.e., from 2000 to 2009 and from 2010 to 2019, and (iii) inter-comparison of SA-derived long-term ASL trend. The results are discussed in Section [6], whereas Section [7] concludes this paper.

2. Methodology

Conventions of the used DT data need to be considered in the development of the sea-level trend estimation methodology from the TG and SA observations. Modern TGs contain observation sensors, which automatically record the height of the coastal water level with high precision and temporal resolution (e.g., hourly). Contrastingly, the quality of historical TG records could be quite heterogeneous, due to the usage of mechanical mareographs or visual staff readings (e.g., twice a day). The TG zeros usually coincide with (or can be converted to) the zero of the vertical datum, which nowadays is often a geoid-based one [52]. Also, TG data could refer to different charts or national vertical data. Since the land-bound TG observations yield the RSL, which is the movement of the sea relative to land, to obtain ASL, the VLM effect needs to be removed from the TG observations (Figure [1]). The SA-derived SSH is computed by subtracting the distance between the satellite altitude (determined in a global geocentric coordinate system) and the instantaneous sea surface. The SA data, therefore, are not VLM-affected, thus reflecting the true sea-level rise. Also, SA data are referenced to ITRF (e.g., realizations of 2008, 2014, etc.), while the regional/national geoid model could refer to another coordinate system, e.g., the ETRF (European Terrestrial Reference Frame). Hence, the aforementioned differences are necessary to be accounted for to achieve consistency in comparisons that contain SA and TG data.
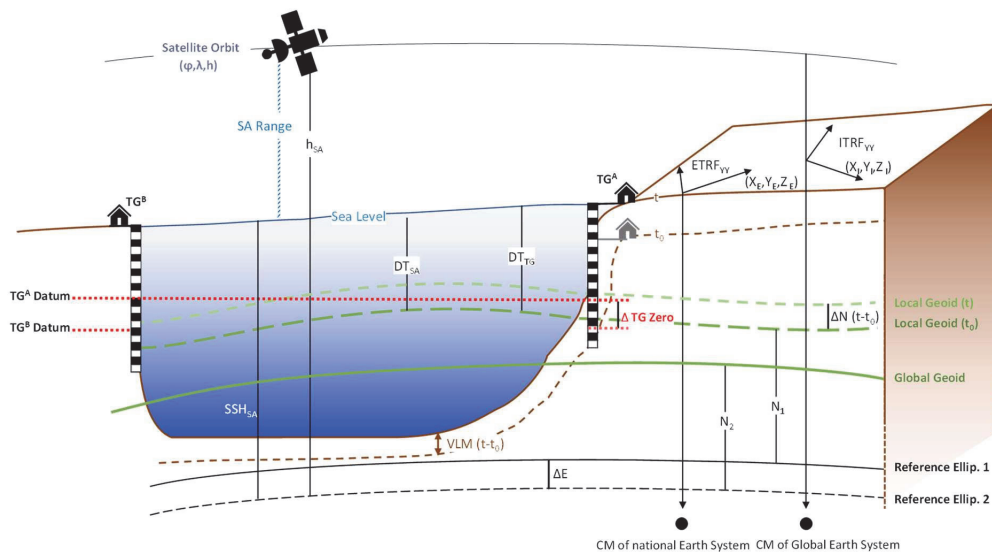
Figure 1. Inter-relations between the participating datasets (TG, and SA), geoid model, and different reference ellipsoids (ΔE) and relevant coordinate systems. The geoid change (ΔN) and vertical land motion (VLM) at the time instants (t) need to be considered for TG readings according to the reference time epoch (t_0). TGs could refer to different national/pan-continental datums (e.g., ETRF) while SA data refer to different global reference frames (e.g., ITRF). For the rest of the used abbreviations, see the main body of the text.

To obtain the ASL-associated $DT_{TG}(\varphi_{TG}, \lambda_{TG}, t_i)$ at the location of the TG ($\varphi_{TG}, \lambda_{TG}$), the TG observations ($DT_{obs}$) need to account for the VLM and geoid change (ΔN) corrections:

$$DT_{TG}(\varphi_{TG}, \lambda_{TG}, t_i) = DT_{obs}(\varphi_{TG}, \lambda_{TG}, t_i) + VLM(\varphi_{TG}, \lambda_{TG}).(t_i - t_0) + \Delta N(\varphi_{TG}, \lambda_{TG}).(t_i - t_0) \qquad (1)$$

where the selected reference time epoch is denoted by t_0 and the TG observation time instant by t_i. The VLM value (denoted by $VLM(\varphi_{TG}, \lambda_{TG})$) and geoid changes (denoted by $\Delta N(\varphi_{TG}, \lambda_{TG})$) can be obtained from an appropriate VLM model. To obtain the TG-derived sea level, $DT_{TG@SA\ cycle}$, for the SA overfly instant, t_{cycle}, the DT_{TG} data need to be selected within a predefined time window, w (before and after t_{cycle}). The matching TG data to the time instant, t_{cycle}, is estimated by the following linear (timewise) interpolation:

$$DT_{TG@SA\ cycle}\left(\varphi_{TG}, \lambda_{TG}, t_{cycle}\right) = interp\left(DT_{TG}\left(\varphi_{TG}, \lambda_{TG}, t_{cycle} \pm w\right)\right) \qquad (2)$$

The instantaneous SA-derived along-track DT data point $DT_{SA}\left(\varphi, \lambda, t_{cycle}\right)$ at an arbitrary location (φ, λ), determine by subtracting the geoidal height (N) from the SSH using the following expression:

$$DT_{SA}\left(\varphi, \lambda, t_{cycle}\right) = SSH\left(\varphi, \lambda, t_{cycle}\right) - \Delta E(\varphi) - N(\varphi, \lambda) \qquad (3)$$

where $SSH\left(\varphi, \lambda, t_{cycle}\right)$ is the SA-derived instantaneous SSH data point by

$$SSH\left(\varphi, \lambda, , t_{cycle}\right) = h_{SA} - (R + \Delta R) \qquad (4)$$

where ΔR are the necessary geophysical corrections that need to be applied to the SA range, R. Certainly, the outliers of the SA data must first be identified and removed from further computations using a certain method (e.g., see Section 4.1 for further details). Since initial datasets of different SA missions may refer to different reference ellipsoids, then ellipsoidal correction $(\Delta E(\varphi))$ for each SA data point is required. This ellipsoidal correction (associated with reference ellipsoid parameters) refers all participating SA measurements to the same reference ellipsoid [33].

For making the SA-derived DT comparable with $DT_{TG@SA\ cycle}$, a certain amount of the DT_{SA} data points close the TG station for each SA mission and at each pass/cycle need to be spatially averaged to yield the following:

$$DT_{SA@TG}\left(\varphi_{TG}, \lambda_{TG}, t_{cycle}\right) = \frac{1}{m}\sum_{j=1}^{m} DT_{SA}\left(\varphi_j, \lambda_j, t_{cycle}\right) \qquad (5)$$

where m is the number of j-th data points within the SA track segment up to a certain radius from each TG station. The resulting DT_{TG}, $DT_{TG@SA\ cycle}$, and $DT_{SA@TG}$ time series will be used for estimating the sea-level trends for each dataset. The most common method to estimate the sea-level trend is the ordinary least-squares (OLS) estimator [53–56]. The main advantages of using the OLS estimator for climate variables are that (i) it is consistent with previous estimators of sea-level trends and that (ii) the OLS estimate does not depend on the estimated variance–covariance matrix. This also means that the uncertainty estimates only depend on the variance–covariance matrix construction [13]. Hence, the linear regression model can be fitted to both SA and TG data to estimate the sea-level trend from each dataset. A linear model is defined as an equation that is linear in its coefficients:

$$Y(X) = \beta X + \epsilon \qquad (6)$$

where the model is denoted by $Y(X)$, X is a suitable datum and β is an unknown coefficient that can be estimated through OLS solution, and ϵ is an unknown error (residual noise). The least-squares estimator of β (denoted by $\hat{\beta}$) can be derived as follows:

$$\hat{\beta} \sim \left(X^t X\right)^{-1} X^t Y \qquad (7)$$

In most cases, $\hat{\beta}$ follows a normal distribution ($N(\mu, \sigma^2)$), where μ is the sample mean and σ^2 is the sample variance. The trend estimate uncertainty can be found by using the coefficient confidence. The coefficient confidence intervals (CIs) provide a measure of precision for regression coefficient estimates. A $100(1 - \alpha)\%$ CI gives the range that the corresponding regression coefficient will be within $100(1 - \alpha)\%$ confidence, meaning that $100(1 - \alpha)\%$ of the intervals resulting from repeated experimentation will contain the true value of the coefficient. The $100(1 - \alpha)\%$ CIs for regression coefficients are as follow [57]:

$$\hat{\beta} \pm t_{(1-\alpha/2,\, n-p)} SE(\hat{\beta}) \tag{8}$$

where $SE(\hat{\beta})$ is the standard error of the $\hat{\beta}$ coefficient estimate (minimum error gives the best solution), $t_{(1-\alpha/2,\, n-p)}$ is the $100(1 - \alpha/2)$ percentile of t-distribution with n–p degrees of freedom, n is the number of observations, and p is the number of regression coefficients (e.g., for 95% confidence, α = 0.05). In our case, a linear regression is fitted to the DT time series (for both SA- and TG-derived ones) to determine the sea-level trend estimates (the line slope β shows the trend). The estimated β now represents the sea-level trend (in mm/yr unit) (where $Y(X) = DT$ and $X = t$ in Equations (6) and (7)) and the corresponding uncertainties are obtainable using Equation (8).

Finally, the estimated (e.g., from SA data) and observed (e.g., from TG data) trends are statistically evaluated by using the root mean square error (RMSE):

$$RMSE = \sqrt{\frac{1}{n}\sum_{t=1}^{n}(\beta_t^o - \beta_t^e)^2} \tag{9}$$

where n is the total number of estimated trends during the study period; β^e and β^o are estimated (e.g., by SA) and observed (e.g., by TG) trend values at time t (at different time windows), respectively.

Note that the OLS-determined linear trend has its limitations, such as sensitivity to outliers, yielding extreme values and outliers which can skew the regression line and influence the estimated trend. Also, OLS assumes a linear relationship between the variables, which might not always represent the true nature of the sea level, especially over too-short periods. Hence, in this study, various non-linear methods, including the enveloping method [58] and sliding trend analysis [59,60] were additionally tested. These alternative approaches provided similar trend estimates to the OLS results. Therefore, for the sake of the conciseness of this paper, only the OLS-based linear trend estimation results will be explained and discussed. Figure 2 shows the flowchart of the applied methodology and data processing steps.
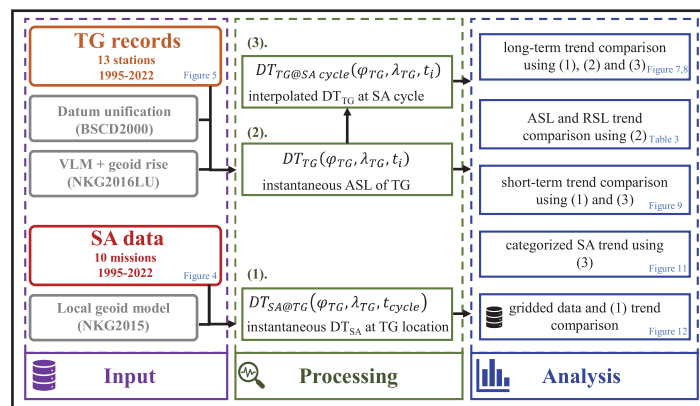

Figure 2. Flowchart of the applied method.

3. Study Area

The Baltic Sea is a semi-enclosed microtidal sea with geographical limits of 53°N–66°N and 10°E–30°E and roughly a 54 m mean depth, with a 393,000 km^2 total surface area. The sea is linked to the open ocean solely through narrow Danish Straits [61] (cf. Section 4.2). The sea-level dynamics of the Baltic Sea are affected by several meteorological and oceano-graphical components, including the variation in temperature, salinity, precipitation, and evaporation (in a decadal time frame), as well as extreme sea levels (in a short-time frame) as a result of storm surges due to the interaction of strong winds, waves, and pressure [62]. It features a dual stratification, marked by a seasonal thermocline in the summer and a persistent, robust halocline throughout the year. The halocline, at approximately 60–80 m, divides the brackish surface water with a salinity of about 7 psu from the deeper water, with 12 psu salinity. The surface salinities vary from 32 psu in the Kattegat to 1–2 psu in the northern parts [63]. Sequential (year to year) annual average sea-level variations in this region could exceed ±8 cm, whereas the maximum difference within the entire study period (1995–2022) could reach 25 cm, as presented in Figure A1. This large annual mean variation in sea level is challenging for short-term (decadal) sea-level trend estimations. The ASL of the Baltic Sea is also influenced by (i) expansion in the world ocean sea level (due to thermal seawater expansion and the melting of glaciers), which also propagates into the semi-enclosed Baltic Sea; (ii) low salinity, which causes an additional steric component, elevating the ASL specifically in the innermost parts of the sea, where the lowest densities occur; and (iii) local atmospheric forces, including wind and air pressure [33].

Over the past 50 years, previous studies have noted that the Baltic ASL increase is larger than the GMSL [63,64]. Also, the ongoing viscoelastic response of the Earth to the last deglaciation contributes to the sea-level variation in the Baltic Sea together with other effects such as North Atlantic and GMSL changes, wind, and waves affecting erosion and sediment transport [64]. Also, the spatial variations in the Baltic Sea level rates are mainly due to the (i) occasions of massive water entrance from the North Sea, (ii) intensified westerly winds, (iii) the poleward shift of low-pressure systems, and (iv) other minor contributions derived from local changes in baroclinicity, causing a basin-internal redistribution of water [64].

The changes in sea-level extremes depend on many variables, including storm surges [65], coastal upwellings [66], and wave-breaking processes [67], which can cause a devastating impact on small islands and their inhabitants. Hence, the cumulative effect of sea-level rises could lead to serious consequences over the Baltic Sea regions, where numerous archipelagos and small islands exist. Recent studies exploring future climate scenarios show an anticipated rise (around 6 mm/yr) in Baltic Sea levels (e.g., [29,30]). In contrast to the current study, many of these research works utilize gridded SA data or SLA for determining sea-level trends.

4. Datasets

This study determines RSL and ASL trends by using both TG (13 stations) and SA (10 missions) time series over the Baltic Sea for the period of 1995–2022. The beginning of the time series, 1995, considers the availability of reliable SA datasets.

4.1. Satellite Altimetry

In this study, ten available SA missions' data (Figure 3), including European Remote-Sensing Satellite-2 (ERS2), Envisat (ENV), Jason-1 (JA1), Jason-2 (JA2), Cryosat-2 (CS2), SARAL/AltiKa (SRL), Sentinel-3A (S3A), Jason-3 (JA3), Sentinel-3B (S3B), and Sentinel-6A Michael Freilich Jason-CS (S6A), are examined to determine the instantaneous DT_{SA}. These SA missions have different temporal coverage and resolution; see Figure 3 and Table 1. The highest-frequency SA data were used, i.e., distributed at a 20 Hz rate for most of the missions, except for 40 Hz for SARAL, and 18 Hz for Envisat.
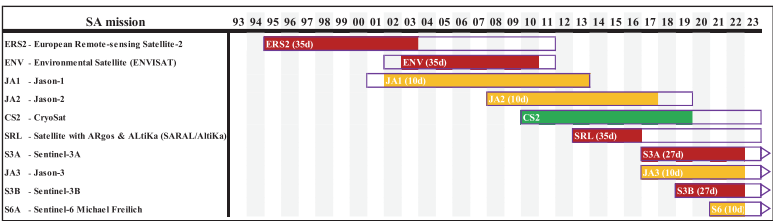
Figure 3. Available satellite altimeter missions are used in this study. The coloured (corresponding to the orbit inclination; ~66°: yellow, ~98°: red, ~92°: green) portion of bars demonstrate the duration (arrow for the presently ongoing missions) of the SA missions. The SA revisit cycles in days (d) are also indicated for each mission in the brackets.

Table 1. Characteristics of the used SA missions (ordered by their launch dates) and related data spans.

ID	SA	Altitude [km]	Inclination [°]	Cycle [Days]	Data Frequency [Hz]	Data Period (Baltic + SEAL)		Data Period (Standard Data)	
1	ERS2	785	98.5	35	20	16 May 1995	01 Jul 2003	-	-
2	ENV	800	98.5	35	18	18 Jun 2002	18 Oct 2010	-	-
3	JA1	1324	66	10	20	15 Jan 2002	20 Jun 2013	-	-
4	JA2	1324	66	10	20	12 Jul 2008	17 May 2017	-	-
5	CS2	717	92	w/o exact revisit cycle	20	19 Jul 2010	04 May 2019	-	-
6	SRL	800	98.5	35	40	14 Mar 2013	04 Jul 2016	-	-
7	S3A	814	98.6	27	20	04 Jan 2017	13 Jun 2019	13 Jun 2019	31 Dec 2022
8	JA3	1336	66	10	20	17 Feb 2016	31 May 2019	31 May 2019	31 Dec 2022
9	S3B	814	98.6	27	20	01 Nov 2018	19 May 2019	19 May 2019	31 Dec 2022
10	S6A	1336	66	10	20	-	-	1 Apr 2022	31 Dec 2022

Compared to the open ocean, the SA data quality is degraded near the shoreline due to land contamination, seasonal sea ice conditions, and, possibly, erroneous corrections (e.g., wet tropospheric correction). Therefore, from the trend estimates of this study, the SA data points closer than 5 km to the shoreline were removed. Also, an iterative data screening approach [33] was applied to remove the outliers from the remaining SA data. Firstly, the gross errors ($|DT_{SA@TG}| > 1.5$ m) were removed from the SA datasets, followed by using median absolute deviation (MAD) for outlier detection. Figure 4 demonstrates the spatial distribution of the selected TG stations, which are mostly around the open parts of the sea (Baltic Proper) where more SA tracks can be acquired at these locations and has the smallest effect on ice coverage is apparent during the winter seasons (cf. [33]). High-quality SA along-track data were extracted up to 50 km from each TG station (see Figure 4). Equation (5) was then applied to obtain the averaged SA-derived DT estimates, whereas the number of SA data (*m*) varied from 1 to 326. In Figure 4, the selection of SA data at the location of the TG stations near the coast is illustrated, where the data points within 5–50 km from the shoreline of each SA mission are represented by different colours.
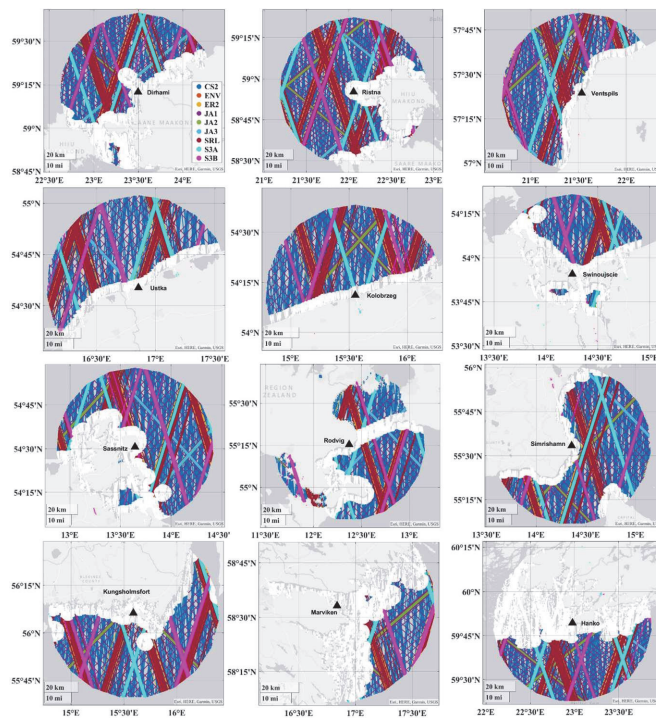
Figure 4. Spatial distribution of SA data at locations of selected TG stations within the 50 km radius. The white points represent the removed SA data within 5 km distance from the coastline.

The European Space Agency's Baltic + Sea Level (ESA Baltic + SEAL) Project dataset is an enhanced sea-level product that is specifically developed for the Baltic Sea [68]. However, this dataset contains the data only up to 2019; hence, in the present study, the "standard" EUMETSAT data were used to extend the trend estimation period from 2019 up to 31 December 2022. The Baltic + SEAL retracked data are available on request from http://balticseal.eu/outputs (accessed on 23 March 2021), whereas the standard data originated from the European Organization for the Exploitation of Meteorological Satellites (EUMETSAT), which can be downloaded from the EUMETSAT Earth Observation Portal at https://eoportal.eumetsat.int/ (accessed in 23 March 2023). The consistency of sea-level data from these two sources during the tandem phase of both datasets has been examined prior to our study. It should be noted that the former dataset includes a homogeneous estimate of multi-mission ASL, which has shown better results (as compared to the TG observations), rather than standard products [33]. Also, the necessary corrections (denoted by ΔR) applied to all SA data consistently:

$$\Delta R = (\text{wet tropospheric} + \text{dry tropospheric} + \text{ionospheric} + \text{sea state bias} + \text{solid Earth tide} + \text{pole tide} + \text{radial orbit error} + \text{inverse barometric height} + \text{DAC}) - \text{DAC} \tag{10}$$

Note that the dynamic atmospheric correction (DAC) on the right-hand side of Equation (10) denotes the removal of the DAC from the used SA datasets. Also, the ocean tide corrections are not included in the instantaneous SA data, considering that the TG data were extracted at the exact time instants of SA cycles. This makes the SA-derived DT compatible with TG records, which inherently contain the atmospheric pressure and the Baltic micro-tide contribution to the sea level. To achieve a consistent SA dataset, all the corrections were processed and applied uniformly, even though certain corrections may use different models (e.g., the wet tropospheric correction model varies depending on the

Baltic + SEAL mission data). It was determined that the impact due to differences between these models is negligible for the SA-derived trend estimation.

The quality of SA data over the Baltic Sea is affected by two main features that limit the use of SA [33]: (i) the presence of sea ice and the proximity of the coast. For example, the northern part of the sea (62.1°N–65.8°N) is covered 110–190 days of the year by sea ice during the winter–spring seasons [69]. (ii) Also, the Baltic Sea contains the largest archipelagos in the world, with 30,500 islands and a 23 m average water depth only near Finnish coast [70]. Hence, this study focuses on the study area region (around the Baltic Proper), where these undesirable effects have the minimum impact on the SA sea-level trend estimates. The SA data need to account for other adjustments, including the permanent tide system [71] and the terrestrial reference frame unification. The ITRF transformation was carried out using the method explained by [72] in which the SA terrestrial reference frame is transferred from $ITRF_{2008}$ or $ITRF_{2014}$ to $ETRF_{YYYY}$, which is an ETRF realization of the year "YYYY" (e.g., 1995) related to the time epoch (YYYY) of the observations [33]. This includes marginal intra-plate velocity deformations and the transformation between ITRF and ETRF.

4.2. Tide Gauge Data

TG records provide an exclusive and comprehensive knowledge of sea-level changes and variations. However, they are land-bound, which means that the TG data reflect the RSL. Thus, to obtain the ASL, they need to correct for the VLM effect. In this study, the TG-derived ASL is compared with the SA-derived ASL trend estimates. The Baltic Sea has one of the world's densest observational tide gauge networks with remarkably long-term and high-quality local sea-level records [73]. Within the study area, 13 TG stations were selected that match the time span (1995–2022) of available SA data. Most TG stations provide hourly data for the entire study period, whereas a couple of used stations had only a few daily readings within the first decade of the study period. Some of the TG stations have longer data gaps due to the malfunctioning or change of the sensors; for more details, see Tables 2 and A1 and Figure 5b.

Table 2. Overview of the used TG data for the study period from 1 January 1995 to 31 December 2022. Significant (>18%) data gaps are highlighted in bold font.

ID	Station	Latitude [°]	Longitude [°]	Country	VLM [mm/yr]	ΔN [mm/yr]	No. Hourly Data (i)	Missing Hourly Data [%]
1	Dirhami	59.21	23.50	Estonia	3.09	0.4	117,833	**51.99** [1]
2	Ristna	58.92	22.06	Estonia	3.46	0.4	244,427	0.42
3	Ventspils	57.40	21.53	Latvia	1.56	0.3	200,199	**18.41**
4	Ustka	54.59	16.85	Poland	0.13	0.1	175,622	**28.45**
5	Kolobrzeg	54.19	15.55	Poland	−0.06	0.1	170,399	**30.58**
6	Swinoujscie	53.91	14.25	Poland	−0.18	0.1	175,157	**28.64**
7	Sassnitz	54.51	13.64	Germany	0.09	0.1	237,694	2.58
8	Rodvig	55.25	12.37	Denmark	0.62	0.2	226,479	**7.73**
9	Simrishamn	55.56	14.36	Sweden	0.89	0.2	234,745	0.00
10	Kungsholmsfort	56.11	15.59	Sweden	1.36	0.2	245,439	0.00
11	Marviken/Arkö [2]	58.55	16.84	Sweden [3]	4.46	0.4	245,448	0.00
12	Hanko	59.82	22.98	Finland	4.16	0.4	245,448	0.00
13	Pori	61.59	21.46	Finland	7.44	0.7	244,728	0.29

[1] Dirhami TG station includes visually recorded historical data twice a day up to 2010; consequently, the overall number of missing hourly data is the highest for this TG station. Hence, up to 2010, the maximum time span between the TG reading and the SA flyover instant could reach up to 6 h. From 2011 onward, the hourly observations from a pressure sensor are available. [2] The tide gauge Marviken was operational up to 10 January 2019; hence, another station close (~10 km) to this TG is used for the remaining time period: Arkö station, with a latitude of 58.4843° and a longitude of 16.9607°. [3] All Swedish stations have manual data recording up to 2004, cf. Table A1.

The selected TG stations are operated by the national tide gauge authorities. The TG readings refer to the corresponding national realization of the EVRS2000 (European Vertical Reference System 2000) vertical datum (e.g., [74]), the zero level of which is the Normaal Amsterdams Peil (NAP). In addition, the TG zero level was transformed into the mean permanent tide system. The locations of TG stations are shown in Figure 5, where the VLM effect is illustrated in the background and the geoid rise (ΔN) is also shown with red isolines; for more details, see Section 4.4.
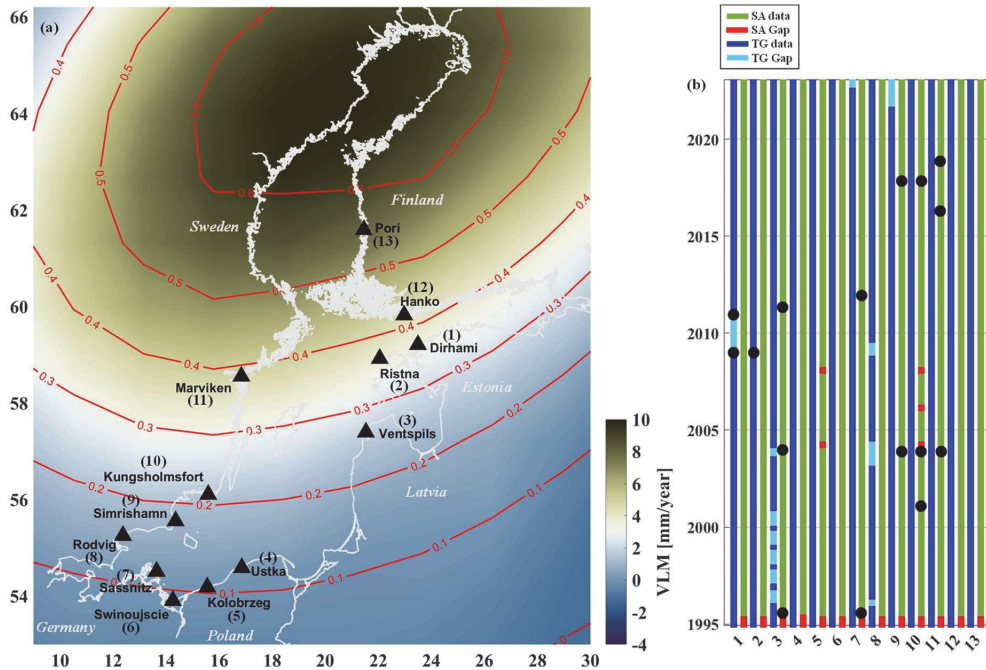
Figure 5. TG stations used in this study: (**a**) VLM rate [mm/year] over the Baltic Sea region according to the NKG2016LU model [75]. The geoid changes (rise over the Baltic Sea) [mm/yr] are also shown with red isolines. The numbered triangles denote the location of TG stations used in this study. (**b**) TG (blue) and SA (green) monthly data availability during the study period at each TG station (TG monthly averaged data are used for illustration). Gaps of data are illustrated in different colours (TG data gaps in light blue and SA data gaps in red). The black dots represent the TG sensor installation events (full details in Table A1).

All the available TG hourly data were used for the ASL and RSL trend estimates as the ground truth. Note that the SA-derived $DT_{SA@TG}\left(\varphi_{TG}, \lambda_{TG}, t_{cycle}\right)$ is also compared with $DT_{TG@SA\ cycle}$ in order to examine whether the SA data random and diverse temporal sampling is sufficient for deriving the SA-based ASL trend estimates. Therefore, to obtain $DT_{TG@SA\ cycle}$ using Equation (2), the DT_{TG} readings only within 2 h before and after the t_{cycle} time window (resulting in a total duration of 5 h for w) are included in the temporal interpolation (TG records beyond this specified time window are excluded). Consequently, if there is a gap in the TG record within the time window, w, the resulting $DT_{TG@SA\ cycle}$ remain as a NaN value. In other words, in $DT_{TG@SA\ cycle}$- and $DT_{SA@TG}$-based sea-level trend estimates, different DT values may participate; such discrepancies are addressed later, in Section 5.3.2. It is important to note that there might be a gap in the TG precisely at t_{cycle}. However, employing $DT_{TG@SA\ cycle}$ allows us to effectively represent the DT derived from TG, considering the relatively low fluctuations in DT within the w time frame.

Note that, during the study period, four TG stations had significant data gaps (cf. Table 2) which may negatively affect the TG-derived sea-level trend estimates. For instance, for the Dirhami (#1) station, sea-level data were visually captured twice a day up to end of 2009; for the entire year 2010, there were no data record at all, whereas the hourly TG data records started from 2011. The monthly averaged TG data enable the detection of longer data gaps in the TG and SA time series; see Figure 5b, which may be different from the instantaneous data gap (mentioned in Table 1). In this study, the longest data gap (Dirhami) reaches up to one year.

4.3. Geoid Model

The regional NKG2015 quasi-geoid model [76] was used to retrieve DT_{SA} from SA-derived SSH data, as explained in Section 2. It is referred to as the Geodetic Reference System 1980 (GRS80) ellipsoid and covers the area from 53° to 73°N and from 0° to 34°E, with a grid spacing of 0.01° × 0.02°. NKG2015 has a good agreement with GNSS/levelling control points, with a standard deviation (STD) of 3.0 cm [76]. Various studies have estimated the NKG2015 geoid error that could reach up to 15 cm over certain marine areas. Such deficient geoid modelling areas were associated with the poor coverage of marine gravity data. Contrastingly, the global geoid models that are customarily used by the satellite altimetry community are less accurate and with a poorer spatial resolution (typically 0.1° × 0.1°, e.g., EGM2008). It should be noted that the geoid model deficiencies do not affect the trend estimation studies; however, a precise geoid is needed for the examination of oceanographic processes (e.g., [50,51]). Although, the geoid model may also be constrained by some problematic areas, which were investigated by [33,51]. These areas are avoided in this study.

4.4. Vertical Land Motion and Geoid Rise Models

In order to obtain the ASL trend values from the TG-derived RSL, the VLM needs to be considered. VLM may occur due to glacial isostatic adjustment (GIA), tectonic motion, and anthropogenic effects. Over the Baltic Sea region, VLM is dominated by GIA, caused by ice shield melting after the last deglaciation over the Fennoscandia. Slow crustal recovery from the pressure of the ice sheet that covered the area during the last glacial period causes post-glacial land uplift up to around 10 mm/yr in the north part of the sea (centre of the former ice sheet) and decreases to nearly zero at the edges of the former ice sheet (south). The southern part of the Baltic Sea therefore experiences a land subsidence as a compensating effect. This causes the RSL to increase in the north and decrease in the south part of the Baltic Sea, as can be seen from TG records (cf. Figures 5 and 6). In recent decades, an acceleration has been seen in the long-term sea-level trends since the 1960s [77], consistent with the global signal [2]. On the other hand, SA and GPS (Global Positioning System) provide independent measurements of sea-level change and VLM, with respect to a global geocentric coordinate system. To assess the separate effects of sea-level change and land uplift, accurate information on land uplift is essential in the Baltic Sea region, as the VLM value varies throughout the region. In this study, the land uplift effect is removed from TG observations using the NKG2016LU model to convert the TG readings (DT_{obs}) to the actual DT (DT_{TG}), i.e., relative to the Earth's centre of mass. This model includes the latest GIA land uplift model for the Baltic Sea region, developed by the Nordic Commission of Geodesy (NKG, www.nordicgeodeticcommission.com (accessed on 26 August 2021), and it covers an area from 49° to 75°N and 0° to 50°E [75]. The VLM correction reference time epoch (i.e., $t_0 = 2000.0$) is applied to the TG observation time record (i.e., t_i) by adding it to the TG readings using Equation (1). Also, the geoid change (ΔN) is primarily due to GIA, which causes a rise in the geoid in the Baltic Sea (cf. Figure 4). The ΔN rate is approximately 10–15% of the VLM rate in the Baltic Sea [34]. Figure 6 shows annual DT variations of TG observations (hourly data) before (black) and after (blue) VLM correction for six selected TG stations.
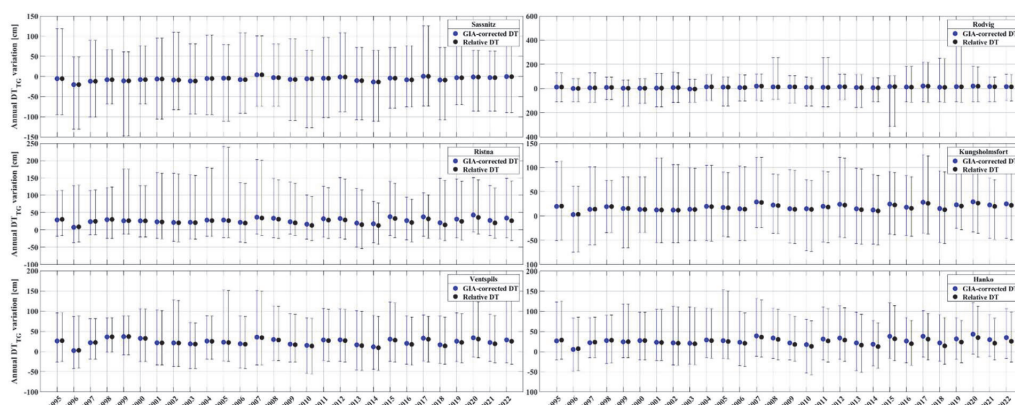
Figure 6. Annual DT variation of TG observations (hourly data) before (black, RSL) and after (blue, ASL) application of the VLM correction for six selected TG stations during 1995–2022. The bars represent the sea-level variations (minimum and maximum) in each year. The dots represent the DT annual average.

In this study, both RSL and ASL are considered for trend estimation, as illustrated in Figure 6 (RSL in black and ASL in blue dots) to illustrate the VLM effect. This figure shows the annual DT variation of six selected TGs (one for each country), for example, before (black) and after GIA correction (blue). Accordingly, a significant deviation of ASL and RSL can be observed over intense land uplift areas (e.g., the Pori and Hanko stations), as was expected. The dots show the average DT of each year, and the bars represent the maximum and minimum DTs, whereas the STD of the annual MDT value varies within 5 to 8 cm. Additionally, the annual fluctuation in MDT, calculated as the difference between the maximum and minimum MDT values for each year, ranges from 20 to 30 cm during the period from 1995 to 2022 across all stations. These significant fluctuations in annual MDT could result in a notably high degree of variability in estimated sea-level trends, particularly when using short-term time-series data. Also, Figure A2 represents the median values and the 25th and 75th percentiles of the annual DT variations for six stations (the same as in Figure 6).

4.5. Model Data

To validate our ASL trend estimation method, we conduct an additional examination using standard products that have been used in earlier studies. Hence, in addition to instantaneous along-track SA and TG data, three monthly gridded model data were employed to estimate the trends which are discussed in Section 5.4.3. These datasets are as follows:

1. Global SA gridded SLA (https://doi.org/10.48670/moi-00148 (accessed on 9 October 2023)) computed with respect to a twenty-year 1993–2012 mean from the Copernicus Marine Data Store (www.data.marine.copernicus.eu (accessed on 9 October 2023)): This SLA (denoted as global gridded SLA in Section 5.4.3) is estimated by Optimal Interpolation, merging the Level-3 along-track measurement from the different available SA data. This product is processed by the DUACS (Data Unification and Altimeter Combination System) multi-mission altimeter data processing system.
2. The Baltic Sea Physical Reanalysis product (https://doi.org/10.48670/moi-00013 (accessed on 15 May 2023), which provides a reanalysis of the physical conditions of the whole Baltic Sea area: The product (denoted by Baltic Sea Nemo, gridded in Section 5.4.3) is produced by using the ice–ocean model system Nemo. The data are available at the native model resolution (1-nautical-mile horizontal resolution, 56 vertical layers).

3. Baltic + SEAL gridded SA data over the Baltic Sea region: This product provides SSH after the multi-mission cross-calibration and outlier detection [29]. In this product, the SA observations are interpolated on an unstructured triangular grid (i.e., geodesic polyhedron) with a spatial resolution of 6–7 km.

It is important to consider that these models may have challenges related to vertical data incoherency (e.g., [33,50,51]). However, it needs to be emphasized that despite potential discrepancies in the vertical data, these issues are not anticipated to significantly impact the outcomes of sea-level trend estimations.

5. Results

This section presents the estimated sea-level trends for locations within the Baltic Sea region. Given the variations in data sources and time spans considered, four main aspects are examined: (i) long-term (1995–2022) relative sea level (RSL) and absolute sea level (ASL) trends are calculated using only hourly TG data at each station (Section 5.1), (ii) a comparison of long-term ASL estimates by both TG and along-track SA (Section 5.2), (iii) a comparison of decadal ASL trend estimates by TG and SA (Section 5.3), (iv) and inter-comparisons of the estimated SA-based trend (Section 5.4), which includes an examination of ASL sea-level trend calculations using different distances from the coast (Section 5.4.1), an examination of ASL calculated using different SA missions (Section 5.4.2), and a comparison of ASL trend estimates using other available sea-level datasets (Section 5.4.3).

5.1. ASL and RSL Trends by Hourly TG Observations

The long-term (1995–2022, 28 years) RSL and ASL trends were calculated using hourly data of DT_{obs} and DT_{TG} (VLM-corrected) based on Equation (6) (Section 2). The achieved RSL and ASL rates and their uncertainty from TG observations for the period 1995 to 2022 are listed in Table 3 and Figure A3.

Table 3. TG hourly data based on RSL and ASL estimates, their formal OLS-based uncertainties, and mean dynamic topography (MDT) of hourly TG observation [cm] for each station (during 1995–2022).

ID	Station	MDT [cm]	ASL Trend [mm/yr]	RSL Trend [1] [mm/yr]	ASL–RSL Difference [mm/yr]
1	Dirhami	29.03	3.58 ± 0.024	0.49	3.09
2	Ristna	26.87	4.56 ± 0.012	1.11	3.45
3	Ventspils	23.73	2.12 ± 0.014	0.56	1.56
4	Ustka	18.46	2.36 ± 0.014	2.22	0.14
5	Kolobrzeg	18.10	2.06 ± 0.014	2.12	-0.06
6	Swinoujscie	15.29	2.66 ± 0.014	2.84	-0.18
7	Sassnitz	10.66	3.22 ± 0.010	3.13	0.09
8	Rodvig	10.55	5.13 ± 0.011	4.51	0.62
9	Simrishamn	17.60	3.55 ± 0.010	2.66	0.89
10	Kungsholmsfort	18.34	4.81 ± 0.009	3.45	1.36
11	Marviken	19.57	4.90 ± 0.009	0.44	4.46
12	Hanko	26.79	5.37 ± 0.011	1.21	4.16
13	Pori	28.67	5.41 ± 0.011	-2.02	7.43

[1] Note that the RSL trend uncertainties are the same as for the corresponding ASL.

In general, the RSL varies within the magnitude of -2 to 4.5 mm/yr, while the ASL rate spans from 2 to 5.4 mm/yr. Another notable characteristic is the spatial variance among the stations, mainly due to the VLM effect (cf. Figure A3 and Table 2). It is evident that the largest differences between RSL and ASL are observed at the northern stations, which tend to experience large VLM effects, for example, at stations Dirhami (0.49 vs. 3.58 mm/yr), Ristna (1.11 vs. 4.56 mm/yr), Marviken (0.44 vs. 4.9 mm/yr), Hanko (1.21 vs. 5.37 mm/yr), and Pori (-2.02 vs. 5.41 mm/yr). Note the opposite trend sign for the (northernmost) Pori TG station, where the land uplift exceeds the sea-level rise. Note that the differences between the ASL and RSL rates (cf. Table 3, last column) are almost equal to the VLM

at these locations (cf. Table 2, sixth column). This validates the reliability of our trend estimation methodology.

Previous studies have also observed a decreasing RSL trend toward the north, whereas the ASL trend increased toward the south [29,45,46,78]. Note that, in various studies, the trend estimates may differ due to the adoption of the time period examined, the source of measurement, the method of computation, and the exact locations of measurement. For instance, within the same region, [78] estimated an RSL within the approximate range of -8 to 1 mm/yr. In the study by [45], a similar range of RSL trends was calculated using a TG and hydrodynamic model (HDM) for the period 1915 to 2014. The ASL trends varied from 1 to 6 mm/yr, a range similar to what was observed by [29] using gridded monthly SA and TG data. These results indicate that, despite the differences in time frames and the sources of sea-level data (such as TG, HDM, SA), the long-term sea-level trends calculated across these studies generally align. These studies also verify the importance of accounting for the VLM in sea-level trend studies. This prompts the question as to whether any major difference truly occurs between utilizing TG and SA data sources for sea-level trend estimations, and whether computing sea-level trends over shorter periods, like decades, yields comparable values. These questions are examined in the following sections.

5.2. Long-Term ASL Trend

The long-term (1995 to 2022) ASL trend results using both SA and TG are illustrated in Figure 7. The ASL trends are calculated using (i) hourly TG observations (dark blue); (ii) TG-derived $DT_{TG@SA\ cycle}$ (light blue); and (iii) SA instantaneous data (red). The RMSE of the paired estimates for all stations are computed by Equation (10), where β^o is either $trend(DT_{TG})$ (Figure 7b) or $trend(DT_{TG@SA\ cycle})$ (Figure 7c), whereas $\beta^e = trend(DT_{SA})$.
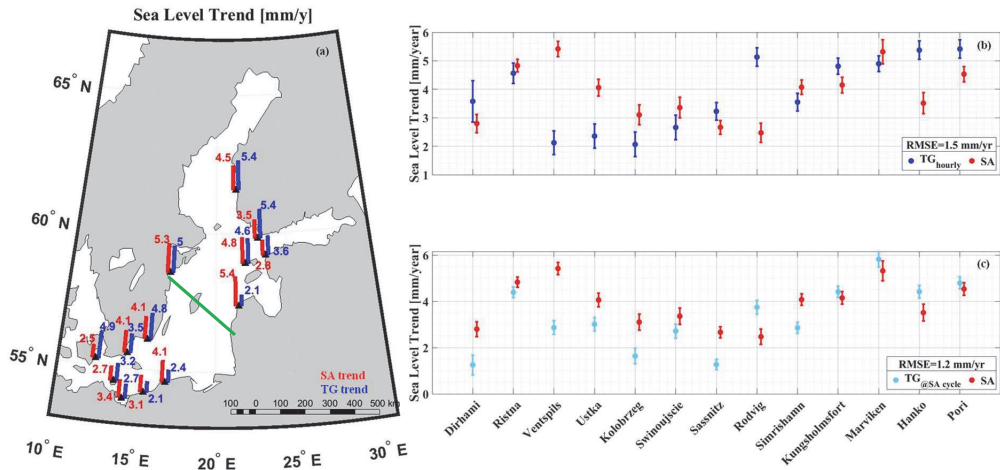
Figure 7. SA- and TG-derived ASL trend estimates for the period 1995 to 2022. (**a**) Spatial distribution of the SA (red)- and hourly TG (blue)-based trend estimates. (**b**) Estimated trends using both instantaneous SA (red) and TG hourly data at each station (dark blue) with the corresponding RMSE = 1.5 mm/yr, and (**c**) $DT_{TG@SA\ cycle}$-based trend (light blue) compared with instantaneous SA-derived trend (red), with the corresponding RMSE = 1.2 mm/yr. The whiskers in (**b**,**c**) represent the estimated trend uncertainties within the 95% confidence error of each dataset. The green line in (**a**) divides the study area into north-eastern and south-western sections.

The comparison of the TG and SA sea-level trends also reveals a spatial variability among the stations (Figures 7 and 8). In the north-eastern study area, certain stations (such as Pori, Hanko, Ristna, and Marviken) exhibit higher sea-level trend values (observed in both SA and TG) ranging around 4 to 5 mm/yr. Previous studies have also noted larger

ASL trends in the north-eastern Baltic Sea region (e.g., [29,45,46,63]). This was suggested to be attributed to fluctuations in air pressure [79,80] and intensified westerly winds that push the water masses toward the north-east [29,63]. Additionally, a poleward shift in low-air-pressure systems was observed, contributing to local sea-level increases via the inverted barometer effect. Moreover, an increased influx of freshwater from the northern Baltic Sea has been suggested as a factor leading to the rise in the mean sea level over the northern and western Baltic Sea sections [63]. However, within the south-western section, the trend values mostly varied between 2 and 4 mm/yr. Notably, stations Rodvig (#8) and Kungsholmsfort (#10) revealed large TG-derived trend values of nearly 5 mm/yr (Figure 7).
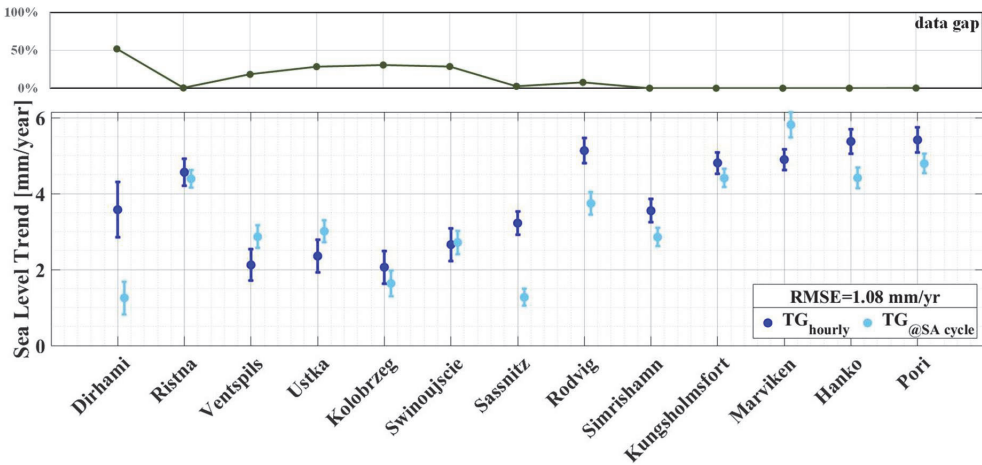
Figure 8. Sea-level trend estimates using hourly TG records (dark blue) and TG data at the time of SA cycles (light blue) for the period of 1995–2022 and the corresponding amount (%) of missing data in each station. The RMSE between the two estimated trends is 1.08 mm/yr. The whiskers represent the estimated trend uncertainties within 95% CI of each dataset. In general, the stations with missing data show larger discrepancies between the DT_{TG} and $DT_{TG@SA\ cycle}$-based trend estimates.

At most stations, the sea-level trends of $DT_{SA@TG}$ and DT_{TG} data (Figure 7b) vary from 2.1 to 5.4 mm/yr. A closer examination of individual stations in Figure 7b reveals that 9 stations (out of 13) agreed within ± 1 mm/yr. The most notable differences appear to occur at stations Ventspils (#3, with a difference of 3.3 mm/yr), Ustka (#4, difference of 1.7 mm/yr), Rodvig (#8, with a difference of 2.6 mm/yr), and Hanko (#12, with a difference of 1.9 mm/yr) (cf. Figure 7b). Similarly, the $DT_{SA@TG}$ and $DT_{TG@SA\ cycle}$ trends (Figure 7c) vary overall from 1.3 to 5.8 mm/yr. The differences in the $DT_{SA@TG}$ and $DT_{TG@SA\ cycle}$ trends in Figure 7c indicate that out of the 13 stations assessed, only the trends of six stations remain within a ± 1 mm/yr tolerance. Broadening the allowable differences to ± 1.5 mm/yr, however, revealed that 11 out of 13 stations are in agreement. The largest differences were determined at the TG stations Rodvig (#8) and Kolobrzeg (#5), with 2.5 mm/yr and 1.5 mm/yr, respectively.

Further examination suggests that large differences within the range of 1–1.5 mm/yr may indicate issues with the SA or TG data for these specific stations. For instance, trend estimates are potentially affected by extensive data gaps (cf. Table 2, Figure 8) in stations such as Dirhami (#1), Ventspils (#3), Ustka (#4), Kolobrzeg (#5), and Swinoujscie (#6). Moreover, upon examining individual stations, it became evident that the $DT_{SA@TG}$ and DT_{TG} pairs tended to yield more reliable results, showing agreement within a difference of ± 1 mm/yr. Figure 7a,b show that the $DT_{SA@TG}$ and $DT_{TG@SA\ cycle}$ pairs display slightly improved agreement, with an RMSE of 1.2 mm/yr, compared to that of the DT_{TG} and $DT_{SA@TG}$ pairs, which yield an RMSE of 1.5 mm/yr. Also, the overall average ASL trend of the 13 stations is 3.9 mm/yr using favourably hourly TG data, whereas utilizing instantaneous

(but time-wise irregular) SA data yields a trend estimate of 4.8 mm/y in the Baltic Sea. This experiment demonstrates that the temporal frequency of the instantaneous SA data could be sufficient for sea-level trend estimates, yielding an agreement of ± 1 mm/yr with the hourly TG data series (cf. Figure 8).

Figure 7b,c suggest that SA data stand out as a dependable method to accurately determine ASL trends in proximity to the coast, with an accuracy of 1 to 1.5 mm/yr. This is of particular significance given the challenges associated with obtaining precise sea-level estimates in these coastal areas, especially within the unique characteristics of the Baltic Sea [33]. Moreover, it highlights the constraints of TG data for estimating RSL trends, especially for stations with missing data. While, historically, TG data records have been extensively utilized for sea-level trend determinations, the presence of data gaps and outliers can lead to distorted trend estimates, particularly on a regional scale. Therefore, SA data emerge as a reliable resource for determining sea-level trends on a regional scale, particularly over such areas where the quality or presence of TG stations may be insufficient.

5.3. Decadal Regional ASL Trend

The decadal SA-derived ASL trend was examined and compared with TG for two distinct periods—1 January 2000 to 31 December 2009 and 1 January 2010 to 31 December 2019—using the OLS-estimated linear trend (Equations (6) and (7)). The outcomes are presented in Figure 9, employing various DT calculations such as instantaneous SA data ($DT_{SA@TG}$), hourly TG data (DT_{TG}), and TG data at the time of the SA cycle ($DT_{TG@SA\ cycle}$). While all three methods yielded slightly different results (as detailed in Section 5.3.2), several main characteristics remained consistent across all approaches. These are described below in terms of (i) a comparison with the long-term trends (1995–2022) and (ii) a comparison between the different decades.
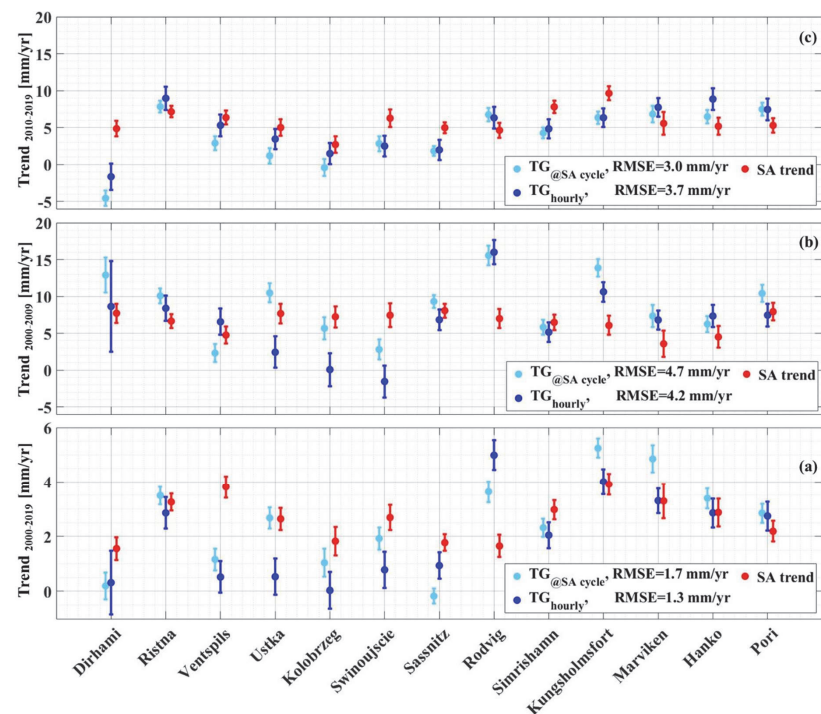
Figure 9. Decadal sea-level trend using hourly TG records (dark blue) and TG data at the time of SA cycles (light blue) and SA data (red) over (**a**) the period of 2000–2019, (**b**) the 2000–2009 decade,

and (**c**) the 2010–2019 decade. The RMSE is computed between two corresponding datasets. The deviation between the estimated trend values (especially during 2000–2009) is due to the data gaps. The whiskers represent uncertainties using 95% CI.

5.3.1. Comparison between Long-Term and Decadal Trends

By comparing the decadal (2000–2009 and 2010–2019) trends with the long-term trend, two major observations emerged: Firstly, both decades revealed a spatial variation in sea-level trend among the stations. The northern stations (stations #1, #2, #3, #11, and #13) exhibited higher rates compared to the southern (#4, #5, #6, and #7) and western stations (#8, #9, and #10) (Figure 9). A similar spatial trend pattern was also observed with the long-term trends (Figure 7). The increased rates in the northern stations were attributed to air pressure fluctuations and intensified westerly winds that push the water masses to the north-east [29,63]. Additionally, for both examined decadal periods, the trend rates notably exceeded the long-term trend rates. For instance, the SA-derived values ranged from 2.7 to 9.6 mm/yr for the decadal trend compared to 2.5 to 5.4 mm/yr for the long-term trend (Figures 7 and 8). This implies a substantial increase (almost doubled) for the decadal period trends in comparison to the long-term trend (1995–2022) at several stations (e.g., Dirhami (#1), Kolobrzeg (#5), Swinoujscie (#6)), and even almost tripled (e.g., Sassnitz (#7)). Also, for each decade, there was a variety of differences amongst the stations.

5.3.2. Decadal Trend from SA and TG

Certainly, while the decadal sea-level trends appear to be higher than the long-term values, a closer examination also reveals a wide variation in the calculated decadal trend values from the two sources of TG and SA data. For instance, the decadal trend rates derived from SA ($DT_{SA@TG}$) for both periods (2000–2009 and 2010–2019) ranged from 2.7 to 9.6 mm/yr. However, the TG-based trends, utilizing both $DT_{TG@SA \ cycle}$ and DT_{TG}, showed a broader range of −4.6 to 16 mm/yr. The TG data exhibited notably extreme higher and lower values, notably evident at specific stations. For instance, the Dirhami (#1) station displayed an ASL rate of 12.9 mm/yr for 2000–2009 and −1.7 mm/yr for 2010–2019. During 2000–2009, Swinoujscie (#6) and Rodvig (#8) showed an ASL rate of −1.5 mm/yr and 16 mm/yr, respectively. Similarly, Kungsholmsfort (#10) indicated an ASL rate of 10.6 mm/yr during 2000–2009, whereas Kolobrzeg (#5) showed an ASL of −0.4 mm/yr during 2010–2019. Notably, a majority of these extreme TG-based trend values were observed during the decade 2000–2009, suggesting potential issues with the reliability of the TG data.

Investigating the TG data for the period 2000–2009 (detailed in Table 4) revealed notable data gaps at specific TG stations. Particularly, some of them were limited to sea-level readings only twice a day (cf. Table A1). For instance, Dirhami (#1) experienced a missing data rate of 61%, Ventspils (#3) 6%, Kolobrzeg (#5) 9%, and Rodvig (#8) 20%. These gaps potentially influenced the calculated trend estimates at these TG stations. Insufficient data availability at these stations potentially impacted the comprehensive assessment of sea-level trends for the respective periods under study. However, stations Swinoujscie (#6, ASL rate of −1.5 mm/yr during 2000–2009) and Kungsholmsfort (#10, ASL rate of 10.6 mm/yr during 2000–2009) displayed extreme sea-level trends during 2000–2009, yet major TG data gaps were not identified at these stations. This suggests that other underlying issues might be affecting the data quality at these specific stations.

TG data have traditionally served as a common method to calculate sea-level trend estimates. However, their reliability can become questionable due to inherent issues, like data gaps, often stemming from resolution limitations and missing data. As can be seen from the results mentioned above, there seems to be a correlation between TG data gaps and the resulting calculated trends. The outcomes of Table 5 indicate that despite SA data potentially representing only a single value at a specific time of the month (depending on the SA cycle), they are still able to capture a realistic trend comparable to the TG data. For instance, during the period of 2000–2009, the average ASL rate ranged around 2.7 mm/yr

for TG data and 3.9 mm/yr for SA data. Similarly, for the period of 2010–2019, these rates were 8.1 and 7.6 mm/yr, respectively. As highlighted in Section 5.2, there appears to be an approximately 1 to 1.5 mm/yr difference between the source and method utilized for calculating sea-level results.

Table 4. Number of SA and TG datasets at the time of SA cycle ($DT_{TG@SA\ cycle}$) at each TG station during different time periods. Diff = the difference between them; the missing data percentage is in brackets.

ID	1995–2022			January 2000–December 2009			January 2010–December 2019			January 2000–December 2019		
	SA	TG	Diff (%)	SA	TG	Diff (%)	SA	TG	Diff (%)	SA	TG	Diff (%)
1	2954	2094	860 (29%)	962	373	589 (61%)	1498	1391	107 (7%)	2460	1764	696 (28%)
2	3600	3578	22 (1%)	1286	1283	3 (0%)	1721	1705	16 (1%)	3007	2988	19 (1%)
3	3229	3010	219 (7%)	1059	996	63 (6%)	1572	1566	6 (0%)	2631	2562	69 (3%)
4	2781	2780	1 (0%)	956	956	0 (0%)	1390	1389	1 (0%)	2346	2345	1 (0%)
5	1843	1786	57 (3%)	482	438	44 (9%)	987	974	13 (1%)	1469	1412	57 (4%)
6	2854	2853	1 (0%)	1004	1004	0 (0%)	1505	1505	0 (0%)	2509	2509	0 (0%)
7	3211	3141	70 (2%)	1129	1129	0 (0%)	1633	1622	11 (1%)	2762	2751	11 (0%)
8	3272	2995	277 (8%)	1206	960	246 (20%)	1598	1583	15 (1%)	2804	2543	261 (9%)
9	2806	2714	92 (3%)	989	989	0 (0%)	1319	1319	0 (0%)	2308	2308	0 (0%)
10	2582	2581	1 (0%)	653	653	0 (0%)	1401	1401	0 (0%)	2054	2054	0 (0%)
11	2812	2811	1 (0%)	873	873	0 (0%)	1542	1542	0 (0%)	2415	2415	0 (0%)
12	3717	3716	1 (0%)	1349	1349	0 (0%)	1857	1857	0 (0%)	3206	3206	0 (0%)
13	3225	3206	19 (1%)	1118	1118	0 (0%)	1628	1615	13 (1%)	2746	2733	13 (0%)

Table 5. The estimated ASL trend from SA data ($DT_{SA@TG}$), hourly TG data (DT_{TG}), and TG data at the time of SA cycle ($DT_{TG@SA\ cycle}$) over different decades and during the whole study period. Units: mm/yr.

ID	$DT_{SA@TG}$		DT_{TG}		$DT_{TG@SAcycle}$		$DT_{SA@TG}$	DT_{TG}	$DT_{TG@SAcycle}$
	January 2000–December 2009	January 2010–December 2019	January 2000–December 2009	January 2010–December 2019	January 2000–December 2009	January 2010–December 2019	1995–2022	1995–2022	1995–2022
1	7.7 ± 0.04	4.9 ± 0.04	8.6 ± 0.20	−1.7 ± 0.06	12.9 ± 0.08	−4.6 ± 0.03	2.8 ± 0.01	3.6 ± 0.02	1.3 ± 0.01
2	6.7 ± 0.03	7.1 ± 0.03	8.4 ± 0.06	9.0 ± 0.05	10.1 ± 0.03	7.8 ± 0.03	4.8 ± 0.01	4.6 ± 0.01	4.4 ± 0.01
3	4.8 ± 0.04	6.4 ± 0.03	6.6 ± 0.06	5.3 ± 0.05	2.3 ± 0.04	2.9 ± 0.03	5.4 ± 0.01	2.1 ± 0.01	2.9 ± 0.01
4	7.7 ± 0.04	5.0 ± 0.04	2.4 ± 0.07	3.4 ± 0.05	10.5 ± 0.04	1.2 ± 0.04	4.1 ± 0.01	2.4 ± 0.01	3.0 ± 0.01
5	7.2 ± 0.05	2.7 ± 0.04	0.1 ± 0.07	1.5 ± 0.05	5.7 ± 0.05	−0.4 ± 0.04	3.1 ± 0.01	2.1 ± 0.01	1.6 ± 0.01
6	7.4 ± 0.05	6.3 ± 0.04	−1.5 ± 0.07	2.5 ± 0.05	2.8 ± 0.05	2.8 ± 0.03	3.4 ± 0.01	2.7 ± 0.01	2.7 ± 0.01
7	8.1 ± 0.03	5.0 ± 0.02	6.8 ± 0.05	2.0 ± 0.05	9.3 ± 0.03	1.8 ± 0.02	2.7 ± 0.01	3.2 ± 0.01	1.3 ± 0.01
8	7.0 ± 0.04	4.6 ± 0.03	16.0 ± 0.05	6.3 ± 0.05	15.6 ± 0.04	6.7 ± 0.03	2.5 ± 0.01	5.1 ± 0.01	3.7 ± 0.01
9	6.5 ± 0.04	7.8 ± 0.03	5.1 ± 0.04	4.8 ± 0.04	5.8 ± 0.03	4.3 ± 0.03	4.1 ± 0.01	3.5 ± 0.01	2.9 ± 0.01
10	6.1 ± 0.04	9.6 ± 0.03	10.6 ± 0.04	6.3 ± 0.04	13.9 ± 0.04	6.4 ± 0.03	4.1 ± 0.01	4.8 ± 0.01	4.4 ± 0.01
11	3.6 ± 0.06	5.6 ± 0.05	6.8 ± 0.04	7.7 ± 0.04	7.3 ± 0.05	6.8 ± 0.04	5.3 ± 0.01	4.9 ± 0.01	5.8 ± 0.01
12	4.5 ± 0.05	5.2 ± 0.04	7.3 ± 0.05	8.9 ± 0.05	6.2 ± 0.04	6.5 ± 0.03	3.5 ± 0.01	5.4 ± 0.01	4.4 ± 0.01
13	7.9 ± 0.04	5.3 ± 0.03	7.5 ± 0.05	7.5 ± 0.05	10.4 ± 0.04	7.5 ± 0.03	4.5 ± 0.01	5.4 ± 0.01	4.8 ± 0.01
				Mean			3.87	3.83	3.23

Another major observation, confirmed by both TG and SA, is that seven out of the thirteen examined stations showed a difference in their decadal trends (2000–2009 vs. 2010–2019) exceeding 1 mm/yr. Specifically, higher values were indicated during the 2000–2009 period at Dirhami (#1), Ustka, (#4), Kolobrzeg (#5), Sassnitz (#7), Rodvig (#8), Kungsholmsfort (#10), and Pori (#13). These stations are dispersed across the Baltic Proper, and there is no obvious geographic correlation. The RMSE value was also found to be larger for 2000–2009, ranging from 4.2 to 4.7 mm/yr, while for 2010–2019, the RMSE was 3.0 to 3.7 mm/yr (Figure 9). This discrepancy might indicate some phenomena or problems during this decade that may have impacted these stations. Furthermore, there were stations where

the sea-level trend experienced a large change between the decades (i.e., <1 mm/yr). This occurred in five out of the thirteen stations. These stations were at Ristna (#2), Ventspils (#3), Swinoujscie (#6), Simrishamn (#9), and Hanko (#12).

It is important to note that during the period 2000–2009, stations Dirhami (#1), Ventspils (#3), Ustka (#4), Kolobrzeg (#5), and Swinoujscie (#6) experienced the most significant data gaps, totalling 945 h of missing data for all stations during this period, compared to the period 2010–2019, which had a total of 182 h of missing data. However, it is notable that other stations with minimal data gaps (i.e., <10%) also exhibited higher decadal rates for 2000–2009, such as Sassnitz (#7), Rodvig (#8), Kungsholmsfort (#10), and Pori (#13). This suggests that while data gaps might have influenced the results of 2000–2009, they might not be the only reason for potential phenomena or issues affecting these stations during that decade. Further examination is needed to better understand these patterns.

5.4. Inter-Comparisons of SA-Based ASL Trends

5.4.1. SA Data Optimality Regarding the Distance to TG

The utilization of along-track SA data provides an opportunity to investigate how sea-level trend estimates change regarding the distance from the coastline. Figure 10 and Table 6 present the SA-derived sea-level trend results, which range from 5 to 50 km away from the coast. In Figure 10, the data within each distance range are averaged, such as averaging the SA data from 5 to 20 km away from the TG station to determine the SA sea-level trend within that distance. Additionally, the TG-derived trend is depicted for comparison, providing insight into the expected sea level at the coast. This comparison aims to illustrate the variability in sea-level trends away from the TG station and potentially explore scenarios where the TG might not consistently offer the optimal location for determining precise sea-level trend estimates, depending on the specific purpose.

Figure 10 illustrates the variability in sea level among stations and distances, highlighting that the dynamics observed at a TG station may not consistently represent the broader coastal area. For instance, at stations like Dirhami (#1) and Pori (#13), the TG trends are higher compared to the SA measurements, whereas at stations like Kolobrzeg (#5), they are lower. These variations may be attributed to persistent marine dynamics influencing coastal areas, such as surface waves causing wave set-up and set-down [81]. However, further investigation is required to fully understand and address these discrepancies in future studies. Meanwhile, Table 6 presents station-specific statistics, revealing only slight variations in RMSE across different distances (ranging from 1.47 to 1.63). Consequently, almost any distance within 50 km appears to be suitable. Notably, the largest RMSEs of 1.63 and 1.53 mm/yr are observed within the 10–15 km ranges from the coast. This discrepancy could be attributed to the specific coastal processes occurring within this distance range.

5.4.2. Sea-Level Trends of Different SA Orbit Inclination Categories

As mentioned earlier, the sea-level trend can be estimated by merging multi-mission SA data over different time frames. However, some studies have shown that various SA missions could lead to different data quality depending on their constellation across different regions, which could also affect the subsequent trend estimation. For instance, over sub-arctic areas, low-inclination SA mission orbits (e.g., the Jason series) are able to provide better data than high-inclination orbit missions (e.g., Envisat, Sentinel series, etc.) that align more closely with ground-truth observations [33], although the high-inclination SA missions have better coverage and larger quantities of data [82]. Therefore, in this study, the SA missions were divided into two distinct groups based on their constellation: high-inclination (SA1) and low-inclination (SA2) orbit satellites (cf. Figure 3). This division aimed to investigate whether these distinctions could impact the SA-derived sea-level trend. The sea-level trend of each orbit category was estimated for the period of 2003–2022 (when the overlapped satellite mission data existed) and compared with the ground truth, the hourly TG-derived trend for the same time period (number of measurements is not normalized). These results are illustrated in Figure 11.
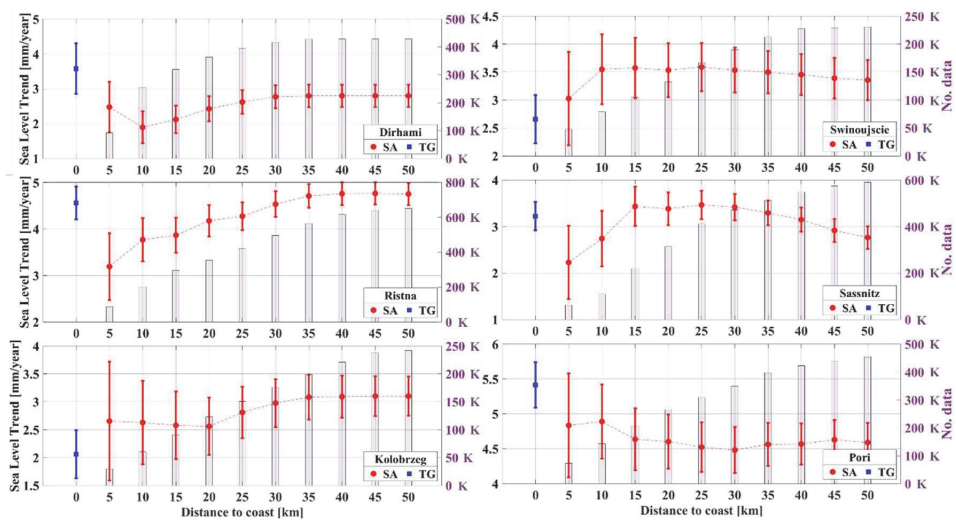
Figure 10. SA-derived sea-level trend (red) moving away from the coast compared to the TG trend (blue) at six stations. The whiskers represent the uncertainties using 95% CI. The number of initial (non-averaged) SA data points within the distance are denoted in the right-hand-side vertical axis with numbers in thousand (K) format.

Table 6. Absolute difference [mm/yr] between TG-derived and SA-derived trends at different distances (Dist) from the coast. The values are highlighted based on colour (i.e., the smallest absolute difference is in green and the largest is in red). The corresponding RMSE and arithmetic average (MEAN) of differences are computed at the bottom of the table [mm/yr].

Dist [km] TG	5	10	15	20	25	30	35	40	45	50
1	1.1	1.7	1.4	1.1	0.9	0.8	0.8	0.8	0.8	0.8
2	1.4	0.9	0.8	0.5	0.4	0.1	0.1	0.1	0.1	0.1
3	2.9	3.3	3.1	3.2	3.4	3.4	3.5	3.5	3.5	3.4
4	1.7	1.7	1.8	1.7	1.6	1.6	1.6	1.6	1.6	1.7
5	0.6	0.6	0.5	0.5	0.7	0.9	1.0	1.0	1.0	1.0
6	0.4	0.9	0.9	0.9	0.9	0.9	0.8	0.8	0.7	0.7
7	1.0	0.5	0.2	0.2	0.2	0.2	0.1	0.1	0.3	0.5
8	2.8	2.9	2.7	2.6	2.6	2.5	2.5	2.5	2.5	2.5
9	0.2	0.1	0.2	0.4	0.5	0.5	0.6	0.5	0.5	0.5
10	1.1	1.1	1.0	0.6	0.3	0.2	0.3	0.6	0.7	0.7
11	0.5	1.1	0.7	0.5	0.4	0.4	0.4	0.4	0.3	0.3
12	1.8	2.1	2.1	2.1	2.0	1.9	1.9	1.9	1.9	1.9
13	0.6	0.5	0.8	0.8	0.9	0.9	0.9	0.8	0.8	0.8
RMSE	1.49	1.63	1.53	1.47	1.48	1.46	1.48	1.48	1.48	1.47
MEAN	0.28	0.16	0.11	0.03	−0.06	−0.12	−0.13	−0.09	−0.08	−0.06
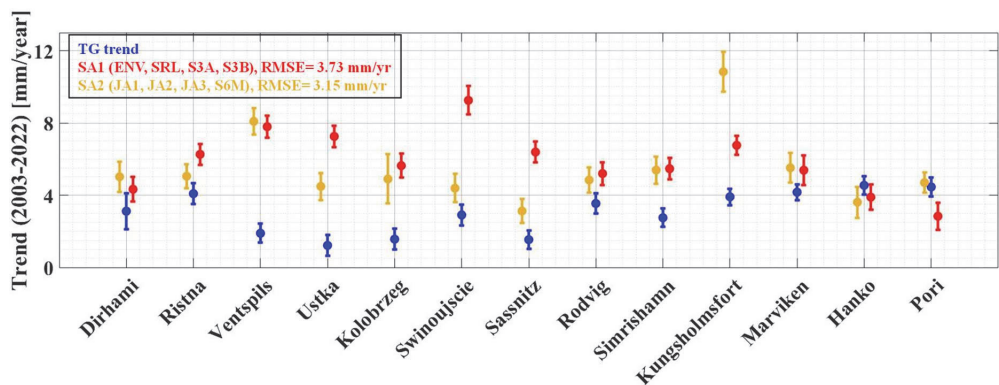
Figure 11. Estimated sea-level trend at the TG locations for two SA orbit inclination (high—red; low—yellow) categories of SA data compared to the TG-derived trend (blue) for the period of 2003–2022. The whiskers represent uncertainties using 95% CI.

The results of the comparison of each SA group with the TG data are represented in Table 7 (the best match with ground truth is highlighted in bold font). In general, the SA2 group (low inclination) with an RMSE of 3.15 mm/yr had a better match with the TG-derived trend compared to the SA1 group, which has an RMSE of 3.73 mm/yr. Over the 13 stations, the average discrepancy of the SA2 group is 2.5 mm/yr, with a maximum discrepancy of 6.9 mm/yr at Kungsholmsfort (#10), while the average discrepancy between the SA1 group and TG trends is 3.2 mm/yr, with the maximum discrepancy of 6.3 mm/yr at Swinoujscie (#6). However, for some stations, both SA groups have large discrepancies, including Ventspils (#3) and Ustka (#4), which could be due to the TG estimation problems, as is also shown in Figure 7b,c.

Table 7. Sea-level trend [mm/yr] from TG observation and different orbit inclination categories of SA missions (high- and low-inclination orbit) during 2003–2022 at different stations. Better agreements with the ground truth are denoted in bold font.

| ID	Station	TG	SA1	SA2
1	Dirhami	3.12 ± 0.33	$\mathbf{4.33 \pm 0.23}$	5.02 ± 0.28
2	Ristna	4.09 ± 0.19	6.26 ± 0.19	$\mathbf{5.05 \pm 0.22}$
3	Ventspils	1.89 ± 0.18	$\mathbf{7.79 \pm 0.20}$	8.09 ± 0.24
4	Ustka	1.22 ± 0.19	7.25 ± 0.20	$\mathbf{4.49 \pm 0.25}$
5	Kolobrzeg	1.57 ± 0.19	5.63 ± 0.22	$\mathbf{4.90 \pm 0.45}$
6	Swinoujscie	2.91 ± 0.19	9.25 ± 0.26	$\mathbf{4.39 \pm 0.26}$
7	Sassnitz	1.54 ± 0.17	6.39 ± 0.19	$\mathbf{3.12 \pm 0.22}$
8	Rodvig	3.54 ± 0.19	5.20 ± 0.21	$\mathbf{4.84 \pm 0.24}$
9	Simrishamn	2.75 ± 0.17	5.47 ± 0.20	$\mathbf{5.39 \pm 0.25}$
10	Kungsholmsfort	3.91 ± 0.15	$\mathbf{6.76 \pm 0.18}$	10.83 ± 0.36
11	Marviken	4.17 ± 0.15	$\mathbf{5.39 \pm 0.27}$	5.51 ± 0.28
12	Hanko	4.55 ± 0.17	$\mathbf{3.89 \pm 0.23}$	3.61 ± 0.29
13	Pori	4.46 ± 0.18	2.84 ± 0.25	$\mathbf{4.70 \pm 0.19}$

5.4.3. Gridded vs. Instantaneous SA-Derived ASL Trends

Gridded SA data are frequently utilized for sea-level trend estimations ([29,45,46,83]; etc.). Gridded data are quite convenient, as they average data from various missions, bridging temporal gaps between them and allowing for mutual usage with other data products. This study has focused on using along-track data for sea-level trend estimates. The results have shown that, for the long-term sea-level trends, the SA-based estimates perform reasonably well when compared with hourly TG-derived trends, yielding RMSEs that vary between 1.2 and 1.5 mm/yr. Recall that the long-term (1995–2022) TG sea-level

trends varied from 2.1 to 5.4 mm/yr and the along-track SA was 2.5 to 5.3 mm/yr (see Section 5.1 and Table 6). These results are more or less comparable with other studies that have also shown long-term trend estimates of 3.4 mm/yr [45] and 3 mm/yr [29].

In practice, gridded SA data employ averaging methods and various techniques in processing, which could potentially result in the misinterpretation of sea-level trends. This effect might be more pronounced in coastal areas, impacting their approach and analysis. Moreover, it is also shown in Section 5.4.2 that different SA missions may give different results, whereas this can vary spatially. Regional sea-level trend estimation using SA is more challenging compared to the utilization of SA products for global-scale studies. It is expected that the Baltic Sea area, which has numerous archipelagos, small islands, and rocks within ~10 km of the mainland, may contaminate the radar signal, making less opportunities for SA beams to interact with the open water and leading to errors [29,33,82]. The question now remains as to whether utilizing the SA along-track instantaneous data for sea-level trend research is advantageous over other gridded products. Consequently, this study performs a comparison of sea-level trends from instantaneous along-track SA data with that of three available gridded datasets within this region. These three gridded datasets consist of (i) a global SA gridded sea-level anomaly, (ii) hydrodynamic model gridded products obtained from Nemo (Baltic Sea Physical Reanalysis), and (iii) Baltic + SEAL gridded SA data over the Baltic Sea region obtained from the Baltic + SEAL dataset. More detailed information on these data sources can be found in Section 4.5.

This examination amongst the different sea-level products is performed from 1995 to 2019 (the upper limit is due to the availability of the Baltic + SEAL project data for along-track and gridded data being available only up to June 2019, cf. Table 2). The result of this comparison is shown in Figure 12. The results of the inter-comparison show that most of the gridded products agreed well with the instantaneous SA-derived trend calculations in the present study. In Figure 12, the long-term (28 years) trend variations (the results of Figure 7 and Table 5) from TGs (DT_{TG}) and SA ($DT_{SA@TG}$) are also illustrated (triangle marker) for comparison. The largest TG trend differences appear to occur with the Baltic+SEAL gridded data, with a difference of 4.7 mm/yr at the Ventspils (#3) station, as well as with the global gridded SLA for Dirhami (#1) of 3.3 mm/yr. The TG data at Ventspils (#3) and Rodvig (#8) also showed somewhat larger differences compared to the other products. Possible reasons are discussed in Section 5.3.
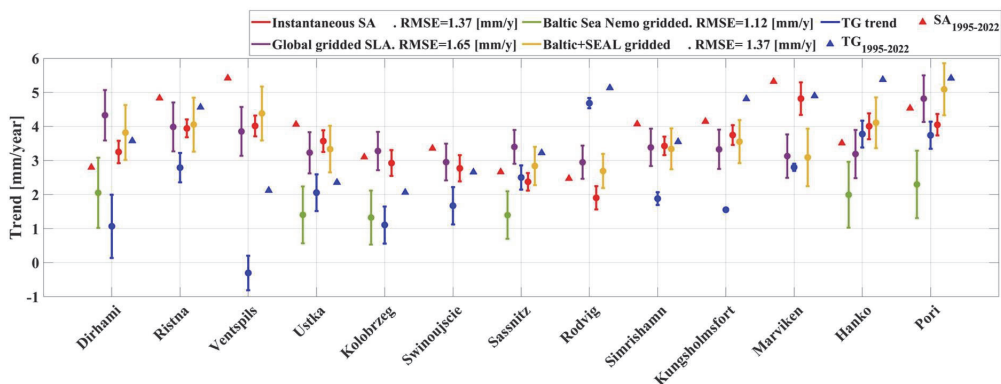
Figure 12. Sea-level trend estimates based on instantaneous SA data (red) and three gridded datasets including global SLA data by Copernicus (purple), gridded Nemo model SLA by Copernicus (green), and Baltic + SEAL gridded SA data (yellow) together with the TG data (blue) in the period of 1995–2019. The whiskers represent uncertainties using 95% CI. The long-term (1995–2022) trend based on $DT_{SA@TG}$ (red triangle) and DT_{TG} (blue triangle) are added as a reference.

Figure [12] shows that, in general, the instantaneous SA-derived ASL trend results match those of the gridded datasets. Note that the gridded SA data of the Copernicus dataset could not come close enough to the coastline to estimate the sea-level trend for seven TG stations. Hence, the RMSE is compared only for the six available stations. Although the instantaneous SA and gridded data from Baltic + SEAL have the same RMSE, the gridded data also could not come close to the two TG stations' (Kolobrzeg and Swinoujscie) estimate. This emphasizes the advantage of using the instantaneous SA-derived DT rather than gridded and SLA data for realistic sea-level trend calculations.

Table [8] also includes the long-term trend (28 years) estimations of both SA and TG (the results from Figure [7] and Table [5]). From this table, the instantaneous SA-derived trend has a better match with TG (bold fonts) for five stations (Ristna, Swinoujscie, Sassnitz, Hanko, and Pori) as compared to other datasets. These results show that the instantaneous along-track data are comparable to those of the gridded SA products, in which SA appears to work better for regional trend estimation over this area at several TG stations. This could be due to averaging the instantaneous DT within 50 km rather than taking one observation (of TG) for trend computation. In Table [8], the RMSE values are calculated between the pair (DT_{TG} and $DT_{SA@TG}$) of long-term (28 years) and 1995–2019 (24 years) trends of 1.78 mm/yr (blue circles and blue triangles) and 0.64 mm/yr (red circle and red triangles), respectively. In Figure [12], the RMSE between DT_{TG} (blue circles) and other datasets over the same period (1995–2019) is also mentioned (stations with any NaN value are excluded). The RMSE between the DT_{TG} trend (blue circles) and the $DT_{SA@TG}$ trend (red circles) is 1.37 mm/yr. The RMSE between DT_{TG} and the Baltic+SEAL gridded data (yellow circles) is 1.37 mm/yr, that of the Nemo gridded data (green circles) is 1.12, and for the global gridded SLA data (purple circles), this is 1.65 mm/yr. The RMSE values also approve the reliability of SA data for trend estimations, which has an insignificant effect on the 4-year difference in the time series.

Table 8. Sea-level trend estimates [mm/yr] during 1995–2019 using hourly TG observations, instantaneous SA-derived DT, and three gridded data products (incl. global gridded SLA, Baltic Sea Nemo gridded data, and Baltic + SEAL gridded data). The best performances compared to TG observations are in bold font. The ASL trend of TG and SA during 1995–2022 (from Figure [7] and Table [6]) is also mentioned. The shape in parenthesis corresponds to the shapes in Figure [12].

ID	TG (●) 1995–2019	SA (●) 1995–2019	Global SLA (●) 1995–2019	Nemo (●) 1995–2019	SEAL (●) 1995–2019	TG (▲) 1995–2022	SA (▲) 1995–2022
1	1.07 ± 0.31	3.25 ± 0.11	4.33 ± 0.0	**2.05 ± 0.0**	3.82 ± 0.03	3.6 ± 0.02	2.8 ± 0.01
2	2.79 ± 0.14	**3.94 ± 0.09**	3.98 ± 0.0	NaN	4.05 ± 0.03	4.6 ± 0.01	4.8 ± 0.01
3	−0.3 ± 0.17	4.01 ± 0.10	**3.85 ± 0.0**	NaN	4.38 ± 0.03	2.1 ± 0.01	5.4 ± 0.01
4	2.06 ± 0.18	3.57 ± 0.11	3.23 ± 0.0	**1.40 ± 0.0**	3.33 ± 0.02	2.4 ± 0.01	4.1 ± 0.01
5	1.11 ± 0.18	2.92 ± 0.13	3.28 ± 0.0	**1.33 ± 0.0**	NaN	2.1 ± 0.01	3.1 ± 0.01
6	1.67 ± 0.18	**2.77 ± 0.13**	2.95 ± 0.0	NaN	NaN	2.7 ± 0.01	3.4 ± 0.01
7	2.50 ± 0.12	**2.37 ± 0.09**	3.40 ± 0.0	1.40 ± 0.0	2.84 ± 0.02	3.2 ± 0.01	2.7 ± 0.01
8	4.68 ± 0.05	1.90 ± 0.11	**2.95 ± 0.0**	NaN	2.69 ± 0.02	5.1 ± 0.01	2.5 ± 0.01
9	1.88 ± 0.06	3.43 ± 0.09	3.38 ± 0.0	NaN	**3.34 ± 0.02**	3.5 ± 0.01	4.1 ± 0.01
10	1.55 ± 0.01	3.75 ± 0.10	**3.33 ± 0.0**	NaN	3.55 ± 0.02	4.8 ± 0.01	4.1 ± 0.01
11	2.80 ± 0.03	4.82 ± 0.16	3.13 ± 0.0	1.85 ± 0.0	**3.09 ± 0.03**	4.9 ± 0.01	5.3 ± 0.01
12	3.78 ± 0.13	**4.00 ± 0.13**	3.19 ± 0.0	1.99 ± 0.0	4.11 ± 0.02	5.4 ± 0.01	3.5 ± 0.01
13	3.74 ± 0.13	**4.05 ± 0.10**	4.82 ± 0.0	2.30 ± 0.0	5.09 ± 0.03	5.4 ± 0.01	4.5 ± 0.01
RMSE between TG (blue circle and triangle) and SA (red circle and triangle) pairs						1.78	0.64

6. Discussion

In this study, an analysis was conducted on sea-level trends covering a long-term period (28 years, from 1995 to 2022) as well as decadal scales (2000–2009 and 2010–2020) with the focus mainly on the Baltic Proper within the Baltic Sea region. The dataset utilized

included information from 13 TG stations along with multi-mission along-track SA. Below is a summary of the key findings.

To begin, on average, the long-term ASL trend calculated for the entire Baltic across the period 1995–2022 revealed consistent results: on average, 3.83 (cf. Table 5) mm/yr for TG hourly data, 3.87 mm/yr for instantaneous SA data, and 3.32 mm/yr for TG at the time of the SA pass (as indicated in Table 5). Notably, all three calculation methods demonstrated relatively similar outcomes. These findings align with prior studies over the same study area: [45] reported trend estimates of 3.4 mm/yr, [29] indicated 3 mm/yr, and [46] achieved comparable results for different time periods using SA, TG, and hydrodynamic models. When compared to the global mean sea level (GMSL) trends obtained from TG and SA data, which exhibited rates ranging from 3.2 mm/yr over the period 1993–2015 to 3.6 mm/yr over the period 2006–2015 [5], the long-term sea-level trend calculated for the Baltic Sea appeared consistent. Importantly, this trend seemed unaffected by the considered time span or the specific data source examined.

This study also explored the long-term RSL and ASL derived from TG hourly data spanning 1995–2022. The findings indicate the significance of accounting for VLM in accurately quantifying trend rates (Section 5.1). For instance, in this analysis, the RSL trends ranged from −2 to 4.5 mm/yr, while the ASL trends varied between 2 and 5.4 mm/yr. Notably, given the spatial variability of VLM rates, the most substantial disparities between the RSL and ASL were observed in locations significantly affected by pronounced VLM. Consequently, in the northern and eastern regions of the Baltic Sea, a distinct pattern emerged, where the ASL displayed an increasing trend from south to north, while the RSL exhibited a decreasing trend from north to south, as evidenced, for instance, at the Pori station (#13). This discrepancy highlights the impact of VLM on sea-level measurements in these specific areas. Moreover, the ASL trend derived from satellite altimetry (SA) data can be effectively compared to the RSL trend derived from TG data. This comparison serves the purpose of either refining or validating the models designed to account for VLM.

The analysis revealed a spatial variation in sea-level trends within the Baltic Sea region, indicating larger values (ranging from 4 to 5 mm/yr) in the north-eastern section compared to stations situated in the south-west (between 2 and 4 mm/yr). Previous studies, such as by [63], suggested that this discrepancy could be attributed to an escalation in the frequency and intensity of westerly winds. Additionally, an increase in cyclones occurring above 52°N has exposed the Baltic Sea to more vigorous westerly storms, potentially contributing to these observed trends. Supporting these findings, a recent report by [84] noted a general pattern of rising water temperatures, a reduced ice extent, and an overall uptick in annual mean precipitation across the northern region. Specifically, in the northern Baltic Sea and the Gulf of Finland, there is a statistical association between larger river runoff and warmer air temperatures coupled with increased precipitation. Conversely, in more southerly regions, a decline in annual runoff corresponds with rising air temperatures. These observations collectively support the notion of varied influences impacting sea-level trends across different sections of the Baltic Sea.

The long-term trends consistently highlight larger rates in the northern section, aligning with findings from earlier studies. Interestingly, these results reveal an anomaly in certain south-western stations, specifically at Rodvig (#8) and Kungsholmsfort (#10), where higher-than-normal trends of approximately 5.1 mm/yr and 4.8 mm/yr, respectively, were calculated using TG hourly data. These rates notably exceed the trends observed at other south-western stations, which typically range within 2 to 4 mm/yr. These unexpected findings require further investigations for a deeper understanding of the main drivers behind this. Understanding the main drivers behind these discrepancies is crucial for a comprehensive and accurate interpretation of sea-level trends in these specific south-western stations.

Examining sea-level trend values at decadal scales revealed notable circumstances. During the period from 2000–2009, a majority of stations (9 out of 13) exhibited an increase in sea-level trends compared to the subsequent decade, 2010–2019. While some stations

might have been affected by data gaps during this period (Table 4), others remained unaffected. The larger trends observed could potentially be attributed to increased westerly winds, augmented precipitation, and fluctuations in air pressure, as suggested in studies such as by Reißmann et al. (2009) and Gräwe et al. (2019). Further exploration of the possible reasons for these decadal variations may be necessary. Also, it should be noted that the calculated decadal trends diverge significantly from the long-term trend (1995–2022), showcasing variations that nearly triple in some stations. Furthermore, each decade displayed its unique pattern of variation, as outlined in Table 5. These results demonstrate that the interpretation of decadal trends can be more complex, with many more variations existing for several different reasons.

In this study, the inter-comparison of multi-SA missions with different orbit constellations showed that low-inclination satellites appear to give slightly better results for the trend estimation across the studied sites in the Baltic Sea for the period of nineteen years of overlapped data (2003–2022). Also, the superiority of instantaneous SA-derived DT for the sea-level trend estimates, rather than gridded SLA datasets, is illustrated in Figure 12. Although the gridded data product results are comparable to TG and along-track SA data, they may suffer from issues of replicating data close to the coast, and this made the trend estimation unavailable for some stations. So, in conclusion, the along-track data are better for representing the coastal sea-level trends. By comparing the results of Figure 12 and Table 8, which include the trend value during 1995–2022 (triangles) and 1995–2019 (circles), the trend derived from averaging instantaneous SA appears to have better performance than TG observations (lower RMSE value between these years). This could be due to averaging the SA-derived DT within the specific radius (50 km) of the TG station. The TG-derived trend is more sensitive to the time-series length, and changing the time window of TG data could affect the trend estimations in larger values. This was also shown by comparing the $DT_{TG@SA\ cycle}$ and $DT_{SA@TG}$ trends over a decadal time frame.

Also, TGs are located at the coast, so they may also be influenced by other processes, such as wave set-up and set-down [81], which may not always be captured by the SA. This may suggest that TG may not be the ideal dataset to represent sea-level variation, especially with trend estimates. However, the ability to precisely compare the variability in sea level between TG and along-track SA at various distances from the coast provides a valuable insight into ocean dynamics. It also highlights that in areas without the presence of TGs, along-track SA can offer an alternative that may yield even more accurate results. As a result, the utilization of the high-resolution geoid for SA to determine DT, coupled with geoid-referenced TG data, enabled a realistic quantification of these differences. Future research could further examine the comparison of TG and along-track SA in coastal areas and the possible identification of coastal processes.

7. Conclusions

This examination of coastal sea-level trends, calculated using tide gauges (TGs) and multi-mission along-track satellite altimetry (SA) for the period 1995–2022, showed that the average absolute sea-level trend for TG and along-track SA varies between 3.32 and 3.86 mm/yr. This agrees with previous regional Baltic Sea studies, with average values of 3 mm/yr, and that of the global mean sea level (GMSL) rate from TG and SA observations, which showed rates of 3.2 mm/yr over the period 1993–2015 to 3.6 mm/yr over the period 2006–2015. A spatial distribution of larger sea-level trends was observed in the northern and eastern areas of the Baltic Sea, and this may be due to increased days of intense westerly winds, lower air pressure, and increased sea temperature. Decadal sea-level trends showed quite a variation in rates, and a possible increase may have occurred in the decade 2000–2009. This study demonstrates that along-track instantaneous SA data can be reasonably utilized for sea-level trend estimates, and that they give a very good alternative for areas where TGs may not be present and for areas that may be influenced by gaps in TG data.

Author Contributions: M.M.: conceptualization, methodology, validation, formal analysis, writing, visualization. A.E.: conceptualization, writing—review and editing, supervision, funding. N.D.-E.:

conceptualization, writing—review and editing, supervision. All authors have read and agreed to the published version of the manuscript.

Data Availability Statement: The employed NKG2015 geoid model was provided by [76], and the NKG2016LU VLM model was provided by [75]. The Baltic + SEAL dataset is available on request from http://balticseal.eu/, and standard SA data are available from https://eoportal.eumetsat.int/. TG observations are downloadable based on the data provider, which is mentioned in Table A1. Post-processed data are available based on request.

Conflicts of Interest: The authors declare no conflicts of interest. The founders had no role in the design of the study; in the collection, analyses, or interpretation of data; in the writing of the manuscript; or in the decision to publish the results.

Appendix A
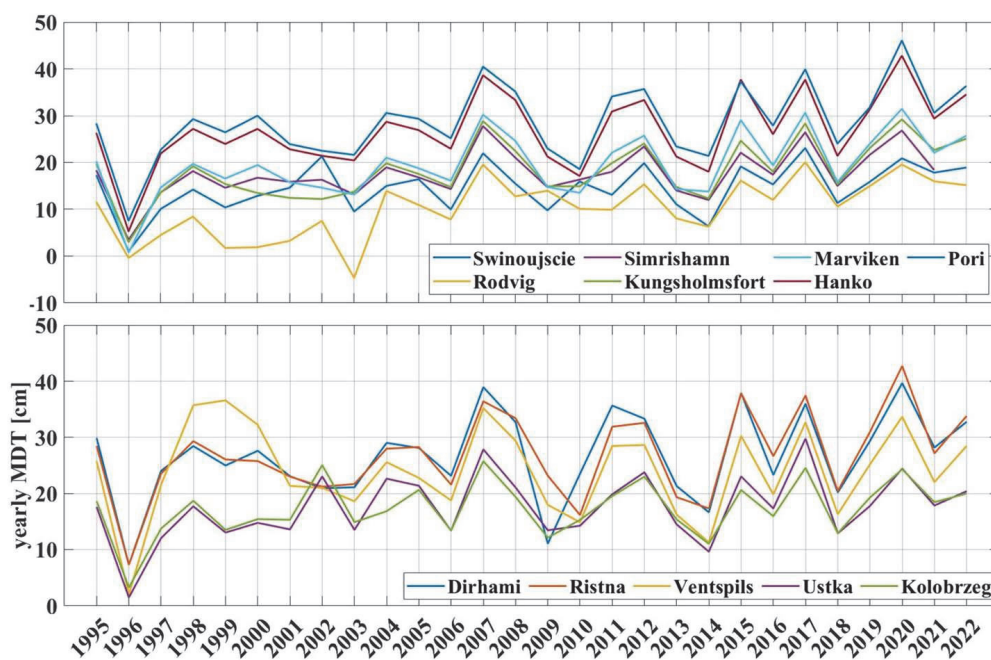
Figure A1. Annual variations in TG-derived MDT in mean tide system refer to NAP during 1995–2022; the time epoch is 2000.0 (the VLM effect is accounted for). The mean of sequential fluctuations of all stations exceeds ±8 cm, and the maximum fluctuation could reach 25 cm (e.g., 2018–2019).

**Table A1.** History of measurement devices for each TG station.

ID	Station	Measurement Device History	Data Provider
1	Dirhami	**01.01.1995–30.04.2009:** manual observations, twice a day at 06 and 18 UTC. **21.09.2010–present:** high-precision-level sensor PAA-36XW/H from Keller AG.	www.keskkonnaagentuur.ee
2	Ristna	**01.01.1995–24.09.2010:** mareograph. **22.09.2010–present:** high-precision-level sensor PAA-36XW/H from Keller AG.	
3	Ventspils	**23.02.1996–25.08.2004:** HMS—1820 sensor from MARIMATECH **26.08.2004–13.09.2011:** OTT ODS sensor from OTT HydroMet. **14.09.2011–present:** OTT PLS sensor from OTT HydroMet	
4	Ustka	**1995–2015.12.1:** Limnigraph LPU-10 from Zootechnics **2005.09.01–2023.07.05:** Float Telemetry from Sutron **2023.07.06–present:** Pressure sensor DST 22 from Seba	www.imgw.pl
5	Kolobrzeg	**1995–2009.06.01:** Limnigraph LPU 10 Zootechnics **2009.01.07–2012.04.30:** Limnimeter ORPHEUS from OTT **2004.05.19–2023.08.23:** Float Telemetry Xlite 9210 from Sutron **2023.08.24–present:** HD-01 from Envag	
6	Swinoujscie	**1995–2015.12.2:** Limnigraph LPU-10 from Zootechnics **2006.02.08–2019.06.26:** Float Telemetry from Sutron 2019.06.27–2023.09.24: OTT PLS device (subpress) from OTT **2023.05.09–present:** Pressure sensor DST 22 from Seba	
7	Sassnitz	**1970–1996:** STEREMAT-Recording Stage indicator (Model 195109) **01.06.1996–2013:** angle encoder from Rittmeyer and beginning of water level remote transmission. **20.10.2013–present:** Ott-Hydromet pressure sensor (Model 194772) as redundant system.	www.bsh.de
8	Rodvig	**1995–February 2015:** Data collected by Farvandsvæsenet institute and not enough details of the instruments are available. **February 2015–October 2021:** CBS–Compact Bubbler Sensor by OTT **October 2021–present:** Radar measurement Time-of-Flight Micropilot FMR52 from Endress	www.dmi.dk
9	Simrishamn	**1995–07.08.2004:** Float measurement collection, data manual dialling of the station (telepegel). **07.08.2004–15.05.2018:** Shaft encoder AD150A **2018.05.15–Present:** Radar Vega puls61	www.videscentrs.lvgmc.lv
10	Kungsholmsfort	**1995–08.07.2004:** Float measurement collection, data manual dialling of the station (telepegel). **28.11.2002–12.11.2018:** Shaft encoder AD150A. **12.11.2018–Present:** Radar Vega puls61.	
11	Marviken/Arkö	**1995–07.08.2004:** Float measurement collection, data manual dialling of the station (telepegel). **03.05.2004–01.10.2019:** Shaft encoder AD150A (station closed). **29.08.2017–Present:** Radar Vega Puls 61 (from 01.10.2019, Arkö data are used).	
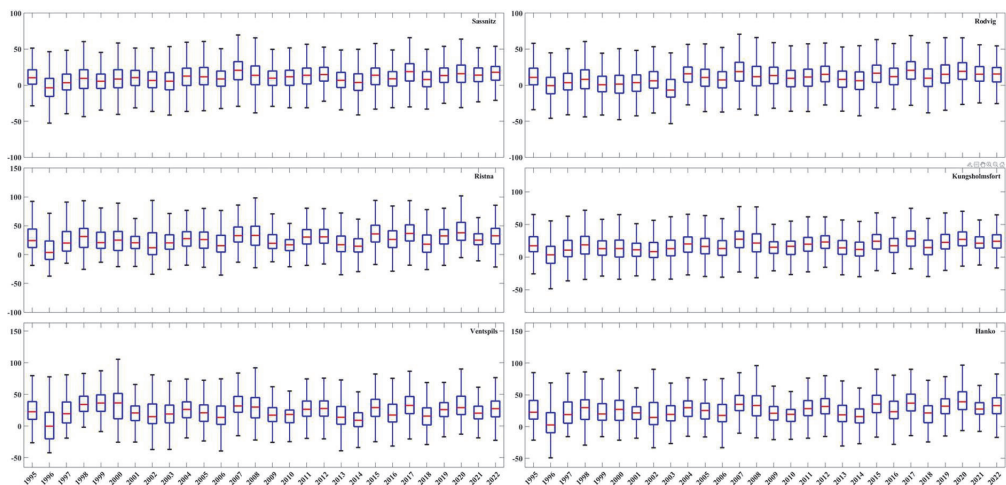
Figure A2. Annual DT [cm] variation in TG observations (hourly data) of ASL (GIA-corrected) for six selected TG stations during 1995–2022. The bottom and top of each bar are the 25th and 75th percentiles of the DT and the line in the middle of each box is the median value at each year.
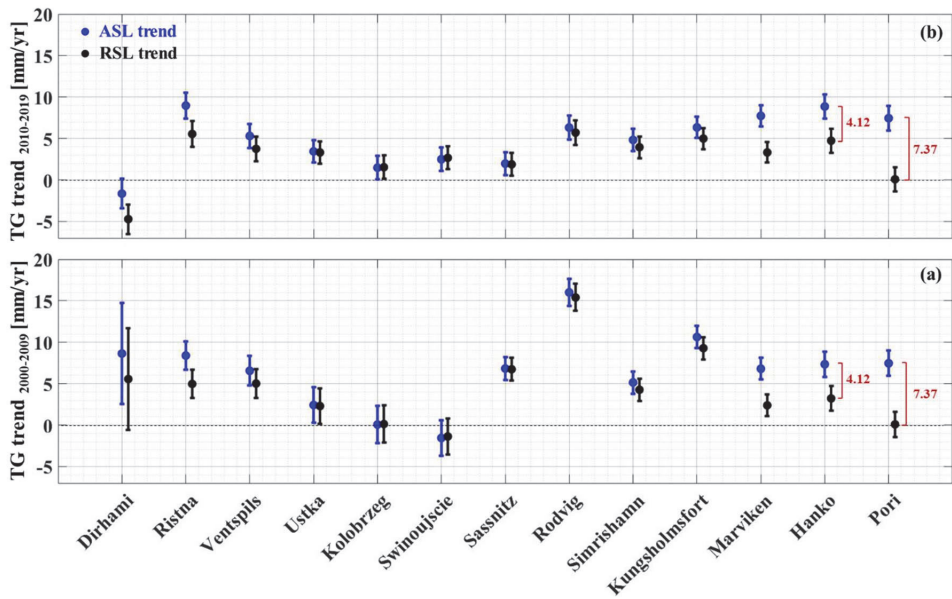
Figure A3. Decadal sea-level trends using hourly TG records. The TG trend before (black) and after (blue) VLM correction (RSL and ASL trends) for the period 2000–2009 (**a**) and the period of 2010–2019 (**b**); the whiskers represent the uncertainties using 95% CI. Both ASL and RSL rates increased in 2010–2019 over subpolar latitude areas. The differences between ASL and RSL trends are illustrated for two stations in red font.
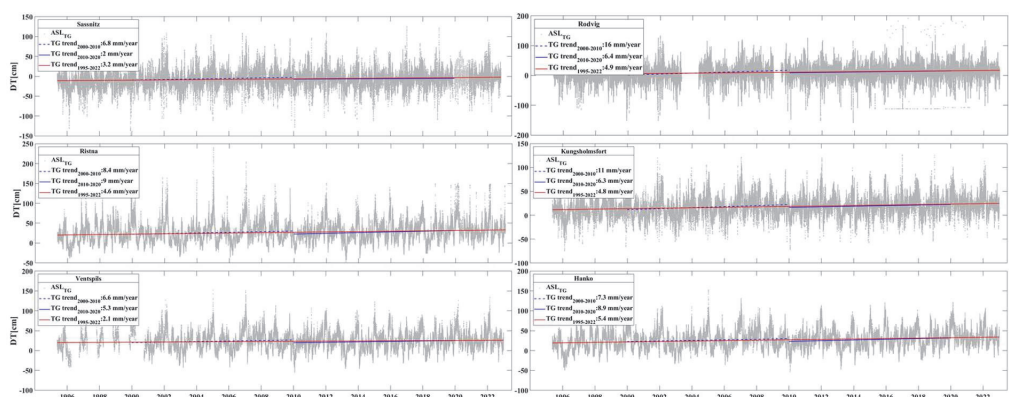
Figure A4. DT variation over 6 TG stations as example. The trend rates over the whole study period (red line) together with the decadal trend (blue lines) are also mentioned in the figures.

Table A2. Number of hourly data and associated gap (%) of data for TGs during whole study period also during each decade.

ID	TG Data (hourly)							
	1995–2022		2000–2009		2010–2019		2000–2019	
	No.	Gap	No.	Gap	No.	Gap	No.	Gap
1	117,833	52.0	6807	92.2	81,110	7.5	87,917	49.9
2	244,427	0.4	87,475	0.2	86,824	0.9	174,299	0.6
3	200,199	18.4	76,839	12.4	87,141	0.6	163,980	6.5
4	175,622	28.4	50,654	42.2	87,622	0.0	138,276	21.1
5	170,399	30.6	47,122	46.3	85,944	1.9	133,066	24.1
6	175,157	28.6	50,114	42.8	87,595	0.1	137,709	21.5
7	237,694	2.6	87,672	0.0	86,278	1.6	173,950	0.8
8	226,479	7.7	72,081	17.8	86,621	1.2	158,702	9.5
9	234,745	0.0	87,672	0.0	87,648	0.0	175,320	0.0
10	245,439	0.0	87,672	0.0	87,648	0.0	175,320	0.0
11	245,448	0.0	87,672	0.0	87,648	0.0	175,320	0.0
12	245,448	0.0	87,672	0.0	87,648	0.0	175,320	0.0
13	244,728	0.3	87,672	0.0	86,928	0.8	174,600	0.4

References

1. Hooijer, A.; Vernimmen, R. Global LiDAR land elevation data reveal greatest sea-level rise vulnerability in the tropics. *Nat. Commun.* **2021**, *12*, 3592. [CrossRef]
2. Dangendorf, S.; Hay, C.; Calafat, F.M.; Marcos, M.; Piecuch, C.G.; Berk, K.; Jensen, J. Persistent acceleration in global sea-level rise since the 1960s. *Nat. Clim. Change* **2019**, *9*, 705–710. [CrossRef]
3. Church, J.A.; White, N.J. Sea-level rise from the late 19th to the early 21st century. *Surv. Geophys.* **2011**, *32*, 585–602. [CrossRef]
4. Church, J.A.; White, N.J.; Konikow, L.F.; Domingues, C.M.; Cogley, J.G.; Rignot, E.; Gregory, J.M.; van den Broeke, M.R.; Monaghan, A.J.; Velicogna, I. Revisiting the Earth's sea-level and energy budgets from 1961 to 2008. *Geophys. Res. Lett.* **2011**, *38*, 4066. [CrossRef]
5. Oppenheimer, M.; Glavovic, B.; Hinkel, J.; Van de Wal, R.; Magnan, A.K.; Abd-Elgawad, A.; Cai, R.; Cifuentes-Jara, M.; Deconto, R.M.; Ghosh, T.; et al. Sea Level Rise and Implications for Low Lying Islands, Coasts and Communities. In *The Ocean and Cryosphere in a Changing Climate*; Cambridge University Press: Cambridge, UK, 2019. [CrossRef]
6. Abdalla, S.; Kolahchi, A.A.; Ablain, M.; Adusumilli, S.; Bhowmick, S.A.; Alou-Font, E.; Amarouche, L.; Andersen, O.B.; Antich, H.; Aouf, L.; et al. Altimetry for the future: Building on 25 years of progress. *Adv. Space Res.* **2021**, *68*, 319–363. [CrossRef]
7. Pytharouli, S.; Chaikalis, S.; Stiros, S.C. Uncertainty and bias in electronic tide-gauge records: Evidence from collocated sensors. *Measurement* **2018**, *125*, 496–508. [CrossRef]
8. Slangen, A.B.; Church, J.A.; Agosta, C.; Fettweis, X.; Marzeion, B.; Richter, K. Anthropogenic forcing dominates global mean sea-level rise since 1970. *Nat. Clim. Change* **2016**, *6*, 701–705. [CrossRef]

9. Marzeion, B.; Cogley, J.G.; Richter, K.; Parkes, D. Attribution of global glacier mass loss to anthropogenic and natural causes. *Science* **2014**, *345*, 919–921. [CrossRef] [PubMed]

10. Prandi, P.; Meyssignac, B.; Ablain, M.; Spada, G.; Ribes, A.; Benveniste, J. Local Sea level trends, accelerations, and uncertainties over 1993–2019. *Sci. Data* **2021**, *8*, 1. [CrossRef] [PubMed]

11. Ablain, M.; Cazenave, A.; Valladeau, G.; Guinehut, S. A new assessment of the error budget of global mean sea level rate estimated by satellite altimetry over 1993–2008. *Ocean. Sci.* **2009**, *5*, 193–201. [CrossRef]

12. Ablain, M.; Cazenave, A.; Larnicol, G.; Balmaseda, M.; Cipollini, P.; Faugère, Y.; Fernandes, M.J.; Henry, O.; Johannessen, J.A.; Knudsen, P.; et al. Improved sea level record over the satellite altimetry era (1993–2010) from the Climate Change Initiative project. *Ocean Sci.* **2015**, *11*, 67–82. [CrossRef]

13. Ablain, M.; Meyssignac, B.; Zawadzki, L.; Jugier, R.; Ribes, A.; Spada, G.; Benveniste, J.; Cazenave, A.; Picot, N. Uncertainty in satellite estimates of global mean sea-level changes, trend and acceleration. *Earth Syst. Sci. Data* **2019**, *11*, 1189–1202. [CrossRef]

14. Watson, C.S.; White, N.J.; Church, J.A.; King, M.A.; Burgette, R.J.; Legresy, B. Unabated global mean sea-level rise over the satellite altimeter era. *Nat. Clim. Change* **2015**, *5*, 565–568. [CrossRef]

15. Guérou, A.; Meyssignac, B.; Prandi, P.; Ablain, M.; Ribes, A.; Bignalet-Cazalet, F. Current observed global mean sea level rise and acceleration estimated from satellite altimetry and the associated measurement uncertainty. *Ocean Sci.* **2023**, *19*, 431–451. [CrossRef]

16. Wöppelmann, G.; Letetrel, C.; Santamaria, A.; Bouin, M.N.; Collilieux, X.; Altamimi, Z.; Williams, S.D.P.; Miguez, B.M. Rates of sea-level change over the past century in a geocentric reference frame. *Geophys. Res. Lett.* **2009**, *36*, L12607. [CrossRef]

17. Jevrejeva, S.; Moore, J.C.; Grinsted, A.; Woodworth, P.L. Recent global sea level acceleration started over 200 years ago? *Geophys. Res. Lett.* **2008**, *35*. [CrossRef]

18. Cazenave, A.; Dieng, H.B.; Meyssignac, B.; Von Schuckmann, K.; Decharme, B.; Berthier, E. The rate of sea-level rise. *Nat. Clim. Change* **2014**, *4*, 358–361. [CrossRef]

19. Ablain, M.; Legeais, J.F.; Prandi, P.; Marcos, M.; Fenoglio-Marc, L.; Dieng, H.B.; Benveniste, J.; Cazenave, A. Satellite Altimetry-based Sea Level at Global and Regional Scales. In *Integrative Study of the Mean Sea Level and Its Components*; Springer International Publishing: Cham, Switzerland, 2017; pp. 9–33. [CrossRef]

20. Chen, X.; Zhang, X.; Church, J.A.; Watson, C.S.; King, M.A.; Monselesan, D.; Legresy, B.; Harig, C. The increasing rate of global mean sea-level rise during 1993–2014. *Nat. Clim Change* **2017**, *7*, 492–495. [CrossRef]

21. Hay, C.C.; Morrow, E.; Kopp, R.E.; Mitrovica, J.X. Probabilistic reanalysis of twentieth-century sea-level rise. *Nature* **2015**, *517*, 481–484. [CrossRef] [PubMed]

22. Legeais, J.F.; Ablain, M.; Zawadzki, L.; Zuo, H.; Johannessen, J.A.; Scharffenberg, M.G.; Fenoglio-Marc, L.; Fernandes, M.J.; Andersen, O.B.; Rudenko, S.; et al. An improved and homogeneous altimeter sea level record from the ESA Climate Change Initiative. *Earth Syst. Sci. Data* **2018**, *10*, 281–301. [CrossRef]

23. Rateb, A.; Scanlon, B.R. Demystifying the Dynamics of Global and Regional Sea Level Trends from 1993 to 2021. *EarthArXiv* **2023**, X5K38R. [CrossRef]

24. Simpson, M.J.; Nilsen, J.E.Ø.; Ravndal, O.R.; Breili, K.; Sande, H.; Kierulf, H.P.; Steffen, H.; Jansen, E.; Carson, M.; Vestøl, O. Sea Level Change for Norway: Past and Present Observations and Projections to 2100. Norwegian Centre for Climate Services Report. no. 1/2015. Available online: https://www.researchgate.net/profile/Jan-Even-Nilsen/publication/281626674_Sea_Level_Change_for_Norway_Past_and_Present_Observations_and_Projections_to_2100/links/55f0774708ae199d47c212f6/Sea-Level-Change-for-Norway-Past-and-Present-Observations-and-Projections-to-2100.pdf (accessed on 20 December 2022).

25. Slangen, A.B.A.; Carson, M.; Katsman, C.A.; Van de Wal, R.S.W.; Köhl, A.; Vermeersen, L.L.A.; Stammer, D. Projecting twenty-first century regional sea-level changes. *Clim. Change* **2014**, *124*, 317–332. [CrossRef]

26. Kopp, R.E.; Horton, R.M.; Little, C.M.; Mitrovica, J.X.; Oppenheimer, M.; Rasmussen, D.J.; Strauss, B.H.; Tebaldi, C. Probabilistic 21st and 22nd century sea-level projections at a global network of tide-gauge sites. *Earth's Future* **2014**, *2*, 383–406. [CrossRef]

27. Grinsted, A.; Jevrejeva, S.; Riva, R.E.; Dahl-Jensen, D. Sea level rise projections for northern Europe under RCP8. 5. *Clim. Res.* **2015**, *64*, 15–23. [CrossRef]

28. Fox-Kemper, B.; Hewitt, H.T.; Xiao, C.; Adalgeirsdóttir, G.; Drijfhout, S.S.; Edwards, T.L.; Golledge, N.R.; Hemer, M.; Kopp, R.E.; Krinner, G.; et al. Ocean, Cryosphere and Sea Level Change. In *Climate Change 2021: The Physical Science Basis. Contribution of Working Group I to the Sixth Assessment Report of the Intergovernmental Panel on Climate Change*; Masson-Delmotte, V., Zhai, P., Anna, P., Conners, S.L., Péan, C., Berger, S., Caud, N., Chen, Y., Goldfarb, L., Gomis, M.I., et al., Eds.; Cambridge University Press: Cambridge, UK; New York, NY, USA, 2021; pp. 1211–1362. Available online: https://www.ipcc.ch/report/ar6/wg1/downloads/report/IPCC_AR6_WGI_Chapter09.pdf (accessed on 20 December 2022).

29. Passaro, M.; Müller, F.L.; Oelsmann, J.; Rautiainen, L.; Dettmering, D.; Hart-Davis, M.G.; Abulaitijiang, A.; Andersen, O.B.; Høyer, J.L.; Madsen, K.S.; et al. Absolute Baltic Sea level trends in the satellite altimetry era: A revisit. *Front. Mar. Sci.* **2021**, *8*, 647607. [CrossRef]

30. Pellikka, H.; Johansson, M.M.; Nordman, M.; Ruosteenoja, K. Probabilistic projections and past trends of sea level rise in Finland. *Nat. Hazards Earth Syst. Sci. Discuss.* **2022**, *2022*, 1613–1630. [CrossRef]

31. IPCC; Pörtner, H.O.; Roberts, D.C.; Masson-Delmotte, V.; Zhai, P.; Tignor, M.; Poloczanska, E.; Weyer, N.M. The Ocean and Cryosphere in a Changing Climate. In *IPCC Special Report on the Ocean and Cryosphere in a Changing Climate*; Cambridge University Press: Cambridge, UK, 2019; p. 1155. [CrossRef]

32. IPCC Working Group III: Climate Change 2022 Mitigation of Climate Change. Available online: https://report.ipcc.ch/ar6/wg3/IPCC_AR6_WGIII_Full_Report.pdf (accessed on 20 December 2022).

33. Mostafavi, M.; Delpeche-Ellmann, N.; Ellmann, A.; Jahanmard, V. Determination of Accurate Dynamic Topography for the Baltic Sea Using Satellite Altimetry and a Marine Geoid Model. *Remote Sens.* **2023**, *15*, 2189. [CrossRef]

34. Varbla, S.; Ågren, J.; Ellmann, A.; Poutanen, M. Treatment of tide gauge time series and marine GNSS measurements for vertical land motion with relevance to the implementation of the Baltic Sea Chart Datum 2000. *Remote Sens.* **2022**, *14*, 920. [CrossRef]

35. Bingham, R.J.; Knudsen, P.; Andersen, O.; Pail, R. An initial estimate of the North Atlantic steady-state geostrophic circulation from GOCE. *Geophys. Res. Lett.* **2011**, *38*. [CrossRef]

36. Knudsen, P.; Bingham, R.; Andersen, O.; Rio, M.H. Enhanced mean dynamic topography and ocean circulation estimation using GOCE preliminary models. *J. Geod.* **2011**, *85*, 861–879. [CrossRef]

37. Knudsen, P.; Andersen, O.; Maximenko, N. A new ocean mean dynamic topography model, derived from a combination of gravity, altimetry and drifter velocity data. *Adv. Space Res.* **2021**, *68*, 1090–1102. [CrossRef]

38. Dean, R.G.; Houston, J.R. Recent sea level trends and accelerations: Comparison of tide gauge and satellite results. *Coast. Eng.* **2013**, *75*, 4–9. [CrossRef]

39. Räike, A.; Oblomkova, N.; Svendsen, L.M.; Kaspersson, R.; Haapaniemi, J.; Eklund, K.; Brynska, W.; Hytteborn, J.; Tornbjerg, H.; Kotilainen, P.; et al. Background Information on the Baltic Sea Catchment Area for the Sixth Baltic Sea Pollution Load Compilation (PLC-6). 2019. Available online: https://helcom.fi/wp-content/uploads/2020/01/PLC-6-background-report.pdf (accessed on 20 December 2022).

40. Ekman, M. Climate changes detected through the world's longest sea level series. *Glob. Planet. Change* **1999**, *21*, 215–224. [CrossRef]

41. Dailidienė, I.; Davulienė, L.; Tilickis, B.; Stankevičius, A.; Myrberg, K. Sea level variability at the Lithuanian coast of the Baltic Sea. *Boreal Environ. Res.* **2006**, *11*, 109–121.

42. Tervo, M.; Poutanen, M.; Koivula, H. Tide gauge monitoring using GPS. In Proceedings of the Dynamic Planet: Monitoring and Understanding a Dynamic Planet with Geodetic and Oceanographic Tools IAG Symposium, Cairns, Australia, 22–26 August 2005; Springer: Berlin/Heidelberg, Germany, 2007; pp. 75–79. [CrossRef]

43. Richter, A.; Groh, A.; Dietrich, R. Geodetic observation of sea-level change and crustal deformation in the Baltic Sea region. *Phys. Chem. Earth Parts A/B/C* **2012**, *53*, 43–53. [CrossRef]

44. Lyszkowicz, A.; Bernatowicz, A. Geocentric changes of the mean sea level of the Baltic Sea from altimeter and tide gauge data. In Proceedings of the 2018 Baltic Geodetic Congress (BGC Geomatics), Olsztyn, Poland, 21–23 June 2018; IEEE: New York, NY, USA, 2018; pp. 202–206. [CrossRef]

45. Madsen, K.S.; Høyer, J.L.; Suursaar, Ü.; She, J.; Knudsen, P. Sea level trends and variability of the Baltic Sea from 2D statistical reconstruction and altimetry. *Front. Earth Sci.* **2019**, *7*, 243. [CrossRef]

46. Kapsi, I.; Kall, T.; Liibusk, A. Sea Level Rise and Future Projections in the Baltic Sea. *J. Mar. Sci. Eng.* **2023**, *11*, 1514. [CrossRef]

47. Pajak, K.; Blaszczak-Bak, W. Baltic sea level changes from satellite altimetry data based on the OptD method. *Acta Geodyn. Geomater.* **2019**, *16*, 235–244. [CrossRef]

48. Couhert, A.; Cerri, L.; Legeais, J.F.; Ablain, M.; Zelensky, N.P.; Haines, B.J.; Lemoine, F.G.; Bertiger, W.I.; Desai, S.D.; Otten, M. Towards the 1 mm/y stability of the radial orbit error at regional scales. *Adv. Space Res.* **2015**, *55*, 2–23. [CrossRef]

49. Ekman, M. Postglacial rebound and sea level phenomena, with special reference to Fennoscandia and the Baltic Sea. *Suom. Geodeettisen Laitok. Julk.* **1993**, *115*, 7–70.

50. Jahanmard, V.; Delpeche-Ellmann, N.; Ellmann, A. Towards realistic dynamic topography from coast to offshore by incorporating hydrodynamic and geoid models. *Ocean Model.* **2022**, *180*, 102124. [CrossRef]

51. Jahanmard, V.; Hordoir, R.; Delpeche-Ellmann, N.; Ellmann, A. Quantification of hydrodynamic model sea level bias utilizing deep learning and synergistic integration of data sources. *Ocean Model.* **2023**, *186*, 102286. [CrossRef]

52. Schwabe, J.; Ågren, J.; Liebsch, G.; Westfeld, P.; Hammarklint, T.; Mononen, J.; Andersen, O.B. The Baltic Sea Chart Datum 2000 (BSCD2000): Implementation of a common reference level in the Baltic Sea. *Int. Hydrogr. Rev.* **2020**, *29*, 63–82.

53. Cazenave, A.; Llovel, W. Contemporary sea level rise. *Annu. Rev. Mar. Sci.* **2010**, *2*, 145–173. [CrossRef] [PubMed]

54. Masters, D.; Nerem, R.S.; Choe, C.; Leuliette, E.; Beckley, B.; White, N.; Ablain, M. Comparison of global mean sea level time series from TOPEX/Poseidon, Jason-1, and Jason-2. *Mar. Geod.* **2012**, *35* (Suppl. 1), 20–41. [CrossRef]

55. Dieng, H.B.; Cazenave, A.; Von Schuckmann, K.; Ablain, M.; Meyssignac, B. Sea level budget over 2005–2013: Missing contributions and data errors. *Ocean Sci.* **2015**, *11*, 789–802. [CrossRef]

56. Nerem, R.S.; Beckley, B.D.; Fasullo, J.T.; Hamlington, B.D.; Masters, D.; Mitchum, G.T. Climate-change–driven accelerated sea-level rise detected in the altimeter era. *Proc. Natl. Acad. Sci. USA* **2018**, *115*, 2022–2025. [CrossRef] [PubMed]

57. Altman, D.G.; Bland, J.M. Standard deviations and standard errors. *bmj* **2005**, *331*, 903. [CrossRef] [PubMed]

58. Hamlington, B.D.; Chambers, D.P.; Frederikse, T.; Dangendorf, S.; Fournier, S.; Buzzanga, B.; Nerem, R.S. Observation-based trajectory of future sea level for the coastal United States tracks near high-end model projections. *Commun. Earth Environ.* **2022**, *3*, 230. [CrossRef]

59. Chang, J.H.; Lee, W.S. A sliding window method for finding recently frequent itemsets over online data streams. *J. Inf. Sci. Eng.* **2004**, *20*, 753–762. [CrossRef]

60. Ku-Mahamud, K.R.; Zakaria, N.; Katuk, N.; Shbier, M. Third Asia International Conference on Modelling & Simulation. In Proceedings of the 2009 Third Asia International Conference on Modelling & Simulation, Bandung, Indonesia, 25–29 May 2009; IEEE: New York, NY, USA, 2009; pp. 45–50. [CrossRef]

61. Delpeche-Ellmann, N.; Giudici, A.; Rätsep, M.; Soomere, T. Observations of surface drift and effects induced by wind and surface waves in the Baltic Sea for the period 2011–2018. *Estuar. Coast. Shelf Sci.* **2021**, *249*, 107071. [CrossRef]

62. Rajabi-Kiasari, S.; Delpeche-Ellmann, N.; Ellmann, A. Forecasting of absolute dynamic topography using deep learning algorithm with application to the Baltic Sea. *Comput. Geosci.* **2023**, *178*, 105406. [CrossRef]

63. Gräwe, U.; Klingbeil, K.; Kelln, J.; Dangendorf, S. Decomposing mean sea level rise in a semi-enclosed basin, the Baltic Sea. *J. Clim.* **2019**, *32*, 3089–3108. [CrossRef]

64. Weisse, R.; Dailidienė, I.; Hünicke, B.; Kahma, K.; Madsen, K.; Omstedt, A.; Parnell, K.; Schöne, T.; Soomere, T.; Zhang, W.; et al. Sea level dynamics and coastal erosion in the Baltic Sea region. *Earth Syst. Dyn.* **2021**, *12*, 871–898. [CrossRef]

65. Pindsoo, K.; Soomere, T. Basin-wide variations in trends in water level maxima in the Baltic Sea. *Cont. Shelf Res.* **2020**, *193*, 104029. [CrossRef]

66. Delpeche-Ellmann, N.; Mingelaitė, T.; Soomere, T. Examining Lagrangian surface transport during a coastal upwelling in the Gulf of Finland, Baltic Sea. *J. Mar. Syst.* **2017**, *171*, 21–30. [CrossRef]

67. Jakimavičius, D.; Kriaučiūnienė, J.; Šarauskienė, D. Assessment of wave climate and energy resources in the Baltic Sea nearshore (Lithuanian territorial water). *Oceanologia* **2018**, *60*, 207–218. [CrossRef]

68. Tuomi, L.; Rautiainen, L.; Passaro, M. *User Manual Along-Track Data Baltic + SEAL. Project: ESA AO/1-9172/17/I-BG-BALTIC+ BALTIC+ Theme 3 Baltic+ SEAL (Sea Level) Requirements Baseline Document/BG-BALTIC+ SEAL (Sea Level) Category: ESA Express Procurement Plus-EXPRO+ Deliverable: D1.1 Code: TUM_BSEAL_RBD*; Baltic SEAL: München, Germany, 2020; Available online: http://balticseal.eu/wp-content/uploads/2020/04/Baltic_SEAL_D1.1_RequirementsBaselineDoc_V3.1-signed.pdf (accessed on 9 October 2023).

69. Müller, K. (Ed.) *Coastal Research in the Gulf of Bothnia*; Springer Science & Business Media: Berlin, Germany, 1982; Volume 45, Available online: https://link.springer.com/book/9789061930983 (accessed on 9 October 2023).

70. Bonsdorff, E.; Blomqvist, E.M.; Mattila, J.; Norkko, A. Long-term changes and coastal eutrophication. Examples from the Aland Islands and the Archipelago Sea, northern Baltic Sea. *Ocean. Acta* **1997**, *20*, 319–329.

71. Mäkinen, J.; Ihde, J. The permanent tide in height systems. In *Observing Our Changing Earth*; Springer: Berlin/Heidelberg, Germany, 2009; pp. 81–87. [CrossRef]

72. Boucher, C.; Altamimi, Z. Memo: Specifications for Reference Frame Fixing in the Analysis of a EUREF GPS Campaign. *Version* **2011**, *8*, 18-05. Available online: http://etrs89.ensg.ign.fr/memo-V8.pdf (accessed on 9 October 2023).

73. Barbosa, S.M. Quantile trends in Baltic sea level. *Geophys. Res. Lett.* **2008**, *35*, L22704. [CrossRef]

74. Kollo, K.; Ellmann, A. Geodetic reconciliation of tide gauge network in Estonia. *Geophysica* **2019**, *54*, 27–38. Available online: https://www.geophysica.fi/pdf/geophysica_2019_54_1_027_kollo.pdf (accessed on 9 October 2023).

75. Vestøl, O.; Ågren, J.; Steffen, H.; Kierulf, H.; Tarasov, L. NKG2016LU: A new land uplift model for Fennoscandia and the Baltic Region. *J. Geod.* **2019**, *93*, 1759–1779. [CrossRef]

76. Ågren, J.; Strykowski, G.; Bilker-Koivula, M.; Omang, O.; Märdla, S.; Forsberg, R.; Ellmann, A.; Oja, T.; Liepins, I.; Parseliunas, E.; et al. The NKG2015 gravimetric geoid model for the Nordic-Baltic region. In Proceedings of the 1st Joint Commission 2 and IGFS Meeting International Symposium on Gravity, Geoid and Height Systems, Thessaloniki, Greece, 19–23 September 2016; pp. 19–23.

77. Agha Karimi, A.; Bagherbandi, M.; Horemuz, M. Multidecadal sea level variability in the Baltic Sea and its impact on acceleration estimations. *Front. Mar. Sci.* **2021**, *8*, 702512. [CrossRef]

78. Olivieri, M.; Spada, G. Spatial sea-level reconstruction in the Baltic Sea and in the pacific Ocean from tide gauges observations. *Ann. Geophys.* **2016**, *59*, P0323. [CrossRef]

79. Omstedt, A.; Pettersen, C.; Rodhe, J.; Winsor, P. Baltic Sea climate: 200 yr of data on air temperature, sea level variation, ice cover, and atmospheric circulation. *Clim. Res.* **2004**, *25*, 205–216. [CrossRef]

80. Lehmann, A.; Getzlaff, K.; Harlaß, J. Detailed assessment of climate variability in the Baltic Sea area for the period 1958 to 2009. *Clim. Res.* **2011**, *46*, 185–196. [CrossRef]

81. Soomere, T.; Pindsoo, K.; Kudryavtseva, N.; Eelsalu, M. Variability of distributions of wave set-up heights along a shoreline with complicated geometry. *Ocean Sci.* **2020**, *16*, 1047–1065. [CrossRef]

82. Mostafavi, M.; Delpeche-Ellmann, N.; Ellmann, A. Accurate sea surface heights from Sentinel-3A and Jason-3 retrackers by incorporating high-resolution marine geoid and hydrodynamic models. *J. Geod. Sci.* **2021**, *11*, 58–74. [CrossRef]

83. Naeije, M.; Di Bella, A.; Geminale, T.; Visser, P. CryoSat Long-Term Ocean Data Analysis and Validation: Final Words on GOP Baseline-C. *Remote Sens.* **2023**, *15*, 5420. [CrossRef]

84. HELCOM, Climate Change in the Baltic Sea. 2021 Fact Sheet. Baltic Sea Environment Proceedings n°180. HELCOM/Baltic Earth 2021. Available online: https://helcom.fi/post_type_publ/climate-change-in-the-baltic-sea-2021-fact-sheet/ (accessed on 9 October 2023).

Curriculum vitae

Personal data:

Name:	Majid Mostafavi
Date of birth:	07. October. 1989
Place of birth:	Tehran, Iran
Citizenship:	Iran

Contact data:

E-mail:	majid.mostafavi@taltech.ee / majid.mostafavi@live.com

Education:

2019–2023	Tallinn University of Technology, PhD
2012–2015	Tehran Azad University, MSc
2008–2012	Tehran Azad University, BSc

Language competence:

Persian	Native
English	Fluent
German	Intermediate
Estonian	Elementary

Professional employment:

2019–2024	Tallinna Tehnikaülikool, PhD student

Publications

Articles in peer-reviewed journals indexed in reputable databases (ETIS 1.1):

- Mostafavi, M., Ellmann, A., and Delpeche-Ellmann, N., 2024. Long-term and Decadal Sea Level Trend of the Baltic Sea using Along-track Satellite Altimetry. Remote Sens. 16, 760. https://doi.org/10.3390/rs1605076.
- Mostafavi, M., Delpeche-Ellmann, N., Ellmann, A. and Jahanmard, V., 2023. Determination of Accurate Dynamic Topography for the Baltic Sea Using Satellite Altimetry and a Marine Geoid Model. Remote Sensing, 15(8), p. 2189. DOI: 10.3390/rs15082189
- Mostafavi, M., Delpeche-Ellmann, N. and Ellmann, A., 2021. Accurate sea surface heights from Sentinel-3A and Jason-3 retrackers by incorporating high-resolution marine geoid and hydrodynamic models. Journal of Geodetic Science, 11(1), pp. 58–74. DOI: 10.1515/jogs-2020-0120.
- Mostafavi, M., Rooh, S., Emadi, R., and Torabi Azad, M., 2018. River Monitoring Over Amazon and Danube Basin Using Multi-Mission Satellite Radar Altimetry. J Hydrogeol Hydrol Eng 7: 2. of, 10, pp. 12–14. DOI: 10.4172/2325-9647.1000166.
- Mirsane, H., Maghsoudi, Y., Emadi, R. and Mostafavi, M., 2018. Automatic Coastline Extraction Using Radar and Optical Satellite Imagery and Wavelet-IHS Fusion Method. International Journal of Coastal, Offshore and Environmental Engineering, 3(2), pp. 11–20. DOI: 10.29252/ijcoe.2.2.11.

Other publications (ETIS 5.2):

- Mostafavi, M. et al., 2023, Accurate Dynamic Topography by Satellite Altimetry and Marine Geoid Model, 13th Coastal Altimetry Workshop & Coastal Altimetry Training, 6-10 February 2023, Universidad de Cádiz, Spain.
- Mostafavi M., 2023, Satellite Altimetry and Hydrodynamic Model derived Accurate Dynamic Topography utilizing Marine Geoid Model in Baltic Sea (2017-2019). DOI: 10.17882/94461.
- Mostafavi, M. et al., 2023. Quantifying Absolute Dynamic Topography by Synergy of Satellite, Geoid and Hydrodynamic Model. XXVIII General Assembly of the International Union of Geodesy and Geophysics (IUGG), 11-17 July, Berlin, Germany. GFZ German Research Centre for Geosciences. DOI: 10.57757/IUGG23-2385.
- Mostafavi, M. et al., 2023. Coastal sea level trend using multi mission along track satellite altimetry for the Baltic Sea. XXVIII General Assembly of the International Union of Geodesy and Geophysics (IUGG), 11-17 July, Berlin, Germany. GFZ German Research Centre for Geosciences. DOI: 10.57757/IUGG23-4967.
- Mostafavi, M. et al., 2022. Satellite Altimetry Performance Verified to Enhanced Hydrodynamic Model of the Baltic Sea. Living Planet Symposium (LPS22), Bonn, Germany, May 23-27, 2022. European Space Agency's 2022 Living Planet Symposium.
- Mostafavi, M. et al., 2022. 24 Years Sea Level Trend of Baltic Sea Using Resampled Machine Learning Satellite Altimetry Data. Living Planet Symposium (LPS22), Bonn, Germany, May 23-27, 2022: European Space Agency's 2022 Living Planet Symposium.
- Mostafavi, M, et al., 2022. Applying Machine Learning with Satellite Altimetry data for prediction of Absolute Dynamic Topography for the Baltic Sea. Nordic Geodetic Commission General Assembly: Planet Ocean and Geodesy, Copenhagen, Denmark, September 5-8, 2022. Nordic Geodetic Commission, 26–26.
- Mostafavi, M. et al., 2022. Reconstruction of Dynamic Topography Using Cyclostationary Empirical Orthogonal Functions in the Baltic Sea. Nordic Geodetic Commission General Assembly: Planet Ocean and Geodesy, Copenhagen, Denmark, September 5-8, 2022. Nordic Geodetic Commission, 25–25.
- Mostafavi, M, et al., 2022. Absolute Sea Level Trend Forecasting using an Ensemble Empirical Mode Decomposition Method for Satellite Altimetry data. Nordic Geodetic Commission General Assembly: Planet Ocean and Geodesy, Copenhagen, Denmark, September 5-8, 2022. Session: 1. Planet Ocean and Geodesy: Nordic Geodetic Commission, 26–26.
- Mostafavi, M, et al., 2022. Bi-directional Sea Level Data Gap-filling using High-inclination Satellite Altimetry Missions in Baltic Sea. Science Forum and BALTICITIES Kick off meeting 2022, 30 November- 1 December. Helsinki City Hall, Finland.
- Mostafavi, M. et al., 2021. 24 Years Sea Level Trend of Gulf of Finland Using Resampled Machine Learning Satellite Altimetry Data. The Gulf of Finland Science Days 2021, "New start for the Gulf of Finland co-operation", Tallinn, 29-30 November 2021. Estonian Academy of Sciences, 64.

- Amini, A., Agar, P., Mostafavi, M., Sabilian, A. and Roohi, S. 2021. A New Approach of Waveform Re-Tracking for Monitoring Sea Surface Topography in the Strait of Hormuz.
- Mostafavi, M. et al., 2020. River Water Level Monitoring from Satellite Radar Altimetry Multi Missions: A Case Study of the Amazon and Danube Rivers.12th Coastal Altimetry, ESA-ESRIN, 4-7 February 2020. Frascati (Rome), Italy: ESA

Elulookirjeldus

Isikuandmed

Nimi:	Majid Mostafavi
Sünniaeg:	07.10.1989
Sünnikoht:	Tehran, Iraan
Kodakondsus:	Iraani

Kontaktandmed

E-post:	majid.mostafavi@taltech.ee / majid.mostafavi@live.com

Hariduskäik

2019–2023	Tallinna Tehnikaülikool, PhD
2012–2015	Tehran Azad University, MSc

Keelteoskus

Pärsia keel	emakeel
Inglise keel	kõrgtase
Saksa keel	edasijõudnud
Eesti keel	algtase

Teenistuskäik

2019–2024	Tallinna Tehnikaülikool, doktorant

Teaduspublikatsioonide nimekiri on esitatud inglise keelse elulookirjelduse all.